

Modeling of 3D Magnetostrictive Systems with Application to Galfenol and Terfenol-D Transducers

Dissertation

Presented in Partial Fulfillment of the Requirements for the Degree
Doctor of Philosophy in the Graduate School of The Ohio State
University

By

Suryarghya Chakrabarti, B.S.

Graduate Program in Mechanical Engineering

The Ohio State University

2011

Dissertation Committee:

Marcelo Dapino, Advisor

Rajendra Singh

Ahmet Kahraman

Junmin Wang

© Copyright by
Suryarghya Chakrabarti
2011

Abstract

Magnetostrictive materials convert energy between the mechanical and magnetic domains. They deform in response to applied magnetic fields and change their magnetic state when stressed. Because these processes are due to moment realignments, magnetostrictive materials are well suited for sensing and actuation mechanisms with a bandwidth of a few kHz. Significant research has been focused on two magnetostrictive alloys: Terfenol-D ($\text{Tb}_x\text{Dy}_{1-x}\text{Fe}_{1.9-2.0}$, $0.27 \leq x \leq 0.3$) and Galfenol ($\text{Fe}_{1-x}\text{Ga}_x$, $0.15 \leq x \leq 0.3$), for their ability to produce large magnetostrictive strains at moderate fields. Both alloys have strengths and weaknesses. Terfenol-D has higher energy density and magnetomechanical coupling factor than Galfenol but it is brittle and suffers from poor machinability. Galfenol on the other hand has excellent structural properties. It can be machined, welded, and extruded into complex shapes for use in transducers with 3D functionality. However, Galfenol exhibits lower energy density (almost ten times smaller than Terfenol-D) and lower magnetomechanical coupling.

When employing magnetostrictive materials in transducers, advanced modeling tools are necessary both at the constitutive and system level. At the constitutive level these materials exhibit nonlinear and hysteretic coupling between the magnetic and mechanical domains while at the system level electromagnetic coupling is present. This work addresses the development of a unified modeling framework to serve as a design tool for 3D, dynamic magnetostrictive transducers. Maxwell's equations for

electromagnetics and Navier’s equations for mechanical systems are formulated in weak form and coupled using a generic constitutive law. The overall system is approximated hierarchically; first, piecewise linearization is used to describe quasistatic responses and perform magnetic bias calculations. A linear dynamic solution with piezomagnetic coefficients computed at the bias point describes the system dynamics for moderate inputs. Dynamic responses at large input fields and stresses are described through an implicit dynamic solution method based on the trapezoidal rule. The framework simultaneously describes the effect of magneto-structural dynamics, flux leakage, eddy currents, and transducer geometry. Being a fully coupled formulation, it yields system level input-output relationships and is applicable to both actuators and sensors. The framework is unified in the sense that it works for any magnetostrictive material as long as a differentiable 3D constitutive law for the material is supplied.

An anhysteretic 3D discrete energy-averaged constitutive law for Galfenol is incorporated into the framework to describe the dynamic performance of Galfenol transducers. A parameter identification algorithm is developed which takes as input the 1D magnetomechanical characterization curves of the material and calculates the 3D constitutive model parameters. The parameter identification algorithm is integrated with the finite element model such that the only inputs required are the constitutive parameters for passive materials (permeability, conductivity, Young’s modulus etc.), the transducer geometry, and the 1D magnetostrictive material characterization curves. A case study on a Galfenol unimorph actuator illustrates the model’s ability to accurately describe the dynamic mechanical and magnetic response of Galfenol transducers.

A new energy-averaged model is formulated for Terfenol-D based on an implicit definition of domain volume fractions and a weighted anisotropy energy. The model is shown to simultaneously describe the strain-field and magnetization-stress behavior of a large number of Terfenol-D alloys including the composition commercially produced by Etrema Products, Inc. The model is formulated in a form which is straightforward to implement in the unified finite element framework. Since most Terfenol-D transducers are axisymmetric, the 3D unified model is reduced to a 2D axisymmetric form to exploit the axisymmetric geometry of the transducer. A case study on a hydraulically amplified Terfenol-D mount actuator illustrates the framework's ability to model Terfenol-D transducers. Apart from describing the dynamic electrical and mechanical response of the actuator, a parametric study on the transducer reveals key design parameters which can be changed to achieve over 100 % performance improvement compared to the current design.

To my parents

who taught me to appreciate the good things in life

Acknowledgments

I would like to thank my advisor Prof. Marcelo Dapino for his excellent guidance and support during my Ph.D work. The time and effort he has spent towards my overall development as a researcher is invaluable. Through his constant attention to details, Prof. Dapino has helped me understand the importance of achieving perfection in technical documentation and presentation of research. I will strive hard to implement his advice throughout my professional life.

I am grateful to my committee members Prof. Ahmet Kahraman, Prof. Raj Singh, and Prof. Junmin Wang for their support and cooperation. I owe my knowledge of dynamic systems and vibrations largely to Prof. Kahraman. It is because of his excellent teaching that I developed love and understanding of the subject.

Thanks to my colleagues in the Smart Materials and Structures Laboratory for their friendship and understanding. I had many insightful discussions with Phillip Evans, who helped me understand the intricacies of modeling nonlinear systems. My interaction with Arjun Mahadevan, Shravan Bharadwaj, Liang Shu, John Larson, and Ryan Hahnen over the last few years was particularly enjoyable.

I want to thank my badminton friends with whom I had the most amazing time during my graduate life. Badminton kept me physically and mentally fit, and gave me a reason to be happy whenever I would hit a wall in my research. In particular I would like to mention Tejas Kinjawadekar, Satyajeet Deshpande, and Shubhanan

Deshpande who gave me immense support during my tenure as the president of the badminton club.

I give special thanks to my girlfriend Anjali Singhal for her unconditional love and support during my graduate studies. She has been the only person with whom I have shared all my joys and sorrows during the last five years. Finally, I am deeply indebted to my parents for making me the person I am and teaching me to distinguish right from wrong.

Vita

June 2, 1985	Born - Jamshedpur, JH INDIA
2007	B.S. Manufacturing Science and Engineering
2007-present	Graduate Research Associate, Ohio State University Columbus, OH

Publications

Research Publications

S. Chakrabarti and M.J. Dapino, “A dynamic model for a displacement amplified magnetostrictive driver for active mounts,” *Smart Materials and Structures*, Vol. 19, pp. 055009, 2010.

S. Chakrabarti and M.J. Dapino, “ Nonlinear finite element model for 3D Galfenol systems,” *Smart Materials and Structures*, Vol. 20, pp. 105034, 2011.

S. Chakrabarti and M.J. Dapino, “Hydraulically amplified Terfenol-D actuator for adaptive powertrain mounts,” *ASME Journal of Vibration and Accoustics*, (accepted for publication)

S. Chakrabarti, M.J. Dapino, “Hydraulically amplified magnetostrictive actuator for active engine mounts,” *in Proceedings of the ASME conference on Smart Materials Adaptive Structures and Intelligent Systems*, Vol. 1, pp. 795-802, October 2008.

S. Chakrabarti, M.J. Dapino, “Design and modeling of a hydraulically amplified magnetostrictive actuator for automotive engine mounts,” *in Proceedings of SPIE*, Vol. 7290, April 2009.

S. Chakrabarti, M.J. Dapino, “Modeling of a displacement amplified magnetostrictive actuator for active mounts,” *in Proceedings of the ASME conference on Smart Materials Adaptive Structures and Intelligent Systems*, Vol. 2, pp. 325-334, October 2009.

S. Chakrabarti, M.J. Dapino, “Design and modeling of a hydraulically amplified magnetostrictive actuator for automotive engine mounts,” *in Proceedings of SPIE*, Vol. 7645, April 2010.

S. Chakrabarti, M.J. Dapino, “Coupled axisymmetric finite element model of a magneto-hydraulic actuator for active engine mounts,” *in Proceedings of SPIE*, Vol. 7979, April 2011.

S. Chakrabarti, M.J. Dapino, “3D dynamic finite element model for magnetostrictive Galfenol-based devices,” *in Proceedings of SPIE*, Vol. 7978, April 2011.

Fields of Study

Major Field: Mechanical Engineering

Studies in:

- Smart Materials and Structures
- Finite element method
- Electromagnetism
- Nonlinear dynamics

Table of Contents

	Page
Abstract	ii
Dedication	v
Acknowledgments	vi
Vita	viii
List of Figures	xiv
List of Tables	xix
List of Symbols	xx
1. Introduction	1
1.1 Overview of Magnetostrictive Materials	1
1.2 Terfenol-D	4
1.3 Galfenol	9
1.4 Constitutive Modeling	11
1.5 Magnetostrictive Transducer Modeling	14
1.6 Research Objectives and Dissertation Outline	20
2. Background	26
2.1 Electromagnetism	26
2.1.1 Special cases	28
2.1.2 Electrodynamics of moving media	30
2.1.3 Electric and magnetic potentials	31
2.1.4 Boundary conditions	34
2.1.5 Magnetic materials	37

2.2	Structural Dynamics	40
2.2.1	Stress	41
2.2.2	Strain	43
2.2.3	Equations of motion	48
2.3	Magnetomechanical Coupling	49
2.3.1	Magnetomechanical coupling at the system level	49
2.3.2	Magnetomechanical coupling at the material level	51
2.4	Numerical Solution of Electro-magneto-mechanical systems	53
3.	Unified Approach to Modeling Magnetostrictive Transducers	64
3.1	Finite Element Framework	65
3.2	Incorporation of Nonlinear Coupled Constitutive Laws	65
3.2.1	Piecewise-linear implementation	67
3.2.2	Nonlinear dynamic implementation	71
3.3	Implementation on COMSOL and MATLAB	74
4.	Galfenol Transducers	82
4.1	Parameter estimation of a discrete energy-averaged model from 1D measurements	83
4.1.1	Discrete energy-averaged constitutive model	85
4.1.2	Parameter optimization procedure	90
4.1.3	Results	94
4.2	Galfenol Constitutive Law Incorporation	99
4.3	Case Study: Galfenol Unimorph Actuator	102
4.3.1	Piecewise-linear quasistatic solution	103
4.3.2	Linear dynamic simulation about bias point	103
4.3.3	Nonlinear dynamic simulation	108
4.4	Concluding Remarks	108
5.	Terfenol-D Transducers	111
5.1	Fully Coupled Discrete Energy Averaged Model for TerfenolD	111
5.1.1	Problem description	114
5.1.2	Model formulation	116
5.1.3	Anhysteretic model results	123
5.1.4	Extension to hysteretic model	125
5.1.5	Hysteretic model results	127
5.1.6	Concluding remarks	131
5.2	Coupled Axisymmetric Finite Element Model for TerfenolD trans- ducers	134

5.2.1	Incorporation of constitutive laws	136
5.3	Case Study: Terfenol-D Mount Actuator	140
5.3.1	Magneto-hydraulic actuator (MHA) design	143
5.3.2	Model augmentation	144
5.3.3	Results and parametric study	147
6.	Summary and Future Work	154
6.1	Research Summary	155
6.1.1	Unified model	155
6.1.2	Application to Galfenol transducers	156
6.1.3	Application to Terfenol-D transducers	157
6.2	Contributions	160
6.3	Findings	162
6.4	Future Work	162
Appendices		164
A.	Vector Calculus	164
A.1	Vector Calculus Operators	164
A.2	Vector Calculus Identities	165
A.3	Theorems	165
B.	Magneto-Hydraulic Actuator for Active Engine Mounts: Design and Comparison with a Commercial Mount Actuator	167
B.1	Introduction to Active Engine Mounts	167
B.2	Actuator Design	168
B.2.1	Estimation of actuator requirements	168
B.2.2	Actuator gain	169
B.2.3	Magnetic circuit and preload	170
B.3	Benchmarking Against a Commercial Electrodynamic Mount Actuator	171
B.3.1	Electrical power requirement	173
C.	Magneto-hydraulic Actuator Drawings	174
D.	Dynamic model for a displacement amplified magnetostrictive driver for active mounts	183
D.1	Model Structure	183

D.2	Magnetic Field Diffusion	184
D.3	Jiles-Atherton Equations	185
D.4	Mechanical Model	187
D.5	Model Results	188
Bibliography		191

List of Figures

Figure	Page
1.1 Crystallographic structure of Terfenol-D.	6
1.2 1D transducer-level modeling approaches with magnetic field diffusion (a) one-way coupled model (b) two-way coupled model.	17
2.1 Boundary surface between media 1 and 2 with an elemental cylinder and loop used to derive the boundary conditions on \mathbf{B} and \mathbf{H}	35
2.2 Body with cutting plane S and the corresponding force vector $\Delta \mathbf{f}$ acting on ΔS	42
2.3 Traction vectors on the three coordinate planes at a point P	42
2.4 Cartesian stress components in their positive sense.	44
2.5 Deformation of a body from a reference condition to current condition.	44
2.6 Cartoon depiction of magnetostriction.	52
3.1 Flowchart of the piecewise-linear solution process.	70
3.2 Outline of a single time step of the nonlinear dynamic solution algo- rithm. The flowchart shows how quantities at time $t + \Delta t$ are obtained with knowledge about all variables at time t	75
3.3 Screenshot of the global expressions relating flux density and strain to the vector magnetic potential and displacements.	76
3.4 Screenshots of the weak and time-dependent weak terms (dweak) for the mechanical subdomain.	77

3.5	Screenshots of the weak and time-dependent weak terms (dweak) for the magnetic subdomain.	78
3.6	Screenshot showing the function definition for HX and declaration of the derivative functions.	80
4.1	A schematic representation for the solution of a 3D finite element model showing how a parameter optimization algorithm can eliminate the need for complex 3D measurements and subsequent interpolation. . .	85
4.2	Comparison of model outputs with and without normalizing \mathbf{m}^k . Simulations run at constant prestresses of 20, 50 and 80 MPa.	89
4.3	Extracted anhysteretic curves from measurements on single crystal $\langle 100 \rangle$ $\text{Fe}_{81.5}\text{Ga}_{18.5}$ grown with FSZM at constant stress values of 0.32, 8.00, 13.4, 23.1, 32.3 MPa (compression) and constant field values of 1.85, 3.24, 5.65, 8.88 kA/m (Measurements collected by Phillip Evans [33]).	92
4.4	Comparison of anhysteretic model to the extracted anhysteretic curves from measurements on a $\text{Fe}_{81.5}\text{Ga}_{18.5}$ sample. Actuation measurements are at constant compressive stresses of 0.32, 8, 13.4, 23.1, and 32.3 MPa while sensing measurements are at constant bias fields of 1.85, 3.24, 5.65, and 8.88 kA/m.	95
4.5	Anhysteretic model fit to the extracted anhysteretic curves with optimized parameters for unannealed $\langle 100 \rangle$ textured polycrystalline $\text{Fe}_{81.6}\text{Ga}_{18.4}$. Measurements are at constant compressive pre-stresses of 1.38 , 13.8, 27.6, 41.4, 55.2, 69.0, 82.7, and 96.5 MPa.	96
4.6	Anhysteretic model fit to the extracted anhysteretic curves with optimized parameters for annealed $\langle 100 \rangle$ textured polycrystalline $\text{Fe}_{81.6}\text{Ga}_{18.4}$. Measurements are at constant compressive pre-stresses of 1.38 , 13.8, 27.6, 41.4, 55.2, 69.0, 82.7, and 96.5 MPa.	97
4.7	Galfenol unimorph actuator used for model validation, (a) actuator configuration, and (b) finite element mesh.	103
4.8	Quasistatic model results, (a) voltage-deflection, (b) voltage-current. .	104

4.9	Experimental and model results at 10 Hz, (a) tip displacement, (b) current.	105
4.10	Experimental and model results at 50 Hz, (a) tip displacement, (b) current.	105
4.11	Experimental and model results at 100 Hz, (a) tip displacement, (b) current.	106
4.12	Experimental and model results at 200 Hz, (a) tip displacement, (b) current.	106
4.13	Experimental and model results at 500 Hz, (a) tip displacement, (b) current.	107
4.14	Actuator response to harmonic excitation at 10 Hz.	109
4.15	Actuator response to harmonic excitation at 50 Hz.	109
4.16	Actuator response to harmonic excitation at 100 Hz.	109
4.17	Actuator response to harmonic excitation at 200 Hz.	110
5.1	Comparison of magnetization and magnetostriction curves for Terfenol-D at 13.5 MPa compressive stress [31] with the Armstrong model [2] and the Discrete Energy Averaged Model (DEAM) [32].	114
5.2	Armstrong model [2] and DEAM [32] with high smoothing factors for 13.5 and 41.3 MPa prestress. The higher prestress curve shows the reappearance of kinks in both models.	115
5.3	Armstrong model [2] and DEAM [32] with low smoothing factors showing the magnitude of the two kinks with increasing stress.	116
5.4	(a) Ω -field and (b) strain-field curves for compressive prestresses of 0, 6.5, 13.5, 27.4, 41.3, and 55.3 MPa.	121
5.5	(a) Ω -stress and (b) magnetization-stress curves for constant bias fields of 0, 32.2, 64.4, 96.6, 128.8, 161 and 193.2 kA/m.	122

5.6	Flowchart for the anhysteretic model. Details of the energy minimization is shown in section 4.1.1.	124
5.7	Comparison of the two modeling approaches with actuation data [62] for compressive prestresses of 6.9, 15.3, 23.6, 32.0, 40.4, 48.7, 57.1, and 65.4 MPa.	125
5.8	Performance of the two modeling approaches in predicting the stress-strain behavior of Terfenol-D [62] for bias field values of 11.9, 31.8, 55.7, 79.3, 103, 127, 151, and 175 kA/m with parameters estimated from the strain-field curves.	126
5.9	Comparison of the two modeling approaches with sensing data from [51] for bias magnetic fields of 16.1, 48.3, 80.5, 112.7, 144.9, and 193.2 kA/m.	126
5.10	Comparison of hysteretic model with data from Moffett et al [62] for compressive prestresses of 6.9, 15.3, 23.6, 32.0, 40.4, 48.7, 57.1, and 65.4 MPa. Parameters optimized for actuation curves.	130
5.11	Comparison of hysteretic model with sensing data from Kellogg et al [62] for bias magnetic fields of 16.1, 48.3, 80.5, 112.7, 144.9, and 193.2 kA/m.	130
5.12	Comparison of hysteretic model with magnetostriction measurements provided by Etrema Products Inc. [43] for compressive prestresses of 1, 4, 8, and 16 KSI (6.9, 27.6, 55.2, 110.4 MPa).	133
5.13	Flowchart showing the process followed to incorporate the Terfenol-D constitutive law in the model.	141
5.14	Physical actuator (left) and cutout (right).	143
5.15	Geometry of the transducer used in this study.	145
5.16	Axial magnetic field distribution in the magnetic circuit due to the permanent magnet.	148
5.17	Comparison of modeled voltage-displacement and voltage-current loops with measurements. (a) 20 Hz, (b) 50 Hz, (c) 100 Hz, and (d) 200 Hz.	152

5.18	Percentage improvement in the unloaded stroke of the actuator with variation in (a) mechanical model parameters and (b) magnetic model parameters.	153
B.1	Schematic of the active mount model (Lee et. al. [57]).	169
B.2	Assembled and exploded view of the magneto-hydraulic actuator. . .	170
B.3	Displacement in mechanically-free condition with both devices driven at full power.	172
B.4	Free displacement orders of (a) MHA and (b) CMA.	173
B.5	Power consumption of the MHA and CMA.	173
D.1	Flowchart for the actuator model.	184
D.2	Schematic representation of the actuator's mechanical model.	187
D.3	Output pushrod displacement at different actuation frequencies. . . .	189
D.4	Output pushrod displacement orders.	190
D.5	Output pushrod displacement magnitude and phase (first order). . . .	190

List of Tables

Table	Page
1.1 Table summarizing the capabilities of prior work on magnetostrictive transducer modeling	25
3.1 Subdomain expressions for the piecewise-linear model	81
4.1 Optimized model parameters for the different data sets.	98
4.2 Mean normalized modeling error % with model parameters found using different levels of experimental information.	99
5.1 Mean % Errors obtained with the full and reduced models. Max. % errors in ().	129
5.2 Optimized model parameters for the different data sets.	132
B.1 List of Terfenol-D actuator components.	171

List of Symbols

Symbol	Description
\mathbf{A}	Magnetic vector potential
\mathbf{B}	Magnetic flux density
\mathbf{C}_e	Discrete curl operator
\mathbf{c}^k	k^{th} easy axis
\mathbf{D}	Electric displacement
\mathbf{E}	Electric field
\mathbf{F}	Vector of internal forces
F_c	Coulomb friction force
F_s	Static friction force
\mathbf{G}_e	Discrete gradient operator
\mathbf{G}^k	Gibbs free energy in the vicinity of the k^{th} easy axis
\mathbf{H}	Magnetic field
\mathbf{J}	Electrical current density
\mathbf{m}^k	local energy minimum about the k^{th} easy axis
$\hat{\mathbf{m}}^k$	normalized local energy minimum about the k^{th} easy axis
\mathbf{N}^A	Shape function matrix for the magnetic degrees of freedom
\mathbf{N}^u	Shape function matrix for the mechanical degrees of freedom
\mathbf{q}_e^A	Nodal magnetic degrees of freedom in an element
\mathbf{q}_e^u	Nodal mechanical degrees of freedom in an element
\mathbf{R}	Vector of external forces

Symbol	Description
\mathbf{S}	Strain
\mathbf{S}_m	Magnetostrictive strain tensor
\mathbf{T}	Stress
\mathbf{T}^M	Maxwell's stress tensor
ΔV_C	change in fluid chamber volume due to deformation of the casing
ΔV_f	change in fluid chamber of the engine mount actuator
ΔV_L	change in fluid chamber volume due to deformation of the driven piston
v_L	sliding velocity of the driven piston seal
ΔV_P	change in fluid chamber volume due to deformation of the drive piston
Z_L	bristle deflection state for the driven piston seal
β	bulk modulus of the hydraulic fluid
ϵ	permittivity
λ_{100}	Magnetostriction coefficient for the $\langle 100 \rangle$ orientations
λ_{111}	Magnetostriction coefficient for the $\langle 111 \rangle$ orientations
μ	permeability
Ω	smoothing factor
Φ	Magnetic scalar potential
ρ_e	Volume density of free electric charges
σ	Electrical conductivity
σ_0	LuGre bristle stiffness coefficient
σ_1	LuGre bristle damping coefficient
σ_2	LuGre viscous damping coefficient
ξ_{an}^k	volume fraction of domains along the k^{th} local minimum
$\bar{\xi}$	Homogeneous domain volume fractions

Chapter 1: INTRODUCTION

1.1 Overview of Magnetostrictive Materials

Magnetostrictive materials exhibit coupling between the magnetic and mechanical energy domains. They undergo lattice deformation in response to applied magnetic fields and change their magnetic state when stressed. Short response times (in the millisecond range) combined with resolutions in the order of microstrains make these materials well-suited to precision sensing and actuation mechanisms.

Magnetostriction was first found in ferromagnetic materials such as nickel, cobalt, iron and their alloys. However, magnetostrictive strains were restricted to below 100 ppm. Early applications such as use of magnetostrictive nickel-based alloys in SONAR transducers during the first world war generated interest in magnetostrictive material research. However, emergence of piezoelectric ceramic materials capable of delivering higher frequency bandwidths and strains of the order of 1000 ppm in the late 1940s [60] shifted the focus away from magnetostrictive materials.

In the 1970s researchers at the US Naval Ordinance Laboratory first synthesized a new alloy of terbium, iron and dysprosium called Terfenol-D which is capable of generating giant strains (≈ 1600 ppm) with moderate applied magnetic fields (200 kA/m) at room temperature. The emergence of Terfenol-D (Ter - terbium, fe - iron, D-

dysprosium, and nol - Naval Ordinance Laboratory) generated renewed interest in magnetostrictive transducer technologies. Being brittle and thus difficult to machine, Terfenol-D is available only in 1D geometries such as rods or bars. As a result, transducers employing Terfenol-D primarily have one-dimensional functionality. Further, because of its low tensile strength, Terfenol-D transducers are restricted to work in the compressive regime only.

To overcome the poor machinability and low tensile strength of Terfenol-D, a new magnetostrictive alloy of iron and gallium (Galfenol) was developed at the Naval Ordinance Laboratory. Galfenol uniquely combines moderate magnetostriction (≈ 250 ppm) at very low fields (≈ 10 kA/m) and steel-like structural properties. It can be machined, rolled, welded, and extruded into intricate shapes opening up avenues for magnetostrictive transducers with 3D functionality. Galfenol is capable of withstanding tension, compression, and shock loads making it uniquely well-suited for application in sensors and actuators which can perform structural functions as well.

The response of magnetostrictive materials is nonlinear and history dependent. The main nonlinearities are due to anisotropy and saturation. However, magnetostrictive transducers are often biased and operated with moderate inputs so that the resulting material response can be approximated by a set of linear simultaneous equations known as the linear piezomagnetic relationships:

$$\Delta \mathbf{B} = \boldsymbol{\mu}^T \Delta \mathbf{H} + \mathbf{d} \Delta \mathbf{T}, \quad (1.1)$$

$$\Delta \mathbf{S} = \mathbf{d}^T \Delta \mathbf{H} + \mathbf{s}^H \Delta \mathbf{T}. \quad (1.2)$$

Here \mathbf{B} and \mathbf{H} are the magnetic flux density and magnetic field vectors while \mathbf{S} and \mathbf{T} are mechanical stress and strain tensors. $\boldsymbol{\mu}^T$ is the differential permeability at constant stress while \mathbf{s}^H is the compliance at constant stress. The matrix \mathbf{d} relates

strain to field and flux density to stress. Together $\mu^{\mathbf{T}}$, $\mathbf{s}^{\mathbf{H}}$, and \mathbf{d} are known as the piezomagnetic coefficients. Although these equations are a considerably simplified representation of the actual processes, they are helpful in defining figures of merit of a magnetostrictive material. For example, *free strain* is defined as the strain induced in the sample at constant stress ($\mathbf{S} = \mathbf{d}^{\mathbf{T}}\Delta\mathbf{H}$). This gives a measure of the maximum stroke that can be obtained from a sample. Similarly, *blocked stress* is the stress generated in the rod at zero strain ($\mathbf{s}^{\mathbf{H}-1}\mathbf{d}\Delta\mathbf{H}$), and gives a measure of the maximum force that the sample can generate.

Another feature of these materials which can be understood through the linear piezomagnetic equations is the ΔE effect or change in apparent Young's modulus of the material. The compliance under magnetically blocked condition ($\Delta\mathbf{B} = 0$) can be obtained as $\mathbf{s}^{\mathbf{H}} - d^{\mathbf{T}}(\mu^{\mathbf{T}})^{-1}\mathbf{d}$. Thus the compliance in the magnetically blocked condition reduces by $d^{\mathbf{T}}(\mu^{\mathbf{T}})^{-1}\mathbf{d}$.

Assuming linear material behavior, the energy density of the material is given by half the product of blocked stress and free strain. For a 1D case when the applied magnetic field (ΔH) is low enough to assume linear operation, the energy density is given by $d^2\Delta H/s^H$. An important factor which determines the transduction efficiency of the material is the magnetomechanical coupling factor,

$$k = \frac{G_{coupling}}{\sqrt{G_{mech}G_{mag}}}, \quad (1.3)$$

where the energies can be defined by breaking the Gibbs free energy into three parts using (1.1) and (1.2):

$$\begin{aligned} G &= \frac{1}{2}(\mathbf{T} \cdot \mathbf{S} + \mathbf{H} \cdot \mathbf{B}) \\ &= \underbrace{\frac{1}{2}\mathbf{T} \cdot \mathbf{s}^{\mathbf{H}}\mathbf{T}}_{G_{mech}} + \underbrace{\frac{1}{2}(\mathbf{T} \cdot \mathbf{d}^{\mathbf{T}}\mathbf{H} + \mathbf{H} \cdot \mathbf{d}\mathbf{T})}_{G_{coupling}} + \underbrace{\frac{1}{2}\mathbf{H} \cdot \mu^{\mathbf{T}}\mathbf{H}}_{G_{mag}}. \end{aligned} \quad (1.4)$$

For the 1D case the magnetomechanical coupling coefficient simplifies to $d/\sqrt{\mu^T s^H}$.

The following sections of this chapter provide a review of the magnetomechanical properties and structure of Terfenol-D and Galfenol, followed by a literature review on available constitutive and transducer level models for these materials. The last section introduces the main objectives of this research and outlines the flow of this dissertation.

1.2 Terfenol-D

Early magnetostrictive alloys of nickel, cobalt, and iron provided magnetostriction below 100 ppm. The emergence of piezoelectrics and electrostrictives capable of producing induced strains on the order of 1000 ppm over a bandwidth of 1 MHz and higher hindered research on magnetostrictive materials. In the early 1960s, with the advancement in low temperature measurement techniques, researchers at the US Naval Ordnance Laboratory found that some rare earth metals such as terbium and dysprosium showed giant magnetostriction ($\approx 5,000$ ppm) at temperatures close to absolute zero but the strain became negligible close to room temperatures. These elements were alloyed with iron to form compounds of the form RFe_2 which showed high magnetostriction at room temperature. However, because of the large magnetocrystalline anisotropy, the fields required to reach the saturation strains were extremely large ($\approx 10^6$ kA/m) [22]. It was observed that the anisotropy constants of $TbFe_2$ and $DyFe_2$ had opposite signs which led to attempt at combining the two alloys to achieve anisotropy cancellation. Subsequent studies led to the determination of an optimal combination of terbium and dysprosium which minimizes the anisotropy. Clark et

al. [19] first suggested the alloy $\text{Tb}_{0.3}\text{Dy}_{0.7}\text{Fe}_2$ with the fourth order anisotropy constant $K_1 = -0.06 \times 10^6$ which exhibited saturation magnetostriction of ≈ 1600 ppm at room temperatures at moderate applied magnetic fields (≈ 200 kA/m).

Crystal structure and magnetization process

The negative anisotropy constant of Terfenol-D implies that moments prefer to align along the $\langle 111 \rangle$ orientations when no stress or field is applied, i.e., the $\langle 111 \rangle$ directions are the easy magnetization axes. Terfenol-D has a large magnetostriction anisotropy, where the strain constant along the $\langle 111 \rangle$ directions is much larger than the $\langle 100 \rangle$ directions ($\lambda_{111} = 1640$ ppm, $\lambda_{100} = 90$ ppm). Fabrication of $\langle 111 \rangle$ -oriented single crystals is complex and time consuming [81]. Under normal conditions Terfenol-D exhibits a $[11\bar{2}]$ dendritic growth with $[111]$ plane normal (Figure 1.1). The application of field and stress along the $[11\bar{2}]$ axis gives rise to five sets of $\langle 111 \rangle$ directions with different energies (depending on their angle with $[11\bar{2}]$) - $[11\bar{1}]$ (19.5°), $[1\bar{1}\bar{1}]$ and $[\bar{1}\bar{1}\bar{1}]$ (61.9°), $[111]$ and $[\bar{1}\bar{1}\bar{1}]$ (90°), $[1\bar{1}\bar{1}]$ and $[\bar{1}\bar{1}1]$ (118.1°), $[11\bar{1}]$ (160.5°). For single crystal samples, the magnetization process is expected to proceed by domains preferentially aligning along the first set of $\langle 111 \rangle$ for positive saturation fields ($+H_s$), to the last set for negative saturation fields ($-H_s$) and occupying the intermediate sets for moderate fields. However, the crystal growth along $[11\bar{2}]$ allows for the easy development of twins formed through a 180° rotation about the $[111]$ twin plane normal thus making the magnetization process more complex. The inability of domain-rotation based models in describing Terfenol-D's slow approach to saturation has mainly been attributed to this twin formation. Many theories have been put forward regarding the effect of twins on the magnetization process of Terfenol-D. Clark et al. [25] proposed

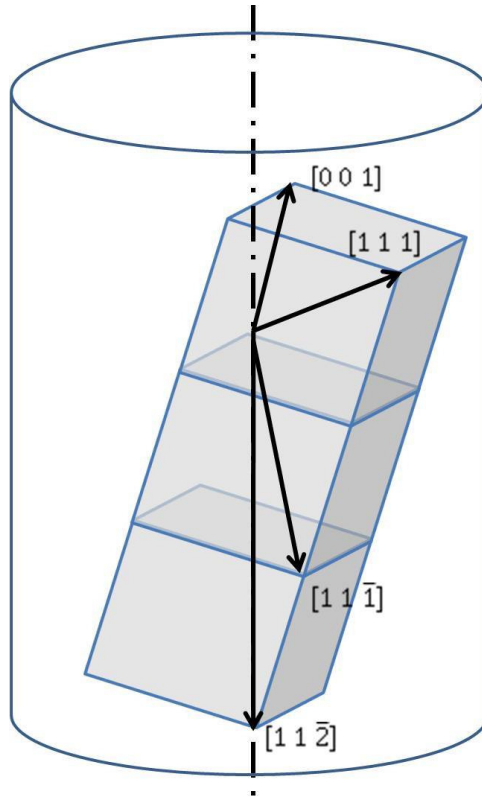


Figure 1.1: Crystallographic structure of Terfenol-D.

that the two twins react very differently to applied fields. While the magnetization of one twin jumps to the $[11\bar{1}]$, the other twin undergoes gradual domain rotation leading to a slow approach to saturation. However, no quantitative analysis of this theory was presented. Zhao and Lord [88] proposed that the magnetization process of Terfenol-D can be broken up into two phases. In the first stage, the domains aligned along the $[111]$ axis by the applied stress rapidly redistribute to the $[11\bar{1}]$ direction closest to the applied field as well as to the $[1\bar{1}\bar{1}]$ and $[\bar{1}\bar{1}\bar{1}]$ directions; and during the second stage, the domains occupying the $[1\bar{1}\bar{1}]$ and $[\bar{1}\bar{1}\bar{1}]$ directions redistribute to the $[11\bar{1}]$ successively by non-180 domain-wall motion. Only qualitative comparisons with measurements were presented. Zhao and Lord [89] proposed another theory that the redistribution of domains results in the accumulation of magnetic charges on the twin boundaries and consequently gives rise to demagnetization fields normal to the plane of twin boundary. The parent or twin platelet dimension along $[111]$ axis was found to be much smaller than those along $[11\bar{2}]$ and $[110]$ respectively and therefore, each platelet can be considered as an infinitely thin foil with plane normal along $[111]$. No validation for the model against experiments was provided. The micromagnetic phase field model of Huang and Jin [42] showed that there is strong interaction between the domains across the twin boundaries giving rise to complex domain microstructure evolution. There is considerable magnetization rotation causing domains to significantly deviate from the easy axes. The exact magnetization process for twinned Terfenol-D crystals remains unclear.

Characterization

Basic characterization of magnetostrictive materials for actuation requires the determination of the magnetization-field and strain-field curves at different prestress values. Determination of the sensing curves (magnetization and strain versus stress at different bias fields) is useful for sensor design. Additional characterization includes the effects of temperature variation. Clark et al. [22] reported room temperature magnetostriction for the alloy $\text{Tb}_{0.3}\text{Dy}_{0.7}\text{Fe}_2$. Clark et al. [19] showed that the anisotropy constants for the alloy were low but strongly dependent on chemical composition. It was also shown that anisotropy constants became positive below 10°C , thus making the $\langle 100 \rangle$ axes magnetically easy and drastically reducing the saturation magnetostriction. Clark et al. [21] reported magnetostriction measurements on twinned $\text{Tb}_{0.27}\text{Dy}_{0.73}\text{Fe}_2$. The measurements performed by Moffett et al. [62] on grain oriented $\text{Tb}_{0.27}\text{Dy}_{0.73}\text{Fe}_{1.93}$ has been used for transducer design and constitutive model validation for Terfenol-D. Clark et al. [20] investigated the temperature dependence of Terfenol-D's magnetostriction. Busbridge [10] and Mei et al. [61] reported the magnetostrictive properties of twin-free $\langle 111 \rangle$ oriented single crystal Terfenol-D. Kellogg et al. [51] characterized the Young's modulus of Terfenol-D based on both major and minor loops. Etrema Products, Inc. provide magnetostriction measurements for commercially available Terfenol-D [43]. Characterization of Terfenol-D is challenging because of the apparent high variability in performance of the material fabricated under similar conditions [45]. A statistical analysis of the material properties by Dapino et al. [27] revealed that such variations are typically due to imperfect control of operating conditions during testing.

1.3 Galfenol

Magnetostrictive iron-gallium (Fe-Ga) alloys (Galfenol) promise to address some of the limitations of Terfenol-D [24]. Fe-Ga alloys exhibit moderate saturation magnetostriction (250 ppm) at low fields (10 kA/m). The reduced saturation magnetostriction is compensated by its mechanical reliability, ability to be manufactured with conventional techniques such as machining [78] and welding [79], and ability to be packaged into smaller transducers due to its high permeability.

Crystal structure and magnetization process

Galfenol has a body centered cubic structure with Ga atoms randomly substituted throughout the lattice structure. Galfenol has a positive fourth order anisotropy constant which implies that the $[100]$ directions are the easy axes. Fe-Ga crystals exhibit a $[100]$ growth front with $\lambda_{100} \gg \lambda_{111}$. The fact that the axis of maximum magnetostriction is also the easy magnetization axis and the axis for crystal growth, makes the magnetization process much simpler than that of Terfenol-D. A typical Galfenol rod has its $[100]$ and $[\bar{1}00]$ directions aligned with the sample axis and the other four $\langle 100 \rangle$ orientations orthogonal to this axis. This means that application of compressive stress aligns the moments along one of these four orientations while application of field along the axis results in gradual rotation of domains towards the axial $[100]$ direction. At a critical field, the Zeeman energy overcomes the anisotropy and moments switch to the easy axis of application of field. Unlike Terfenol-D since the direction of field application is aligned with the easy axis orientation, no further domain rotation takes place and hence there is no noticeable increase in magnetization or magnetostriction after saturation.

Characterization

Clark et al. [26] showed that maximum room temperature magnetostriction in these alloys was obtained at 19 at. % Ga. Experiments conducted on Fe-Ga alloys with Ga concentrations varying from 4 % to 27 % revealed that there are two peaks in λ_{100} as a function of Ga content, with $\lambda_{100} = 265$ ppm near 19 % Ga and $\lambda_{100} = 235$ ppm near 27 % Ga [23]. Kellogg et al. [54] performed tensile testing on [100] and [110] single crystal Galfenol (17 % Ga). Both samples had an ultimate tensile strength above 500 MPa and displayed negative Poisson's ratio. Kellogg et al. [53] compared the performance of single crystal $\text{Fe}_{81}\text{Ga}_{19}$ and polycrystalline $\text{Fe}_{81}\text{Ga}_{19}$ textured using 3 different techniques (directionally solidified, extruded, and extruded plus annealed [52]). Saturation magnetostriction of the single crystal sample reduced by 12 % over the -21 °C to 80 °C temperature range. Magnetostrictive strains in the polycrystalline samples were found to fall far short of their single crystal counterparts. Wun-Fogle et al. [85] measured the properties of stress-annealed Galfenol and found that with stress-annealing nearly full magnetostrictive response can be obtained without applying any pre-stress. Summers et al. [77] characterized polycrystalline $\text{Fe}_{81.6}\text{Ga}_{18.4}$ grown by the zone melt crystal growth method. It was shown that upon machining, a 15 % increase in magnetostriction was observed due to removal of off-axis grains located at the periphery of the sample. Rafique et al. [67] measured the magnetocrystalline anisotropy constants of five different Galfenol alloys with Ga concentration ranging from 5 % to 20 %. Atulasimha et al. [5] measured the sensing response of two different Galfenol alloys with 19 % and 24 % Ga. The lower % Ga sample was found to have better sensitivity in the 20-80 MPa stress range while the higher % Ga sample was more sensitive in the 0-20 MPa range. Evans [33]

characterized [100] oriented single crystal Galfenol alloys with 18.5 % and 20.9 % Ga (both research grade and production grade). Remarkable kinematic reversibility in magnetomechanical coupling in both grades was reported.

1.4 Constitutive Modeling

Jiles-Atherton model

The Jiles-Atherton model [49] was first formulated for isotropic ferromagnetic hysteresis. The total magnetization is modeled as the sum of a reversible component due to domain wall bowing and an irreversible component due to domain wall motion. The non-linear shape of the M-H curve is obtained by using an analytical function for the anhysteretic magnetization. The exact form of the function depends on the form of anisotropy in the material. The model has been extended to include the effects of anisotropy [68, 69] and stress [48] on the magnetization of the material. The extensions were achieved by making appropriate modifications to the anhysteretic magnetization curve. Hysteresis in the magnetization versus stress curves was modeled by extending the original law of approach [48] to include terms which are analogous to those in the Rayleigh law [58]. Extensions were also made to include dynamic terms in the formulation to model eddy current losses [46]. Although the original model is scalar in nature, a vector generalization was proposed by Bergqvist [9]. This model has been widely used to describe the dynamic response of Terfenol-D based actuators [30, 74].

Phenomenological models

Phenomenological models use the Taylor series expansion of an energy functional and use analytical relationships (usually formulated phenomenologically) to express

the derivatives of the energy functional with respect to the independent variables. Carman et al. [12] expanded the Gibbs free energy in a Taylor series up to the second order terms resulting in an expression for strain which is quadratically dependent on field with one coefficient dependent on the pre-stress. The model produces reasonable fits for the strain-field curves of Terfenol-D in the low and moderate field region. However, it is incapable of describing saturation and thus has significant deviations from measurements at high fields. Wan et al. [82] extended the model by using hyperbolic tangent functions in the Gibbs free energy definition to model magnetic saturation. However, extremely high errors ($\approx 100\%$) were recorded in the strain-field curves in the moderate field region. Zheng and Liu [90] increased the accuracy of these models by including higher order terms in the Gibbs energy expansion and using a Langevin function to describe the nonlinear magnetization-field relationship. Additional terms are added to model the effects of varying stress on magnetization. Similarly, strain is described as a function of stress and magnetization enabling the model to describe the ΔE effect. The model is well suited for engineering applications as it can generate the strain-field curves with good accuracy with only five parameters which can be easily estimated from measurements.

Models based on energy-averaging

Energy-averaged models describe bulk properties of materials based on an expected value of a number of possible energy states. The Armstrong model [3] describes the magnetization and magnetostriction behavior of anisotropic magnetostrictive materials based on energy-weighted averaging principles. The energy functional is based

on the sum of magnetocrystalline anisotropy, magnetoelastic, and magnetic field energy terms. Bulk magnetization and strain are obtained as an expected value of a large number of possible energy states (or moment orientations) with an energy-based probability density function. An energy distribution parameter, ω , models the effect of material impurities by controlling the spread in the density function distribution about the minimum. A larger value of ω implies a material with more impurities and hence a wider distribution. To increase the model efficiency, Armstrong et al. [2] restricted the choice of moment orientations to the easy magnetization axes and used a discrete version of the probability density function. Hysteresis is introduced by considering irreversible losses in the evolution of volume fractions due to field application only. As a result the model yields hysteretic curves for field application and anhysteretic curves for stress application. The increase in model efficiency due to restriction of possible moment orientations however came at the cost of reduced accuracy. This is because with fixed orientations, the model could not describe domain rotation exhibited at low fields and moderate stresses by both Terfenol-D and Galfenol. Atulasimha [4] overcame this restriction in the Armstrong model by expanding the number of possible orientations to 98 important crystallographic directions.

Evans and Dapino [32] proposed an alternative approach to increase the efficiency of the energy-averaged class of models. Instead of evaluating the energies over a large number of possible orientations, they restricted the number of possible orientations by considering only those orientations which minimized an energy functional locally defined around each easy axis. Macroscopic behavior is obtained by conducting an energy weighted sum of the magnetization and magnetostriction of domains in each of

these orientations. This approach models domain rotation as the minima are allowed to rotate with the application of field and stress.

The discrete energy-averaged model employs a new general formulation for magnetocrystalline anisotropy energy. Rather than defining a global energy which includes the local energy minima or preferred orientations, the energy is defined locally about the known preferred orientations. This approach has two significant advantages. First, the model can be applied to materials with any crystal symmetry which is particularly useful for Galfenol as its crystal symmetry can be changed through stress annealing. Secondly, it allows for the derivation of analytical expressions for orientations which minimize the energy functional locally defined about each easy axis. These analytical expressions enable the model to preserve accuracy while restricting the choice of domain orientations to the local energy minima. This makes the model up to 100 times faster than previous energy weighting models. Another significant improvement offered by this model is that it describes magnetic hysteresis for both magnetic field and stress application. The effect of reversible changes in domain walls from wall bowing is included, while restricting the effect of irreversible processes so as to exclude the unphysical behavior of negative susceptibility.

1.5 Magnetostrictive Transducer Modeling

The main idea behind magnetostrictive transducer modeling is to obtain relationships between transducer level input-output variables (voltage, current, field, displacement) by solving the equations describing the structural and magnetic dynamics of the system. Complete magnetostrictive transducer models use constitutive laws to

couple three main components - voltage-field relationships, structural dynamics, and eddy currents.

Description of voltage-field relationships and eddy currents typically requires information of complete transducer geometry and solution of the 3D Maxwell's equations. Hence, many 1D and 2D transducer models take magnetic field as the input and assume magnetostatic operation eliminating the need to solve Maxwell's equations. In some cases, effects of variation of stress on magnetization of the magnetostrictive material are neglected resulting in a unidirectionally coupled model where the constitutive law takes magnetic field as the input and computes the magnetostriction which is used as an input to the structural dynamics model. Dapino et al. [30] followed this principle and coupled the Jiles-Atherton model with a partial differential equation describing the axial vibrations. The main advantage of this approach is its quick convergence due to the assumed one-way coupling. However, the accuracy of these models may be poor when stress variation has considerable effects on the magnetostrictive material. In such cases, a constitutive law capable of describing the effects of stress on magnetization must be incorporated and the model must be solved with two-way coupling [29].

In case of dynamic operation at high frequencies, the effect of eddy currents may become significant. Eddy currents result in heating up of the material and a spatial variation in the magnetic field distribution. Eddy currents inside the magnetostrictive material can be described either in the constitutive law or (for cylindrical samples) by solving the 1D magnetic field diffusion equation. Huang et al. [41] followed the first procedure and coupled a lumped parameter vibratory model with the Jiles-Atherton

equations extended to model eddy currents [46]. Sarawate and Dapino [74] implemented the second strategy by coupling the 1D magnetic field diffusion equation with a lumped parameter model describing the structural dynamics using the Jiles-Atherton constitutive law. A constant permeability and conductivity assumption yields an analytical solution of the diffusion equation for harmonic field application. This provides an analytical expression for the radial variation in magnetic field inside the magnetostrictive rod. Since the vibratory model is not radially variant, an averaging must be done over the cross-section of the rod to reduce it to a scalar form. This averaging can either be done directly on the magnetic field [74] (before it is entered to the constitutive model) to obtain a mean field, or it can be done on a radially dependent magnetostriction (obtained by entering the radially dependent field in the constitutive model) to obtain an average magnetostriction which can be used as an input to the lumped parameter mechanical system model [14]. Both these works included a one-way coupled constitutive law. Evans [33] coupled a lumped parameter vibratory model and the radial diffusion equation using a fully-coupled discrete energy averaged constitutive law. The nonlinear two way coupled model is solved numerically using Newton-Raphson iterations. Figure 1.2 illustrates the difference between the one-way and two-way coupled modeling approaches with the magnetic diffusion equation.

Higher dimensional finite element models are significantly more complex than their one-dimensional counterparts due to implementation of nonlinear constitutive laws and Maxwell's equations in higher dimensions. Finite element formulations for electro-magneto-mechanical systems usually employ a scalar or a vector magnetic potential as the solution variable. The vector magnetic potential is kinematically related to magnetic flux density through the curl operator while the scalar magnetic

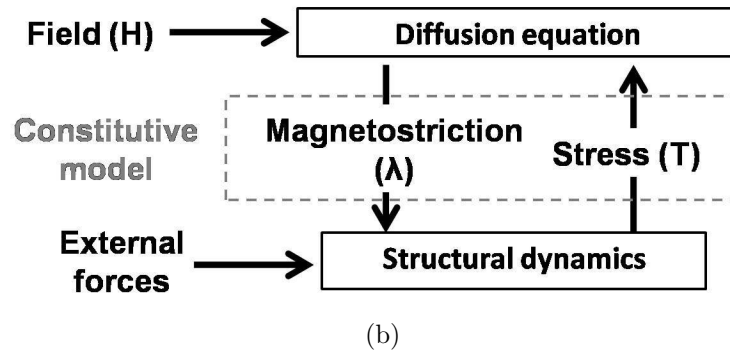
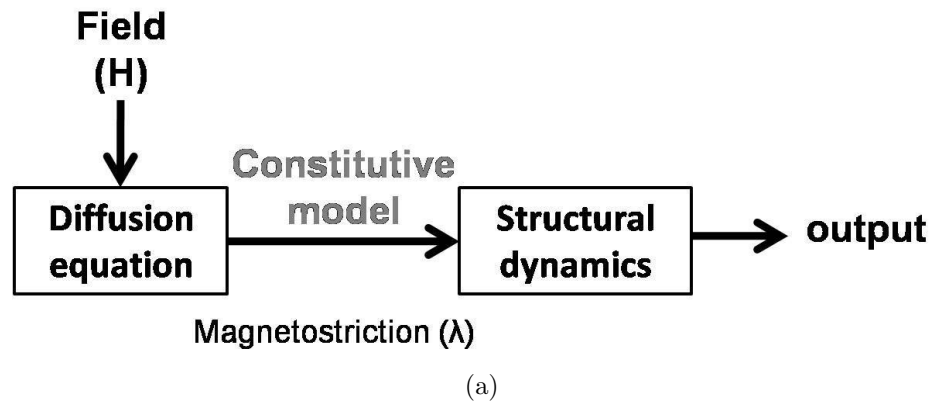


Figure 1.2: 1D transducer-level modeling approaches with magnetic field diffusion (a) one-way coupled model (b) two-way coupled model.

potential is kinematically related to magnetic field through the gradient operator. The advantage of using a vector magnetic potential is that eddy currents can be very conveniently modeled through the time derivative of the potential. However, it requires inversion of the constitutive model. The scalar magnetic potential, on the other hand does not require inversion of the constitutive law but necessitates additional techniques to model eddy currents [83].

Early works on two dimensional finite element modeling of magnetostrictive devices were magnetostatic in nature to avoid the complexities involved in modeling eddy currents. Benbouzid [7] formulated a vector magnetic potential based 2D bidirectionally coupled magnetostatic model where Terfenol-D constitutive behavior is incorporated using surface splines. The coupled problem is solved through successive mechanical and magnetic finite element computations. This is known as the weak coupling strategy as opposed to the strong coupling strategy in which both physics are solved simultaneously. Kannan and Dasgupta [50] formulated a scalar magnetic potential based 2D magnetostatic model with bi-directionally coupled magnetomechanical relations, current induced magnetic fields and electromagnetic body forces. A piecewise-linear solution process is used with constitutive laws incorporated in an incremental manner. Material model coefficients are obtained from bi-cubic spline fits to measurements. Zhou et al. [92] developed a dynamic finite element model of a unimorph actuator with one-way magnetomechanical coupling. Applied magnetic field is computed explicitly as a function of the current in the coil and axial coordinate. Constitutive nonlinearities are incorporated through the Zheng-Liu model [90]. The one way coupled 3D model of Kim and Jung [55] describes force due to magnetostriction driving a coupled fluid-structural model for a sonar transducer. Magnetic

field is computed *a priori* and magnetostriction is described by fitting sixth order polynomials to the strain-field characterization curves. A different polynomial is used for every different pre-stress.

All the models described above take as input externally applied field or compute the magnetic field explicitly as a function of applied currents. The models described next aim at modeling the full coupling between the electromagnetic and mechanical boundary value problems. Ghosh et al. [37] described a magnetostatic finite element model for composite laminates incorporating magnetostrictive materials modeled using a linear anhysteretic constitutive law. A comparison between a one-way coupled and a two-way coupled implementation revealed significant differences emphasizing the need for fully-coupled models. Aparicio and Sosa [65] described a 3D, fully-coupled vector magnetic potential based finite element model including dynamic effects but provided a very simple implementation for a magnetostrictive material with a single element. Slaughter [76] implemented a model for magnetostrictive transducers in the finite element software COMSOL by coupling the Structural Mechanics and AC/DC modules using linear piezomagnetic relations for the magnetostrictive material. Mudivartha et al. [63] used a fully-coupled, magnetostatic formulation to describe stress-induced flux density changes in Galfenol with no current-induced fields. An updated version of the model includes current induced fields but is still magnetostatic in nature [40]. Galfenol constitutive behavior is incorporated through look up tables generated *a priori* by running the Armstrong model [3] for a large number of induction and stress values. Although the Armstrong model is capable of describing 3D Galfenol behavior, look up tables were generated for 1D induction and stress

inputs. Evans and Dapino [35] presented a fully coupled dynamic model for 3D magnetostrictive transducers based on a vector magnetic potential based finite element formulation. Displacement currents and electromagnetic body forces are neglected. The model simultaneously describes the effects of eddy currents, structural dynamics, and flux leakage on transducer performance. Due to the restriction of COMSOL Multiphysics being unable to handle vectorized functions, linear constitutive behavior is assumed. Solution is obtained using the strong coupling method (simultaneous solution of multiple coupled physics).

1.6 Research Objectives and Dissertation Outline

The objectives of this research are to

1. develop a unified modeling framework for design and analysis of 3D magnetostrictive transducers driven over nonlinear regimes with dynamic inputs. The framework must
 - be sufficiently general such that it can be applied to a wide variety of magnetostrictive alloys
 - provide a structured platform to allow for incorporation of nonlinear coupled constitutive laws
 - describe effects of transducer geometry such as flux leakages and model dynamic magnetization losses (eddy currents)
 - yield relationships between transducer level input-output quantities such as voltage, current, force, and deflection

- be packaged together with a commercial software such that it can be used as a magnetostrictive transducer design tool by engineers
2. display the applicability of the framework to specific Terfenol-D and Galfenol transducers. This includes
 - development of constitutive models which describe the magnetomechanical behavior of Terfenol-D and Galfenol alloys and are in a format suitable for integration within the unified framework
 - formulation of a procedure to identify the constitutive model parameters from experimental characterization of these materials
 3. incorporate suitable techniques for efficiently solving large-scale nonlinear-coupled system of equations obtained from the modeling framework.

Chapter 2 reviews various fundamental concepts on electromagnetism, structural dynamics, magnetomechanical coupling, and methods of solving electro-magneto-mechanical systems. The section on electromagnetism consists of a brief explanation of Maxwell's equations along with common approximations used to simplify the system. Magnetic and electric potentials are introduced which reduce the number of equations to be solved. Sources of magnetism in magnetic materials are discussed with special focus on magnetization processes in ferromagnetic materials. The section on structural dynamics revises the fundamental concepts behind stress and strain, and derives the equations of motion for a loaded body. A brief section on magnetomechanical coupling describes magnetomechanical coupling both at the system and constitutive level. The last section deals with discussion of methods to solve the magnetic and mechanical boundary value problems. Weak form equations are derived for both the mechanical

and electromagnetic systems using the Galerkin's method of weighted residuals. A vector magnetic potential based finite element formulation using linear tetrahedral elements is shown and the resulting equations for a system with no magnetomechanical coupling is derived. This forms the basis of the work done in chapters 3-5. Chapter 3 represents the heart of the dissertation. It discusses the unified modeling framework while chapters 4 and 5 describe specific techniques used for modeling Galfenol and Terfenol-D transducers respectively using the unified model.

Unified approach to modeling magnetostrictive transducers

This chapter presents a generalized framework for modeling the dynamic performance of magnetostrictive transducers where the magnetostrictive driver is driven with large inputs such that the material behavior is nonlinear. The finite element method is used based on the weak formulations derived from Maxwell's equations for electromagnetics and Navier's equations for mechanical systems. Two different strategies are proposed for incorporation of magnetostrictive material constitutive laws depending on the operating conditions. For quasistatic conditions, a piecewise linear approach is adopted where the solution is obtained as a series of small incremental steps. Within every step the magnetostrictive material is modeled using the linear piezomagnetic equations with the piezomagnetic coefficients updated at the end of each step through analytical or numerical differentiation of the constitutive law. The coefficients are declared as interpolated data functions such that they can be computed at a few selected locations and obtained at the remaining nodes through interpolation, thereby increasing the computational efficiency of the model. The piecewise-linear model can be used either for obtaining the quasistatic major

loops of the transducer or for generating accurate bias points. A linear dynamic simulation with the piezomagnetic coefficients computed at the bias point can model the dynamic performance of the transducer successfully for moderate inputs. To model the dynamic response of transducers driven with large inputs, a nonlinear dynamic solution strategy is implemented in which an implicit time integration scheme based on the trapezoidal rule is combined with numerical inversion of the constitutive law. Finally, the implementation of the framework on COMSOL 3.5a is presented.

Galfenol transducers

This chapter incorporates a nonlinear discrete energy-averaged constitutive model for Galfenol into the general framework described in Chapter 3. First, a parameter optimization algorithm is proposed which takes as input the 1D characterization curves for the Galfenol alloy used in the transducer and calculates the 3D constitutive model parameters using a least squares optimization routine. The parameter optimization algorithm can be integrated with the finite element model such that the only external inputs required are the constitutive parameters of the passive materials, the transducer geometry, and the 1D characterization curves for Galfenol. Next, analytical differentiation of the constitutive model is carried out to evaluate the material Jacobian (the matrix of piezomagnetic coefficients) which is used in the piecewise-linear solution process. The constitutive law is numerically inverted to implement the nonlinear dynamic solution procedure. The model is validated with respect to experiments conducted on a Galfenol unimorph actuator.

Terfenol-D transducers

This chapter deals with the application of the unified modeling framework to Terfenol-D transducers. The chapter is split into three main sections. The first section deals with the development of an efficient 3D energy-averaged constitutive law capable of describing the full nonlinear magnetomechanical coupling in Terfenol-D. The second section deals with the reduction of the 3D finite element framework of chapter 3 to an axisymmetric model. This is useful because Terfenol-D is commercially available in cylindrical rods resulting in Transducers which are usually axisymmetric in nature. The third section deals with the validation of the model against measurements conducted on a hydraulically amplified Terfenol-D mount actuator. The example shows how the framework can be combined with additional physics such as fluid-structure interaction and friction.

Chapter 6 summarizes the key contributions of this dissertation as well as possible future work which can be done using this dissertation as a platform. The first appendix revises vector calculus identities and theorems used throughout the formulation. The next three deal with the development and lumped parameter modeling of the Terfenol-D engine mount actuator which is the subject for case study in Chapter 5.

Table 1.1: Table summarizing the capabilities of prior work on magnetostrictive transducer modeling

Model	1D/2D/3D	one-way/two-way coupling	magnetically static or dynamic (eddy currents)	electromagnetic body forces	linear/non-linear constitutive law	constitutive incorporation	law
Dapino et al. [30]	1D	one-way	static	No	nonlinear	model-based	
Dapino et al. [29]	1D	two-way	static	No	nonlinear	model-based	
Huang et al. [41]	1D	one-way	dynamic	No	nonlinear	model-based	
Sarawate et al. [74]	1D	one-way	dynamic	No	nonlinear	model-based	
Evans [33]	1D	two-way	dynamic	No	nonlinear	model-based	
Benbouzid [7]	2D	two-way	static	No	nonlinear	surface-splines	
Kannan et al. [50]	2D	two-way	static	Yes	nonlinear	bi-cubic splines	
Zhou et al. [92]	2D	one-way	static	No	nonlinear	model-based	
Kim et al. [55]	3D	one-way	static	No	nonlinear	sixth order polynomials	
Ghosh et al. [37]	3D	Both	static	No	linear	model-based	
Aparicio et al. [65]	3D	two-way	dynamic	Yes	-	-	
Slaughter et al. [76]	3D	two-way	static	No	linear	model-based	
Mudivarthi et al. [63],	3D	two-way	static	No	nonlinear	look-up tables	
Graham et al. [40],							
Evans et al. [35]	3D	two-way	dynamic	No	linear	model-based	
Model presented in this work	3D	two-way	dynamic	No	nonlinear	model-based	

Chapter 2: BACKGROUND

Distributed parameter modeling of magnetostrictive transducers consists of three main components - electromagnetism, structural dynamics, and solution of coupled systems. This chapter provides an overview of these three components. The section on electromagnetism describes the Maxwell's equations along with relevant boundary conditions. A brief description of magnetic materials reviews the different kinds of magnetic materials with emphasis on magnetization processes in ferromagnetic materials. The section on structural dynamics discusses the equations of motion along with the relevant boundary conditions. Finally, methods for solving electromagneto-mechanical systems are introduced with special emphasis on the finite element method. A vector magnetic potential based finite element formulation is presented, which is the basis for the framework in chapter 3.

2.1 Electromagnetism

Electromagnetism deals with the study of interdependence of electrical and magnetic quantities on each other. The magnetic variables are the magnetic flux density (\mathbf{B}) and its work conjugate magnetic field (\mathbf{H}), while the electrical variables are electric flux density (\mathbf{D}), its work conjugate - electric field (\mathbf{E}), and current density (\mathbf{J}).

Relationships between these quantities are summarized by the Maxwell's equations:

$$\nabla \times \mathbf{H} = \mathbf{J} + \frac{\partial \mathbf{D}}{\partial t}. \quad (2.1)$$

$$\nabla \times \mathbf{E} = -\frac{\partial \mathbf{B}}{\partial t}, \quad (2.2)$$

$$\nabla \cdot \mathbf{D} = \rho_e, \quad (2.3)$$

$$\nabla \cdot \mathbf{B} = 0, \quad (2.4)$$

where ρ_e is the volume density of free electric charges. Equation (2.1) is also known as Ampère's law (with Maxwell's correction) and it describes how magnetic fields are generated by electric currents or time varying electric flux densities. Equation (2.2) is known as the Faraday's law and it describes the generation of electric fields through a time varying magnetic flux density. The generated electric fields give rise to currents in an electrically conducting medium. These currents are known as eddy currents and their direction is such that the field they generate through (2.1) opposes the change in field which induced the currents. Equation (2.3) is known as the Gauss' law for electricity. It states that the divergence of the electric flux density depends on the electric charge density. This can also be stated as the flux of the electric displacement field over a Gaussian surface is equal to the free charges enclosed by the surface ($\Phi_{D,S} = Q_{free}$). Application of the divergence theorem yields (2.3). Similarly Gauss' law for magnetism (2.4) states that the divergence of the magnetic flux density should equal the magnetic charge density. However, due to the non-existence of magnetic monopoles the magnetic charge density is identically zero. This is because magnetic charges are always present in couples which cancel the divergence of each other resulting in a solenoidal (zero divergence) magnetic flux density. This difference

between the divergences of the electrical and magnetic flux density creates asymmetry between the magnetic and electrical variables.

Maxwell's equations must be supplemented with constitutive laws. For linear isotropic materials they can be written as

$$\mathbf{J} = \sigma \mathbf{E}, \quad \mathbf{B} = \mu \mathbf{H}, \quad \mathbf{D} = \epsilon \mathbf{E}. \quad (2.5)$$

Here σ is the electrical conductivity, μ is the magnetic permeability and ϵ is the dielectric constant of the material. These parameters may become tensors for anisotropic materials or even functions of different variables in case the material properties are nonlinear.

2.1.1 Special cases

The complexity of Maxwell's equations makes it extremely important to utilize any appropriate assumption to simplify the analysis. These simplifications are mostly on the basis of the time rate of change of variables involved in (2.1) and (2.2). This section presents two simplifying cases - one in which all dynamics are considered to be negligible and second in which only certain dynamics are neglected based on material properties and the frequency band of operation.

Electrostatics and magnetostatics

This is the simplest situation where there is no (or negligible) time dependence in both the electrical and magnetic quantities. The displacement current term drops out from (2.1) giving

$$\mathbf{J} = \nabla \times \mathbf{H}, \quad (2.6)$$

which implies that the current density \mathbf{J} follows the law

$$\nabla \cdot \mathbf{J} = 0, \quad (2.7)$$

since the divergence of curl is identically zero. This means that current lines are solenoidal (they either close in on themselves or extend to infinity). Similarly, the right hand side of (2.2) vanishes with the assumption of no magnetic flux density variation giving,

$$\nabla \times \mathbf{E} = 0. \quad (2.8)$$

The net outcome is that there is no interdependence between electric and magnetic fields and they can be analyzed separately. An electrostatic analysis is usually done to obtain the magnetic field distribution due to an applied current density.

Quasistationary magnetic fields

Depending on the time rate of variation of the inputs, and the properties of the material within which the equations are being solved, the effect of some dynamic terms can be considered to be negligible compared to others. Consider the case of harmonic time variation of the variables. Substituting the constitutive relationships for \mathbf{J} and \mathbf{D} in terms of \mathbf{E} from (2.5) into (2.2) and noting the harmonic variation of the electric field ($\mathbf{E} = \mathbf{E}_0 e^{i\omega t}$) one gets

$$\nabla \times \mathbf{H} = \sigma \mathbf{E}_0 e^{i\omega t} \left[1 + i \frac{\omega \epsilon}{\sigma} \right]. \quad (2.9)$$

If $\omega \epsilon / \sigma \ll 1$ then displacement currents can be neglected in comparison to conduction currents. Further, the frequency of operation should be such that Ohm's law is valid. For metals, this constraint is reached at a much lower frequencies than when the inequality is satisfied [56]. Still, almost all materials used in electromechanical

devices (including magnetostrictive transducers) satisfy both these requirements for frequency ranges in which they are operated (< 100 kHz). Thus the quasistationary magnetic field approximation is an extremely useful tool and has been used widely in formulations for electromechanical transducers. The modeling approach followed in the chapter 3 is also based on this approximation.

2.1.2 Electrodynamics of moving media

Often electromechanical transducers consist of moving parts which carry considerable current densities and are exposed to magnetic fields. In order to model electromagnetic systems with moving components, Maxwell's equations must be formulated in a moving coordinate system. For non-relativistic velocities (which is usually the case), the Maxwell-Galilean transformation is used. The corresponding fields in the moving coordinate system are defined as

$$\mathbf{E}' = \mathbf{E} + \mathbf{v} \times \mathbf{B}, \quad (2.10)$$

$$\mathbf{H}' = \mathbf{H} - \mathbf{v} \times \mathbf{D}, \quad (2.11)$$

$$\mathbf{J}' = \mathbf{J} - \rho_e \mathbf{v}, \quad (2.12)$$

and $\mathbf{B}' = \mathbf{B}$, $\mathbf{D}' = \mathbf{D}$, $\rho'_e = \rho_e$. The ∇ operator remains unchanged while the time derivative is transformed to the convective time derivative defined as

$$\frac{\partial}{\partial t'} = \left(\frac{\partial}{\partial t} + \mathbf{v} \cdot \nabla \right) \quad (2.13)$$

Under these transformations the Ampère's and Faraday's laws can be written as

$$\nabla \times \mathbf{H}' = \sigma (\mathbf{E} + \mathbf{v} \times \mathbf{B}) + \frac{\partial \mathbf{D}}{\partial t} - \nabla \times (\mathbf{v} \times \mathbf{D}) + \rho_e \mathbf{v}, \quad (2.14)$$

$$\nabla \times \mathbf{E}' = -\frac{\partial \mathbf{B}}{\partial t} + \nabla \times (\mathbf{v} \times \mathbf{B}), \quad (2.15)$$

while the constitutive laws remain unaffected by the transformation.

2.1.3 Electric and magnetic potentials

The study of relationships between current density and field distribution is based on the solution of Maxwell's equations. However, obtaining a solution to the Maxwell's equations in a form described earlier (2.1-2.4) is an extremely formidable task. The idea behind using electric and magnetic potentials is to transform some of the variables such that some of the equations are identically satisfied leading to a reduction in both the complexity and the number of equations to be solved. In general, whenever the curl of a certain quantity vanishes, that quantity can be described by the gradient of a scalar potential (since curl of gradient is always zero). Similarly when the divergence of a vector field vanishes, the vector can be described as the curl of a vector potential (since divergence of curl is always zero). For example, in electrostatics since the curl of the electric field vanishes, it can be represented by the gradient of a scalar potential as $\mathbf{E} = -\nabla U$. Following similar logic two potentials are very commonly used for the solution of Maxwell's equations - the scalar magnetic potential and the vector magnetic potential. Both are used under specific conditions and have their own set of advantages and disadvantages.

The scalar magnetic potential The scalar magnetic potential (Φ) is defined as

$$\mathbf{H} = -\nabla\Phi. \quad (2.16)$$

Taking the curl of this equation leads to $\nabla \times \mathbf{H} = 0$ which means that this method is only valid only when there is no externally imposed surface current density or displacement currents. Equation 2.16 can be substituted into the Gauss' law of magnetism to obtain a single equation describing the magnetic state of the system. For

materials with constant permeability this reduces to Laplace's equation in terms of the magnetic potential:

$$\mu \nabla \cdot \nabla \Phi = 0. \quad (2.17)$$

The main advantage of solving (2.17) instead of solving Ampère's vectorial equations is that the magnetic problem can be solved by one differential equation instead of a system of three simultaneous differential equations for the three components of the vector field. For materials with a nonlinear B-H relationship, the equation has the form

$$\nabla \cdot \mathbf{B}(-\nabla \Phi) = 0. \quad (2.18)$$

The advantage of using the scalar magnetic potential compared to the vector magnetic potential is that the solution of the equation requires information of \mathbf{B} as a function of $(-\nabla \Phi$ or \mathbf{H} which is the form in which most constitutive models are formulated. Thus model inversion is not required. Another advantage is the fewer degrees of freedom required in this method (one dof per node for the scalar magnetic potential compared to 3 dofs per node for the vector magnetic potential). The limitation of using the conventional scalar magnetic potential approach is that it can be used only for current-free regions.

To extend the scalar magnetic potential based approach to model magnetostatic problems with externally imposed current densities, the magnetic field is broken down to two components - a magnetization induced component modeled by the scalar magnetic potential and an external current induced component (modeled using a Biot-Savart computation) [50]. To extend the model to describe eddy currents an vector electric potential (\mathbf{T}) can be introduced such that $\mathbf{H} = \mathbf{T} - \nabla \Omega$ and $\nabla \times \mathbf{T} = \mathbf{J}$ [83].

This approach however makes it challenging to specify boundary conditions and leads to large percentage errors due to similar magnitudes of \mathbf{T} and $\nabla\Omega$.

The vector magnetic potential The vector magnetic potential \mathbf{A} is defined as

$$\mathbf{B} = \nabla \times \mathbf{A}, \quad (2.19)$$

such that (2.4) is identically satisfied. Substitution of (2.19) in to Faraday's law yields

$$\nabla \times \left(\mathbf{E} + \frac{\partial \mathbf{A}}{\partial t} \right) = 0. \quad (2.20)$$

Since the curl of the quantity $(\mathbf{E} + \frac{\partial \mathbf{A}}{\partial t})$ is zero, it can be represented as the gradient of a scalar potential (say U) as

$$-\nabla U = \mathbf{E} + \frac{\partial \mathbf{A}}{\partial t}. \quad (2.21)$$

Substituting the constitutive relationship $\mathbf{J} = \sigma \mathbf{E}$ one gets

$$\mathbf{J} = \underbrace{-\sigma \nabla U}_{\mathbf{J}_s} - \underbrace{\sigma \frac{\partial \mathbf{A}}{\partial t}}_{\mathbf{J}_e}, \quad (2.22)$$

where \mathbf{J}_s is the applied current density and \mathbf{J}_e is the eddy (or induced) current density.

The applied current density is considered to be given. For the quasistationary magnetic field problem, Maxwell's equations reduce to one equation:

$$\nabla \times \mathbf{H}(\nabla \times \mathbf{A}) = \mathbf{J}_s - \sigma \frac{\partial \mathbf{A}}{\partial t}. \quad (2.23)$$

This implies that the magnetic field must be calculated as a function of $\nabla \times \mathbf{A}$ or \mathbf{B} . Since most constitutive models are formulated to calculate \mathbf{B} as a function of \mathbf{H} , use of this equation requires constitutive model inversion. For a linear material with constant permeability μ , 2.23 reduces to

$$\nabla \times \nabla \times \mathbf{A} = \mu \mathbf{J}_s - \sigma \mu \frac{\partial \mathbf{A}}{\partial t}. \quad (2.24)$$

The main advantage of using the vector magnetic potential is that it can capture source currents as well as eddy currents arising from dynamic magnetization changes. The drawbacks include constitutive law inversion and more degrees of freedom per node.

The vector magnetic potential is extensively used to model electromechanical systems since they work in the quasi-stationary frequency band and are exposed to electrical currents (both source and eddy). Magnetostrictive systems operate in a similar frequency band and are exposed to similar conditions. Thus in this work, the vector magnetic potential based formulation will be used.

2.1.4 Boundary conditions

A key component of modeling electromagnetic systems containing different materials is accurately describing the interface (boundary) conditions on the solution variables. Boundary conditions are better explained through the integral form of Maxwell's equations. Consider for example, the integral form of the Gauss' law of magnetism given by $\oint \mathbf{B} \cdot d\mathbf{s} = 0$ applied over a closed cylindrical surface placed at the interface of two media, depicted by the subscripts 1 and 2 (Figure 2.1). If the thickness of the cylinder (Δh) approaches zero, then effectively no flux leaks through the side walls. The integral can then be computed as

$$(\mathbf{n}_1 \cdot \mathbf{B}_1 + \mathbf{n}_2 \cdot \mathbf{B}_2) \Delta s = 0. \quad (2.25)$$

Since the ends of the cylinder now coincide with the interface of the two materials one can relate the surface normals as $\mathbf{n} = \mathbf{n}_2 = -\mathbf{n}_1$. This gives

$$\mathbf{n} \cdot (\mathbf{B}_2 - \mathbf{B}_1) = 0, \quad (2.26)$$

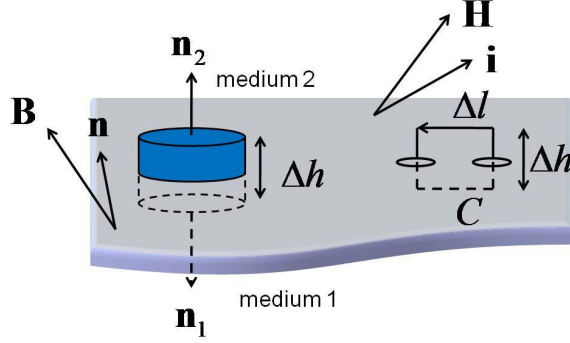


Figure 2.1: Boundary surface between media 1 and 2 with an elemental cylinder and loop used to derive the boundary conditions on \mathbf{B} and \mathbf{H} .

which implies that the normal component of flux density must be continuous across the interface of two media. Similarly to derive boundary conditions for the magnetic field, Ampère's law for quasistationary conditions is used in the integral form:

$$\oint_C \mathbf{H} \cdot d\mathbf{l} = \int_S \mathbf{J} \cdot d\mathbf{s}. \quad (2.27)$$

Physically this says that the line integral of \mathbf{H} around a closed contour C is equal to the total normal current flowing through the surface S bounded by C . Performing the line integral and setting $\Delta h \rightarrow 0$, one gets

$$\mathbf{n} \times (\mathbf{H}_2 - \mathbf{H}_1) = \mathbf{i}, \quad (2.28)$$

where \mathbf{i} is the surface current density defined as $\mathbf{i} = \lim_{\Delta h \rightarrow 0} (\mathbf{J} \Delta h)$. If the boundary is current free, the right hand side of (2.28) becomes zero implying that the tangential components of magnetic field across a boundary must be continuous. Thus the boundary conditions of the magnetic variables across the internal boundaries are such that they ensure continuity of normal flux density and tangential field. The continuity of one automatically implies the discontinuity of the other since flux density and field

are related by the material constitutive parameter μ which is different for different materials. Thus the normal component of magnetic field and tangential components of flux density is typically discontinuous across boundaries.

The boundary conditions for the electric flux density and electric field can be derived using a similar procedure starting from the integral form of the Gauss' law for electricity and Faraday's law. This yields

$$\mathbf{n} \times (\mathbf{E}_2 - \mathbf{E}_1) = 0, \quad (2.29)$$

$$(\mathbf{D}_2 - \mathbf{D}_1) \cdot \mathbf{n} = r_e, \quad (2.30)$$

where r_e is the surface density of charges defined as $r_e = \lim_{\Delta h \rightarrow 0} (\rho_e \Delta h)$. Of the four boundary conditions only two are independent, one from (2.26) and (2.29) and the other from (2.28) and (2.30).

Boundary condition in terms of \mathbf{A} : As mentioned earlier, it is extremely common to model electro-magneto-mechanical systems in the dynamic regime with the vector magnetic potential based formulation. It is therefore beneficial to express the boundary conditions in terms of \mathbf{A} . A typical electromechanical system to be solved consists of copper coils, iron laminates for flux return, and structural components for load transmission surrounded by an air volume. Magnetically, the external boundaries consist of the outer boundaries of the air envelope while all other boundaries are internal. It can be shown that the vector magnetic potential is single-valued and continuous across internal boundaries. This is another advantage over the scalar magnetic potential formulation where the magnetic potential must be discontinuous across interfaces to maintain continuity of the normal component of flux density. The

vector magnetic potential however, ensures the continuity of the normal component of the magnetic flux density by definition.

At the external boundaries, $\mathbf{A} = \mathbf{0}$ sets the normal component of magnetic field to zero. This means that no flux escapes from the air envelope. Care must be taken to make the air envelope sufficiently large so that the $\mathbf{A} = \mathbf{0}$ boundary condition represents the true picture. This is the Dirichlet boundary condition and eliminates rigid body modes magnetically. The Neumann boundary condition comes from specifying the tangential component of the magnetic field given by $\mathbf{H} \times \mathbf{n}$ where \mathbf{n} is the unit normal of the boundary on which the condition is applied. Any unmodeled externally applied magnetic field can be imposed through this boundary condition.

2.1.5 Magnetic materials

In Maxwell's equations, the relationship between \mathbf{B} and \mathbf{H} is given by constitutive laws. In order to understand the B-H relationship in magnetic materials, fundamental causes for magnetization must be discussed at an atomic level. A magnetic field is generated when there is a charged particle in motion. Conversely, a magnetic field exerts force on a charged particle in motion thereby altering its path. All materials contain negatively charged particles (electrons) in motion. An electron exhibits two kinds of motion. First, it revolves around the nucleus causing a magnetic field perpendicular to the plane of revolution. Secondly, it spins about its own axis creating a magnetic field along its axis. Consequently application of an external magnetic field would alter the electron's orbit and tend to rotate the spin of the electron to align along the direction of applied field. The combined effect of these two motions

is called a magnetic moment and the density of magnetic moments per unit volume of the material is known as magnetization.

The magnetism produced by the spin motion is much more powerful than the orbital motion. However, in most materials, electrons are paired with opposite spin vectors such that they cancel the effect of each other. Ferromagnetic materials contain unpaired electrons which cause large changes in the material's magnetic state when exposed to magnetic fields. Under no externally applied field, the alignment of moments in a ferromagnetic material depends on the balance between the exchange energy due to interaction between neighboring moments and thermal energy. Above a certain temperature known as the Curie temperature, the thermal energy dominates the exchange energy and moments are randomly aligned throughout the material. When the material is cooled below the Curie temperature, the exchange energy dominates the thermal energy and gives rise to spontaneous ordering of magnetic moments. Neighboring magnetic moments align along the same direction at a micro-scale to give regions of uniform magnetization called domains. Each domain has a magnetization M_s caused by the aligned moments. However, in the absence of any external magnetic field these domains are oriented in different directions such that there is no net macro-scale magnetization.

Often ferromagnetic materials also exhibit magnetocrystalline anisotropy. This implies that even without the application of any external field domains prefer to align along specific orientations known as the easy magnetization axes. Mathematically these orientations can be determined by minimizing the anisotropy energy (E_A) which is expressed in terms of \mathbf{m} (the unit magnetization direction vector for a domain). The exact form of E_A is determined by performing a series expansion in terms of \mathbf{m} and

obtaining the relevant coefficients empirically. For example, cubic magnetocrystalline anisotropy can be mathematically expressed as

$$E_A = K_4 (m_1^2 m_2^2 + m_2^2 m_3^2 + m_3^2 m_1^2), \quad (2.31)$$

where K_4 is the fourth order anisotropy constant for the material. Minimization of this expression with respect to \mathbf{m} yields the easy magnetization axes as $\langle 100 \rangle$ or the $\langle 111 \rangle$ crystal orientations depending on the sign of K_4 . Adjacent domains are separated by domain walls which are transition regions within which moments realign from one domain to the other. The width of domain walls is determined by a balance between the exchange energy and anisotropy energy [47].

When a ferromagnetic material is exposed to external magnetic fields, it imparts an additional energy to the domains known as the field energy (or Zeeman energy). For an external magnetic field \mathbf{H} acting on a domain aligned along \mathbf{m} , the Zeeman energy is defined as $-\mu_0 M_s \mathbf{m} \cdot \mathbf{H}$. The magnetization process in ferromagnetic materials is governed by a balance between the exchange energy, Zeeman energy, and the magnetocrystalline anisotropy energy. There are three mechanisms by which bulk magnetization changes occur in ferromagnetic materials:

- Domain rotation: This process occurs when the field energy is not sufficiently large to overcome the anisotropy energy completely but it causes the magnetization of the domains to rotate towards the direction of application of field. Usually this process is reversible and does not contribute to any hysteresis.
- Domain wall motion: This occurs when the exchange energy and field energy of domains overcome the anisotropy energy and moments in the wall reorient from their original orientation to the easy axis orientation closest to the direction

of field application causing the domain wall to move. As a result the domains aligned along the easy axes closest to the direction of application of field grow in size relative to the other domains. This process is usually irreversible because domain walls get pinned at material defects and impurities where they use up additional energy to continue their motion.

- **Forced magnetization:** This is the final stage in the magnetization process and occurs usually when the entire material has been converted to a single domain material. Further application of magnetic fields improve the moment alignment within the single domain material thereby increasing its saturation magnetization M_s . This gives rise to a very slow increase in the bulk saturation magnetization of the material at very high fields.

Another source of energy which affects the magnetization process especially for magnetostrictive materials is the magnetoelastic coupling energy which accounts for the work done by a magnetostrictive material in deforming against an external stress field. Section 2.3.2 discusses the effects of stress on the magnetization process of magnetostrictive materials.

2.2 Structural Dynamics

The study of structural dynamics relates the state of stress in a material to applied dynamic loads. Derivation of the equations of motion for a system necessitates understanding of the concept of stress and strain in a body and how they relate with each other. A material typically deforms when exposed to external loads and develops internal forces to balance the external loading. Stress is a measure of these

internal forces while strain is a measure of the amount of deformation of the body. The relationship between stress and strain is an intrinsic property of the material.

2.2.1 Stress

Stress represents the average force per unit area on a surface within the body. Consider, for example the body shown in Figure 2.2 for which the stress at point P must be described. To calculate stress, the body is cut along the plane \mathcal{S} passing through the point P with plane normal $\hat{\mathbf{n}}$. The stress vector or the traction vector ($\mathbf{t}^{(\hat{\mathbf{n}})}$) is defined as

$$\lim_{\Delta\mathcal{S} \rightarrow 0} \frac{\Delta\mathbf{f}}{\Delta\mathcal{S}} = \frac{d\mathbf{f}}{d\mathcal{S}} = \mathbf{t}^{(\hat{\mathbf{n}})}, \quad (2.32)$$

where $\Delta\mathbf{f}$ is the resultant internal force vector and the superscript $(\hat{\mathbf{n}})$ on \mathbf{t} implies that the computed stress vector is valid only for the specific cutting plane with normal $\hat{\mathbf{n}}$. Thus for an infinite number of cutting planes possible through the point P , each having a different $\hat{\mathbf{n}}$, there exists an infinite number of traction vectors for the same external loading condition. To define the state of stress at P a rectangular coordinate system (x_1, x_2, x_3) is introduced with unit vectors $(\hat{e}_1, \hat{e}_2, \hat{e}_3)$. In addition to the original cutting plane \mathcal{S} which has a traction vector ${}^*\mathbf{t}^{\hat{n}}$ and area $d\mathcal{S}$ associated with it, the body is cut with the three coordinate planes such that the part of the body enclosed between the four planes is in the shape of a tetrahedron (Figure 2.3). The asterisk on any vector denotes that it is an averaged quantity over the area on which it acts. Similarly, the average traction vectors associated with the coordinate planes are ${}^*\mathbf{t}^{\hat{e}_i}$ and the areas are dS_i ($i=1,2,3$) with unit normals $\hat{\mathbf{e}}_i$. In Einstein notation the average traction vectors on the coordinate planes can be written as

$${}^*\mathbf{t}^{(\hat{e}_i)} = {}^*t_j^{(\hat{e}_i)} \hat{\mathbf{e}}_j. \quad (2.33)$$

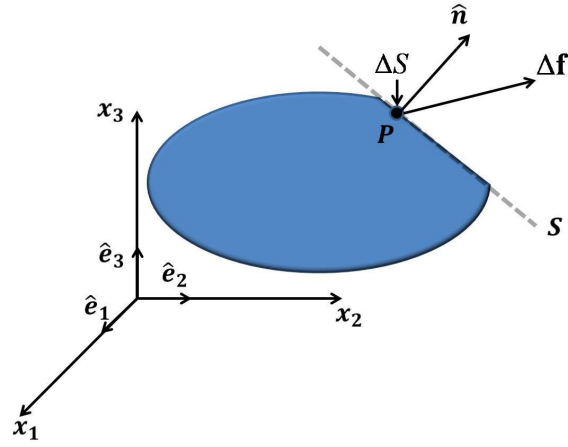


Figure 2.2: Body with cutting plane S and the corresponding force vector $\Delta \mathbf{f}$ acting on ΔS .

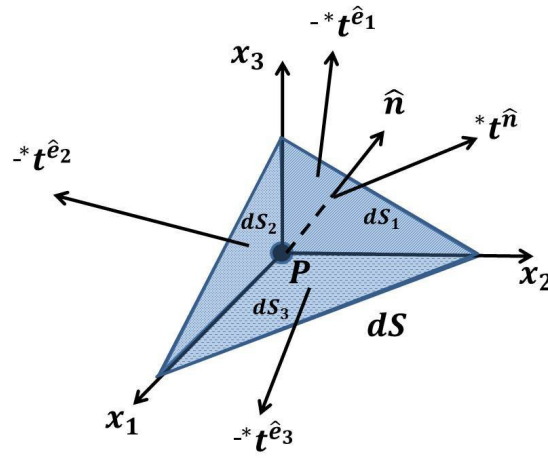


Figure 2.3: Traction vectors on the three coordinate planes at a point P .

and the areas dS_i are the projections of dS on the coordinate planes, given by

$$dS_i = n_i dS \quad (2.34)$$

Equilibrium requires that the vector sum of all forces on the tetrahedron to be zero.

This gives

$${}^*t_i d\mathcal{S} - {}^*t_i^{\hat{e}_j} n_j d\mathcal{S} + \rho {}^*b_i \Delta V = 0, \quad (2.35)$$

where *b_i is an average body force. By letting the tetrahedron shrink to the point P , the body force term drops out because $\Delta V \rightarrow 0$ and the average (starred) quantities are replaced by the actual values at the point P , giving

$$t_i^{(\hat{n})} = t_i^{(\hat{e}_j)} n_j. \quad (2.36)$$

Expressing $t_i^{(\hat{e}_j)}$ as T_{ij} (2.36) can be written in matrix notation as

$$\begin{bmatrix} t_1^{(\hat{n})} \\ t_2^{(\hat{n})} \\ t_3^{(\hat{n})} \end{bmatrix} = \underbrace{\begin{bmatrix} T_{11} & T_{12} & T_{13} \\ T_{21} & T_{22} & T_{23} \\ T_{31} & T_{32} & T_{33} \end{bmatrix}}_{\mathbf{T}} \begin{bmatrix} n_1 \\ n_2 \\ n_3 \end{bmatrix}. \quad (2.37)$$

The matrix \mathbf{T} represents the stress tensor which contains nine components depicted graphically in Figure 2.4. Further by balancing moments for a body containing no concentrated body forces, it can be shown that the stress tensor is symmetric (i.e. $T_{ij} = T_{ji}$) implying that six independent components are required to describe the state of stress at a point.

2.2.2 Strain

Strain is a measure of the amount of deformation of a body. It is a purely geometric entity and can be derived using kinematic operators on a given displacement field. Figure 2.5 shows a body in an initial undeformed (reference) condition and a final

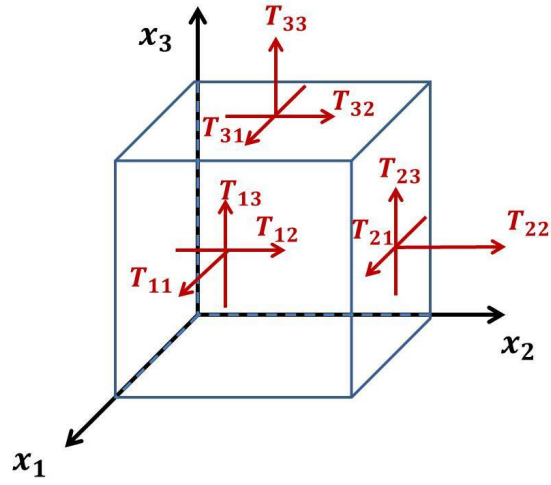


Figure 2.4: Cartesian stress components in their positive sense.

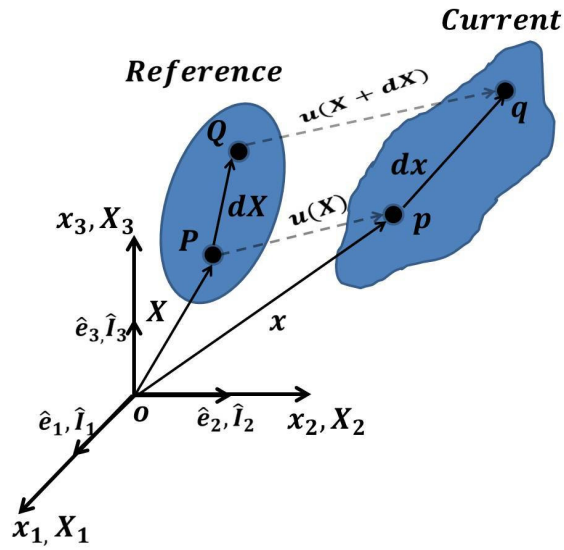


Figure 2.5: Deformation of a body from a reference condition to current condition.

deformed (current) condition. The axes $OX_1X_2X_3$ form the reference coordinate frame with unit vectors $\hat{I}_1, \hat{I}_2, \hat{I}_3$ while $Ox_1x_2x_3$ forms the spatial coordinate frame. Consider two points P and Q in the neighborhood of each other. In the reference configuration the position of P is \mathbf{X} while that of Q is $\mathbf{X} + d\mathbf{X}$. In a deformation process described by a displacement field $\mathbf{u}(\mathbf{X})$, the point P moves to position p with coordinate \mathbf{x} and in the spatial coordinate frame where $\mathbf{x} = \mathbf{X} + \mathbf{u}(\mathbf{X})$ and the point Q moves to position q whose coordinate $\mathbf{x} + d\mathbf{x}$ can be written as

$$\begin{aligned}
\mathbf{x} + d\mathbf{x} &= \mathbf{X} + d\mathbf{X} + \mathbf{u}(\mathbf{X} + d\mathbf{X}), \\
\Rightarrow d\mathbf{x} &= \mathbf{X} + d\mathbf{X} + \mathbf{u}(\mathbf{X} + d\mathbf{X}) - \mathbf{x}, \\
\Rightarrow d\mathbf{x} &= d\mathbf{X} + \mathbf{u}(\mathbf{X} + d\mathbf{X}) - \mathbf{u}(\mathbf{X}), \\
\Rightarrow d\mathbf{x} &= (\mathbf{I} + \nabla_{\mathbf{x}}\mathbf{u}) d\mathbf{X},
\end{aligned} \tag{2.38}$$

where the operator ∇_x stands for $\partial/\partial\mathbf{X}$. The quantity $(\mathbf{I} + \nabla_{\mathbf{x}}\mathbf{u})$ is known as the deformation gradient tensor and is denoted by $\mathbf{F}(\mathbf{X})$. A common measure of deformation is obtained by taking the difference of the squared initial and final lengths ($d\mathbf{x}^T d\mathbf{x} - d\mathbf{X}^T d\mathbf{X}$). Using the definition of \mathbf{F} , this can be reduced as follows

$$d\mathbf{x}^T d\mathbf{x} - d\mathbf{X}^T d\mathbf{X} = d\mathbf{X}^T (\mathbf{F}^T \mathbf{F} - \mathbf{I}) d\mathbf{X}. \tag{2.39}$$

The Lagrangian finite strain tensor is defined as

$$\mathbf{E} = \frac{1}{2} (\mathbf{F}^T \mathbf{F} - \mathbf{I}), \tag{2.40}$$

which can be represented as a function of the displacement field as

$$\mathbf{E} = \frac{1}{2} \left(\frac{\partial \mathbf{u}}{\partial \mathbf{X}} \right)^T + \frac{1}{2} \frac{\partial \mathbf{u}}{\partial \mathbf{X}} + \frac{1}{2} \left(\frac{\partial \mathbf{u}}{\partial \mathbf{X}} \right)^T \left(\frac{\partial \mathbf{u}}{\partial \mathbf{X}} \right). \tag{2.41}$$

It is useful to describe the strain tensor as a function of displacement because most numerical solution strategies calculate the displacement field. If the gradient of the

displacement field is much smaller than unity such that second or higher order terms can be neglected, then the last term in (2.41) drops out giving:

$$\mathbf{E} \approx \frac{1}{2} \left(\frac{\partial \mathbf{u}}{\partial \mathbf{X}} \right)^T + \frac{1}{2} \frac{\partial \mathbf{u}}{\partial \mathbf{X}} = \mathbf{S}, \quad (2.42)$$

which is known as the infinitesimal strain tensor. This approximation is particularly useful for analysis of magnetostrictive systems since magnetostrictive strains are of the order of 0.1 %. Clearly the infinitesimal strain tensor \mathbf{S} is symmetric ($\mathbf{S}^T = \mathbf{S}$). This can also be seen when the strain displacement relationship is written in the matrix form:

$$\mathbf{S} = \begin{bmatrix} \frac{\partial u_1}{\partial X_1} & \frac{1}{2} \left(\frac{\partial u_2}{\partial X_1} + \frac{\partial u_1}{\partial X_2} \right) & \frac{1}{2} \left(\frac{\partial u_1}{\partial X_3} + \frac{\partial u_3}{\partial X_1} \right) \\ \frac{1}{2} \left(\frac{\partial u_2}{\partial X_1} + \frac{\partial u_1}{\partial X_2} \right) & \frac{\partial u_2}{\partial X_2} & \frac{1}{2} \left(\frac{\partial u_2}{\partial X_3} + \frac{\partial u_3}{\partial X_2} \right) \\ \frac{1}{2} \left(\frac{\partial u_1}{\partial X_3} + \frac{\partial u_3}{\partial X_1} \right) & \frac{1}{2} \left(\frac{\partial u_2}{\partial X_3} + \frac{\partial u_3}{\partial X_2} \right) & \frac{\partial u_3}{\partial X_3} \end{bmatrix}. \quad (2.43)$$

Contracted notation: Although both stress and strain are second order tensors, for mathematical convenience they can be represented as vectors with six independent components:

$$\mathbf{T} = [T_{11} \quad T_{22} \quad T_{33} \quad T_{12} \quad T_{23} \quad T_{13}]^T, \quad (2.44)$$

$$\mathbf{S} = [S_{11} \quad S_{22} \quad S_{33} \quad 2S_{12} \quad 2S_{23} \quad 2S_{13}]^T. \quad (2.45)$$

This representation of the stress and strain tensor as vectors with six components is known as contracted notation. The factor of two for the shear strains comes as result of maintaining equality of the strain energy density ($\mathbf{T} \cdot \mathbf{S}$) using the two notations. The matrix notation is convenient as stress-strain and strain-displacement relationships can now be expressed as a matrix. For example, the strain-displacement relationship can be written in a more compact manner as $\mathbf{S} = \nabla_S \mathbf{u}$ where the operator

∇_S is defined as

$$\nabla_S = \begin{bmatrix} \partial/\partial X_1 & 0 & 0 \\ 0 & \partial/\partial X_2 & 0 \\ 0 & 0 & \partial/\partial X_3 \\ \partial/\partial X_2 & \partial/\partial X_1 & 0 \\ 0 & \partial/\partial X_3 & \partial/\partial X_2 \\ \partial/\partial X_3 & 0 & \partial/\partial X_1 \end{bmatrix}. \quad (2.46)$$

However, while performing coordinate transformations both stress and strain would need to be represented in the tensor form and transformed according to the laws of second order tensor transformation.

Stress-strain relations: The relationship between stress and strain in a material can be nonlinear and path dependent depending on the amount and nature of loading. However, for engineering purposes most materials are operated in the elastic regime where they obey a linear stress-strain relationship described by the Hooke's law,

$$\mathbf{T} = \mathbf{c}\mathbf{S}. \quad (2.47)$$

The stiffness tensor \mathbf{c} is a fourth order tensor; however since the stress and strain tensors are symmetric with only six independent components, the number of unknowns in \mathbf{c} is reduced to thirty six. When \mathbf{T} and \mathbf{S} are represented in the contracted notation \mathbf{c} can be represented as a six by six matrix. Additionally the stiffness matrix can be shown to be symmetric through the following procedure. The strain energy density at a point with stress \mathbf{T} and strain \mathbf{S} can be written as

$$U = \mathbf{T}^T \mathbf{S} = \mathbf{S}^T \mathbf{c} \mathbf{S}. \quad (2.48)$$

Since U is a scalar it should be equal to its transpose. Thus

$$U^T = U = \mathbf{S}^T \mathbf{T} = \mathbf{S}^T \mathbf{c} \mathbf{S}. \quad (2.49)$$

Equations (2.48) and (2.49) imply $\mathbf{c} = \mathbf{c}^T$. For materials with cubic symmetry such as Terfenol-D and Galfenol, there is no coupling between shear strains and normal stresses. Additionally the shear stresses are dependent only on the corresponding shear strains. This reduces the stiffness matrix to the form

$$\mathbf{c} = \begin{bmatrix} c_{11} & c_{12} & c_{12} & 0 & 0 & 0 \\ c_{12} & c_{11} & c_{12} & 0 & 0 & 0 \\ c_{12} & c_{12} & c_{11} & 0 & 0 & 0 \\ 0 & 0 & 0 & c_{44} & 0 & 0 \\ 0 & 0 & 0 & 0 & c_{44} & 0 \\ 0 & 0 & 0 & 0 & 0 & c_{44} \end{bmatrix}. \quad (2.50)$$

2.2.3 Equations of motion

The equations of motion can be derived by applying Newton's laws of motion which states that the time rate of change of linear momentum of a body is equal to the total force acting on it. The linear momentum for an infinitesimal volume is given by the product of mass density and the velocity field. External forces are in the form of body forces or surface tractions. In the integral form this can be written as

$$\frac{d}{dt} \int_V \rho \mathbf{v} dV = \int_S \mathbf{t}^{(\hat{n})} dS + \int_V \rho \mathbf{b} dV. \quad (2.51)$$

Applying the divergence theorem on the first term on the right hand side one gets

$$\int_V (\rho \dot{\mathbf{v}} - \nabla \cdot \mathbf{T}^{(\hat{n})} - \rho \mathbf{b}) dV = 0, \quad (2.52)$$

As the equation holds for any arbitrary control volume V , the integrand must equal zero, giving

$$\rho \dot{\mathbf{v}} - \nabla \cdot \mathbf{T}^{(\hat{n})} - \rho \mathbf{b} = 0. \quad (2.53)$$

This vector equation yields three scalar equations (one for each component of the orientation vectors) which are known as the local equations of motion. In contracted

notation it can be written as

$$\nabla_S^T \mathbf{T} + \rho \mathbf{b} = \rho \ddot{\mathbf{u}}. \quad (2.54)$$

For solving these equations it is convenient to express them in terms of the displacement field alone. This can be done by expressing the stress in terms of strain utilizing (2.47) and the strain in terms of displacement using the strain displacement relation $\mathbf{S} = \nabla_S \mathbf{u}$, giving

$$\nabla_S^T \mathbf{c} \nabla_S \mathbf{u} + \rho \mathbf{b} = \rho \ddot{\mathbf{u}}. \quad (2.55)$$

2.3 Magnetomechanical Coupling

Magnetomechanical coupling refers to the interdependence of the mechanical and magnetic boundary value problems (BVPs) on each other. This coupling can take place either at the system level through magnetic body forces or at the material level through magnetomechanical coupling in the material.

2.3.1 Magnetomechanical coupling at the system level

When a system contains only passive materials, the magnetic BVP influences the mechanical BVP through Lorentz forces while the mechanical BVP affects the magnetic BVP through geometrical changes in the system. System level magnetomechanical coupling is conveniently expressed through the Maxwell's stress tensor. Similar to the way mechanical body forces are represented as the divergence of Cauchy's stress tensor, magnetic body forces can be obtained from divergence of Maxwell's stress tensor. Assuming homogeneous material properties and quasi-stationary conditions, the total magnetic force acting on a body with volume V enclosed by a surface S can

be written as $\int_V \mathbf{f}_B dV$ where the magnetic force density is given by

$$\begin{aligned}
\mathbf{f}_B &= \mathbf{J} \times \mathbf{B}, \\
&= (\nabla \times \mathbf{H}) \times \mathbf{B}, \\
&= \mu (\mathbf{H} \cdot \nabla) \mathbf{H} - \mu \frac{1}{2} \nabla H^2.
\end{aligned} \tag{2.56}$$

The total magnetic body force can be written as

$$\begin{aligned}
\mathbf{F} &= \int_V \mathbf{f}_B dV = \int_V \mu \left((\mathbf{H} \cdot \nabla) \mathbf{H} - \mu \frac{1}{2} \nabla H^2 \right) dV, \\
&= \oint_S \mu \mathbf{H} (\mathbf{H} \cdot d\mathbf{S}) - \frac{1}{2} \oint_S \mu H^2 d\mathbf{S}, \\
&= \oint_S \mu \left[\mathbf{H} (\mathbf{H} \cdot \mathbf{n}) - \frac{1}{2} H^2 \mathbf{n} \right] dS.
\end{aligned} \tag{2.57}$$

Alternatively, if the force density were to be written as the divergence of a tensor (say \mathbf{T}^M), then the total magnetic force could be written as

$$\begin{aligned}
\mathbf{F} &= \int_V \nabla \cdot \mathbf{T}^M, \\
&= \int_S \mathbf{T}^M \cdot \mathbf{n} dS.
\end{aligned} \tag{2.58}$$

Comparing (2.57) and (2.58) it can be seen that

$$\mathbf{T}^M = \mu \begin{bmatrix} \frac{1}{2} (H_1^2 - H_2^2 - H_3^2) & H_1 H_2 & H_1 H_3 \\ H_1 H_2 & \frac{1}{2} (H_2^2 - H_3^2 - H_1^2) & H_2 H_3 \\ H_1 H_3 & H_2 H_3 & \frac{1}{2} (H_3^2 - H_1^2 - H_2^2) \end{bmatrix}. \tag{2.59}$$

This tensor \mathbf{T}^M is known as the Maxwell's magnetic stress tensor since its divergence yields the magnetic force density. In Einstein notation, it can be conveniently expressed as $T_{ik}^M = \mu \{ H_i H_k - \frac{1}{2} \delta_{ik} H^2 \}$. Similarly, for electrostatic forces a Maxwell's electrostatic stress tensor may be derived as $T_{ik}^E = \epsilon \{ E_i E_k - \frac{1}{2} \delta_{ik} E^2 \}$ [56]. Expressions for Maxwell's stress tensor have also been derived for the fully dynamic

case of Maxwell's equations. However, expressions obtained in this section are particularly relevant for electromechanical devices since they primarily operate in the quasi-stationary frequency band.

2.3.2 Magnetomechanical coupling at the material level

In magnetostrictive transducers, components carrying current densities (coil) are mechanically inactive, while components which are structurally active do not contain significant current densities. Hence, magnetic body forces may be neglected. The magnetic and mechanical BVPs interact with each other primarily through the magnetomechanical coupling present in the magnetostrictive material.

The magnetomechanical coupling energy is defined as the work done by the material when it undergoes magnetostrictive strain in the presence of externally applied loads. Many key features of magnetostriction can be qualitatively understood from the simplified schematic shown in Figure 2.6. Domains are represented as elliptical shapes with the major axis aligned with the domain's magnetization. Physically this signifies that the lattice strain is linked to the direction of magnetization of the domain. Application of magnetic field aligns the domain magnetization in the direction of applied field thereby causing an increase in length of the sample. Reversing the direction of field aligns the domains in the opposite direction; however it still leads to an increase in length of the sample. Similarly, application of tensile stress favors alignment of domains along the direction of stress while compressive stress favors alignment of domains perpendicular to the direction of stress application causing a corresponding decrease in magnetization. For actuators, a commonly used strategy is to apply a compressive pre-stress to align domains perpendicular to the axis such that

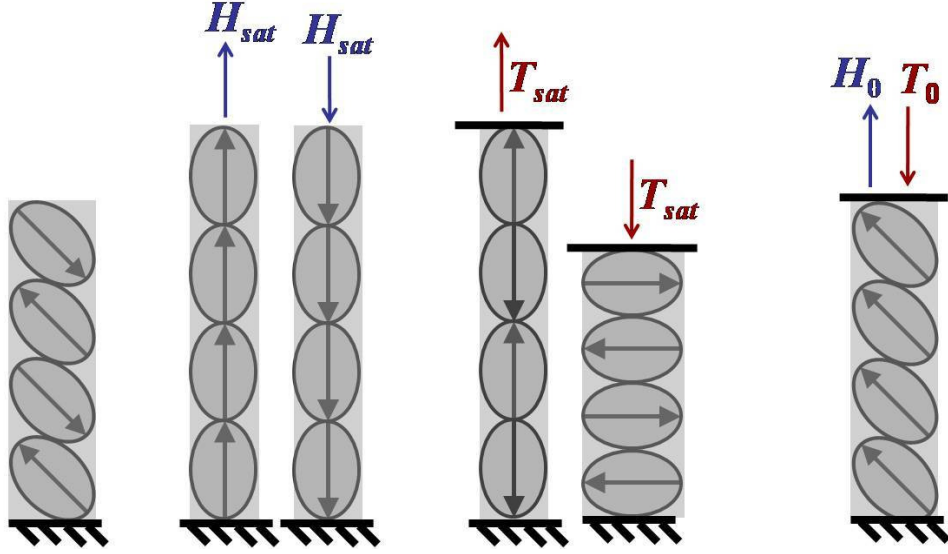


Figure 2.6: Cartoon depiction of magnetostriction.

on application of field, maximum deformation is obtained. Similarly for sensors, a bias field aligns the domains along the axis so that considerable magnetization change can be obtained when the material is compressed. Mathematically, magnetostrictive lattice strain or magneto-strain (\mathbf{S}_m) is linked with the orientation of domains \mathbf{m} through the relation

$$\mathbf{S}_m = \begin{Bmatrix} (3/2)\lambda_{100}(m_1^2 - 1/3) \\ (3/2)\lambda_{100}(m_2^2 - 1/3) \\ (3/2)\lambda_{100}(m_3^2 - 1/3) \\ 3\lambda_{111}m_1m_2 \\ 3\lambda_{111}m_2m_3 \\ 3\lambda_{111}m_3m_1 \end{Bmatrix}, \quad (2.60)$$

where λ_{100} and λ_{111} are magnetostriction constants which denote the maximum magnetostriction of a material along the $\langle 100 \rangle$ and $\langle 111 \rangle$ directions starting from an unbiased condition. Apart from magnetostrictive strains, magnetostrictive materials also exhibit usual elastic strains which can be related to the applied stress through (2.47). The total strain can then be written as the sum of the magneto-strain and

the elastic strain as

$$\mathbf{S} = \mathbf{S}_m + \mathbf{c}^{-1}\mathbf{T}. \quad (2.61)$$

Thus in magnetostrictive materials, flux density (\mathbf{B}) and strain (\mathbf{S}) are nonlinear functions of both stress (\mathbf{T}) and magnetic field (\mathbf{H}). These constitutive relationships nonlinearly couple the mechanical boundary value problem to the magnetic boundary value problem. The next section deals with numerical techniques for solving such coupled BVPs.

2.4 Numerical Solution of Electro-magneto-mechanical systems

Analytical solutions have the advantages of being exact, yielding mathematical relations which can be used directly for parametric studies and analysis, and being computationally cheap. Unfortunately, analytical solution schemes for electromagnetic systems are restricted to a very small class of problems which include some one-dimensional systems and some highly symmetric two-dimensional systems. With presence of nonlinear magnetomechanical coupling as is the case with magnetostrictive transducers, the possibility of obtaining analytical solutions is almost eliminated.

Numerical methods on the other hand provide a generic approach to approximating a solution over the solution domain, which satisfies the boundary and initial conditions. Most numerical schemes for boundary value problems proceed by spatial and temporal discretization of the problem. The following discussion briefly outlines the capabilities of various numerical methods available for solution of BVPs.

Finite difference methods (FDM): The finite difference method approximates both spatial and time derivatives with values of the function itself. With this

method the solution is valid only at the discretization points (or nodes). The spatial resolution of the solution can be improved by adding more nodes in the solution domain.

Finite element method (FEM): The finite element method is different in that the space is discretized by domains of finite volume and the solution is approximated within each volume. Unlike the finite difference method where the solutions are defined only at the nodes, in the finite element method the solution exists everywhere in the geometry. This is because the solution is interpolated between the nodes using polynomials of the desired degree. Finite element methods are more efficient in discretization of space, especially for complex geometries; however approximations in time are generally done by finite differencing.

Boundary element method (BEM) : Boundary element methods are modified finite element methods that use the integral form of field equations. Solutions are obtained in terms of equivalent sources which are defined on the boundary of the geometry under consideration. The main advantage of this method is that since only the surface of the geometry is considered, the dimensionality of the problem is reduced by one. However, a detailed solution in the volume is not obtained which might be crucial for magnetostrictive systems. Another drawback of BEM is that nonlinear materials cannot be modeled. To model nonlinear materials, the relevant domain must be solved using finite elements and a combined FEM/BEM solution scheme is used. This often negates the advantages of BEM. Although BEM reduces the dimensionality of the problem, the system matrices are usually full as compared to FEM system matrices which

are sparse. This may give rise to higher solution times even though the matrix size is smaller.

Among these methods, the finite element method is more suitable for modeling magnetostrictive transducers because of nonlinear material behavior, possibility of complex geometries and the requirement of studying stresses and fields in interior volumes.

The finite element method

In the finite element method the approximate solution is expressed as a linear combination of some pre-selected basis vectors. Since the solution is approximate, in general it will not satisfy the governing equations at every point in the solution domain. The task is to determine the coefficients of the linear combination of the basis vectors such that it minimizes the error between the approximate and exact solutions. In most cases polynomial basis functions are used because of their ability to approximate a wide variety of curves, and the ease of differentiation and integration. Since exact solutions are almost always unavailable (which is the primary reason for performing the finite element analysis), the error is quantified by substituting the solution in the governing equation and computing the residual ($R(x)$) where x is the solution variable.

Various strategies can be used for defining the error functional. In the collocation method, the residual is forced to be zero at some pre-determined points on the solution domain. The number of points depends on the number of unknown constants in the approximate solution. For example, if the assumed solution is a first order polynomial which has two unknown coefficients, then the residual can be forced to zero only at two

points. The drawback of this method is that although the residual is forced to zero at selected locations, the error may be very large at other locations. To overcome this, instead of making the residual vanish at selected points, it is minimized in a more average sense. In case of the least squares approximation, solution is obtained by minimizing the least squares integral defined as $\int_V [R(x)]^2 dx$. A more general process is to minimize the integral $\int_V W(x)R(x)dx$, where $W(x)$ is an arbitrary weighting function. This process of determining the approximate solution is known as the weighted residual method and the reformulated equation obtained on multiplying the governing equation with the weighting function is known as the weak form equation. The name ‘weak form’ is due to the fact that the solutions obtained from it do not satisfy the governing equations at every point in the domain, but rather satisfy the equations in a weak or average sense with respect to a particular class of testing functions. Galerkin’s method is a special procedure for deriving the weak form, in which the weighting function is expanded on the same basis as the assumed solution. The next sections deal with application of the Galerkin’s method to obtain the weak forms for (2.23) and (2.54).

Galerkin’s method for Maxwell’s quasistationary equation

The first step in the Galerkin’s method is to multiply the equation by a weighting function Ψ^A and integrate over the solution domain (a volume V enclosed by a surface ∂V):

$$\int_V \left[\nabla \times \mathbf{H} - \left(\mathbf{J}_s - \sigma \frac{\partial \mathbf{A}}{\partial t} \right) \right] \cdot \Psi^A dV = 0 \quad (2.62)$$

The first term can be broken up using the identity (A.10) to give

$$\int_V \nabla \cdot (\mathbf{H} \times \Psi^A) dV + \int_V \mathbf{H} \cdot (\nabla \times \Psi^A) dV = \int_V \left(\mathbf{J}_s - \sigma \frac{\partial \mathbf{A}}{\partial t} \right) \cdot \Psi^A dV. \quad (2.63)$$

Application of the divergence theorem A.12 to the first term yields

$$\int_V \nabla \cdot (\mathbf{H} \times \Psi^A) dV = \int_{\partial V} (\mathbf{H} \times \Psi^A) \cdot \mathbf{n} dS + \int_V \mathbf{H} \cdot (\nabla \times \Psi^A) dV. \quad (2.64)$$

The second term can be manipulated using the scalar triple product formula $((\mathbf{H} \times \Psi^A) \cdot \mathbf{n} = (\mathbf{n} \times \mathbf{H}) \cdot \Psi^A = -(\mathbf{H} \times \mathbf{n}) \cdot \Psi^A$). Substituting these relationships in (2.64), one gets

$$\int_V \mathbf{H} \cdot (\nabla \times \Psi^A) dV = \int_{\partial V} (\mathbf{H} \times \mathbf{n}) \cdot \Psi^A dS + \int_V \left(\mathbf{J}_s - \sigma \frac{\partial \mathbf{A}}{\partial t} \right) \cdot \Psi^A dV. \quad (2.65)$$

This equation is known as the weak form representation of (2.23). The difference is that while (2.23) demands the solution to hold at every point on the domain, (2.65) requires that the solution hold in an average sense over the entire volume of the domain. Since the weighting function is expanded on the same basis as the solution (\mathbf{A}), it can also be thought of as a virtual generalized displacement ($\Psi^A = \delta \mathbf{A}$). With this definition (2.65) can be written as

$$\int_V \mathbf{H} \cdot (\nabla \times \delta \mathbf{A}) dV = \int_{\partial V} (\mathbf{H} \times \mathbf{n}) \cdot \delta \mathbf{A} dS + \int_V \left(\mathbf{J}_s - \sigma \frac{\partial \mathbf{A}}{\partial t} \right) \cdot \delta \mathbf{A} dV. \quad (2.66)$$

It is evident that the equation expresses a balance of energy. Since $\nabla \times \delta \mathbf{A} = \delta \mathbf{B}$, which is the work conjugate of \mathbf{H} . The term $\mathbf{H} \cdot \delta \mathbf{B}$ refers to the internal magnetic energy of the system, $\sigma \dot{\mathbf{A}} \cdot \delta \mathbf{A}$ models the energy loss due to eddy currents, the terms $\mathbf{J}_s \cdot \delta \mathbf{A}$ and $(\mathbf{H} \times \mathbf{n}) \cdot \delta \mathbf{A}$ describes the energy added to the system by source currents and applied tangential fields at the boundary of the domain.

Galerkin's method for structural dynamics

The weak form equations corresponding to (2.54) can be derived using the Galerkin's method of weighted residuals similar to the Maxwell's quasistationary equations. However, to avoid complexity of notation due to the presence of second order tensors, it

is convenient to express the equation in Einstein notation,

$$\int_V T_{ij,j} \Psi_i^u dV = \int_V (\rho \ddot{u}_i + c \dot{u}_i - f_{B_i}) \Psi_i^u dV, \quad (2.67)$$

where the term $c \dot{u}_i$ has been added on the right hand side to model structural damping. Integrating the first term by parts and applying the divergence theorem, one gets

$$\int_V T_{ij} \Psi_{i,j}^u dV + \int_V (\rho \ddot{u}_i + c \dot{u}_i) \Psi_i^u dV = \int_{\partial V} T_{ij} \Psi_i^u n_j dS + \int_V f_{B_i} \Psi_i^u dV. \quad (2.68)$$

Using the symmetry of the stress tensor, the integrand in the first term can be written as

$$T_{ij} \Psi_{i,j}^u = T_{ij} \left[\frac{1}{2} (\Psi_{i,j}^u + \Psi_{j,i}^u) \right]. \quad (2.69)$$

Once again, Ψ^u can be thought of as the virtual generalized displacements ($\delta \mathbf{u}$) and the weak form equation can be written in matrix notation as

$$\int_V \mathbf{T} \cdot \nabla_S \delta \mathbf{u} dV + \int_V (\rho \ddot{\mathbf{u}} + c \dot{\mathbf{u}}) \cdot \delta \mathbf{u} dV = \int_{\partial V} \mathbf{T} \mathbf{n} \cdot \delta \mathbf{u} dS + \int_V \mathbf{f}_B \cdot \delta \mathbf{u} dV. \quad (2.70)$$

Similar to the electromagnetic case, this equation represents a balance of internal and external virtual work where the term $\mathbf{T} \cdot \nabla_S \delta \mathbf{u} = \mathbf{T} \cdot \delta \mathbf{S}$ is the internal virtual work stored as strain energy density, $(\rho \ddot{\mathbf{u}} + c \dot{\mathbf{u}}) \cdot \delta \mathbf{u}$ is the work done by inertia and damping forces, and the last two terms represent the virtual work due to external body forces and traction. These weak form equations form the basis of the finite element formulation discussed in the next section.

Finite element formulation for electro-magneto-mechanical systems

In finite elements the solution domain is discretized into numerous smaller volumes (or finite elements) and the weak form equations are integrated over each element.

Within every element the vector potential (\mathbf{A}_e) and displacements (\mathbf{u}_e) are interpolated from the nodal values \mathbf{q}_e^A and \mathbf{q}_e^u using shape functions \mathbf{N}^A and \mathbf{N}^u respectively,

$$\mathbf{A}_e = \mathbf{N}^A \mathbf{q}_e^A, \quad \mathbf{u}_e = \mathbf{N}^u \mathbf{q}_e^u. \quad (2.71)$$

Since the testing functions are expanded on the same basis in the Galerkin method, the same shape functions are used for the virtual quantities,

$$\delta \mathbf{A}_e = \mathbf{N}^A \delta \mathbf{q}_e^A, \quad \delta \mathbf{u}_e = \mathbf{N}^u \delta \mathbf{q}_e^u. \quad (2.72)$$

The shape functions are defined in terms of local or natural coordinates $\boldsymbol{\xi}$ to generalize the integration process for all elements. The size of the shape function matrices depends on the number of nodes per element and the number of degrees of freedom per node associated with the corresponding solution variable. For example, if a 4-noded tetrahedral element with linear interpolation functions is chosen, then the matrix \mathbf{N}^A will have dimensions of three by twelve since there are three unknown components of the vector potential at each node giving rise to twelve unknowns for the element. Similarly, \mathbf{N}^u will also have the same size since there are three unknown components of displacement at each node. Thus if the same element is used for both the vector potential and displacements then the shape function matrices will be the same ($\mathbf{N}^A = \mathbf{N}^u = \mathbf{N}$). The shape function matrix comprises a separate function (N_i) associated with each node which satisfy the properties

$$\sum_{i=1}^4 N_i = 1, \quad \xi_i N_j = \delta_{ij}, \quad (2.73)$$

where δ_{ij} is the kronecker delta. In terms of the natural coordinates the shape functions are given by

$$N_1 = \xi_1, \quad (2.74)$$

$$N_2 = \xi_2, \quad (2.75)$$

$$N_3 = \xi_3, \quad (2.76)$$

$$N_4 = 1 - \xi_1 - \xi_2 - \xi_3, \quad (2.77)$$

and the shape function matrix has the form

$$\mathbf{N}(\boldsymbol{\xi}) = \begin{bmatrix} N_1 & 0 & 0 & N_2 & 0 & 0 & N_3 & 0 & 0 & N_4 & 0 & 0 \\ 0 & N_1 & 0 & 0 & N_2 & 0 & 0 & N_3 & 0 & 0 & N_4 & 0 \\ 0 & 0 & N_1 & 0 & 0 & N_2 & 0 & 0 & N_3 & 0 & 0 & N_4 \end{bmatrix}, \quad (2.78)$$

To perform the integrations in (2.65) and (2.68) the magnetic flux density, magnetic field, stress, and strain within the element need to be obtained in terms of the nodal degrees of freedom \mathbf{q}_e^A and \mathbf{q}_e^u . Flux density and strain are kinematically related to the solution vectors as

$$\mathbf{B}_e = \nabla \times \mathbf{A}_e = \nabla \times (\mathbf{N}^A \mathbf{q}_e^A) := \mathbf{C}_e \mathbf{q}_e^A \quad (2.79)$$

$$\mathbf{S}_e = \nabla \mathbf{u}_e = \nabla (\mathbf{N}^u \mathbf{q}_e^u) := \mathbf{G}_e \mathbf{q}_e^u. \quad (2.80)$$

The matrices \mathbf{C}_e and \mathbf{G}_e are the discrete curl and gradient operators which contain derivatives of the local coordinates ξ_i with respect to the global coordinates x_i . Substituting these relations in the weak form expressions, one gets

$$\begin{aligned} & \sum_{e=1}^{N^A} \left(\int_{\Delta} \mathbf{H}_e \cdot \mathbf{C}_e \delta \mathbf{q}_e^A J_e d\Delta + \int_{\Delta} \sigma_e \mathbf{N}^A \frac{\partial \mathbf{q}_e^A}{\partial t} \cdot \mathbf{N}^A \delta \mathbf{q}_e^A J_e d\Delta \right) = \\ & \sum_{b=1}^{N_S^A} \int_{\Delta} \mathbf{H}_{T,b} \cdot \mathbf{N}^A \delta \mathbf{q}_b^A J_{b,S} d\Delta_S + \sum_{e=1}^{N^A} \int_{\Delta} \mathbf{J}_{s,e} \cdot \mathbf{N}^A \delta \mathbf{q}_e^A J_e d\Delta, \end{aligned} \quad (2.81)$$

$$\begin{aligned}
& \sum_{e=1}^{N^u} \left(\int_{\Delta} \mathbf{T}_e \cdot \mathbf{G}_e \delta \mathbf{q}_e^u J_e d\Delta + \int_{\Delta} \rho_e \mathbf{N}^u \frac{\partial^2 \mathbf{q}_e^u}{\partial t^2} \cdot \mathbf{N}^u \delta \mathbf{q}_e^u J_e d\Delta + \right. \\
& \left. \int_{\Delta} c_e \mathbf{N}^u \frac{\partial \mathbf{q}_e^u}{\partial t} \cdot \mathbf{N}^u \delta \mathbf{q}_e^u J_e d\Delta \right) = \sum_{b=1}^{N_S^u} \int_{\Delta_S} \mathbf{t}_b \cdot \mathbf{N}^u \delta \mathbf{q}_b^u J_{b,S} d\Delta_S,
\end{aligned} \tag{2.82}$$

where N^A and N^u are the number of elements in the magnetic and mechanical domains respectively. The subscript b refers to the element number on the boundary. The number of elements on the boundary on which a magnetic field is applied is N_S^A and the number of boundary elements to which a traction is applied is N_S^u . The integral $\int_{\Delta} J_e d\Delta$ refers to the integral over the element in natural coordinates and is the volume of the element,

$$\int_{\Delta} J_e d\Delta := \int_{-1}^1 \int_{-1}^1 \int_{-1}^1 \det \left(\frac{\partial \mathbf{x}}{\partial \xi} \right) d\xi_1 d\xi_2 d\xi_3 = V_e, \tag{2.83}$$

and the integral $\int_{\Delta_S} J_{b,S} d\Delta_S$ gives the surface area of the element face on the boundary,

$$\int_{\Delta_S} J_{b,S} d\Delta_S := \int_{-1}^1 \int_{-1}^1 \det \begin{bmatrix} \frac{\partial x_i}{\partial \xi_i} & \frac{\partial x_i}{\partial \xi_j} \\ \frac{\partial x_j}{\partial \xi_i} & \frac{\partial x_j}{\partial \xi_j} \end{bmatrix} d\xi_i d\xi_j = A_b. \tag{2.84}$$

The field and stresses in the element must be supplied by constitutive laws. Here, linear decoupled constitutive laws will be covered to illustrate the basic steps of the finite element method. Incorporation of nonlinear coupled constitutive laws for magnetostrictive materials in the finite element framework is discussed in detail in chapter 3. Considering the material for the element to have constant isotropic permeability μ_e and a constant stiffness tensor \mathbf{c}_e , the decoupled constitutive laws can be written as

$$\mathbf{H}_e = \mu_e^{-1} \mathbf{B}_e = \mu_e^{-1} \mathbf{C}_e \mathbf{q}_e^A, \quad \mathbf{T}_e = \mathbf{c}_e \mathbf{S}_e = \mathbf{c}_e \mathbf{G}_e \mathbf{q}_e^u. \tag{2.85}$$

These relations can now be substituted into the finite element approximation for the virtual work given by (2.82) and (2.81). This yields matrix equations for increments

of the vector potential and displacement nodal values, since they can be pulled from the integral. To illustrate, the following matrices are defined,

$$\mathbf{k}_e^u = \int_{\Delta} \mathbf{G}_e^T \mathbf{c}_e \mathbf{G}_e J_e d\Delta, \quad (2.86)$$

$$\mathbf{k}_e^A = \int_{\Delta} \mathbf{C}_e^T \mu_e^{-1} \mathbf{C}_e J_e d\Delta, \quad (2.87)$$

$$\mathbf{d}_e^A = \int_{\Delta} (\mathbf{N}^A)^T \sigma_e \mathbf{N}^A J_e d\Delta, \quad (2.88)$$

$$\mathbf{d}_e^u = \int_{\Delta} (\mathbf{N}^u)^T c_e \mathbf{N}^u J_e d\Delta, \quad (2.89)$$

$$\mathbf{m}_e = \int_{\Delta} (\mathbf{N}^u)^T \rho_e \mathbf{N}^u J_e d\Delta, \quad (2.90)$$

and the following vectors are defined,

$$\mathbf{f}_b^u = \int_{\Delta_S} (\mathbf{N}^u)^T \mathbf{t}_b J_{b,S} d\Delta_S, \quad (2.91)$$

$$\mathbf{f}_b^A = \int_{\Delta_S} (\mathbf{N}^A)^T \mathbf{H}_T J_{b,S} d\Delta_S, \quad (2.92)$$

$$\mathbf{f}_e^J = - \int_{\Delta} (\mathbf{N}^A)^T \mathbf{J}_{s,e} J_e d\Delta. \quad (2.93)$$

With these definitions, the finite element approximations for the magnetic and mechanical virtual work balance are

$$\sum_{e=1}^{N^A} (\mathbf{d}_e^A \dot{\mathbf{q}}_e^A + \mathbf{k}_e^A \mathbf{q}_e^A) \cdot \delta \mathbf{q}_e^A = \sum_{e=1}^{N_A} \mathbf{f}_e^J \cdot \delta \mathbf{q}_e^A + \sum_{b=1}^{N_S^A} \mathbf{f}_b^A \cdot \delta \mathbf{q}_b^A, \quad (2.94)$$

$$\sum_{e=1}^{N^u} (\mathbf{m}_e \ddot{\mathbf{q}}_e^u + \mathbf{d}_e^u \dot{\mathbf{q}}_e^u + \mathbf{k}_e^u \mathbf{q}_e^u) \cdot \delta \mathbf{q}_e^u = \sum_{b=1}^{N_S^u} \mathbf{f}_b^u \cdot \delta \mathbf{q}_b^u + \sum_{p=1}^{N_p^u} \mathbf{P}_p \cdot \delta \mathbf{q}_p^u. \quad (2.95)$$

On globally assembling these matrices (see chapter 3 of [18]), one gets the finite element model equations as

$$(\mathbf{D}^A \dot{\mathbf{Q}}^A + \mathbf{K}^A \mathbf{Q}^A - \mathbf{F}^A) \cdot \delta \mathbf{Q}^A, \quad (2.96)$$

$$(\mathbf{M}^u \ddot{\mathbf{Q}}^u + \mathbf{D}^u \dot{\mathbf{Q}}^u + \mathbf{K}^u \mathbf{Q}^u - \mathbf{F}^u) \cdot \delta \mathbf{Q}^u. \quad (2.97)$$

Since the virtual generalized displacements $\delta \mathbf{Q}^A$ and $\delta \mathbf{Q}^u$ are arbitrary, the equation holds only if the coefficients of the virtual quantities are identically zero. This gives the following two matrix equations for the finite element model.

$$\mathbf{D}^A \dot{\mathbf{Q}}^A + \mathbf{K}^A \mathbf{Q}^A = \mathbf{F}^A, \quad (2.98)$$

$$\mathbf{M}^u \ddot{\mathbf{Q}}^u + \mathbf{D}^u \dot{\mathbf{Q}}^u + \mathbf{K}^u \mathbf{Q}^u = \mathbf{F}^u. \quad (2.99)$$

Note that the two equations are decoupled because the constitutive laws in the formulation are decoupled. Use of magnetomechanically coupled constitutive laws leads to coupling between the two equations which is mainly reflected in off-diagonal entries in the combined stiffness matrix of the system. Nonlinearity in constitutive laws results in a state dependent stiffness matrix. Chapter 3 deals with solution strategies for such coupled systems.

Chapter 3: UNIFIED APPROACH TO MODELING MAGNETOSTRICTIVE TRANSDUCERS

This chapter aims at developing a comprehensive finite element modeling framework for magnetostrictive transducers by describing the coupling between the electrical, magnetic, and mechanical domains. The electrical and magnetic boundary value problems are coupled through Maxwell's equations while the mechanical and magnetic boundary value problems are coupled through the magnetostrictive material constitutive laws. This chapter presents a unified approach to model magnetostrictive transducers by incorporating nonlinear coupled constitutive laws in the finite element model described in section 2.4. For quasistatic conditions, an efficient piecewise linear solution strategy is devised in which the solution is obtained as a sequence of incremental steps with the magnetostrictive material being modeled by the linear piezomagnetic equations within each step. The piezomagnetic coefficients are updated after every step using nonlinear constitutive laws. The piecewise linear model can be used to determine quasistatic major loops or accurate bias points. A linear dynamic solution with piezomagnetic coefficients computed at the bias point can be used to describe the system dynamics for moderate inputs. Finally, a nonlinear dynamic solution algorithm is implemented which can yield the transducer dynamics for large inputs. The finite element model equations are coded into the commercial

finite element package COMSOL which is used for geometric modeling, meshing, and global assembly of matrices. The piecewise linear and nonlinear dynamic solvers are coded up as MATLAB functions.

3.1 Finite Element Framework

The finite element framework used in this work is based on (2.81) and (2.82) described in Chapter 2. In magnetostrictive materials stress and field are a function of both flux density and strain. Thus the governing equations for the finite element model can be written as

$$\begin{aligned} \sum_{e=1}^{N^A} \left(\int_{\Delta} \mathbf{H}_e(\mathbf{B}_e, \mathbf{S}_e) \cdot \mathbf{C}_e \delta \mathbf{q}_e^A J_e d\Delta + \int_{\Delta} \sigma_e \mathbf{N}^A \frac{\partial \mathbf{q}_e^A}{\partial t} \cdot \mathbf{N}^A \delta \mathbf{q}_e^A J_e d\Delta \right) = \\ \sum_{b=1}^{N_S^A} \int_{\Delta} \mathbf{H}_{T,b} \cdot \mathbf{N}^A \delta \mathbf{q}_b^A J_{b,S} d\Delta_S + \sum_{e=1}^{N^A} \int_{\Delta} \mathbf{J}_{s,e} \cdot \mathbf{N}^A \delta \mathbf{q}_e^A J_e d\Delta, \end{aligned} \quad (3.1)$$

$$\begin{aligned} \sum_{e=1}^{N^u} \left(\int_{\Delta} \mathbf{T}_e(\mathbf{B}_e, \mathbf{S}_e) \cdot \mathbf{G}_e \delta \mathbf{q}_e^u J_e d\Delta + \int_{\Delta} \rho_e \mathbf{N}^u \frac{\partial^2 \mathbf{q}_e^u}{\partial t^2} \cdot \mathbf{N}^u \delta \mathbf{q}_e^u J_e d\Delta + \right. \\ \left. \int_{\Delta} c_e \mathbf{N}^u \frac{\partial \mathbf{q}_e^u}{\partial t} \cdot \mathbf{N}^u \delta \mathbf{q}_e^u J_e d\Delta \right) = \sum_{b=1}^{N_S^u} \int_{\Delta_S} \mathbf{t}_b \cdot \mathbf{N}^u \delta \mathbf{q}_b^u J_{b,S} d\Delta_S. \end{aligned} \quad (3.2)$$

The next section describes two different methods of incorporating nonlinear constitutive laws in these equations and formulating equivalent matrix equations for the system.

3.2 Incorporation of Nonlinear Coupled Constitutive Laws

Incorporation of nonlinear constitutive behavior poses a significant challenge in the formulation of coupled finite element models for magnetostrictive systems. The most common method to describe magnetostrictive material behavior has been by obtaining polynomial fits to data. For example, Benbouzid et al. [8] used surface splines

to fit experimental data while Kannan and Dasgupta [50] used constitutive relations in an incremental form with coefficients obtained from bi-cubic spline fits to measurements. Kim et al. [55] used 6th order polynomials to fit the strain-field behavior with a different set of coefficients for each preload condition. The use of spline functions has the advantages of easy differentiability and implementation for 1D cases. However, the procedure becomes rather complex if complete 3D material behavior is required. This would require 3D measurements to be performed, and bulky splines with 9 components (3 for field and 6 for stress) to be fitted to those measurements. Graham et al. [40] implemented Galfenol constitutive behavior through look-up tables generated using the Armstrong model *a priori* for a large number of induction and stress values. Although the Armstrong model is three dimensional, look-up tables were generated for 1D induction and stress inputs. As is the case with splines, extension to a full 3D version will add significant complexity because it will require generation of bulky tables with 9 inputs and 9 outputs. For these reasons, using an efficient constitutive law coded up as functions is beneficial for 3D boundary value problems.

Most available constitutive laws take magnetic field (\mathbf{H}) and stress (\mathbf{T}) as input and compute flux density \mathbf{B} and strain (\mathbf{S}) as output.

$$\mathbf{B} = \mathbf{B}(\mathbf{H}, \mathbf{T}), \quad \mathbf{S} = \mathbf{S}(\mathbf{H}, \mathbf{T}). \quad (3.3)$$

Depending on the requirement different strategies can be applied to incorporate the constitutive law. For modeling quasistatic operation a piecewise-linear solution method with no convergence checks can be used (section 3.2.1).

3.2.1 Piecewise-linear implementation

A piecewise-linear implementation of the constitutive law is a useful tool to model transducer responses under quasistatic conditions. Neglecting the dynamic terms, the virtual work balance equations (2.81) and (2.82) can be written in an incremental form as

$$\sum_{e=1}^{N^A} \left(\int_{\Delta} \Delta \mathbf{H}_e \cdot \mathbf{C}_e \delta \Delta \mathbf{q}_e^A J_e d\Delta + \right) = \sum_{b=1}^{N_S^A} \int_{\Delta} \Delta \mathbf{H}_{T,b} \cdot \mathbf{N}^A \delta \Delta \mathbf{q}_b^A J_{b,S} d\Delta_S + \sum_{e=1}^{N^A} \int_{\Delta} \Delta \mathbf{J}_{s,e} \cdot \mathbf{N}^A \delta \Delta \mathbf{q}_e^A J_e d\Delta, \quad (3.4)$$

$$\sum_{e=1}^{N^u} \left(\int_{\Delta} \Delta \mathbf{T}_e \cdot \mathbf{G}_e \delta \Delta \mathbf{q}_e^u J_e d\Delta \right) = \sum_{b=1}^{N_S^u} \int_{\Delta_S} \Delta \mathbf{t}_b \cdot \mathbf{N}^u \delta \Delta \mathbf{q}_b^u J_{b,S} d\Delta_S, \quad (3.5)$$

where $\Delta \mathbf{H}$ and $\Delta \mathbf{T}$ must be computed as a function of $\Delta \mathbf{B}$ and $\Delta \mathbf{S}$. For some field \mathbf{H}_0 and stress \mathbf{T}_0 , the constitutive model computes \mathbf{B} and \mathbf{S} along with the material Jacobian \mathcal{J} given by

$$\mathcal{J} = \begin{bmatrix} \boldsymbol{\mu} = \frac{\partial \mathbf{B}}{\partial \mathbf{H}}(\mathbf{H}_0, \mathbf{T}_0) & \mathbf{d} = \frac{\partial \mathbf{B}}{\partial \mathbf{T}}(\mathbf{H}_0, \mathbf{T}_0) \\ \mathbf{d}^T = \frac{\partial \mathbf{S}}{\partial \mathbf{H}}(\mathbf{H}_0, \mathbf{T}_0) & \mathbf{s} = \frac{\partial \mathbf{S}}{\partial \mathbf{T}}(\mathbf{H}_0, \mathbf{T}_0) \end{bmatrix}. \quad (3.6)$$

For small deviations about \mathbf{H}_0 and \mathbf{T}_0 , the constitutive law can be formulated in incremental form through inversion of the material Jacobian matrix,

$$\begin{bmatrix} \Delta \mathbf{H} \\ \Delta \mathbf{T} \end{bmatrix} = \begin{bmatrix} \boldsymbol{\mu}^{-1} & -\mathbf{a} \\ -\mathbf{a}^T & \mathbf{c} \end{bmatrix} \begin{bmatrix} \Delta \mathbf{B} \\ \Delta \mathbf{S} \end{bmatrix} = \mathcal{J}^{-1} \begin{bmatrix} \Delta \mathbf{B} \\ \Delta \mathbf{S} \end{bmatrix}. \quad (3.7)$$

The stress and field increments can be related to the nodal degrees of freedoms by using (2.79) and (2.80) in the incremental form giving

$$\Delta \mathbf{H}_e = \boldsymbol{\mu}_e^{-1} \mathbf{C}_e \Delta \mathbf{q}_e^A - \mathbf{a}_e \mathbf{G}_e \Delta \mathbf{q}_e^u, \quad (3.8)$$

$$\Delta \mathbf{T}_e = -\mathbf{a}_e^T \mathbf{C}_e \Delta \mathbf{q}_e^A + \mathbf{c}_e \mathbf{G}_e \Delta \mathbf{q}_e^u. \quad (3.9)$$

Substituting (3.8) and (3.9) into (3.4) and (3.5), globally assembling the resulting system, and equating the coefficients of the virtual generalized displacements yields the following system of equations,

$$\begin{bmatrix} \mathbf{K}^A & \mathbf{K}^{uA} \\ (\mathbf{K}^{uA})^T & \mathbf{K}^u \end{bmatrix} \begin{pmatrix} \Delta \mathbf{Q}^A \\ \Delta \mathbf{Q}^u \end{pmatrix} = \begin{pmatrix} \Delta \mathbf{R}^A \\ \Delta \mathbf{R}^u \end{pmatrix}, \quad (3.10)$$

where the global stiffness matrix and load vector components are given by

$$\mathbf{K}^u = \sum_{e=1}^{N^u} \int_{\Delta} \mathbf{G}_e^T \mathbf{c}_e \mathbf{G}_e J_e d\Delta, \quad (3.11)$$

$$\mathbf{K}^A = \sum_{e=1}^{N^A} \int_{\Delta} \mathbf{C}_e^T \boldsymbol{\mu}_e^{-1} \mathbf{C}_e J_e d\Delta, \quad (3.12)$$

$$\mathbf{K}^{uA} = - \sum_{e=1}^{N^A} \int_{\Delta} \mathbf{C}_e^T \mathbf{a}_e \mathbf{G}_e J_e d\Delta, \quad (3.13)$$

$$\Delta \mathbf{R}^u = \sum_{b=1}^{N_S^u} \int_{\Delta_S} (\mathbf{N}^u)^T \Delta \mathbf{t}_b J_{b,S} d\Delta_S, \quad (3.14)$$

$$\Delta \mathbf{R}^A = \sum_{b=1}^{N_S^A} \int_{\Delta_S} (\mathbf{N}^A)^T \Delta \mathbf{H}_T J_{b,S} d\Delta_S + \sum_{e=1}^{N^A} \int_{\Delta} (\mathbf{N}^A)^T \Delta \mathbf{J}_{s,e} J_e d\Delta. \quad (3.15)$$

Since the computed piezomagnetic coefficients ($\boldsymbol{\mu}^{-1}$, \mathbf{c} , and \mathbf{a}) are dependent on stress and field, which have a spatial variation, the coefficients are also spatially variant. To preserve this inhomogeneity, the coefficients are declared as interpolated data functions of spatial coordinates. Each coefficient is a separate function and when called, COMSOL searches in the data file for their values corresponding to that location or interpolates between nearby points if that location is not present in the file.

Ideally, the coefficients must be evaluated at all the integration points present in the magnetostrictive subdomain during the assembly process. However, in a 3D model several thousand integration points are present. Evaluation, inversion and storage of the Jacobian at every integration point is both computationally and memory

intensive. Assuming that the spatial variation in field and stress is not steep, the coefficients are calculated only at selected locations and approximated at the remaining points through interpolation.

Figure 3.1 shows a flowchart of the piecewise-linear solution procedure. The model starts from zero initial conditions and updates the piezomagnetic coefficients by computing the material Jacobian at zero field and stress. The solver then assembles the external load vector and the system matrix and computes the incremental solution vector ($\Delta \mathbf{U}$). The next step is to obtain the stress and field increments from $\Delta \mathbf{U}$. To do this first induction and strain increments are found using the kinematic relationships with the vector magnetic potential and mechanical displacements. Next $\Delta \mathbf{T}$ and $\Delta \mathbf{H}$ are obtained from $\Delta \mathbf{B}$ and $\Delta \mathbf{S}$ using the inverted constitutive law (3.7). The total field and stress vectors are updated with the corresponding increments. This process is repeated till the inputs have reached their final values. The computation is fast as it does not involve iteration loops or convergence checks. Consequently, the solution has a tendency to drift since within every interval a nonlinear response is approximated by linear behavior. The larger the size of each interval the larger is the drift. Thus, depending on the desired accuracy, a sufficiently small step size must be utilized. The piecewise-linear model is useful for two purposes. First, to obtain a measure of quasistatic system performance and secondly to generate accurate bias points which preserve the spatial inhomogeneity in the distribution of field and stress in Galfenol, and hence, in the material coefficients.

An efficient way to obtain the dynamic response of a transducer when excited with moderate inputs about a bias point ($\bar{\mathbf{H}}, \bar{\mathbf{T}}$) is by linearizing the system about the bias point. This can be done by using a constant system stiffness matrix factored

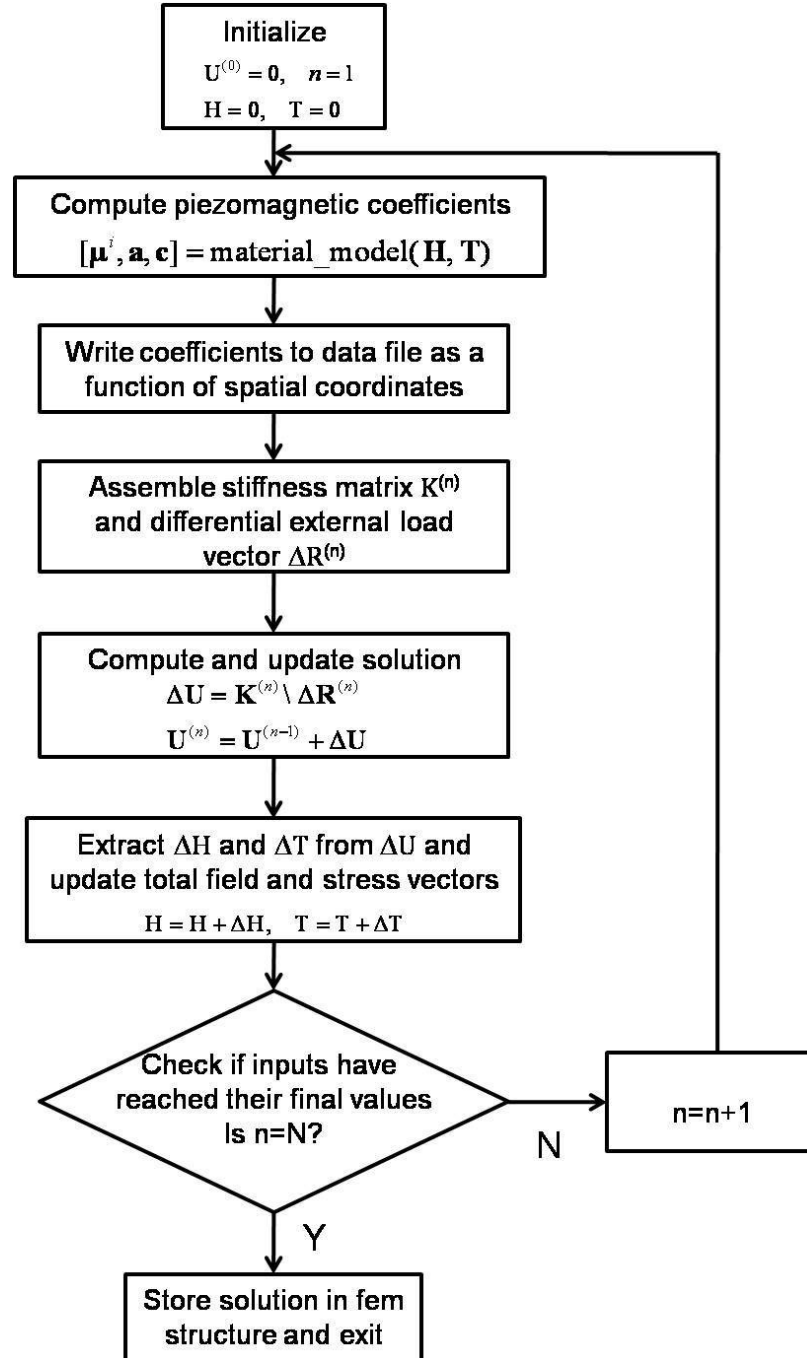


Figure 3.1: Flowchart of the piecewise-linear solution process.

using the material coefficients computed at the bias point and adding the dynamic terms from (2.81) and (2.82) giving

$$\begin{bmatrix} \mathbf{0} & \mathbf{0} \\ \mathbf{0} & \mathbf{M}^u \end{bmatrix} \begin{pmatrix} \Delta \ddot{\mathbf{Q}}^A \\ \Delta \ddot{\mathbf{Q}}^u \end{pmatrix} + \begin{bmatrix} \mathbf{D}^A & \mathbf{0} \\ \mathbf{0} & \mathbf{D}^u \end{bmatrix} \begin{pmatrix} \Delta \dot{\mathbf{Q}}^A \\ \Delta \dot{\mathbf{Q}}^u \end{pmatrix} + \begin{bmatrix} \mathbf{K}^A & -\mathbf{K}^{uA} \\ -(\mathbf{K}^{uA})^T & \mathbf{K}^u \end{bmatrix}_{\bar{\mathbf{H}}, \bar{\mathbf{T}}} \begin{pmatrix} \Delta \mathbf{Q}^A \\ \Delta \mathbf{Q}^u \end{pmatrix} = \begin{pmatrix} \Delta \mathbf{R}^A \\ \Delta \mathbf{R}^u \end{pmatrix}, \quad (3.16)$$

where

$$\mathbf{D}^A = \sum_{e=1}^{N^A} \int_{\Delta} (\mathbf{N}^A)^T \sigma_e \mathbf{N}^A J_e d\Delta, \quad (3.17)$$

$$\mathbf{D}^u = \sum_{e=1}^{N^u} \int_{\Delta} (\mathbf{N}^u)^T c_e \mathbf{N}^u J_e d\Delta, \quad (3.18)$$

$$\mathbf{M}^u = \sum_{e=1}^{N^u} \int_{\Delta} (\mathbf{N}^u)^T \rho_e \mathbf{N}^u J_e d\Delta. \quad (3.19)$$

3.2.2 Nonlinear dynamic implementation

A nonlinear dynamic solution is necessary to obtain the response of the transducer to large scale dynamic inputs. Solution of nonlinear dynamic systems is a particularly challenging task as even unconditionally stable time integration approaches for linear systems may become unstable. The governing equations for the finite element system are formulated in terms of the total (not incremental) quantities.

$$\mathbf{M}\ddot{\mathbf{U}} + \mathbf{D}\dot{\mathbf{U}} = \mathbf{R}(t) - \mathbf{F}(\mathbf{U}, t), \quad (3.20)$$

where the mass matrix \mathbf{M} , damping matrix \mathbf{D} , and state vector \mathbf{U} are of the form

$$\mathbf{M} = \begin{bmatrix} \mathbf{0} & \mathbf{0} \\ \mathbf{0} & \mathbf{M}^u \end{bmatrix}, \quad \mathbf{D} = \begin{bmatrix} \mathbf{D}^A & \mathbf{0} \\ \mathbf{0} & \mathbf{D}^u \end{bmatrix}, \quad \mathbf{U} = \begin{pmatrix} \mathbf{Q}^A \\ \mathbf{Q}^u \end{pmatrix}. \quad (3.21)$$

The vector of externally applied forces $\mathbf{R}(t)$ and the internal nodal force vector $\mathbf{F}(\mathbf{U}, t)$ are of the form

$$\mathbf{R} = \begin{pmatrix} \mathbf{R}^A \\ \mathbf{R}^u \end{pmatrix}, \quad \mathbf{F} = \begin{pmatrix} \mathbf{F}^A \\ \mathbf{F}^u \end{pmatrix}. \quad (3.22)$$

where \mathbf{R}^A includes contributions from coil source current density and externally imposed tangential fields, and \mathbf{R}^u includes contributions from traction on certain boundaries,

$$\mathbf{R}^u = \sum_{b=1}^{N_S^u} \int_{\Delta_S} (\mathbf{N}^u)^T \mathbf{t}_b J_{b,S} d\Delta_S, \quad (3.23)$$

$$\mathbf{R}^A = \sum_{b=1}^{N_S^A} \int_{\Delta_S} (\mathbf{N}^A)^T \mathbf{H}_T J_{b,S} d\Delta_S + \sum_{e=1}^{N^A} \int_{\Delta} (\mathbf{N}^A)^T \mathbf{J}_{s,e} J_e d\Delta. \quad (3.24)$$

Similarly \mathbf{F}^A and \mathbf{F}^u include contributions from the element fields and stresses,

$$\mathbf{F}^A = \sum_{e=1}^{N^A} \int_{\Delta} \mathbf{C}_e^T \mathbf{H}_e (\mathbf{B}_e, \mathbf{S}_e) J_e d\Delta, \quad (3.25)$$

$$\mathbf{F}^u = \sum_{e=1}^{N^u} \int_{\Delta} \mathbf{G}_e^T \mathbf{T}_e (\mathbf{B}_e, \mathbf{S}_e) J_e d\Delta. \quad (3.26)$$

The tangent stiffness matrix is obtained by differentiating \mathbf{F} with respect to \mathbf{U} ,

$$\mathbf{K} = \begin{bmatrix} \frac{\partial \mathbf{F}^A}{\partial \mathbf{Q}^A} & \frac{\partial \mathbf{F}^A}{\partial \mathbf{Q}^u} \\ \frac{\partial \mathbf{F}^u}{\partial \mathbf{Q}^A} & \frac{\partial \mathbf{F}^u}{\partial \mathbf{Q}^u} \end{bmatrix}, \quad (3.27)$$

where

$$\begin{aligned} \frac{\partial \mathbf{F}^A}{\partial \mathbf{Q}^A} &= \sum_{e=1}^{N^A} \int_{\Delta} \mathbf{C}_e^T \frac{\partial \mathbf{H}_e}{\partial \mathbf{q}_e^A} J_e d\Delta \\ &= \sum_{e=1}^{N^A} \int_{\Delta} \mathbf{C}_e^T \frac{\partial \mathbf{H}_e}{\partial \mathbf{B}_e} \frac{\partial \mathbf{B}_e}{\partial \mathbf{q}_e^A} J_e d\Delta \\ &= \sum_{e=1}^{N^A} \int_{\Delta} \mathbf{C}_e^T \frac{\partial \mathbf{H}_e}{\partial \mathbf{B}_e} \mathbf{C}_e J_e d\Delta. \end{aligned} \quad (3.28)$$

Similarly the other components can be obtained as

$$\frac{\partial \mathbf{F}^A}{\partial \mathbf{Q}^u} = \sum_{e=1}^{N^u} \int_{\Delta} \mathbf{C}_e^T \frac{\partial \mathbf{H}_e}{\partial \mathbf{S}_e} \mathbf{G}_e J_e d\Delta, \quad (3.29)$$

$$\frac{\partial \mathbf{F}^u}{\partial \mathbf{Q}^A} = \sum_{e=1}^{N^u} \int_{\Delta} \mathbf{G}_e^T \frac{\partial \mathbf{T}_e}{\partial \mathbf{B}_e} \mathbf{C}_e J_e d\Delta, \quad (3.30)$$

$$\frac{\partial \mathbf{F}^u}{\partial \mathbf{Q}^u} = \sum_{e=1}^{N^u} \int_{\Delta} \mathbf{G}_e^T \frac{\partial \mathbf{T}_e}{\partial \mathbf{B}_e} \mathbf{G}_e J_e d\Delta. \quad (3.31)$$

Thus, determination of the internal nodal force vector requires constitutive model inversion while determination of the tangent stiffness matrix requires computation of the material Jacobian inverse. The inversion process can be carried out using a Newton-Raphson or a Quasi-Newton algorithm. Both approaches can approximate the Jacobian inverse as a part of the inversion process.

Bathe [6] suggested various time-integration algorithms for nonlinear structural problems of similar form. Explicit methods are ruled out since the mass matrix is singular. An implicit scheme based on the trapezoidal rule is implemented, combined with equilibrium iterations. At the k^{th} iteration the system equations can be written as

$$\mathbf{M}^{t+\Delta t} \ddot{\mathbf{U}}^{(k)} + \mathbf{D}^{t+\Delta t} \dot{\mathbf{U}}^{(k)} + {}^{t+\Delta t}\mathbf{K}^{(k-1)} \Delta \mathbf{U}^{(k)} = {}^{t+\Delta t}\mathbf{R} - {}^{t+\Delta t}\mathbf{F}^{(k-1)}, \quad (3.32)$$

$${}^{t+\Delta t}\mathbf{U}^{(k)} = {}^{t+\Delta t}\mathbf{U}^{(k-1)} + \Delta \mathbf{U}^{(k)}. \quad (3.33)$$

According to the trapezoidal rule of time integration, the following assumptions are used:

$${}^{t+\Delta t}\mathbf{U} = {}^t\mathbf{U} + \frac{\Delta t}{2} \left({}^t\dot{\mathbf{U}} + {}^{t+\Delta t}\dot{\mathbf{U}} \right), \quad (3.34)$$

$${}^{t+\Delta t}\dot{\mathbf{U}} = {}^t\dot{\mathbf{U}} + \frac{\Delta t}{2} \left({}^t\ddot{\mathbf{U}} + {}^{t+\Delta t}\ddot{\mathbf{U}} \right). \quad (3.35)$$

The vectors $\ddot{\mathbf{U}}^{(k)}$ and $\dot{\mathbf{U}}^{(k)}$ can be written using (3.33) to (3.35) as

$${}^{t+\Delta t}\ddot{\mathbf{U}}^{(k)} = \frac{4}{\Delta t^2} \left({}^{t+\Delta t}\mathbf{U}^{(k-1)} - {}^t\mathbf{U} + \Delta \mathbf{U}^{(k)} \right) - \frac{4}{\Delta t} {}^t\dot{\mathbf{U}} - {}^t\ddot{\mathbf{U}}, \quad (3.36)$$

$${}^{t+\Delta t}\dot{\mathbf{U}}^{(k)} = \frac{2}{\Delta t} \left({}^{t+\Delta t}\mathbf{U}^{(k-1)} - {}^t\mathbf{U} + \Delta \mathbf{U}^{(k)} \right) - {}^t\dot{\mathbf{U}}. \quad (3.37)$$

Substitution in (3.32) yields the equation of motion for the system,

$$\begin{aligned} \left[{}^{t+\Delta t}\mathbf{K}^{(k-1)} + \frac{4\mathbf{M}}{\Delta t^2} + \frac{2\mathbf{D}}{\Delta t} \right] \Delta \mathbf{U}^{(k)} = {}^{t+\Delta t}\mathbf{R} - \mathbf{M} \left[\frac{4}{\Delta t^2} ({}^{t+\Delta t}\mathbf{U}^{(k-1)} - {}^t\mathbf{U}) - \frac{4}{\Delta t} {}^t\dot{\mathbf{U}} - {}^t\ddot{\mathbf{U}} \right] \\ - \mathbf{D} \left[\frac{2}{\Delta t} ({}^{t+\Delta t}\mathbf{U}^{(k-1)} - {}^t\mathbf{U}) - {}^t\dot{\mathbf{U}} \right] - {}^{t+\Delta t}\mathbf{F}^{(k-1)}. \end{aligned} \quad (3.38)$$

The starting values for the internal force and state vector are considered to be same as the corresponding final values of the previous time step,

$${}^{t+\Delta t}\mathbf{F}^{(0)} = {}^t\mathbf{F}, \quad {}^{t+\Delta t}\mathbf{U}^{(0)} = {}^t\mathbf{U}. \quad (3.39)$$

The convergence criteria used in this work are based on energy and norm of the out-of-balance load vector [6]. Mathematically, these criteria can be written as

$$\frac{\| {}^{t+\Delta t}\mathbf{R} - {}^{t+\Delta t}\mathbf{F}^{(k-1)} - \mathbf{M} {}^{t+\Delta t}\ddot{\mathbf{U}}^{(k-1)} - \mathbf{D} {}^{t+\Delta t}\dot{\mathbf{U}}^{(k-1)} \|}{RNORM} \leq RTOL, \quad (3.40)$$

$$\frac{\Delta \mathbf{U}^{(k)} \cdot \left({}^{t+\Delta t}\mathbf{R} - {}^{t+\Delta t}\mathbf{F}^{(k-1)} - \mathbf{M} {}^{t+\Delta t}\ddot{\mathbf{U}}^{(k-1)} - \mathbf{D} {}^{t+\Delta t}\dot{\mathbf{U}}^{(k-1)} \right)}{\Delta \mathbf{U}^{(1)} \cdot \left({}^{t+\Delta t}\mathbf{R} - {}^t\mathbf{F} - \mathbf{M} {}^t\ddot{\mathbf{U}} - \mathbf{D} {}^t\dot{\mathbf{U}} \right)} \leq ETOL. \quad (3.41)$$

The mass and damping matrix are state-independent and hence are assembled only once for the entire simulation. The internal nodal force vector \mathbf{F} and the tangential stiffness matrix \mathbf{K} are assembled in every iteration as they are state-dependent (Figure 3.2). Thus, efficient computation of \mathbf{F} and \mathbf{K} is vital to the performance of the model.

3.3 Implementation on COMSOL and MATLAB

The modeling framework described in sections 2.4 and 3.2 is implemented on COMSOL 3.5a utilizing its ability to interact with MATLAB functions. The basic template for the model is set-up by using two separate weak-form application modes, one for the mechanical and one for the magnetic degrees of freedom. The variables for

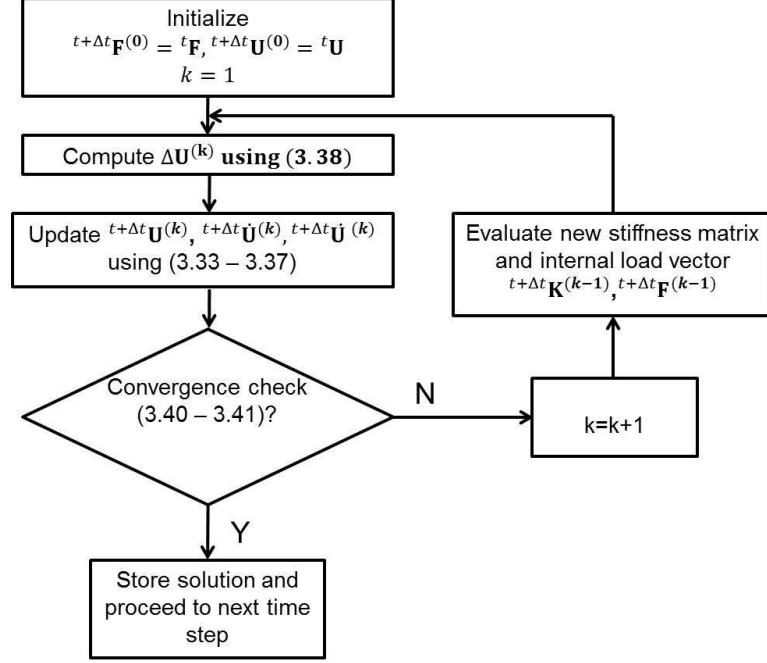


Figure 3.2: Outline of a single time step of the nonlinear dynamic solution algorithm. The flowchart shows how quantities at time $t + \Delta t$ are obtained with knowledge about all variables at time t .

the mechanical mode are uX, uY, uZ while for the magnetic mode are AX, AY, AZ . This separation of the mechanical and magnetic physics allows for reduction of the total degrees of freedom in the model. For example, a component which does not take part in the structural dynamics of the transducer (e.g a coil, air, flux return) is marked 'inactive' in the mechanical application mode. This means that the mechanical degrees of freedom are not solved for in these components.

The next step is to add global expressions in the model. These are essentially kinematic relationships ((2.79) and (2.80)) which are valid irrespective of the material (Figure 3.3). The weak form expressions are added in the subdomain settings. In the domains which are structurally active, the weak terms and time dependent

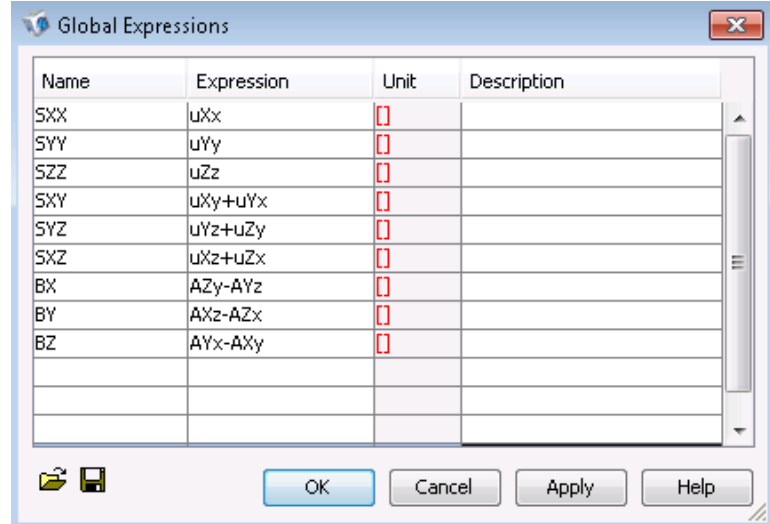


Figure 3.3: Screenshot of the global expressions relating flux density and strain to the vector magnetic potential and displacements.

expressions are entered as shown in Figure 3.4. Similarly, the weak form expressions for the magnetically active domains are entered within the subdomain settings of the magnetic application mode as shown in Figure 3.5. Boundary conditions are entered within the boundary settings dialog box of each application mode. The set-up of the model up till here is common for both the piecewise-linear and the nonlinear implementation. However, the next steps are specific to the solution process being used.

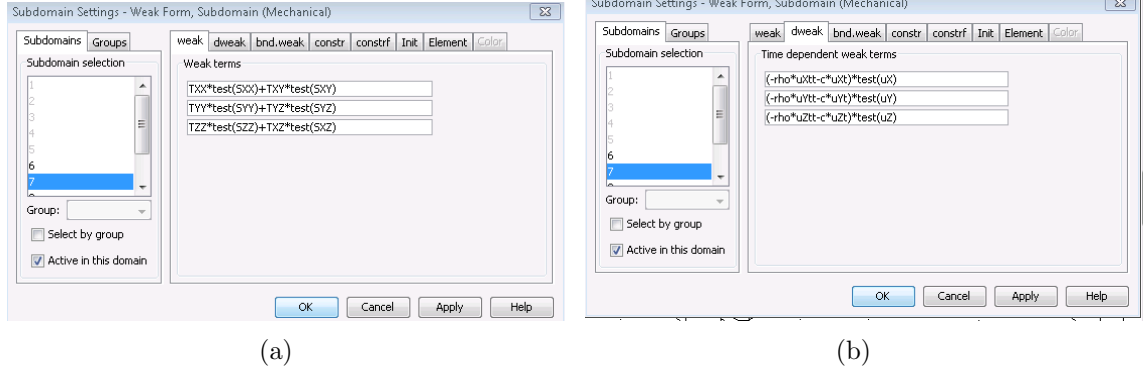


Figure 3.4: Screenshots of the weak and time-dependent weak terms (dweak) for the mechanical subdomain.

Piecewise-linear solution

For the piecewise linear solution, the constitutive laws are entered through subdomain expressions. Consider a magnetostrictive material whose piezomagnetic coefficient matrices are of the form

$$\boldsymbol{\mu}^{-1} = \begin{bmatrix} \mu_{11}^i & \mu_{12}^i & \mu_{13}^i \\ \mu_{12}^i & \mu_{22}^i & \mu_{23}^i \\ \mu_{13}^i & \mu_{23}^i & \mu_{33}^i \end{bmatrix}, \quad \mathbf{a} = \begin{bmatrix} a_{11} & a_{12} & a_{13} & a_{14} & a_{15} & a_{16} \\ a_{21} & a_{22} & a_{23} & a_{24} & a_{25} & a_{26} \\ a_{31} & a_{32} & a_{33} & a_{34} & a_{35} & a_{36} \end{bmatrix},$$

$$\mathbf{c} = \begin{bmatrix} c_{11} & c_{12} & c_{13} & 0 & 0 & 0 \\ c_{12} & c_{22} & c_{23} & 0 & 0 & 0 \\ c_{13} & c_{23} & c_{33} & 0 & 0 & 0 \\ 0 & 0 & 0 & c_{44} & 0 & 0 \\ 0 & 0 & 0 & 0 & c_{55} & 0 \\ 0 & 0 & 0 & 0 & 0 & c_{66} \end{bmatrix}. \quad (3.42)$$

The subdomain expressions required to model this material is shown in Table 3.1. The table also lists the expression used to model other passive materials. The constitutive laws have been grouped depending on the types of energy storage the material participates in. For example, air does not conduct electricity or take part in structural dynamics. It stores energy only in the magnetic form. The drive coil stores energy

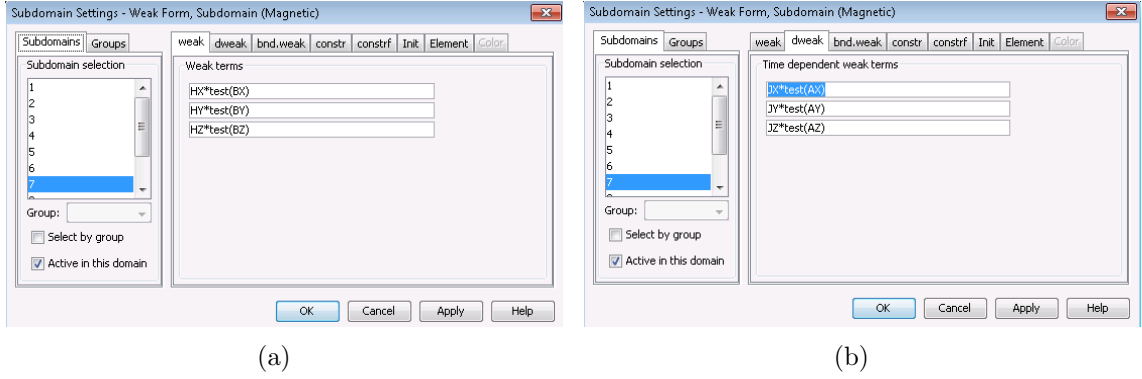


Figure 3.5: Screenshots of the weak and time-dependent weak terms (dweak) for the magnetic subdomain.

in magnetic form, as well as conducts electricity. However, usually it is structurally inactive. Similarly there could be structural metallic elements which store energy in all three forms. The magnetostrictive material always participates in all the energy domains. In the column for the magnetostrictive material, the parameters $\mu G11i$, $\mu G12i$ etc. are the piezomagnetic coefficients which are declared as functions of interpolated data. These functions, when called, read/interpolate the required value from a data file corresponding to the geometric location of the evaluation point. The data file needs to be updated after every step by a MATLAB function which computes the material Jacobian matrix at numerous points distributed throughout the magnetostrictive material. Once all these equations are entered, the model can be exported to an 'm' file and executed from the MATLAB command prompt. This gives the user additional freedom of storing the variables and scripting the solution process. The piecewise-linear solver must be coded to execute the steps outlined in Figure 3.1. The 'assemble' command with the appropriate arguments can be used to assemble the tangent stiffness matrix and the differential load vector at every step. The 'posteval'

command evaluates the stress and field increments using the subdomain expressions entered in the finite element model.

Nonlinear dynamic solution

The subdomain settings for the nonlinear model is entered in a manner similar to the piecewise-linear model except the format for entering the constitutive model for the magnetostrictive material. Rather than entering the constitutive law as expressions with coefficients declared as data functions, each component of the stress and field vectors is declared as a separate function coded up in MATLAB. Each of these functions take as input the three components of flux density and 6 components of strain. Along with the functions themselves, the derivative of every function with respect to each input parameter of that function is also required. These derivatives must be entered as separate functions in the derivatives dialog box as shown in Figure 3.6. The ‘mmodel_deriv’ function must be coded up such that it returns a specific derivative depending on the last parameter. For example when the last parameter is 1, the function must return $\partial HX/\partial BX$, when it is 2, the function must return $\partial HX/\partial BY$ and so on. Just like the piecewise-linear model, the model is exported to MATLAB after entering all the expressions. The nonlinear dynamic system solver is coded as a MATLAB function by following the steps outlined in section 3.2.2. The ‘assemble’ command can be used to assemble the mass and damping matrix at the beginning of the simulation, the stiffness matrix at the beginning of every step, and the out-of-balance load vector at every iteration. While assembling the stiffness matrix and the load vector, COMSOL repeatedly calls the material model functions (including the derivative functions). For computational efficiency, these functions should be

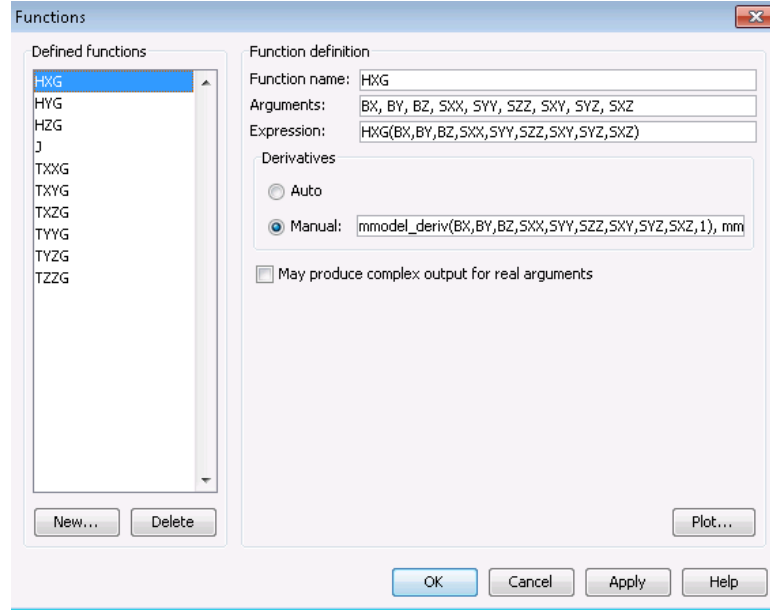


Figure 3.6: Screenshot showing the function definition for HX and declaration of the derivative functions.

coded such that for a particular set of input strain and induction values the model is inverted only once, and the corresponding stress, fields and derivatives are stored in a global data structure. Every time COMSOL calls any of the material model functions with the same induction and strain components, the required components can be returned from the stored data structure without any further computations.

Table 3.1: Subdomain expressions for the piecewise-linear model

Variable	Magnetic, Non- electrical, Non- mechanical, e.g. Air	Magnetic, electrical, Non- mechanical, e.g. Coil	Magnetic, trical, mechanical, Flux return	Elec- Non- e.g.	Magnetic, Electrical, Mechanical, e.g. magnetostrictives	Magnetic, Electrical, Me- chanical, e.g. structural metallic elements
HX	BX/mu0	BX/mu0	BX/mu		BX*muG11i+BY*muG12i+BZ*muG13i - a11*SXX- a12*SY - a13*SZZ - a14*SXY - a15*SYZ - a16*SXX	BX/mu
HY	BY/mu0	BY/mu0	BY/mu		BX*muG12i+BY*muG22i+BZ*muG23i - a21*SXX - a22*SY - a23*SZZ - a24*SXY - a25*SYZ - a26*SXX	BY/mu
HZ	BZ/mu0	BZ/mu0	BZ/mu		BX*muG13i+BY*muG23i+BZ*muG33i - a31*SXX- a32*SY - a33*SZZ- a34*SXY - a35*SYZ- a36*SXX	BZ/mu
TXX	0	0	0		c11G*SXX + c12G*SY + c13G*SZZ - a11*BX - a21*BY - a31*BZ	ES*((1-vS)*SXX+vS*SY+ vS*SZZ)/((1+vS)*(1-2*vS))
TY	0	0	0		c12G*SXX + c22G*SY + c23G*SZZ - a12*BX- a22*BY - a32*BZ	ES*((1-vS)*SY+vS*SXX+ vS*SZZ)/((1+vS)*(1-2*vS))
TZZ	0	0	0		c13G*SXX + c23G*SY + c33G*SZZ - a13*BX- a23*BY - a33*BZ	ES*((1-vS)*SZZ+vS*SY+ vS*SXX)/((1+vS)*(1-2*vS))
TX	0	0	0		c44G*SXY - a14*BX - a24*BY - a34*BZ	0.5*ES*SXY/(1+vS)
TYZ	0	0	0		c55G*SYZ - a15*BX- a25*BY - a35*BZ	0.5*ES*SYZ/(1+vS)
TXZ	0	0	0		c66G*SXZ - a16*BX- a26*BY - a36*BZ	0.5*ES*SXZ/(1+vS)
JX	0	-sig*AXt	-sig*AXt		-sig*AXt	-sig*AXt
JY	0	-sig*AYt	delJ*z/sqrt(y ² +z ²) - sig*AYt		-sig*AYt	-sig*AYt
JZ	0	-sig*AZt	delJ*y/sqrt(y ² +z ²) - sig*AZt		-sig*AZt	-sig*AZt

Chapter 4: GALFENOL TRANSDUCERS

Magnetostrictive iron-gallium alloys (Galfenol) possess structural-grade mechanical properties in addition to exhibiting moderate magnetostriction. These properties make Galfenol uniquely well-suited for integration within three-dimensional (3D) active structures. Galfenol can be used in sensors or actuators capable of withstanding tension, compression, and shock loads. This chapter deals with coupling a nonlinear energy-averaged constitutive law for Galfenol with the finite element framework described in Chapter 3 to describe the full nonlinear coupling between the electrical, magnetic, and mechanical domains in Galfenol systems.

A parameter optimization algorithm is proposed to determine the parameters of the discrete energy averaged model incorporated into the 3D dynamic finite element framework. The algorithm uses the 1D magnetomechanical actuation and sensing curves for the Galfenol alloy as input and computes the model parameters by minimizing an error functional defined between the modeled curves and measurements. Initial guesses on the parameters are obtained by using analytical relationships which relate specific model parameters to certain features in the experimental data. Parameters are optimized for unannealed single crystal $\langle 100 \rangle$ $\text{Fe}_{81.6}\text{Ga}_{18.4}$ and textured polycrystalline $\langle 100 \rangle$ $\text{Fe}_{81.5}\text{Ga}_{18.5}$ alloys with and without stress annealing. A case

study on a Galfenol unimorph actuator reveals the ability of the model to describe the quasistatic and dynamic response of the actuator.

4.1 Parameter estimation of a discrete energy-averaged model from 1D measurements

Implementation of nonlinear coupled constitutive behavior poses a significant challenge in distributed parameter modeling frameworks. Earlier works modeled magnetostrictive behavior using polynomial fits to measurements. For example, Benbouzid et al. [8] fit surface splines to experimental data while Kannan and Dasgupta [50] used constitutive relations in an incremental form with coefficients obtained from bi-cubic spline fits to measurements. Kim et al. [55] used 6th order polynomials to fit the strain-field behavior of Terfenol-D with a different set of polynomial coefficients for each preload condition. The use of spline functions to fit measurements has the advantages of easy differentiability and implementation. However, the procedure becomes rather complex if complete 3D material behavior is required. This would require 3D measurements to be performed, and bulky splines with 9 components (3 for field and 6 for stress) to be fitted to those measurements. Graham et al. [40] implemented Galfenol constitutive behavior through look up tables generated *a priori* using the Armstrong model [3] for a large number of induction and stress values. Although the Armstrong model is capable of describing 3D Galfenol behavior, look up tables were generated for 1D induction and stress inputs. As is the case with splines, extension to a full 3D version will add significant complexity because it will require generation of bulky tables with nine inputs and nine outputs.

To overcome the complexities associated with 3D measurements and subsequent multivariate interpolation, significant emphasis is placed on incorporating efficient

theoretical constitutive laws within distributed parameter models. A physically motivated constitutive law takes advantage of symmetries in the material and is capable of predicting 3D material behavior with reduced order information.

The response of Galfenol varies significantly depending on its composition [23] and material processing techniques [73]. Changes in composition or processing methods can be made as required by an application. For example, increasing Gallium concentration from 18.4% to 20.9% reduces the saturation magnetostriction but increases the stress range over which the material shows a stress dependent susceptibility change making it more suitable for force sensing applications [59]. Through a process called stress-annealing [73, 84] a tetragonal anisotropy can be introduced in Galfenol where the two $\langle 100 \rangle$ easy directions parallel to the direction of magnetic field application have a higher anisotropy energy than the remaining four orientations perpendicular to the sample axis. This enables the alloy to exhibit maximum saturation magnetostriction without any compressive preload. An algorithm which optimizes the constitutive model parameters to describe these variations in Galfenol behavior will greatly improve the applicability of the constitutive law in transducer design.

This work aims at developing a formal procedure to estimate the parameters of the anhysteretic discrete energy averaged model for Galfenol which is incorporated into a finite element framework for transducer level modeling [17]. The parameter optimization algorithm takes as input selected 1D magnetomechanical measurements and calculates the constitutive model parameters such that the only inputs required by the finite element model are the system level parameters (permeability, conductivity, Young's modulus etc. of passive materials) and the 1D magnetostrictive material characterization curves (Figure 4.1). Section 4.1.1 discusses the Galfenol constitutive

large computational effort involved in evaluating the expected values by solving two dimensional integrals numerically, a discrete version of the model was developed [2]. The choice of possible domain orientations was restricted to the easy magnetization axes with volume fraction of domains in each state calculated using a discretized version of the probability density function. The increase in computational speed, however, came at the cost of reduced accuracy. To preserve accuracy without sacrificing efficiency, Evans and Dapino [32] developed a constitutive model for Galfenol by choosing orientations which minimize an energy functional locally defined in the vicinity of each easy axis.

The anisotropy energy G_A^k is formulated about the k^{th} easy axis \mathbf{c}^k as

$$G_A^k = \frac{1}{2} K^k \|\mathbf{m}^k - \mathbf{c}^k\|^2, \quad (4.1)$$

where the constants K^k control the anisotropy energy landscape in the vicinity of the easy axes. The anisotropy energy along each easy axis is, however, identically zero. For materials with cubic anisotropy (such as unannealed Galfenol), the anisotropy energy along each easy axis is the same and the model can be applied in its present form. However, it has been shown that stress annealing induces tetragonal anisotropy in Galfenol [73] where the four $\langle 100 \rangle$ directions perpendicular to the annealing direction have a lower energy than the other two. To make the model capable of describing these effects, the anisotropy energy is modified as

$$G_A^k = \frac{1}{2} K \|\mathbf{m}^k - \mathbf{c}^k\|^2 + K_0^k, \quad (4.2)$$

where K controls the energy landscape in the vicinity of the easy axes and K_0^k specifies the base anisotropy energy along the k^{th} easy axis. Six parameters are required to describe the anisotropy energy (K, K_0^1, \dots, K_0^5) , where K_0^k is defined as the anisotropy

energy relative to the sixth easy axis. Thus, the total number of parameters is same as the earlier description of anisotropy energy [32]. Further, the \mathbf{m} -dependent portion of the anisotropy energy remains unchanged, which means the minimization results remain unaffected.

With this definition, the total free energy of a domain close to the k^{th} easy axis \mathbf{c}^k is formulated as the sum of the local anisotropy energy G_A^k , magnetomechanical coupling energy G_C^k and the Zeeman energy G_Z^k ;

$$G^k = \underbrace{\frac{1}{2}K\|\mathbf{m}^k - \mathbf{c}^k\|^2 + K_0^k}_{G_A^k} - \underbrace{\mathbf{S}_m^k \cdot \mathbf{T}}_{G_C^k} - \underbrace{\mu_0 M_s \mathbf{m}^k \cdot \mathbf{H}}_{G_Z^k}, \quad (4.3)$$

which must be minimized with respect to the orientation vector \mathbf{m}^k in the vicinity of \mathbf{c}^k . The minimization problem is constrained ($\|\mathbf{m}^k\| = 1$) and is formulated as an inhomogeneous eigenvalue problem through the use of Lagrange multipliers. The total energy is written as

$$G^k = \frac{1}{2}\mathbf{m}^k \cdot \mathbf{K}\mathbf{m}^k - \mathbf{m}^k \cdot \mathbf{B}^k + \frac{1}{2}K + K_0^k, \quad (4.4)$$

where the magnetic stiffness matrix \mathbf{K} and force vector \mathbf{B}^k are

$$\mathbf{K} = \begin{bmatrix} K - 3\lambda_{100}T_1 & -3\lambda_{111}T_4 & -3\lambda_{111}T_6 \\ -3\lambda_{111}T_4 & K - 3\lambda_{100}T_2 & -3\lambda_{111}T_5 \\ -3\lambda_{111}T_6 & -3\lambda_{111}T_5 & K - 3\lambda_{100}T_3 \end{bmatrix}, \quad (4.5)$$

$$\mathbf{B}^k = [c_1^k K + \mu_0 M_s H_1 \quad c_2^k K + \mu_0 M_s H_2 \quad c_3^k K + \mu_0 M_s H_2]^T. \quad (4.6)$$

The Lagrange function is constructed as the sum of the energy functional and unity norm constraint on the orientation vectors linearized about the easy axis orientations ($\mathbf{m}^k \cdot \mathbf{m}^k = 1 \approx \mathbf{c}^k \cdot \mathbf{m}^k = 1$):

$$L = \frac{1}{2}\mathbf{m}^k \cdot \mathbf{K}\mathbf{m}^k - \mathbf{m}^k \cdot \mathbf{B}^k + \lambda^k (\mathbf{c}^k \cdot \mathbf{m}^k - 1), \quad (4.7)$$

where λ^k is the Lagrange multiplier corresponding to the k^{th} easy axis. Differentiating the Lagrange function with respect to \mathbf{m}^k and equating to zero one gets

$$\mathbf{m}^k = \mathbf{K}^{-1} [\mathbf{B}^k - \lambda^k \mathbf{c}^k]. \quad (4.8)$$

Substitution of \mathbf{m}^k from (4.8) into the constraint yields the following expression for the Lagrange multiplier:

$$\lambda^k = -\frac{1 - \mathbf{c}^k \cdot (\mathbf{K})^{-1} \mathbf{B}^k}{\mathbf{c}^k \cdot (\mathbf{K})^{-1} \mathbf{c}^k}, \quad (4.9)$$

which on substitution into (4.8) gives the following analytical expression for the orientation which minimizes the energy around the k^{th} easy axis, of the form

$$\mathbf{m}^k = (\mathbf{K})^{-1} \left[\mathbf{B}^k + \frac{1 - \mathbf{c}^k \cdot (\mathbf{K})^{-1} \mathbf{B}^k}{\mathbf{c}^k \cdot (\mathbf{K})^{-1} \mathbf{c}^k} \mathbf{c}^k \right]. \quad (4.10)$$

A limitation of the constitutive law in its current form is that the unity norm constraint on \mathbf{m}^k is not strictly enforced. As a result at very high fields well in the saturation regime, the norm of \mathbf{m}^k can become much greater than unity thus yielding unphysical magnetization and strain calculations (Figure 4.2). This issue can be addressed by strictly enforcing the unity norm constraint rather than using the approximation $\mathbf{m}^k \cdot \mathbf{m}^k = 1 \approx \mathbf{c}^k \cdot \mathbf{m}^k = 1$. However, that leads to a sixth order equation for the Lagrange multiplier requiring numerical techniques for solution thus compromising the efficiency of the model [32]. In order to maintain the stability of the model without sacrificing its efficiency, \mathbf{m}^k is normalized and denoted by the symbol $\hat{\mathbf{m}}^k$ in all future calculations where

$$\hat{\mathbf{m}}^k = \frac{\mathbf{m}^k}{\|\mathbf{m}^k\|}. \quad (4.11)$$

Figure 4.2 shows that the output of the model with and without the normalization is almost the same till the former becomes unstable. Thus normalizing the minima

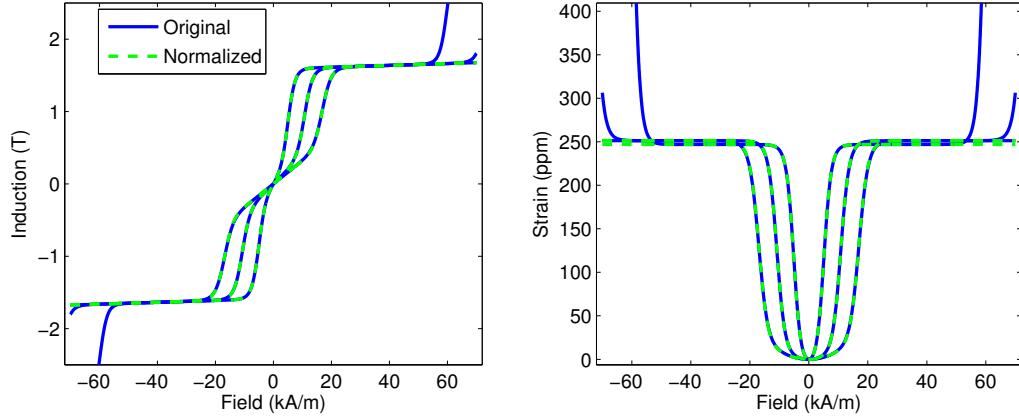


Figure 4.2: Comparison of model outputs with and without normalizing \mathbf{m}^k . Simulations run at constant prestresses of 20, 50 and 80 MPa.

eliminates the instability and preserves the accuracy of the constitutive model with almost the same number of computations. The anhysteretic volume fractions are calculated explicitly using Boltzmann-type averaging,

$$\xi_{an}^k = \frac{\exp(-G^k/\Omega)}{\sum_{j=1}^r \exp(-G^j/\Omega)}, \quad (4.12)$$

where Ω is an averaging factor. Macroscopic anhysteretic material behavior is obtained by summing the individual contributions of each domain weighted by its corresponding volume fraction. The bulk magnetization \mathbf{M} and strain \mathbf{S} are obtained by averaging the properties along the six minima weighted by their respective volume fractions:

$$\mathbf{M} = M_s \sum_{k=1}^r \xi_{an}^k \hat{\mathbf{m}}^k, \quad (4.13)$$

$$\mathbf{S} = \mathbf{sT} + \sum_{k=1}^r \xi_{an}^k \mathbf{S}_m^k. \quad (4.14)$$

The model parameters are the six anisotropy constants, smoothing factor (Ω), magnetostriction constants (λ_{100} , λ_{111}), and the saturation magnetization (M_s). The base anisotropy constants are split into two groups: $K_{0\parallel}$ and $K_{0\perp}$. $K_{0\parallel}$ is the anisotropy energy for the two orientations parallel to the axis of the rod while $K_{0\perp}$ is the anisotropy constant for the four orientations perpendicular to the axis of the rod. Since we are interested only in the relative anisotropy energies, any one of them can be chosen to be zero. In this paper, $K_{0\perp}$ is chosen to be zero, thus reducing the total number of unknown parameters to six. For unannealed Galfenol, $K_{0\parallel}$ is expected to be almost equal to $K_{0\perp}$ which is chosen to be zero, while for annealed Galfenol $K_{0\parallel}$ is expected to be significantly larger than $K_{0\perp}$ due to the induced tetragonal anisotropy.

4.1.2 Parameter optimization procedure

The parameter optimization process consists of two steps. First, anhysteretic curves are obtained from hysteretic measurements through a simple averaging procedure. This is necessary because we are interested in optimizing the anhysteretic model parameters only. Next, a least squares optimization routine is used to minimize the error between the family of modeled curves and the anhysteretic curves obtained from measurements.

Extracting the anhysteretic curves from measurements

The de-hysterized curves are obtained by computing an average value from the upper and lower branches of the hysteresis loops (similar to Benbouzid et al. [8]). As pointed out by Benbouzid et al. [8], this procedure yields an approximate anhysteretic value and may not coincide with experimental anhysteretic curves obtained by superimposing a decaying AC component of the input (field or stress) about a mean

value. Since Galfenol exhibits extremely low hysteresis, the error due to this approximation should be negligible. The anhysteretic curves are obtained by sweeping the input (field or stress) over the entire applied range at discrete steps and finding an average value of the response over a range of inputs. For example, the anhysteretic magnetostriction at a field H_0 is computed as

$$S_{an}(H_0) = AVG(S(H) : H_0 - \delta_H < H < H_0 + \delta_H), \quad (4.15)$$

where δ_H is a small number compared to the maximum applied field. The value of δ_H must be chosen carefully. A large value introduces error due to averaging over a wider range of fields while a very small δ_H might result in non-existence of a data point within that range. By calculating the anhysteretic curves using this method, the data can be sampled at a much lower rate than which it was collected. This is useful because the material model function is executed as many times as the number of points on the extracted anhysteretic curve. Fewer number of data points imply that the material model would be executed fewer times, speeding up the overall optimization procedure. Figure 4.3 shows measurements and the extracted anhysteretic curves for a single crystal $\langle 100 \rangle$ $\text{Fe}_{81.5}\text{Ga}_{18.5}$ sample grown with FSZM.

Estimating the model parameters

Parameter optimization is done using the MATLAB function *fmincon*. This function needs an initial guess and bounds for each parameter. Further it requires a scalar error definition which it minimizes. The aim of the optimization process is to find the model parameters which describe the entire family of curves (consisting of different data sets: magnetization and strain vs field for actuation and vs stress for sensing).

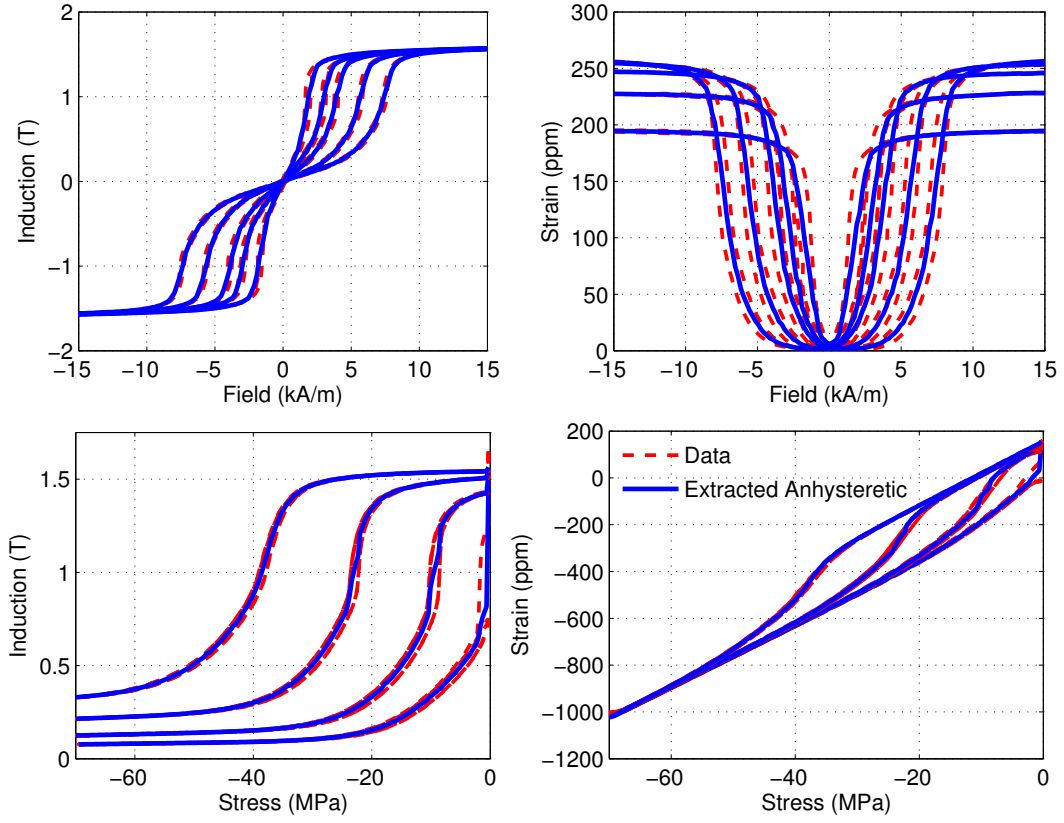


Figure 4.3: Extracted anhysteretic curves from measurements on single crystal $\langle 100 \rangle$ $\text{Fe}_{81.5}\text{Ga}_{18.5}$ grown with FSZM at constant stress values of 0.32, 8.00, 13.4, 23.1, 32.3 MPa (compression) and constant field values of 1.85, 3.24, 5.65, 8.88 kA/m (Measurements collected by Phillip Evans [33]).

Thus the error functional must describe an average error for an entire family of curves. This is done in the following manner.

1. For every curve, the modeling error is quantified using a normalized RMS error definition. The error for the i^{th} curve in a data set is given as

$$\text{error}_i = \frac{1}{\text{range}(\mathbf{X}_i)} \sqrt{\frac{\sum_{j=1}^{N_i} (Y_{ij} - X_{ij})^2}{N_i}}, \quad (4.16)$$

where Y_{ij} and X_{ij} are the j^{th} component of the i^{th} model vector and the extracted anhysteretic data vector respectively each containing N_i points, and $\text{range}(\mathbf{X}_i)$ is the difference between the upper and lower bound for that curve.

2. A mean error for the entire family is obtained by averaging the normalized RMS errors for each curve in the family.

Initial guess and bounds on each parameter

The efficiency of the optimization algorithm can be greatly enhanced by providing a good initial guess on the parameters. M_s and λ_{100} can be directly obtained from the saturation magnetization and magnetostriction respectively. The anisotropy constant K is estimated by calculating the slope of the extracted anhysteretic magnetization-field curve for a particular stress T at zero field and equating it to the expression for low field stress dependent susceptibility $\chi(T)$ described by Evans et al. [34], giving

$$K = \frac{\mu_0 M_s^2}{\chi(T)} + 3\lambda_{100}T. \quad (4.17)$$

The anisotropy constant $K_{0\parallel}$ can be estimated by equating the energies of the orientations perpendicular and parallel to the direction of application of field in the burst

region. These energies are given by

$$E_{\perp} = \frac{(\mu_0 M_s H)^2}{6\lambda_{100}T - 2K}, \quad (4.18)$$

$$E_{\parallel} = -\frac{3}{2}\lambda_{100}T - \mu_0 M_s H + K_{0\parallel}. \quad (4.19)$$

The logic behind this is that the burst region occurs when the energies of two orientations become roughly equal and domains start flipping from one orientation to the other. An average burst field (H_{burst}) is obtained by selecting the magnetic field corresponding to which the gradient of the magnetization-field curve is maximum. Equating 4.18 and 4.19 using this burst field gives

$$K_{0\parallel} = \frac{(\mu_0 M_s H_{burst})^2}{6\lambda_{100}T - 2K} + \frac{3}{2}\lambda_{100}T + \mu_0 M_s H_{burst}. \quad (4.20)$$

The remaining parameters Ω and λ_{111} cannot be estimated directly from measurements. Parameter Ω is given an arbitrary starting value of 2 kJ/m³ while λ_{111} has no effect on the 1D response along the [100] directions with uniaxial stress application. Determination of λ_{111} requires additional experiments with stresses applied along two different $\langle 100 \rangle$ directions. The bounds for all parameters are selected to be 50% above and below the initial guess except the smoothing factor Ω , for which a wide range from 0.5 - 30 kJ/m³ is selected.

4.1.3 Results

The performance of the parameter optimization algorithm is tested with different levels of input information. First, the algorithm is run using the full family of measurements. This gives a measure of the best case performance of the algorithm. Figure 4.4 shows the model performance with optimized parameters, for a single crystal $\langle 100 \rangle$ Fe_{81.5}Ga_{18.5} sample. The location of the burst region is accurately predicted in all the

curves. The model is also capable of describing the lower saturation magnetostriction at low bias stresses. To demonstrate the performance of the model in describing the

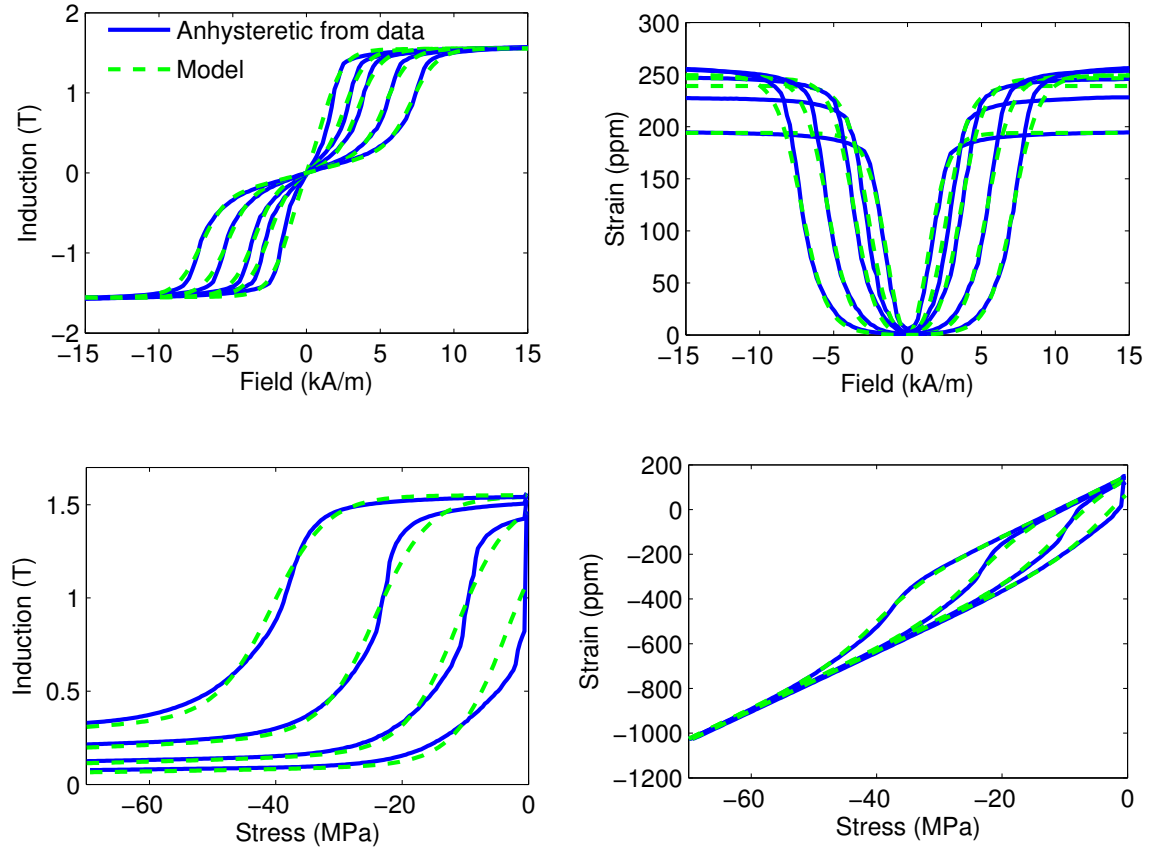


Figure 4.4: Comparison of anhysteretic model to the extracted anhysteretic curves from measurements on a $\text{Fe}_{81.5}\text{Ga}_{18.5}$ sample. Actuation measurements are at constant compressive stresses of 0.32, 8, 13.4, 23.1, and 32.3 MPa while sensing measurements are at constant bias fields of 1.85, 3.24, 5.65, and 8.88 kA/m.

behavior of samples subjected to stress annealing, the parameters are optimized using the measurements collected at the Naval Surface Warfare Center for unannealed

and annealed $\langle 100 \rangle$ textured polycrystalline $\text{Fe}_{81.6}\text{Ga}_{18.4}$ by James Restorff [72]. Figures 4.5 and 4.6 shows that with optimized parameters, the model can describe the magnetomechanical response of both unannealed and annealed Galfenol. Table 4.1 lists down the optimized parameters obtained for all three cases. As expected, $K_{0\parallel}$ is substantially larger for the annealed sample as compared to the unannealed samples. Also the smoothing factor for the textured polycrystalline samples is much larger than the single crystal simple.

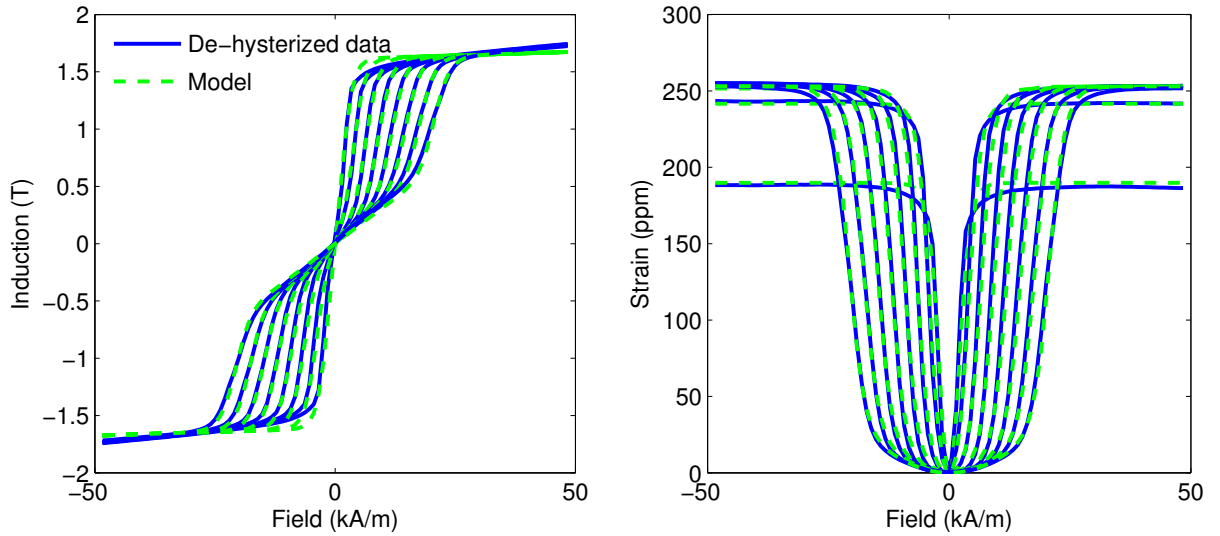


Figure 4.5: Anhyseretic model fit to the extracted anhyseretic curves with optimized parameters for unannealed $\langle 100 \rangle$ textured polycrystalline $\text{Fe}_{81.6}\text{Ga}_{18.4}$. Measurements are at constant compressive pre-stresses of 1.38 , 13.8, 27.6, 41.4, 55.2, 69.0, 82.7, and 96.5 MPa.

From the point of view of the transducer designer, the utility of the parameter optimization algorithm will be greatly enhanced if the model parameters can be

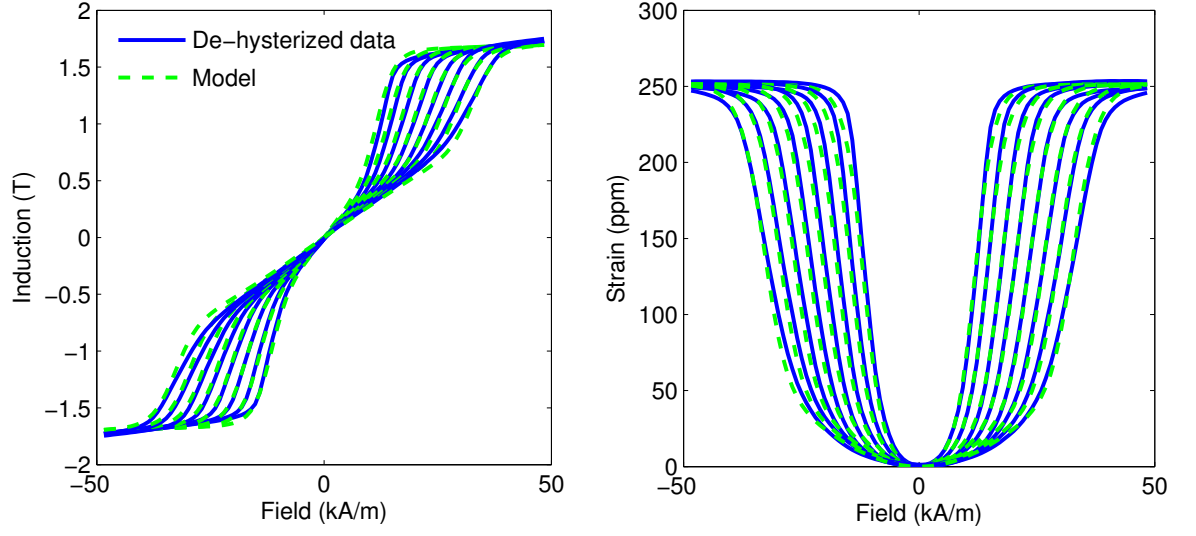


Figure 4.6: Anhysteretic model fit to the extracted anhysteretic curves with optimized parameters for annealed $\langle 100 \rangle$ textured polycrystalline $\text{Fe}_{81.6}\text{Ga}_{18.4}$. Measurements are at constant compressive pre-stresses of 1.38 , 13.8, 27.6, 41.4, 55.2, 69.0, 82.7, and 96.5 MPa.

predicted accurately with reduced number of experiments. Usually actuation measurements are simpler to perform than sensing measurements because it is easier to maintain a constant stress on the sample than constant field. Table 4.2 shows that when the model parameters are optimized using only the actuation measurements for the single crystal sample, the mean modeling error for all the curves (actuation and sensing) increases by only 0.1%. Thus, sensing behavior can be accurately quantified using actuation measurements.

The experimentation process can be further simplified if actuation measurements at only one prestress could be used to estimate the model parameters. The prestress applied on the sample could be anywhere between the lower and upper limit of the working stress range. Table 4.2 shows that it is beneficial to have a moderate to

Table 4.1: Optimized model parameters for the different data sets.

Parameters	Single crystal $\text{Fe}_{81.5}\text{Ga}_{18.5}$	Textured polycrystalline $\text{Fe}_{81.5}\text{Ga}_{18.5}$ (unannealed)	Textured polycrystalline $\text{Fe}_{81.5}\text{Ga}_{18.5}$ (annealed)
$K \times 10^4 \text{ (J/m}^3\text{)}$	3.4842	3.7178	5.255
$K_{0\parallel} \times 10^4 \text{ (J/m}^3\text{)}$	0.0498	0.0224	1.247
$\mu_0 M_s \text{ (T)}$	1.5394	1.5836	1.6006
$\lambda_{100} \times 10^3$	1.6631	1.6844	1.6733
$\lambda_{111} \times 10^3$	-	-	-
$a \times 10^3 \text{ (J)}$	10.147	15.146	21.296
$E_s \text{ (GPa)}$	7.531	-	-

large prestress on the sample while collecting measurements. When parameters are optimized using the lowest prestress measurement, large errors are obtained for the single crystal and unannealed polycrystalline sample. This happens because low prestresses do not align the magnetic domains perpendicular to the axis of the sample and the resulting saturation magnetostriction is lower than $3/2\lambda_{100}$. Since the initial guess for parameter λ_{100} is estimated directly from the saturation magnetostriction, the performance of the optimization algorithm deteriorates. In the annealed sample, the domains are oriented perpendicular to the sample axis because of the tetragonal anisotropy. This causes maximum saturation magnetostriction even with no external prestress applied and the performance of the parameter optimization algorithm does not deteriorate. Application of moderate to high prestress yields maximum saturation magnetostriction for all samples and mean errors less than 4% are obtained in all cases.

Table 4.2: Mean normalized modeling error % with model parameters found using different levels of experimental information.

Parameters	Single crystal Fe _{81.5} Ga _{18.5}	Textured polycrystalline Fe _{81.6} Ga _{18.4} (unannealed)	Textured polycrystalline Fe _{81.6} Ga _{18.4} (annealed)
Full Set	2.1	1.3	1.3
Only actuation curves	2.2	-	-
Actuation curves at a single prestress			
- Lowest prestress	6.4	9.5	1.9
- Intermediate prestress	3.0	1.7	1.4
- Highest prestress	3.4	1.9	1.7

4.2 Galfenol Constitutive Law Incorporation

In this section the Galfenol constitutive law described in Section 4.1.1 will be implemented in the unified finite element framework described in chapter 3 following the techniques described in Sections 3.2.1 and 3.2.2. The first step is to evaluate the material Jacobian matrix.

Evaluating the material Jacobian

Evaluation of the material Jacobian requires computation of the derivatives $\partial \mathbf{B} / \partial \mathbf{H}$, $\partial \mathbf{B} / \partial \mathbf{T}$, $\partial \mathbf{S} / \partial \mathbf{H}$, and $\partial \mathbf{S} / \partial \mathbf{T}$. The tensors \mathbf{S} and \mathbf{T} are written in contracted notation. The derivatives are obtained with respect to H_i ($i=1,2,3$) and T_i ($i=1,2...6$). Magnetic induction is algebraically related to magnetic field and magnetization,

$$\mathbf{B} = \mu_0 (\mathbf{H} + \mathbf{M}) . \quad (4.21)$$

The derivatives of \mathbf{B} with respect to T_i and H_i are

$$\frac{\partial \mathbf{B}}{\partial T_i} = \mu_0 \left(\frac{\partial \mathbf{M}}{\partial T_i} \right), \quad (4.22)$$

$$\frac{\partial \mathbf{B}}{\partial H_i} = \mu_0 \left(\frac{\partial \mathbf{H}}{\partial H_i} + \frac{\partial \mathbf{M}}{\partial H_i} \right). \quad (4.23)$$

The derivatives of \mathbf{M} and \mathbf{S} with respect to H_i and T_i can be obtained by differentiating (4.13) and (4.14),

$$\frac{\partial \mathbf{M}}{\partial H_i} = \sum_{k=1}^r M_s \left(\frac{\partial \hat{\mathbf{m}}^k}{\partial H_i} \xi_{an}^k + \hat{\mathbf{m}}^k \frac{\partial \xi_{an}^k}{\partial H_i} \right), \quad (4.24)$$

$$\frac{\partial \mathbf{M}}{\partial T_i} = \sum_{k=1}^r M_s \left(\frac{\partial \hat{\mathbf{m}}^k}{\partial T_i} \xi_{an}^k + \hat{\mathbf{m}}^k \frac{\partial \xi_{an}^k}{\partial T_i} \right), \quad (4.25)$$

$$\frac{\partial \mathbf{S}}{\partial H_i} = \sum_{k=1}^r \left(\frac{\partial \mathbf{S}_{\mathbf{m}}^k}{\partial H_i} \xi_{an}^k + \mathbf{S}_{\mathbf{m}}^k \frac{\partial \xi_{an}^k}{\partial H_i} \right), \quad (4.26)$$

$$\frac{\partial \mathbf{S}}{\partial T_i} = \mathbf{s} \frac{\partial \mathbf{T}}{\partial T_i} + \sum_{k=1}^r \left(\frac{\partial \mathbf{S}_{\mathbf{m}}^k}{\partial T_i} \xi_{an}^k + \mathbf{S}_{\mathbf{m}}^k \frac{\partial \xi_{an}^k}{\partial T_i} \right). \quad (4.27)$$

Thus, the partial derivatives of $\hat{\mathbf{m}}^k$, $\mathbf{S}_{\mathbf{m}}^k$ and ξ_{an}^k with respect to H_i and T_i must be obtained. The derivatives of $\mathbf{S}_{\mathbf{m}}^k$ can be written as

$$\frac{\partial \mathbf{S}_{\mathbf{m}}^k}{\partial H_i} = \left\{ \begin{array}{c} 3\lambda_{100} \hat{m}_1^k \frac{\partial \hat{m}_1^k}{\partial H_i} \\ 3\lambda_{100} \hat{m}_2^k \frac{\partial \hat{m}_2^k}{\partial H_i} \\ 3\lambda_{100} \hat{m}_3^k \frac{\partial \hat{m}_3^k}{\partial H_i} \\ 3\lambda_{111} \left(\hat{m}_1^k \frac{\partial \hat{m}_2^k}{\partial H_i} + \hat{m}_2^k \frac{\partial \hat{m}_1^k}{\partial H_i} \right) \\ 3\lambda_{111} \left(\hat{m}_2^k \frac{\partial \hat{m}_3^k}{\partial H_i} + \hat{m}_3^k \frac{\partial \hat{m}_2^k}{\partial H_i} \right) \\ 3\lambda_{111} \left(\hat{m}_3^k \frac{\partial \hat{m}_1^k}{\partial H_i} + \hat{m}_1^k \frac{\partial \hat{m}_3^k}{\partial H_i} \right) \end{array} \right\}, \quad (4.28)$$

$$\frac{\partial \mathbf{S}_{\mathbf{m}}^k}{\partial T_i} = \left\{ \begin{array}{c} 3\lambda_{100} \hat{m}_1^k \frac{\partial \hat{m}_1^k}{\partial T_i} \\ 3\lambda_{100} \hat{m}_2^k \frac{\partial \hat{m}_2^k}{\partial T_i} \\ 3\lambda_{100} \hat{m}_3^k \frac{\partial \hat{m}_3^k}{\partial T_i} \\ 3\lambda_{111} \left(\hat{m}_1^k \frac{\partial \hat{m}_2^k}{\partial T_i} + \hat{m}_2^k \frac{\partial \hat{m}_1^k}{\partial T_i} \right) \\ 3\lambda_{111} \left(\hat{m}_2^k \frac{\partial \hat{m}_3^k}{\partial T_i} + \hat{m}_3^k \frac{\partial \hat{m}_2^k}{\partial T_i} \right) \\ 3\lambda_{111} \left(\hat{m}_3^k \frac{\partial \hat{m}_1^k}{\partial T_i} + \hat{m}_1^k \frac{\partial \hat{m}_3^k}{\partial T_i} \right) \end{array} \right\}. \quad (4.29)$$

The derivatives of ξ_{an}^k with respect to H_i and T_i can be found by differentiating (4.12),

$$\frac{\partial \xi_{an}^k}{\partial H_i} = \frac{\xi_{an}^k}{\Omega} \left[\sum_{j=1}^r \xi_{an}^j \left(\frac{\partial G^j}{\partial H_i} \right) - \left(\frac{\partial G^k}{\partial H_i} \right) \right], \quad (4.30)$$

$$\frac{\partial \xi_{an}^k}{\partial T_i} = \frac{\xi_{an}^k}{\Omega} \left[\sum_{j=1}^r \xi_{an}^j \left(\frac{\partial G^j}{\partial T_i} \right) - \left(\frac{\partial G^k}{\partial T_i} \right) \right]. \quad (4.31)$$

The derivatives of G^k with respect to H_i and T_i are

$$\frac{\partial G^k}{\partial H_i} = \hat{\mathbf{m}}^k \cdot \mathbf{K} \left(\frac{\partial \hat{\mathbf{m}}^k}{\partial H_i} \right) - \frac{\partial \hat{\mathbf{m}}^k}{\partial H_i} \cdot \mathbf{B}^k - \hat{\mathbf{m}}^k \cdot \left(\frac{\partial \mathbf{B}^k}{\partial H_i} \right), \quad (4.32)$$

$$\frac{\partial G^k}{\partial T_i} = \hat{\mathbf{m}}^k \cdot \mathbf{K} \left(\frac{\partial \hat{\mathbf{m}}^k}{\partial T_i} \right) + \frac{1}{2} \hat{\mathbf{m}}^k \cdot \left(\frac{\partial \mathbf{K}}{\partial T_i} \right) \hat{\mathbf{m}}^k - \frac{\partial \hat{\mathbf{m}}^k}{\partial T_i} \cdot \mathbf{B}^k. \quad (4.33)$$

The derivatives of the normalized \mathbf{k}^{th} equilibrium orientation with respect to H_i and T_i are

$$\frac{\partial \hat{\mathbf{m}}^k}{\partial H_i} = \frac{1}{\|\mathbf{m}^k\|} \frac{\partial \mathbf{m}^k}{\partial H_i} - \frac{\mathbf{m}^k}{\|\mathbf{m}^k\|^3} \left(\mathbf{m}^k \cdot \frac{\partial \mathbf{m}^k}{\partial H_i} \right), \quad (4.34)$$

$$\frac{\partial \hat{\mathbf{m}}^k}{\partial T_i} = \frac{1}{\|\mathbf{m}^k\|} \frac{\partial \mathbf{m}^k}{\partial T_i} - \frac{\mathbf{m}^k}{\|\mathbf{m}^k\|^3} \left(\mathbf{m}^k \cdot \frac{\partial \mathbf{m}^k}{\partial T_i} \right), \quad (4.35)$$

where

$$\frac{\partial \mathbf{m}^k}{\partial H_i} = (\mathbf{K})^{-1} \left[\frac{\partial \mathbf{B}^k}{\partial H_i} - \left(\frac{\mathbf{c}^k \cdot (\mathbf{K})^{-1} \frac{\partial \mathbf{B}^k}{\partial H_i}}{\mathbf{c}^k \cdot (\mathbf{K})^{-1} \mathbf{c}^k} \right) \mathbf{c}^k \right], \quad (4.36)$$

$$\frac{\partial \mathbf{m}^k}{\partial T_i} = (\mathbf{K})^{-1} \left[- \left(\frac{\partial \mathbf{K}}{\partial T_i} \right) \mathbf{m}^k + \frac{\mathbf{c}^k \cdot \left((\mathbf{K})^{-1} \frac{\partial \mathbf{K}}{\partial T_i} \mathbf{m}^k \right)}{\mathbf{c}^k \cdot (\mathbf{K})^{-1} \mathbf{c}^k} \mathbf{c}^k \right], \quad (4.37)$$

$$\frac{\partial \mathbf{B}^k}{\partial H_1} = \begin{Bmatrix} \mu_0 M_s \\ 0 \\ 0 \end{Bmatrix}, \quad \frac{\partial \mathbf{B}^k}{\partial H_2} = \begin{Bmatrix} 0 \\ \mu_0 M_s \\ 0 \end{Bmatrix}, \quad \frac{\partial \mathbf{B}^k}{\partial H_3} = \begin{Bmatrix} 0 \\ 0 \\ \mu_0 M_s \end{Bmatrix}, \quad (4.38)$$

and

$$\begin{aligned}
\frac{\partial \mathbf{K}}{\partial T_1} &= \begin{bmatrix} -3\lambda_{100} & 0 & 0 \\ 0 & 0 & 0 \\ 0 & 0 & 0 \end{bmatrix}, & \frac{\partial \mathbf{K}}{\partial T_4} &= \begin{bmatrix} 0 & -3\lambda_{111} & 0 \\ -3\lambda_{111} & 0 & 0 \\ 0 & 0 & 0 \end{bmatrix}, \\
\frac{\partial \mathbf{K}}{\partial T_2} &= \begin{bmatrix} 0 & 0 & 0 \\ 0 & -3\lambda_{100} & 0 \\ 0 & 0 & 0 \end{bmatrix}, & \frac{\partial \mathbf{K}}{\partial T_5} &= \begin{bmatrix} 0 & 0 & 0 \\ 0 & 0 & -3\lambda_{111} \\ 0 & -3\lambda_{111} & 0 \end{bmatrix}, \\
\frac{\partial \mathbf{K}}{\partial T_3} &= \begin{bmatrix} 0 & 0 & 0 \\ 0 & 0 & 0 \\ 0 & 0 & -3\lambda_{100} \end{bmatrix}, & \frac{\partial \mathbf{K}}{\partial T_6} &= \begin{bmatrix} 0 & 0 & -3\lambda_{111} \\ 0 & 0 & 0 \\ -3\lambda_{111} & 0 & 0 \end{bmatrix}. \quad (4.39)
\end{aligned}$$

Thus the derivatives of $\hat{\mathbf{m}}^k$, \mathbf{S}_m^k and ξ_{an}^k with respect to H_i and T_i are known. Plugging these back into (4.24) - (4.27) the derivatives of \mathbf{M} and \mathbf{S} with respect to H_i and T_i are obtained. The derivatives of \mathbf{B} with respect to H_i and T_i are computed by plugging (4.24) and (4.25) into (4.22) and (4.23) giving all the derivatives required to compute the Jacobian.

4.3 Case Study: Galfenol Unimorph Actuator

The finite element model is validated using the Galfenol unimorph actuator shown in Figure 4.7(a). The actuator consists of a composite beam having a Galfenol layer bonded to a brass substrate, a drive coil, and steel flux return components. The system is excited by applying a voltage input to the coil; the vertical tip deflection of the beam is measured with a laser displacement sensor. Figure 4.7(b) shows the mesh geometry used for finite element calculations. The lower surface of the stainless steel piece to which the beam is clamped is mechanically fixed ($\mathbf{u} = 0$) to remove rigid body modes. The actuator is surrounded by a sufficiently large air volume such that the magnetic potential is negligible at its outer boundaries, $\mathbf{A} = 0$.

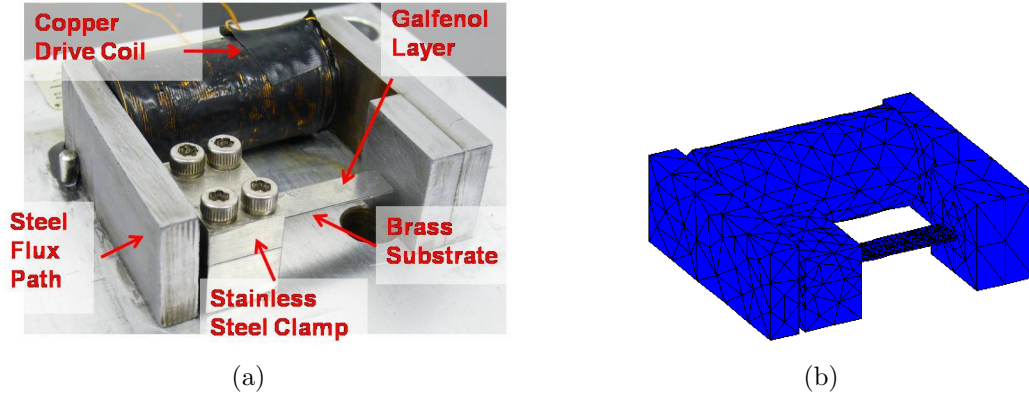


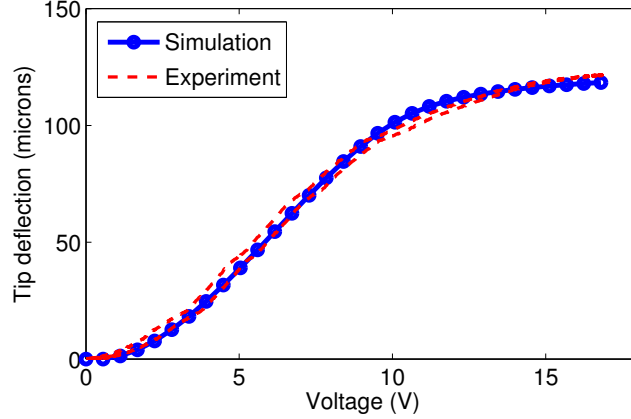
Figure 4.7: Galfenol unimorph actuator used for model validation, (a) actuator configuration, and (b) finite element mesh.

4.3.1 Piecewise-linear quasistatic solution

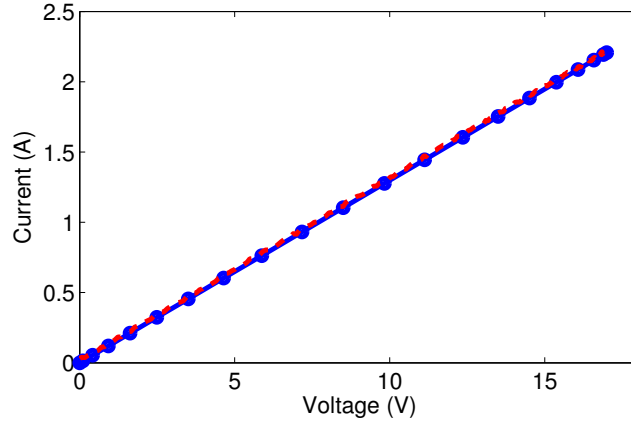
Quasistatic measurements are collected by cycling the voltage at 0.1 Hz. In the model, input is applied in the form of small increments to the coil source current density and solution is obtained using the piecewise-linear approach outlined in Figure 3.1. Beam tip deflection is obtained by integrating the vertical displacement component over the free end of the Galfenol layer. The simulation accurately describes the nonlinearity in the beam deflection response (see Figure 4.8). The voltage current curve is a straight line whose slope is the dc resistance of the coil.

4.3.2 Linear dynamic simulation about bias point

Harmonic response of the beam is obtained by applying a bias voltage of 7 V and sinusoidal voltage inputs at different frequencies. The amplitude of the sinusoidal voltage signal is increased with increasing frequency to keep the current levels comparable so as to obtain good measurable displacement response at the beam tip.



(a)



(b)

Figure 4.8: Quasistatic model results, (a) voltage-deflection, (b) voltage-current.

Figures 4.9-4.13 show the time-domain current and displacement response of the system to sinusoidal voltage inputs ranging from 10 to 500 Hz. The model quantifies the transient dynamic behavior of the beam for all the frequencies using a single set of parameters. At the lower frequencies the model slightly over-predicts the response because of its linear nature. As the frequency increases, the inertia and damping forces dominate the force arising from the nonlinear internal stiffness, thus rendering

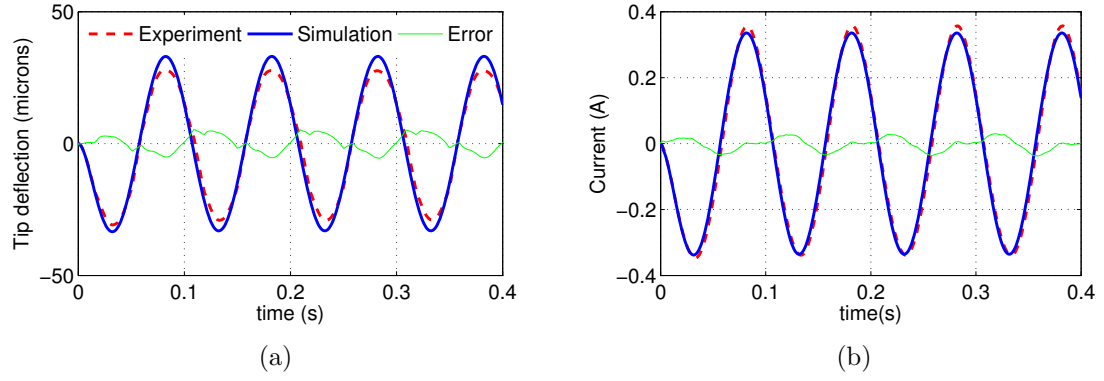


Figure 4.9: Experimental and model results at 10 Hz, (a) tip displacement, (b) current.

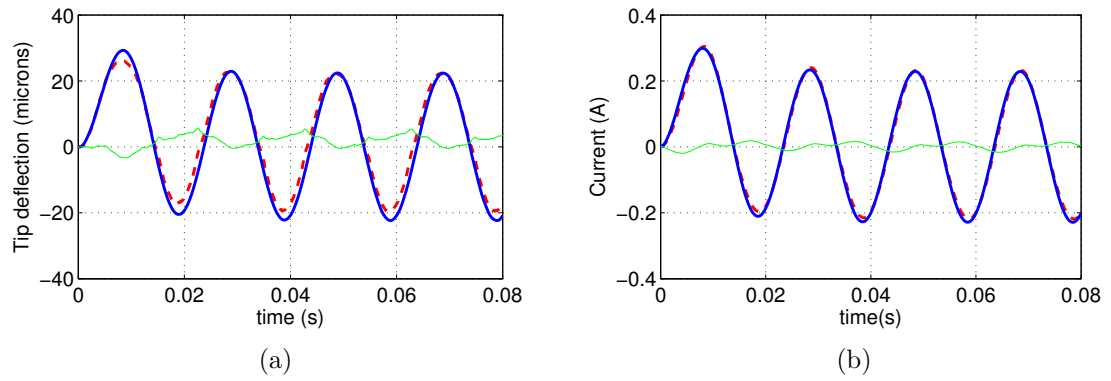


Figure 4.10: Experimental and model results at 50 Hz, (a) tip displacement, (b) current.

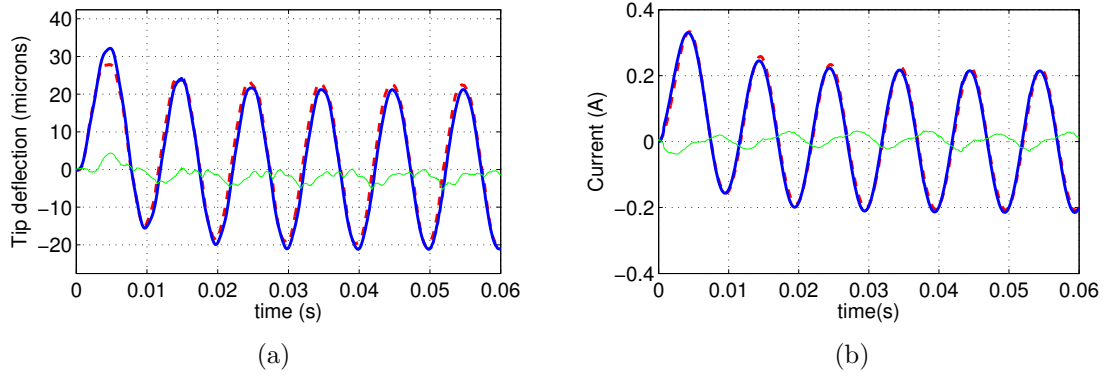


Figure 4.11: Experimental and model results at 100 Hz, (a) tip displacement, (b) current.

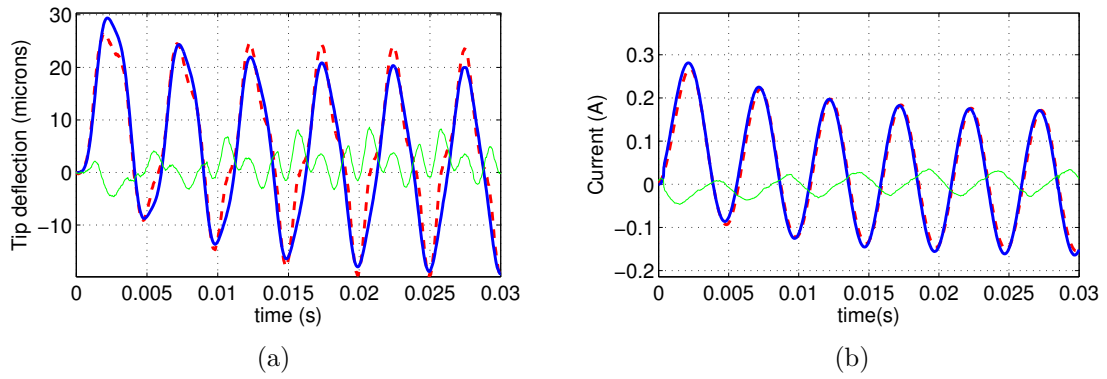


Figure 4.12: Experimental and model results at 200 Hz, (a) tip displacement, (b) current.

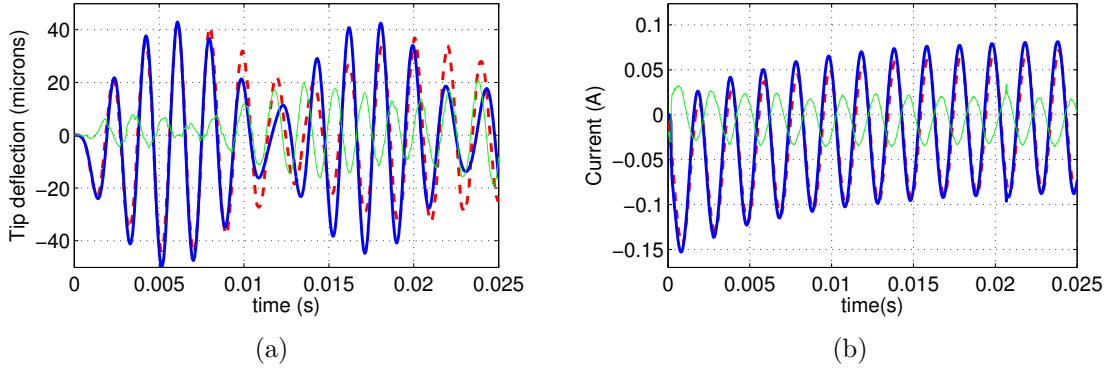


Figure 4.13: Experimental and model results at 500 Hz, (a) tip displacement, (b) current.

the response more smooth. This leads to better correlation between the amplitudes of the modeled and experimental curves. However, because the model does not consider hysteresis in Galfenol, there is a phase difference between the experimental and modeled curves which is negligible till 100 Hz but becomes more noticeable at the higher frequencies. At 200 Hz the measured displacement response is distorted, possibly because some nonlinearities in the material are excited at that frequency due to a particular distribution of stress and field. Since the dynamic model is linear in nature, this effect is not described. The measured current response is undistorted and is accurately described. At 500 Hz the transient tip deflection response exhibits beating behavior, as the excitation frequency is close to the first natural frequency of the actuator (513 Hz). When the harmonic excitation is switched on, the fundamental mode is also excited which interacts with components at the drive frequency giving rise to beats. The current takes a few cycles to reach steady state and the response looks typical of a damped second order system.

4.3.3 Nonlinear dynamic simulation

The same Galfenol unimorph actuator (Figure 4.7) is used to validate the nonlinear dynamic solution procedure. Harmonic excitations ranging from 10 Hz to 200 Hz are applied to the system in the form $V(t) = -V_{bias} + V_0(1 - \cos(\omega_{dr}t))$, where ω_{dr} is the excitation frequency. The finite element model is run only for the time duration of the first few cycles. In order to obtain appreciable displacement response from the beam at higher frequencies, a negative bias voltage (V_{bias}) is applied first before applying the harmonic signal. This ensures that the effective bias point of the cyclic signal is in the burst region. In the model the bias point is obtained in similar fashion by applying the bias voltage smoothed using a hyperbolic tangent function for ease of convergence. Figures 4.14 - 4.17 show the transient response of the transducer for harmonic inputs at 10, 50, 100, and 200 Hz. The modeled responses show good correlation with the experiments particularly for the tip deflection response. An interesting outcome of nonlinear Galfenol behavior can be seen where the quadratic nonlinearity of the magnetostrictive strain at zero field causes frequency doubling in the tip deflection response.

4.4 Concluding Remarks

Nonlinear Galfenol constitutive behavior was successfully incorporated in the unified finite element modeling framework described earlier and validated using a Galfenol unimorph actuator. The piecewise-linear procedure is useful for obtaining quasistatic system response and accurate bias point determination. A linear dynamic simulation with the Galfenol material coefficients computed at the bias point provides an accurate description of system dynamics for moderate inputs. An implicit

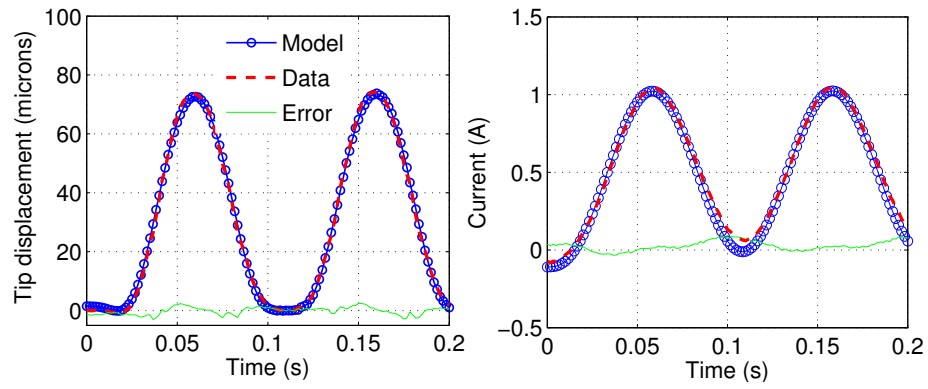


Figure 4.14: Actuator response to harmonic excitation at 10 Hz.

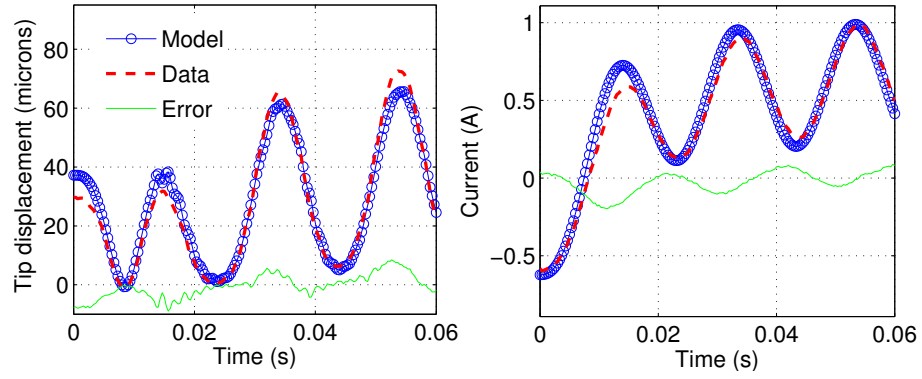


Figure 4.15: Actuator response to harmonic excitation at 50 Hz.

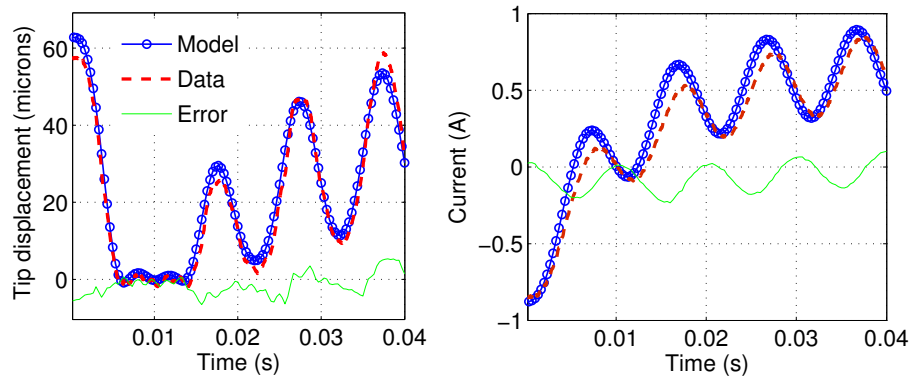


Figure 4.16: Actuator response to harmonic excitation at 100 Hz.

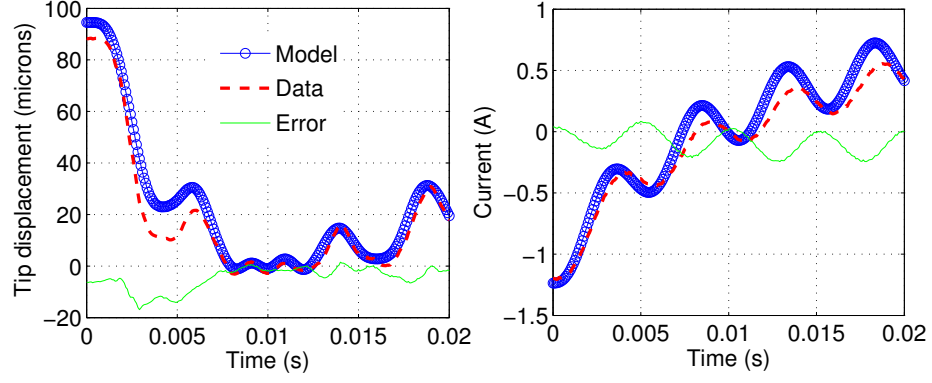


Figure 4.17: Actuator response to harmonic excitation at 200 Hz.

time-integration algorithm based on the trapezoidal rule yields the dynamic system response for large-scale inputs. The constitutive law is inverted numerically using Quasi-Newton iterations. Efficiency is maintained by coding up the material model so that executing the inversion routine once calculates the 6 components of stress, 3 components of field and 81 components of the Jacobian inverse. Results showed that the modeled responses compare well with experiments at moderate frequencies. As the excitation frequency is increased there is an error in the phase description due to the assumed anhyseretic behavior of Galfenol.

Chapter 5: TERFENOL-D TRANSDUCERS

Magnetostrictive Terfenol-D ($\text{Tb}_{0.7}\text{Dy}_{0.3}\text{Fe}_2$) is attractive for practical actuators due to its large magnetostriction (1600 ppm) and moderate saturation fields (200 kA/m). This chapter aims at applying the unified framework developed in Chapter 3 to model Terfenol-D transducers. First, a fully coupled 3D energy averaged model is derived, which describes the magnetomechanical behavior of Terfenol-D. Due to the poor machinability of Terfenol-D, they are mostly available in 1D geometries like cylindrical rods. Thus most Terfenol-D transducers are axisymmetric in nature with the permanent magnet and flux return components concentric with the Terfenol-D driver. To take advantage of this, the 3D finite element model is reduced to a 2D axisymmetric form. It is then used to conduct a parametric study on a hydraulically amplified Terfenol-D actuator designed for use in active engine mounts.

5.1 Fully Coupled Discrete Energy Averaged Model for Terfenol-D

Modeling the constitutive behavior of Terfenol-D has traditionally been a difficult problem. The presence of a large magnetostriction anisotropy, low magnetocrystalline anisotropy, and a twinned dendritic structure gives rise to complex domain level processes which are not completely understood [42]. The aim of this work is to describe

the actuation and sensing response of Terfenol-D over a wide range of magnetic field and stress values using an efficient energy-averaged constitutive model which can be used for design and control of Terfenol-D transducers.

The Jiles-Atherton model [49] was originally formulated for isotropic ferromagnetic hysteresis. The total magnetization of a ferromagnetic material with Weiss-type moment interactions is obtained as the sum of an irreversible component due to domain wall motion and a reversible component due to domain wall bowing. With careful understanding of the difference between local and global anhysteretic responses [29], the model is straightforward to implement and computationally efficient, as it involves only five parameters which can be directly correlated to measurements. For this reason, the Jiles-Atherton model has been used to describe the behavior of Terfenol-D actuators in which the magnetostriction is modeled as a quadratic function of magnetization [11, 41, 14].

The Preisach model [66] generates smooth ferromagnetic hysteresis curves through contributions from a large number of elementary bistable hysterons. Because giant magnetostrictive materials such as Terfenol-D show significant deviation in behavior from elementary Preisach hysterons, Reimers and Della Torre [70, 71] developed a special hysteron with a bimodally distributed susceptibility function to model the 1D actuation response of Terfenol-D.

Carman et al. [12] formulated a model for Terfenol-D using Gibbs free energy expanded in a Taylor series. The exact form of the series, that is the degree of truncation, and the value of the coefficients were dictated by experimental measurements. The model describes Terfenol-D actuation for low to moderate applied fields over a specific range of applied pre-stress. Zheng et al. [91] included higher order terms in

the Taylor series expansion of Gibbs energy and used a Langevin function to describe the magnetization curve. The model, although anhysteretic, accurately describes the nonlinear nature of Terfenol-D's magnetostriction for a wide range of pre-stresses. The ΔE effect is also modeled but validated only qualitatively.

Armstrong et al. [3] formulated a model for Terfenol-D in which bulk magnetization and strain are obtained as an expected value of a large number of possible energy states (or moment orientations) with an energy based probability density function. To increase the model efficiency, Armstrong et al. [2] restricted the choice of moment orientations to the easy magnetization axes (eight $\langle 111 \rangle$ directions for Terfenol-D) and used a discrete version of the probability density function. The increase in computational speed, however, came at the cost of reduced accuracy. To preserve accuracy without sacrificing efficiency, Evans and Dapino [32] developed a constitutive model for Galfenol by choosing orientations which minimize an energy functional locally defined about each easy axis direction. This energy averaged model has major shortcomings when applied to Terfenol-D as detailed in Section 5.1.1. Section 5.1.2 presents an anhysteretic model formulation that addresses each of those challenges; anhysteretic model results are compared with experimental measurements in Section 5.1.3. The proposed anhysteretic version of the model is fully 3D and appropriate for use in finite element modeling frameworks. An extension to model magnetomechanical hysteresis is done in section 5.1.4 by using an evolution equation for the domain volume fractions similar to Evans et al. [32] The hysteretic model can be used for control applications where quantification of additional delay due to material hysteresis is critical for ensuring stability. Section 5.1.5 provides a quantitative description of the model performance.

5.1.1 Problem description

Terfenol-D has eight minima along the $\langle 111 \rangle$ directions. When energy averaged models such as the Armstrong model [2] or the Discrete Energy Averaged Model (DEAM) [32] are compared with measurements, two major discrepancies are observed. First, these models introduce an extra kink in the magnetization and magnetostriction and secondly, the experimentally observed slow approach to saturation is absent (Figure 5.1). Using a sufficiently high smoothing factor (as done by Armstrong [2]) removes the unphysical kink and somewhat smooths out the saturation behavior. However, it results in large inaccuracies in the low to moderate field regions. Moreover, the kinking reappears at high pre-stress values (Figure 5.2). For a

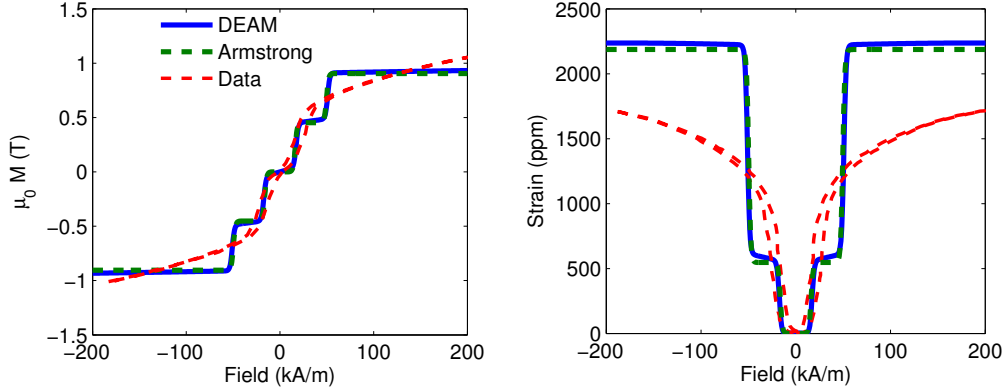


Figure 5.1: Comparison of magnetization and magnetostriction curves for Terfenol-D at 13.5 MPa compressive stress [31] with the Armstrong model [2] and the Discrete Energy Averaged Model (DEAM) [32].

[112]-oriented sample, the magnetization process is governed by two distinct domain jumps: one from the $[11\bar{1}]$ and $[\bar{1}\bar{1}1]$ directions perpendicular to the sample axis to the $[1\bar{1}1]$ and $[\bar{1}11]$ directions oriented 61.9° from the sample growth axis, and the second

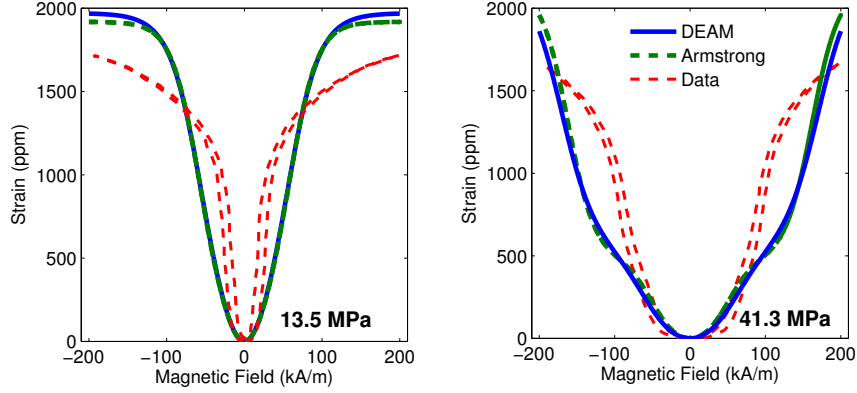


Figure 5.2: Armstrong model [2] and DEAM [32] with high smoothing factors for 13.5 and 41.3 MPa prestress. The higher prestress curve shows the reappearance of kinks in both models.

from $[1\bar{1}1]$ and $[\bar{1}11]$ to the $[111]$ direction oriented 19.5° from the growth axis. When no compressive prestress is applied, all the $\langle 111 \rangle$ orientations have equal energy and the jumps occur at very low magnetic fields. Application of compressive prestress alters the energy of each of the three sets of orientations. The energy due to applied stress increases as the angle between the domain magnetization and sample axis decreases. Thus the increase in energy is largest for the $[111]$ direction and smallest for the $[11\bar{1}]$ and $[\bar{1}\bar{1}1]$ directions. The difference in energy between the three sets of easy axes causes domains to stick at a particular set of orientations until additional magnetic field is applied to overcome the magnetoelastic energy difference between the current and the next set of orientations. This domain attachment causes kinking in the magnetization and magnetostriction curves (Figure 5.3). The magnitude of the kink increases with the amount of applied prestress. Thus a value of smoothing factor Ω which smooths out the kinks for smaller prestresses cannot eliminate the kinking when the applied prestress is increased as observed in Figure 5.2. A value of Ω which

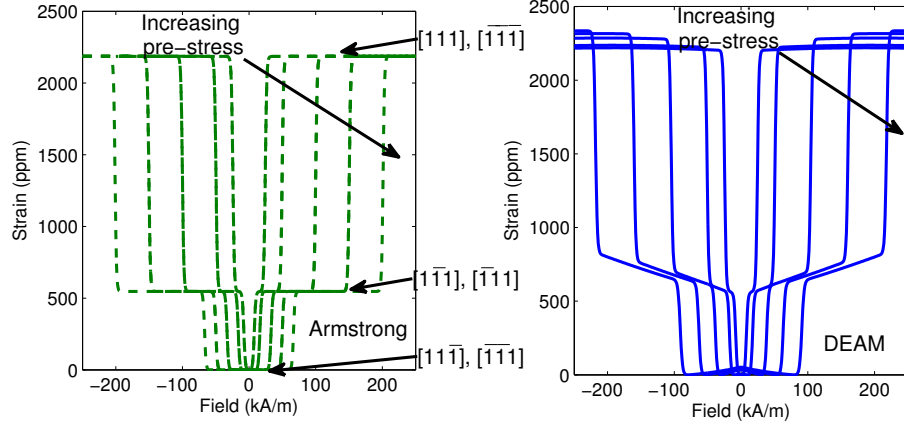


Figure 5.3: Armstrong model [2] and DEAM [32] with low smoothing factors showing the magnitude of the two kinks with increasing stress.

is high enough to smooth out the kinks for all prestresses results in the model overestimating the burst field and underestimating the slope of the magnetostriction-field curve in the burst region. These issues imply that fundamental changes need to be made in order to apply energy-averaged models to Terfenol-D.

5.1.2 Model formulation

Elimination of extra kinks

Assuming a $[112]$ -oriented sample, the intermediate kinks occur when domains align along the $[1\bar{1}1]$ and $[\bar{1}11]$ directions for positive applied fields and $[1\bar{1}\bar{1}]$ and $[\bar{1}\bar{1}1]$ directions for negative applied fields. Absence of kinks in the measurements suggests that domains are prevented from orienting along these directions. This can be modeled by increasing the magnetocrystalline anisotropy energy along these orientations compared to the other easy axis orientations. In the original DEAM

formulation, the anisotropy energy is defined locally around each easy axis as

$$G_A^k = \frac{1}{2} K^k \|\mathbf{m}^k - \mathbf{c}^k\|^2, \quad (5.1)$$

where the anisotropy constant K^k controls how steep the anisotropy energy wells are around the k^{th} easy axis \mathbf{c}^k . Since the anisotropy energy along each easy axis direction is identically zero, achieving variations in the base anisotropy energy between the different easy axes is not possible. To achieve such variation an orientation-dependent global anisotropy energy is superimposed onto the local anisotropy energy defined around each easy axis direction as

$$G_A^k = w^k G_{A_0}^k + \frac{1}{2} K^k \|\mathbf{m}^k - \mathbf{c}^k\|^2. \quad (5.2)$$

Here, $G_{A_0}^k$ is the global anisotropy energy, which for materials with cubic anisotropy is given by

$$G_{A_0}^k = K_4(m_1^{k^2} m_2^{k^2} + m_2^{k^2} m_3^{k^2} + m_3^{k^2} m_1^{k^2}) + K_6(m_1^{k^2} m_2^{k^2} m_3^{k^2}), \quad (5.3)$$

In (5.2), $G_{A_0}^k$ is weighted by w^k , an empirical weighting factor which adjusts the anisotropy energy along the k^{th} easy axis. Physically, the weighting accounts for the change in energy landscape that may occur due to precipitates, dislocations and twin boundaries [1]. The 8 easy axes can be broken down into 3 groups depending upon their angle with the sample axis: the $[111]$ and $[\bar{1}\bar{1}\bar{1}]$ directions oriented 19.5° with the sample axis, the $[11\bar{1}]$ and $[\bar{1}\bar{1}1]$ directions oriented perpendicular to the sample axis, and the $[1\bar{1}1]$, $[\bar{1}11]$, $[1\bar{1}\bar{1}]$, and $[\bar{1}1\bar{1}]$ directions oriented 61.9° from the sample axis. Thus, there are effectively three weights which must be determined, one for each group.

Another way to suppress the kinks is to ignore the minima associated with the four orientations which cause kinking. The global anisotropy energy is still weighted

but there are only two weights to be determined since the set of directions 61.9° from the sample axis is not considered. This way the number of minima is reduced to four. The first approach is more accurate as it has more degrees of freedom while the second approach is more efficient as it involves averaging of only four terms. However, in the second approach, the three dimensional accuracy of the model is expected to suffer due to the loss of four orientations. In this paper the full version of the model is described in detail and its performance is compared to the reduced version in terms of accuracy and efficiency.

Obtaining the slow approach to saturation

The exact reason for the slow approach to saturation in Terfenol-D is not clearly understood. Various explanations have been proposed such as the presence of demagnetization fields [89], or radically different behavior of twins [25], but experimental proof is lacking. Domain observations reported by Engdahl [31] suggest that closure domains become increasingly difficult to remove in Terfenol-D as the sample is magnetized. From these theories and observations it can be postulated that with increasing applied field, there is a tendency of domains to occupy orientations which do not minimize the theoretical energy obtained by summing up the anisotropic, magnetoelastic and Zeeman components. Incorporation of demagnetization fields in the model comes at the expense of an implicit definition for the total energy which means that iterations need to be performed to converge to the correct value of volume fractions. Every iteration will involve computation of the energies, minima, domain volume fractions, and the bulk magnetization ,adding significant computational effort to the model.

An alternative way of incorporating this apparent broadening of domain distribution is to employ a variable smoothing factor which increases as the domain volume fractions move farther and farther away from a homogeneous distribution. Mathematically this can be written as

$$\Omega = a_0 + a_1 \|\boldsymbol{\xi}_{an}(\mathbf{H}, \mathbf{T}) - \bar{\boldsymbol{\xi}}\|^2, \quad (5.4)$$

where $\boldsymbol{\xi}_{an}(\mathbf{H}, \mathbf{T})$ is the vector of anhysteretic domain volume fractions and $\bar{\boldsymbol{\xi}}$ is a vector equal in length to $\boldsymbol{\xi}_{an}$ but with each component as $1/r$, r being the number of easy axis orientations. Both $\boldsymbol{\xi}_{an}$ and $\bar{\boldsymbol{\xi}}$ are r -dimensional vectors, with $r = 8$ for Terfenol-D. When no bias stress or field is applied, assuming cubic magnetocrystalline anisotropy energy distribution, all 8 orientations are equally likely to be occupied by the domains. Thus $\boldsymbol{\xi}_{an} = \bar{\boldsymbol{\xi}}$ and $\Omega = a_0$, its lowest value. On application of stress or field the volume fractions will deviate away from this homogeneous distribution causing Ω to increase. When a bias stress or field is applied, the initial domain distribution is not homogeneous, so for application of field and stress about the bias points Ω does no longer increase monotonically. Figure 5.4(a) shows the variation of Ω with applied field for different bias stress values. At low fields the value of Ω increases with increasing bias stress while at high fields Ω is larger for a lower bias stress. This allows the magnetostriction curves for low bias stress to exhibit a sharp burst region at low fields and a gradual approach to saturation at high fields, while for the high bias stress curves the slope in the burst region is more gradual since Ω is relatively large in the burst region (Figure 5.4(b)). Figure 5.5 shows the Ω -stress curves and the corresponding magnetization-stress curves for different bias fields. For low bias fields, Ω is small at low stresses and larger at higher stress values while for high bias fields, Ω is large for low stresses and relatively small for higher stress values.

Due to the large values of Ω at high bias fields and low stresses, the M-H curves display very gradual saturation in the low stress region. Thus, even for very high bias fields, application of stress almost immediately results in magnetization decrease due to the broad domain distribution. These variations are shown for a crystal having perfect cubic anisotropy. When the anisotropy is weighted as described previously, these variations in Ω will change since at zero applied stress and field the domains will not be homogeneously distributed among the eight directions. Rather they will be concentrated in orientations along which the global anisotropy energy weight is the maximum.

Computational aspects

The computation proceeds in a manner identical to the Galfenol constitutive law up to the computation of the minima. Since the \mathbf{m} -dependent portion of the energy is identical in both cases, expression (4.10) still yield the energy minima. For implementation in finite element models, the computed minima are normalized to prevent unphysical behavior at high fields similar to the Galfenol constitutive model.

The new definition for Ω , expression (5.4), destroys the explicit nature of the model since Ω is defined as a function of ξ_{an} while determination of ξ_{an} requires knowledge of Ω according to the relation

$$\xi_{an}^k = \frac{\exp(-G^k/\Omega(\xi_{an}))}{\sum_{j=1}^r \exp(-G^j/\Omega(\xi_{an}))}, \quad (5.5)$$

where ξ_{an}^k is the volume fraction of the k^{th} easy axis. The difference between this implicit definition and having an implicit definition for energy (as in the case of demagnetization fields) is that here the energy expressions and therefore the minima remain unchanged in every iteration. Only the volume fractions need to be computed

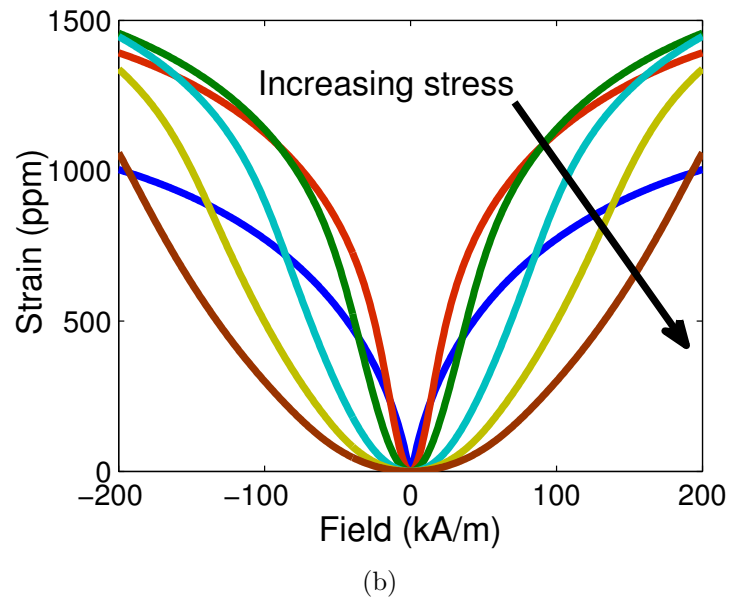
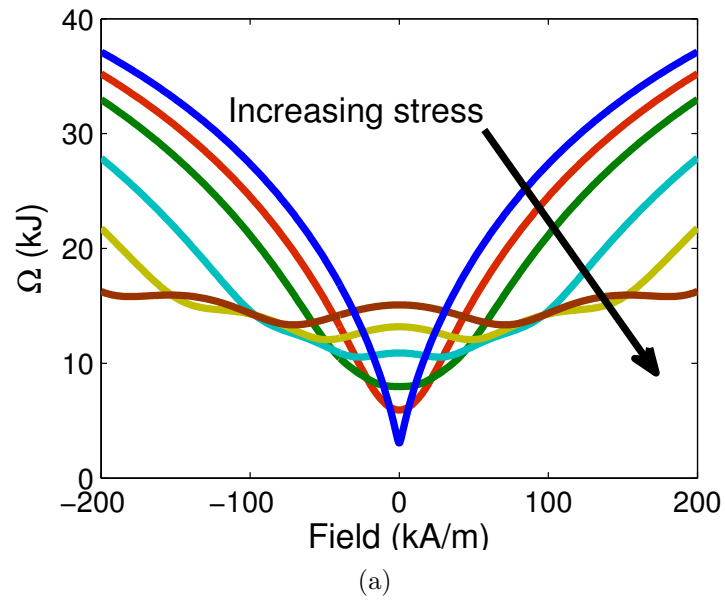


Figure 5.4: (a) Ω -field and (b) strain-field curves for compressive prestresses of 0, 6.5, 13.5, 27.4, 41.3, and 55.3 MPa.

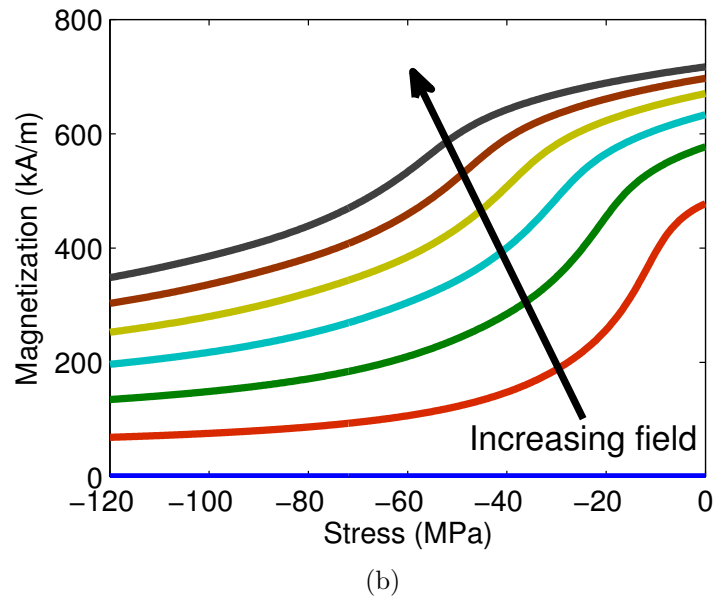
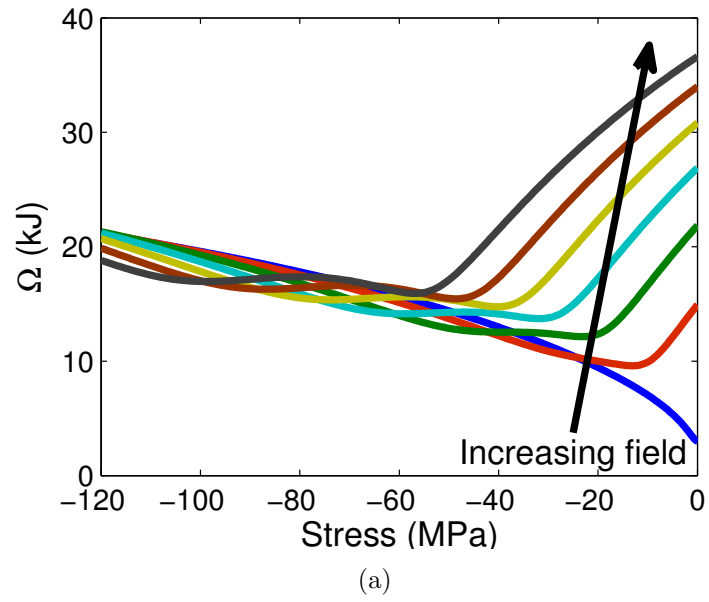


Figure 5.5: (a) Ω -stress and (b) magnetization-stress curves for constant bias fields of 0, 32.2, 64.4, 96.6, 128.8, 161 and 193.2 kA/m.

again. This is illustrated by the flowchart shown in Figure 5.13. The solution loop involves combining (5.4) and (5.5) to obtain a single equation in terms of Ω , giving

$$f(\Omega) = \Omega - a_0 - a_1 \sum_{k=1}^r (\xi_{an}^k - \bar{\xi}^k)^2 = 0. \quad (5.6)$$

Newton-Raphson iterations are performed for quick convergence since the derivative $df/d\Omega$ can be analytically obtained as

$$\frac{df}{d\Omega} = 1 - \frac{1}{\Omega^2} \sum_{k=1}^r 2a_1 (\xi_{an}^k - \bar{\xi}^k) \left(\xi_{an}^k G^k - \xi_{an}^k \sum_{j=1}^r \xi_{an}^j G^j \right). \quad (5.7)$$

Even with strict tolerances, usually two to three iterations are sufficient for convergence. To investigate the effect of this iterative procedure on the model efficiency, the model is run with and without iterations for a large number of inputs. It is found that on an average the iterative version takes only 20 % longer than the non-iterative one.

5.1.3 Anhyseretic model results

The model is compared with actuation measurements from Moffett et al. [62] and sensing measurements from Kellogg et al. [51] Anhyseretic model parameters have been obtained by extracting the anhyseretic curves from data (using simple averaging of values from the upper and lower branches of the major hysteresis loops [8]) and using a least squares optimization algorithm. The full model with 8 minima contains 9 parameters ($K, M_s, \lambda_{100}, \lambda_{111}, a_0, a_1, w^1 = w^2, w^3 = w^4, w^5 = w^6 = w^7 = w^8$) while the model with 4 minima contains 8 parameters due to the absence of w^5 through w^8 .

Figure 5.7 shows the performance of the two models when optimized to describe the magnetostriction measurements of Moffett et al. Both models can describe the measurements. However, the reduced version shows some error near saturation particularly for the high bias stress curves. With parameters optimized for the strain-field

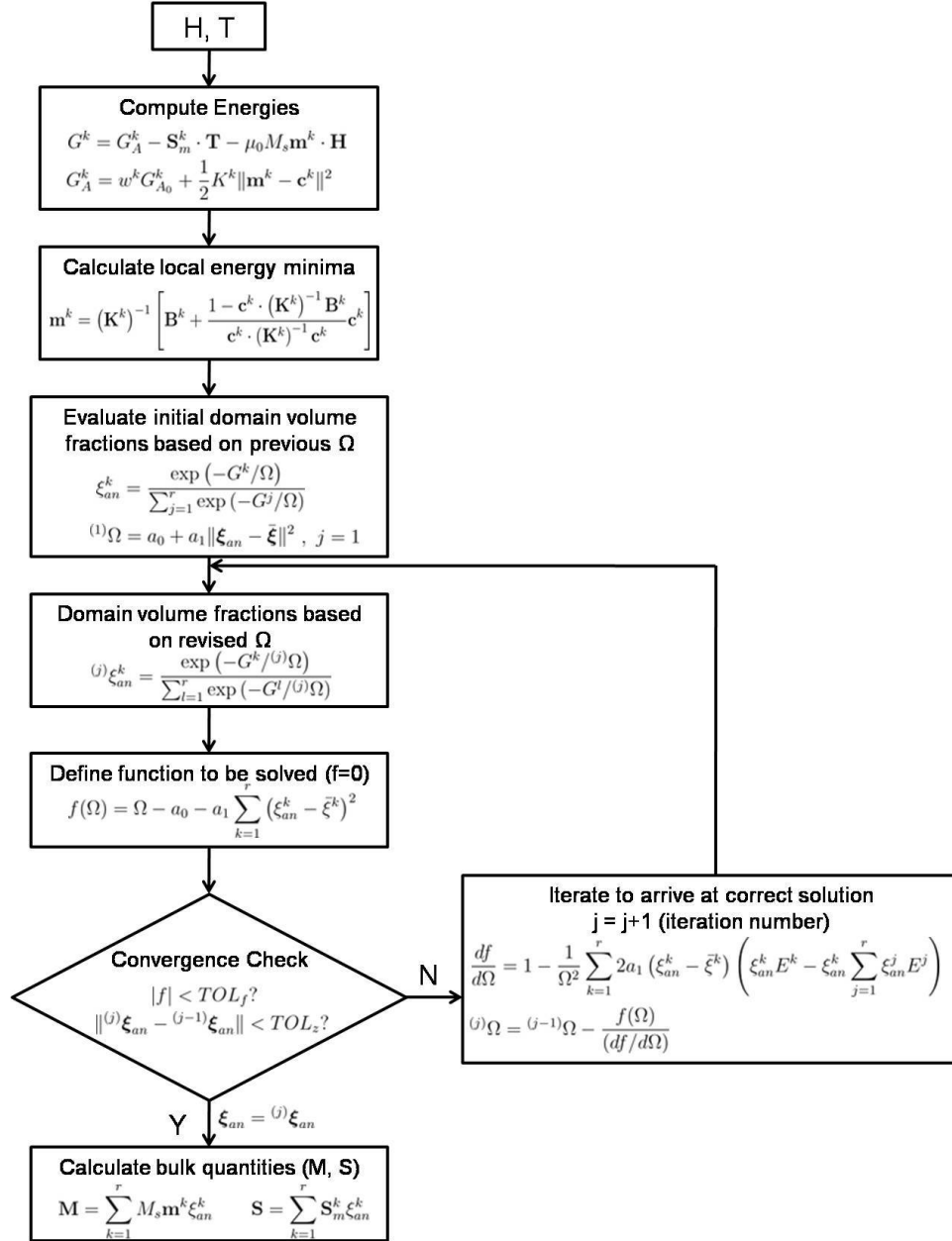


Figure 5.6: Flowchart for the anhysteretic model. Details of the energy minimization is shown in section 4.1.1.

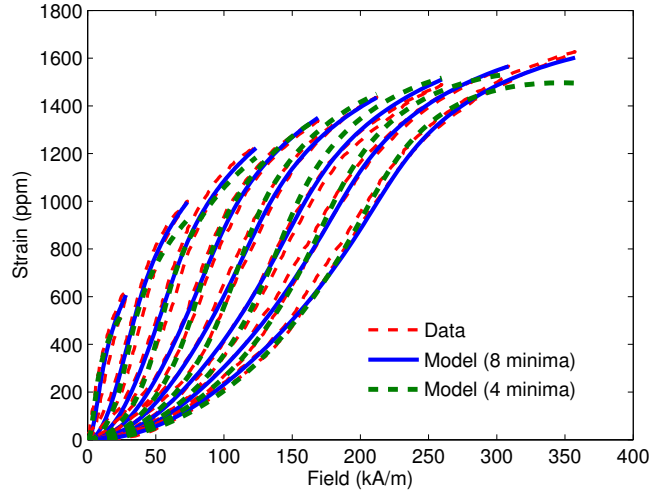


Figure 5.7: Comparison of the two modeling approaches with actuation data [62] for compressive prestresses of 6.9, 15.3, 23.6, 32.0, 40.4, 48.7, 57.1, and 65.4 MPa.

curves (Figure 5.8), the full model accurately describes the stress-strain response. To apply the model to various material compositions and operating conditions, the parameters were also optimized for Terfenol-D sensing measurements reported by Kellogg et al. [51] Throughout the paper an elastic modulus of 115 GPa is used, calculated using the slope of the strain-stress curves at high compressive stresses and low bias fields. Figure 5.9 reveals that the full version of the model is able to describe the trends more accurately than the reduced version with four minima.

5.1.4 Extension to hysteretic model

The model can be extended to include hysteresis with an incremental formulation similar to that done by Evans et al. [32] The total volume fraction increment can be written as a combination of an anhyseretic and an irreversible component,

$$d\xi^k = c d\xi_{an}^k + (1 - c) d\xi_{irr}^k, \quad (5.8)$$

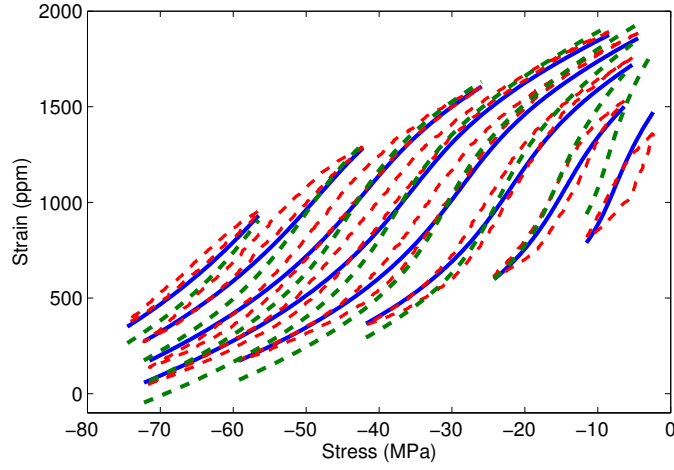


Figure 5.8: Performance of the two modeling approaches in predicting the stress-strain behavior of Terfenol-D [62] for bias field values of 11.9, 31.8, 55.7, 79.3, 103, 127, 151, and 175 kA/m with parameters estimated from the strain-field curves.

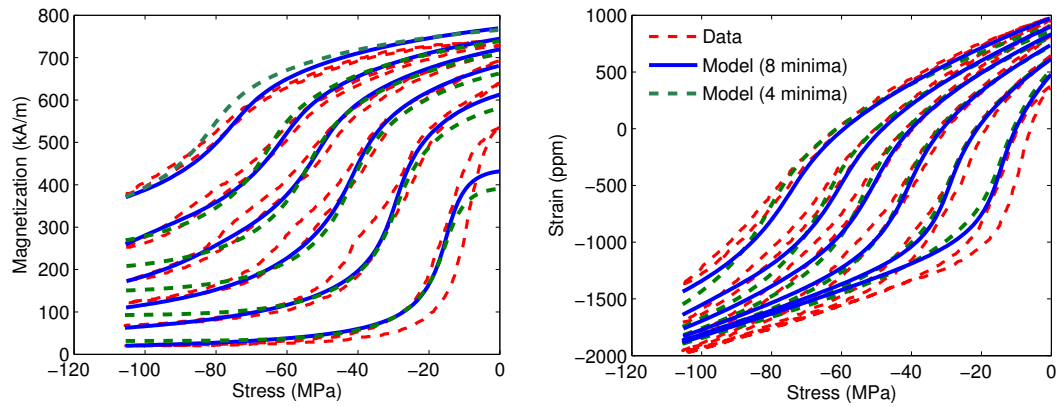


Figure 5.9: Comparison of the two modeling approaches with sensing data from [51] for bias magnetic fields of 16.1, 48.3, 80.5, 112.7, 144.9, and 193.2 kA/m.

where $d\xi_{irr}^k$ is given by

$$d\xi_{irr}^k = \frac{\zeta}{k_p} (\xi_{an}^k - \xi_{irr}^k) [\mu_0 M_s (|dH_1| + |dH_2| + |dH_3|) + (3/2)\lambda_{100}(|dT_1| + |dT_2| + |dT_3|) + 3\lambda_{111}(|dT_4| + |dT_5| + |dT_6|)], \quad (5.9)$$

and $d\xi_{an}^k$ is given by

$$d\xi_{an}^k = \frac{\partial \xi_{an}^k}{\partial \mathbf{H}} d\mathbf{H} + \frac{\partial \xi_{an}^k}{\partial \mathbf{T}} d\mathbf{T}. \quad (5.10)$$

The calculation of partial derivatives $\partial \xi_{an}^k / \partial \mathbf{H}$ and $\partial \xi_{an}^k / \partial \mathbf{T}$ for the traditional energy-averaged model is simple since ξ_{an}^k is explicitly defined in terms of \mathbf{H} and \mathbf{T} . In this case ξ_{an}^k is implicit as given by (5.5). But, it is still possible to obtain an analytical expression for its derivatives given by

$$\frac{\partial \xi_{an}^k}{\partial H_i} = \alpha^k - \xi_{an}^k \sum_{j=1}^r \alpha^j + 2a_1 (\xi_{an} - \bar{\xi}) \cdot \left(\frac{d\xi_{an}}{dH_i} \right) \left(\beta^k - \xi_{an}^k \sum_{j=1}^r \beta^j \right), \quad (5.11)$$

where

$$\alpha^k = -\frac{\xi_{an}^k}{a} \left(\frac{\partial G^k}{\partial H_i} \right), \quad (5.12)$$

$$\beta^k = \frac{\xi_{an}^k}{a^2} G^k, \quad (5.13)$$

$$(\xi_{an} - \bar{\xi}) \cdot \left(\frac{d\xi_{an}}{dH_i} \right) = \frac{\sum_{k=1}^r \left(\alpha^k - \xi_{an}^k \sum_{j=1}^r \alpha^j \right) (\xi_{an}^k - \bar{\xi}^k)}{1 - 2a_1 \sum_{k=1}^r \left(\beta^k - \xi_{an}^k \sum_{j=1}^r \beta^j \right) (\xi_{an}^k - \bar{\xi}^k)}. \quad (5.14)$$

The derivatives $\partial G^k / \partial H_i$ can be obtained similar to (4.32). Equation (5.14) is obtained by multiplying (5.11) by $(\xi_{an}^k - \bar{\xi}^k)$ and summing for all k . The partial derivatives with respect to T_i can be computed following a similar procedure.

5.1.5 Hysteretic model results

The performance of the hysteretic model is described quantitatively in this section by comparing it with the same data sets. Additionally, the parameters have been optimized to describe Terfenol-D magnetostriction data supplied by Etrema Products,

Inc [43]. As done previously, every data set is simulated with a single set of parameters. However, they are allowed to vary from one set to the other since they represent measurements on samples with different compositions. The parameter optimization for the hysteretic model is done using the same least square optimization algorithm as described earlier. The hysteretic model contains two additional parameters (c and k_p) over the anhysteretic version thus making the total number of parameters 11 and 10 for the full and reduced models. However, the optimization routine is less time consuming because the parameter values are very close to what they were for the anhysteretic version. The range for the additional parameters is also easy to estimate as k_p determines the width of the hysteresis loops which is estimated to lie between 4 – 10 kJ while c is the reversibility coefficient whose value is usually between 0.05 and 0.15.

For every curve, the modeling error has been quantified using a normalized RMS error definition. The error for the i^{th} curve in a data set is given as

$$\text{error} = \frac{1}{\text{range}(\mathbf{X})} \sqrt{\frac{\sum_{j=1}^{N_i} (Y_{ij} - X_{ij})^2}{N_i}}. \quad (5.15)$$

where Y_{ij} and X_{ij} are the j^{th} component of the i^{th} model vector and data vector, respectively, each containing N_i points, and $\text{range}(\mathbf{X})$ is the difference between the upper and lower bound for the entire set. A mean error for the entire data set is obtained by averaging the normalized RMS error for all curves in the set. A maximum error is computed by finding the maximum of the error values for all points for all curves in the data set. This gives a measure of the worst case performance of the model. Table 5.1 summarizes the mean and the maximum errors obtained for 3 different data sets. For clarity, in this section only plots for the full version of the

Table 5.1: Mean % Errors obtained with the full and reduced models. Max. % errors in ().

Data	8 minima	4 minima
Moffett et al. [62](strain-field)	1.1 (3.4)	2.3 (11.2)
Moffett et al. [62](strain-stress with parameters optimized for strain-field loops)	2.3 (6.3)	5.7 (20.3)
Etrema Products Inc. [43]	1.2 (5.2)	2.5 (10.3)
Kellogg et al. [51]	1.6 (9.87)	1.97 (12.8)
Simulation time (for Moffett et al. data)	0.206 s	0.146 s

model are shown. Figure 5.10 shows the performance of the hysteretic model in describing the measurements reported by Moffett et al. [62] Once again, the parameters are optimized only for the magnetostriction curves. As shown in Table 5.1, excellent accuracy is achieved not only for the magnetostriction curves (1.1 % mean error) but also for the stress-strain curves (2.3 % mean error) for which no separate parameter optimization was done. The reduced model also gives good overall accuracy except for high fields and stresses. As observed for the anhysteretic version of the reduced model, some errors were found in the stress-strain response, particularly in the low stress, low field region where the maximum error is about 20 %. Similar results are obtained for sensing measurements reported by Kellogg et al. [51] for $\text{Tb}_{0.3}\text{Dy}_{0.7}\text{Fe}_2$. In this case the parameters are optimized for both magnetization-stress and strain-stress curves together and mean errors below 2 % are obtained. The maximum error is somewhat large in both versions of the model due to the discrepancy in the initial (0 stress) magnetization description of the 16.1 kA/m bias field curve.

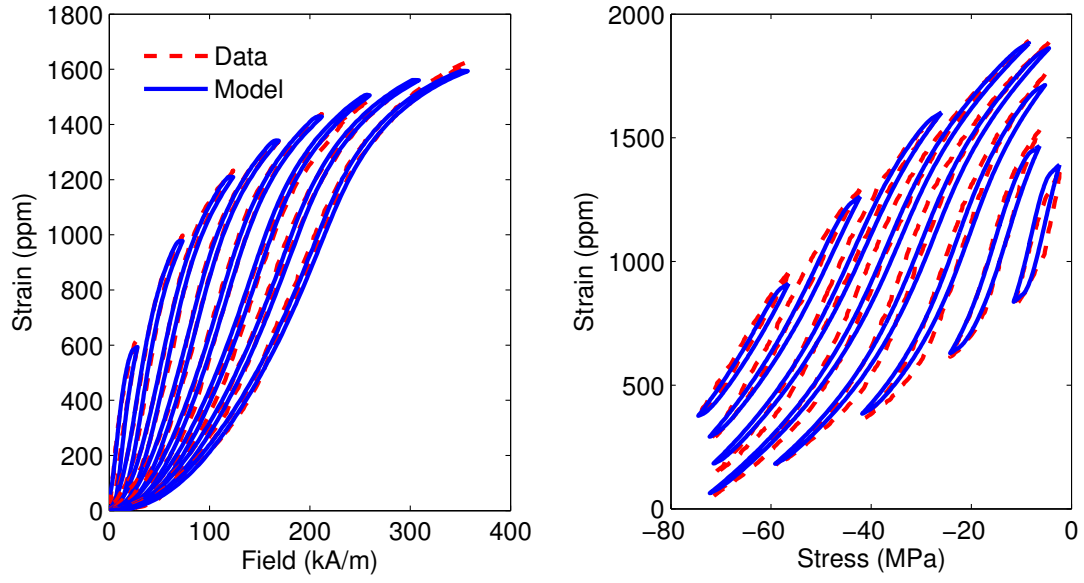


Figure 5.10: Comparison of hysteretic model with data from Moffett et al [62] for compressive prestresses of 6.9, 15.3, 23.6, 32.0, 40.4, 48.7, 57.1, and 65.4 MPa. Parameters optimized for actuation curves.

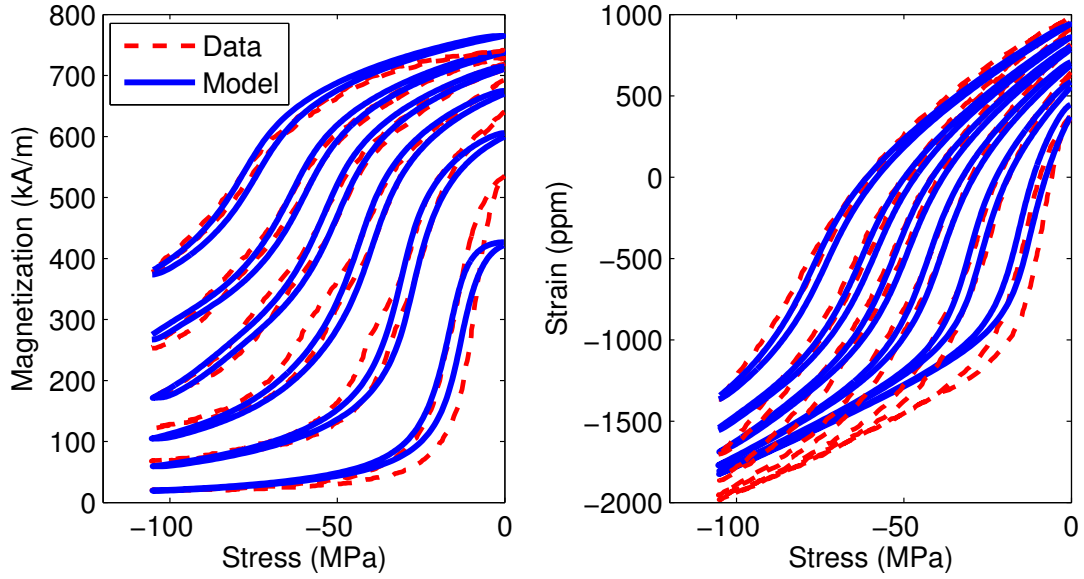


Figure 5.11: Comparison of hysteretic model with sensing data from Kellogg et al [62] for bias magnetic fields of 16.1, 48.3, 80.5, 112.7, 144.9, and 193.2 kA/m.

Finally, the parameters are optimized to describe the magnetostriction curves for commercially available Terfenol-D supplied by Etrema Products, Inc. [43] (Figure 5.12). Not only does the model describe the nonlinear nature of the response with accuracy but it also quantifies the hysteretic regions very accurately. For example, at high compressive prestresses, the magnetization process is dominated by reversible domain rotation giving rise to a nearly anhysteretic response. This is seen both in the experimental and modeled magnetostriction curves at 16 ksi (110.4 MPa). The model also describes the effect of preload on the maximum magnetostriction. For example, the 1 ksi (6.9 MPa) curve exhibits a lower saturation magnetostriction than the 4 ksi (27.6 MPa) and 8 ksi (55.2 MPa) curves. The optimized parameters for every data set for both versions of the model are shown in Table 5.2. To compare the efficiencies of the two models, the time taken by each to simulate the Moffett et al. [62] data set is clocked in Matlab. The reduced model takes about 30 % less time than the full version. Thus, the reduced version can be used in applications where some accuracy can be sacrificed in the interest of computational speed.

5.1.6 Concluding remarks

The energy averaged model derived in this chapter addressed two main discrepancies of previous energy averaged models in modeling Terfenol-D response - presence of an unphysical kink in the modeled response which is absent in measurements and absence of the slow approach to saturation present in Terfenol-D magnetostriction. Use of a weighted global anisotropy energy combined with a variable smoothing factor based on the deviation of domain volume fractions from a homogeneous distribution is able to tackle both issues successfully. The anhysteretic model is fully 3D in nature

Table 5.2: Optimized model parameters for the different data sets.

Parameters	Moffett et al. [62]		Kellogg et al. [51]		Etrema Products Inc. [43]	
	8 minima	4 minima	8 minima	4 minima	8 minima	4 minima
$K \times 10^5 \text{ (J/m}^3\text{)}$	4.306	2.409	17.68	3.049	4.602	2.188
$\mu_0 M_s \text{ (T)}$	1.025	0.892	1.047	0.975	0.964	0.891
$\lambda_{100} \times 10^3$	0.114	0.126	0.093	0.114	0.104	0.094
$\lambda_{111} \times 10^3$	1.546	1.554	1.486	1.348	1.424	1.428
$a_0 \times 10^3 \text{ (J)}$	1.776	0.600	4.611	7.202	1.93	0.6
$a_1 \times 10^3 \text{ (J)}$	92.49	150.4	44.69	50.7	43.11	70.77
$w^{(1,2)}$	1.119	1.149	1.341	1.252	1.068	1.062
$w^{(3,4)}$	0.940	0.846	0.844	0.748	1.056	1.061
$w^{(5,6,7,8)}$	0.915	–	0.575	–	0.873	–
$k_p \times 10^3 \text{ (J)}$	5.582	4.215	8.376	7.802	10	9.297
c	0.15	0.15	0.100	0.104	0.05	0.05
$E_s \text{ (GPa)}$	115	115	115	115	115	115

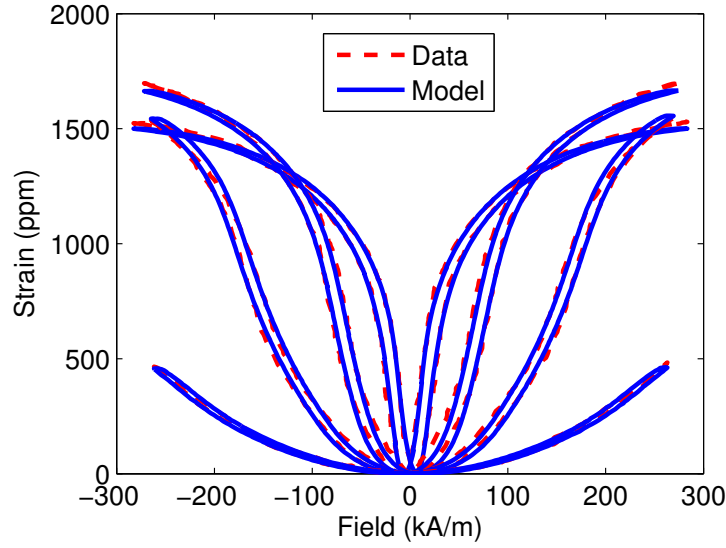


Figure 5.12: Comparison of hysteretic model with magnetostriction measurements provided by Etrema Products Inc. [43] for compressive prestresses of 1, 4, 8, and 16 KSI (6.9, 27.6, 55.2, 110.4 MPa).

and is appropriate for incorporating into the finite element framework of Chapter 3. Although the addition of an implicit relationship for the domain volume fractions requires the need for equilibrium iterations to achieve convergence, the model takes only 20% longer time than its non-iterative counterpart. A hysteretic extension to the model is formulated based on an evolution equation for the domain volume fractions. This model is used to simulate the response of three different data sets, including available data for commercially supplied Terfenol-D by Etrema Products, Inc. The model accurately describes the regions with and without hysteresis and achieves below 3% mean error for all the sets. The reduced version has somewhat reduced accuracy and consumes 30% lower computer time than the full version. The hysteretic model is

useful for implementation in control design where quantifying delays due to hysteresis is of importance.

5.2 Coupled Axisymmetric Finite Element Model for Terfenol-D transducers

The brittle nature of Terfenol-D and its poor machinability restricts its availability to 1D geometries like cylindrical rods. Terfenol-D transducers are commonly built with the cylindrical magnetostrictive rod at the core with concentric components like coil, permanent magnets, and flux return. An axisymmetric formulation can efficiently model such transducers without sacrificing accuracy. The formulation is developed by imposing axisymmetric approximations on the comprehensive 3D framework of Chapter 3. The current density \mathbf{J} and magnetic potential \mathbf{A} are defined as having only an out-of-plane component (J_ϕ and A_ϕ written as J and A respectively for convenience). To avoid singularities in computation, the variables used in the formulation are the modified magnetic potential ($A' = A/r$), modified radial displacement ($u' = u/r$), and axial displacement (w). The magnetic flux density vector (\mathbf{B}) and the strain vector (\mathbf{S}) are kinematically related to A' , u' , and w as

$$\mathbf{B} = [B_r, B_z]^T = \left[-r \frac{\partial A'}{\partial z}, r \frac{\partial A'}{\partial r} + 2A' \right]^T, \quad (5.16)$$

$$\mathbf{S} = [S_{rr}, S_{zz}, S_{rz}, S_{\phi\phi}]^T = \left[r \frac{\partial u'}{\partial r} + u', \frac{\partial w}{\partial z}, r \frac{\partial u'}{\partial z} + \frac{\partial w}{\partial r}, u' \right]^T. \quad (5.17)$$

The corresponding work conjugates - magnetic field (\mathbf{H}) and stress (\mathbf{T}) are related to \mathbf{B} and \mathbf{S} through constitutive laws and have the form

$$\mathbf{H} = [H_r \ H_z]^T, \quad (5.18)$$

$$\mathbf{T} = [T_{rr} \ T_{zz} \ T_{\phi\phi} \ T_{rz}]^T. \quad (5.19)$$

Since Terfenol-D transducers work primarily under axial loading, the main quantity of interest is the axial deformation w . Thus w is solved for in all structurally active domains (i.e. they are ‘axially active’). In some components radial deformation may occur due to the geometry of the transducer. In such components, radial deformation u is also computed. These components are both ‘axially active’ and ‘radially active’. Domains that are only ‘axially active’ (such as Terfenol-D) have a reduced stress and strain vector with only two components (axial and in-plane shear). This reduction has significant advantages in the Terfenol-D constitutive law inversion process detailed in Section 5.2.1.

For an axisymmetric problem the volume integrals can be transformed to area integrals using

$$\int_{V_e} (F) dV = 2\pi \int_{A_e} (rF) dr dz, \quad (5.20)$$

which when applied to (2.66) and (2.70) gives

$$\int_{A_B} r \mathbf{H} \cdot \delta \mathbf{B} \, dr dz + \int_{A_B} r \sigma \frac{\partial A}{\partial t} \delta A \, dr dz = \int_{l_B} r H_T \delta A \, dl + \int_{A_B} r J_s \delta A \, dr dz, \quad (5.21)$$

$$\begin{aligned} \int_{A_u} r (\mathbf{T} \cdot \delta \mathbf{S}) \, dr dz + \int_{A_u} r \rho \frac{\partial^2 \mathbf{u}}{\partial t^2} \cdot \delta \mathbf{u} \, dr dz + \int_{A_u} r c \frac{\partial \mathbf{u}}{\partial t} \cdot \delta \mathbf{u} \, dV \\ = \int_{l_u} r \mathbf{t} \cdot \delta \mathbf{u} \, dl + \int_{A_u} r \mathbf{f}_B \cdot \delta \mathbf{u} \, dA. \end{aligned} \quad (5.22)$$

The weak form equations can be entered in COMSOL using (5.21) and (5.22) as a function of A , u , w , and the corresponding test variables even though the solution variables are A' , u' , and w . This is done by adding global expressions relating A and u to A' and u' [16].

5.2.1 Incorporation of constitutive laws

Terfenol-D constitutive law

In this section the Terfenol-D constitutive law developed in section 5.1 is incorporated into the weak form equations described in the previous section. As is common with vector magnetic potential based formulations, a constitutive model inversion is required such that it takes flux density and strain as inputs and calculates stress and field as outputs. Moreover, since commercially available Terfenol-D rods have their [112] crystal orientation aligned with the sample axis (which is the Z axis of the global coordinate system), a coordinate transformation is required to integrate the constitutive law with the finite element model. Magnetic flux density and field are first order tensors and transform according to

$$\mathbf{X}_m = \mathbf{U}\mathbf{X}_G, \quad \mathbf{X}_G = \mathbf{U}^T\mathbf{X}_m, \quad (5.23)$$

while stress and strain being second order tensors transform according to

$$\mathbf{X}_m = \mathbf{U}^T\mathbf{X}_G\mathbf{U}, \quad \mathbf{X}_G = \mathbf{U}\mathbf{X}_m\mathbf{U}^T. \quad (5.24)$$

Here the subscripts m and G respectively denote the ‘material’ and ‘global’ coordinate system. The transformation matrix \mathbf{U} is formed using the normalized direction vectors in the material coordinate system that are aligned with the global coordinate axes;

$$\mathbf{U} = \left[\frac{\mathbf{u}_R}{\|\mathbf{u}_R\|}, \frac{\mathbf{u}_\phi}{\|\mathbf{u}_\phi\|}, \frac{\mathbf{u}_Z}{\|\mathbf{u}_Z\|} \right]. \quad (5.25)$$

The direction vector $\mathbf{u}_Z = [112]$ while the vectors \mathbf{u}_R and \mathbf{u}_ϕ are not fixed and keep on changing with the circumferential angle ϕ . However, since the Terfenol-D driver has an aspect ratio of 4:1, the radial and circumferential components of stresses and

fields are expected to be much smaller than the axial components. In that case, considering \mathbf{u}_R and \mathbf{u}_ϕ to be fixed should not have a noticeable affect on the accuracy of the model. In this work \mathbf{u}_R and \mathbf{u}_ϕ are selected as $[11\bar{1}]$ and $[[1\bar{1}0]$ respectively.

Piecewise-linear implementation of the constitutive law necessitates computation of the material Jacobian matrix (Section 3.2.1). Because of the coordinate transformation involved, calculation of the material Jacobian is more involved for Terfenol-D. For derivatives the transformation must be undergone twice, once to transform the output variable or the quantity being differentiated and once to transform the input variable with respect to which the differentiation is taking place. For example, the derivative of the induction with respect to field in the global coordinate system can be written as

$$\frac{\partial \mathbf{B}_G}{\partial \mathbf{H}_G} = \left(\frac{\partial \mathbf{B}_G}{\partial \mathbf{B}_m} \right) \left(\frac{\partial \mathbf{B}_m}{\partial \mathbf{H}_m} \right) \left(\frac{\partial \mathbf{H}_m}{\partial \mathbf{H}_G} \right). \quad (5.26)$$

Since both \mathbf{B} and \mathbf{H} are first order tensors, use of (5.23) yields

$$\frac{\partial \mathbf{B}_G}{\partial \mathbf{H}_G} = \mathbf{U}^T \left(\frac{\partial \mathbf{B}_m}{\partial \mathbf{H}_m} \right) \mathbf{U}, \quad (5.27)$$

where $\partial \mathbf{B}_m / \partial \mathbf{H}_m$ can be obtained as derived in section 4.2. This is expected as the derivative of a first order tensor with respect to another first order tensor is a second order tensor and thus follows the second order tensor transformation law. Similarly the derivative of a second order tensor with respect to another second order tensor (for example $\partial \mathbf{S} / \partial \mathbf{T}$) will follow the fourth order tensor transformation law. To simplify the process of higher order tensor transformations, a generalized case is treated first in which the field and stress are applied along an arbitrary direction \mathbf{u} with flux density and strain measured along another direction \mathbf{v} (both \mathbf{u} and \mathbf{v} being defined with respect to the material coordinate system). This is repeated with

different combinations of \mathbf{u} and \mathbf{v} aligned along the global axes to get the transformed derivatives. The algorithm consists of two stages. In the first stage, derivatives with respect to H_u and T_u are found, where H_u and T_u are the scalar field and stress values applied along \mathbf{u} :

$$\mathbf{H}_m = H_u \underbrace{[u_1 \quad u_2 \quad u_3]^T}_{\mathbf{u}}, \quad (5.28)$$

$$\mathbf{T}_m = T_u \underbrace{[u_1^2 \quad u_2^2 \quad u_3^2 \quad u_1 u_2 \quad u_2 u_3 \quad u_1 u_3]^T}_{\mathbf{u}_T}. \quad (5.29)$$

In the second stage the derivatives are projected along \mathbf{v} . The required derivatives can then be calculated as follows:

$$\frac{\partial \mathbf{m}^k}{\partial H_u} = \mu_0 M_s \mathbf{K}^{-1} \left[\mathbf{u} - \frac{\mathbf{c}^k \cdot \mathbf{K}^{-1} \mathbf{u}}{\mathbf{c}^k \cdot \mathbf{K}^{-1} \mathbf{c}^k} \mathbf{c}^k \right], \quad (5.30)$$

$$\frac{\partial \mathbf{m}^k}{\partial T_u} = \mathbf{K}^{-1} \left[- \left(\frac{\partial \mathbf{K}}{\partial T_u} \right) \mathbf{m}^k - \frac{\mathbf{c}^k \cdot \mathbf{K}^{-1} \left(\frac{\partial \mathbf{K}}{\partial T_u} \right) \mathbf{m}^k}{\mathbf{c}^k \cdot \mathbf{K}^{-1} \mathbf{c}^k} \mathbf{c}^k \right], \quad (5.31)$$

$$\frac{\partial \hat{\mathbf{m}}^k}{\partial H_u} = \frac{1}{\|\mathbf{m}^k\|} \frac{\partial \mathbf{m}^k}{\partial H_u} - \frac{\mathbf{m}^k}{\|\mathbf{m}^k\|^3} \left(\mathbf{m}^k \cdot \frac{\partial \mathbf{m}^k}{\partial H_u} \right), \quad (5.32)$$

$$\frac{\partial \hat{\mathbf{m}}^k}{\partial T_u} = \frac{1}{\|\mathbf{m}^k\|} \frac{\partial \mathbf{m}^k}{\partial T_u} - \frac{\mathbf{m}^k}{\|\mathbf{m}^k\|^3} \left(\mathbf{m}^k \cdot \frac{\partial \mathbf{m}^k}{\partial T_u} \right), \quad (5.33)$$

$$\frac{\partial G^k}{\partial H_u} = \frac{\partial \hat{\mathbf{m}}^k}{\partial H_u} \cdot (\mathbf{K} \hat{\mathbf{m}}^k - \mathbf{B}^k) - \mu_0 M_s \hat{\mathbf{m}}^k \cdot \mathbf{u}, \quad (5.34)$$

$$\frac{\partial G^k}{\partial T_u} = \frac{\partial \hat{\mathbf{m}}^k}{\partial T_u} \cdot (\mathbf{K} \hat{\mathbf{m}}^k - \mathbf{B}^k) - \frac{1}{2} \hat{\mathbf{m}}^k \cdot \frac{\partial \mathbf{K}}{\partial T_u} \hat{\mathbf{m}}^k. \quad (5.35)$$

The derivatives of \mathbf{S}_m^k and ξ^k can be obtained using (4.28), (4.29), and (5.11) by substituting H_i and T_i with H_u and T_u respectively. The derivative $\partial \mathbf{K} / \partial T_u$ is given by

$$\frac{\partial \mathbf{K}}{\partial T_u} = - \begin{bmatrix} 3\lambda_{100}u_1^2 & 3\lambda_{111}u_1u_2 & 3\lambda_{111}u_1u_3 \\ 3\lambda_{111}u_1u_2 & 3\lambda_{100}u_2^2 & 3\lambda_{111}u_2u_3 \\ 3\lambda_{111}u_1u_3 & 3\lambda_{111}u_2u_3 & 3\lambda_{100}u_3^2 \end{bmatrix}, \quad (5.36)$$

Finally the derivatives are projected along \mathbf{v} :

$$\frac{\partial M_v}{\partial H_u} = M_s \sum_{k=1}^r \left(\hat{\mathbf{m}}^k \frac{\partial \xi^k}{\partial H_u} + \frac{\partial \hat{\mathbf{m}}^k}{\partial H_u} \xi^k \right) \cdot \mathbf{v}, \quad (5.37)$$

$$\frac{\partial M_v}{\partial T_u} = M_s \sum_{k=1}^r \left(\hat{\mathbf{m}}^k \frac{\partial \xi^k}{\partial T_u} + \frac{\partial \hat{\mathbf{m}}^k}{\partial T_u} \xi^k \right) \cdot \mathbf{v}, \quad (5.38)$$

$$\frac{\partial S_{m_v}}{\partial H_u} = \mathbf{v} \cdot \sum_{k=1}^r \left(\mathbf{S}_m^k \frac{\partial \xi^k}{\partial H_u} + \frac{\partial \mathbf{S}_m^k}{\partial H_u} \xi^k \right) \mathbf{v}, \quad (5.39)$$

$$\frac{\partial S_{m_v}}{\partial T_u} = \mathbf{v} \cdot \sum_{k=1}^r \left(\mathbf{S}_m^k \frac{\partial \xi^k}{\partial T_u} + \frac{\partial \mathbf{S}_m^k}{\partial T_u} \xi^k \right) \mathbf{v}. \quad (5.40)$$

The material Jacobian matrix with the reduced field and stress vectors consists of 16 entries which can be obtained using (5.37)-(5.40) with \mathbf{u} and \mathbf{v} being substituted by different combinations of \mathbf{u}_R and \mathbf{u}_Z . The piecewise linear solution process utilizing the computed material Jacobian is identical to that discussed in Chapter 3. Figure 5.13 shows the sequence of operations involved in incorporating the constitutive model for a nonlinear dynamic implementation. The input to the constitutive law are the flux density and strain tensors calculated kinematically from the vector magnetic potential and displacement values at the integration points. The algorithm starts with an initial guess of zero stress and field and converges to the correct values through Quasi-Newton iterations. In every iteration, first the stress and field vectors are transformed from the global to the material coordinate system; then the response of the material to this input stress and field is computed using the energy-averaged constitutive model, and finally the computed flux density $\mathbf{B}_m^{(k)}$ and strain $\mathbf{S}_m^{(k)}$ (k being the iteration index) are transformed back to the global coordinate system ($\mathbf{B}_G^{(k)}$, $\mathbf{S}_G^{(k)}$) to be compared with the input vectors ($\mathbf{B}_G, \mathbf{S}_G$). In case the difference is greater than the tolerance, a revised stress and field ($\mathbf{H}_G^{(k+1)}$ and $\mathbf{T}_G^{(k+1)}$) is estimated based on the SR1 update formula and the process is repeated till convergence is achieved.

The SR1 formula directly approximates the material Jacobian inverse which is used by COMSOL to assemble the tangent stiffness matrix during the dynamic solution process.

Constitutive laws for passive materials

The stress strain laws for passive structural materials (such as steel) can be written as shown by Chandrupatla and Belegundu [18],

$$\begin{Bmatrix} T_{rr} \\ T_{zz} \\ T_{\phi\phi} \\ T_{rz} \end{Bmatrix} = \frac{E(1-\nu)}{(1+\nu)(1-2\nu)} \begin{bmatrix} 1 & \frac{\nu}{(1-\nu)} & \frac{\nu}{(1-\nu)} & 0 \\ \frac{\nu}{(1-\nu)} & 1 & \frac{\nu}{(1-\nu)} & 0 \\ \frac{\nu}{(1-\nu)} & \frac{\nu}{(1-\nu)} & 1 & 0 \\ 0 & 0 & 0 & \frac{(1-2\nu)}{2(1-\nu)} \end{bmatrix} \begin{Bmatrix} S_{rr} \\ S_{zz} \\ S_{\phi\phi} \\ S_{rz} \end{Bmatrix}. \quad (5.41)$$

Constitutive laws for passive magnetic materials have been modeled using the linear isotropic relationship $\mathbf{H} = \mu^{-1}\mathbf{B}$ where μ is the constant permeability of the material. For permanent magnets this law is modified to include the residual induction B_{res} in the relevant direction. For example, if the residual induction is along the z direction, the constitutive law can be written as

$$H_r = \frac{1}{\mu} B_r, \quad (5.42)$$

$$H_z = \frac{1}{\mu} (B_z - B_{res}). \quad (5.43)$$

Electrically conducting materials have been modeled using a constant conductivity. The resulting system is assembled and solved using the nonlinear dynamic solution technique described in section 3.2.2.

5.3 Case Study: Terfenol-D Mount Actuator

Automotive engine mounts serve two main purposes. First, they isolate low amplitude engine vibrations from the chassis and secondly they prevent engine bounce

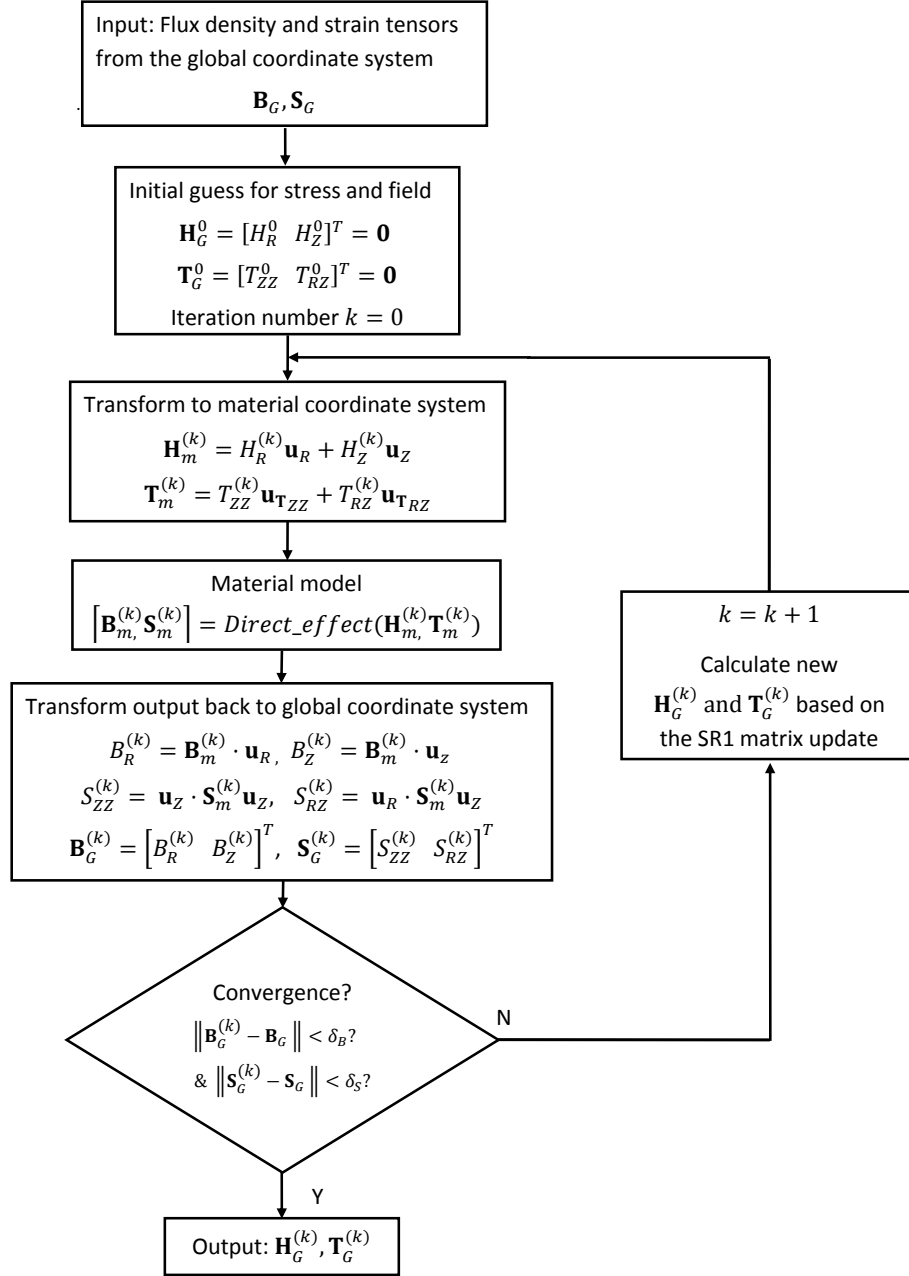


Figure 5.13: Flowchart showing the process followed to incorporate the Terfenol-D constitutive law in the model.

from high amplitude road excitations. Since the frequency of engine vibrations range from 20 Hz at idling to a few hundred Hertz while road excitations are typically below 5 Hz an ideal mount would have high static stiffness and very low dynamic stiffness. Active mounts achieve these characteristics by employing an actuator within a passive hydro-mount. The actuator controls the pressure of the hydraulic fluid inside the mount to reduce its dynamic stiffness. The small response times and high displacement resolution of magnetostrictive materials make them attractive candidates for use in mount actuators.

Because smart material drivers capable of broadband response (such as piezoelectrics and magnetostrictives) possess limited stroke, implementation of these materials in an active mount actuator necessitates stroke amplification. Hydraulic amplification [86, 39] is particularly attractive as it provides large mechanical gains in a restricted space. The fluid used for amplification can either be the hydraulic fluid used in the mount [80] or it can be a different fluid sealed from the mount's hydraulic fluid [75]. The former design is more attractive for its simplicity while the latter is more efficient as the displacement of the smart material driver is not lost directly to the compliance of the mount. Presence of internal friction and fluid chamber compliance greatly influence the performance of these actuators. Because of this, linear models considering 100 percent energy transmission greatly overestimate the performance of such actuators [86, 36].

A magneto-hydraulic actuator (MHA) developed following the second design principle combines a Terfenol-D driver with an area based hydraulic stroke amplification mechanism and obtains millimeter stroke with a bandwidth of over 200 Hz (see Appendix B). Section 5.3.1 briefly describes the designed actuator. Although the lumped

parameter model shown in Appendix D can accurately quantify the dynamic mechanical response of the actuator, it is not suitable for transducer design because parameters such as fluid chamber compliance and current-field relationships are difficult to quantify in lumped parameter models. A finite element model is more appropriate for design optimization as it can describe effects of both geometry and material constitutive parameters (Young's modulus, permeability, electrical conductivity etc.) on the dynamic performance of the transducer. The finite element model developed in Section 5.2 will be used to analyze the performance of the MHA in the following sections.

5.3.1 Magneto-hydraulic actuator (MHA) design

Figure 5.14 shows the geometry of the MHA. It consists of a fluid chamber with a large diameter piston at one end driven by a Terfenol-D rod and a small diameter driven piston at the other end. The magnetic circuit consists of a permanent magnet

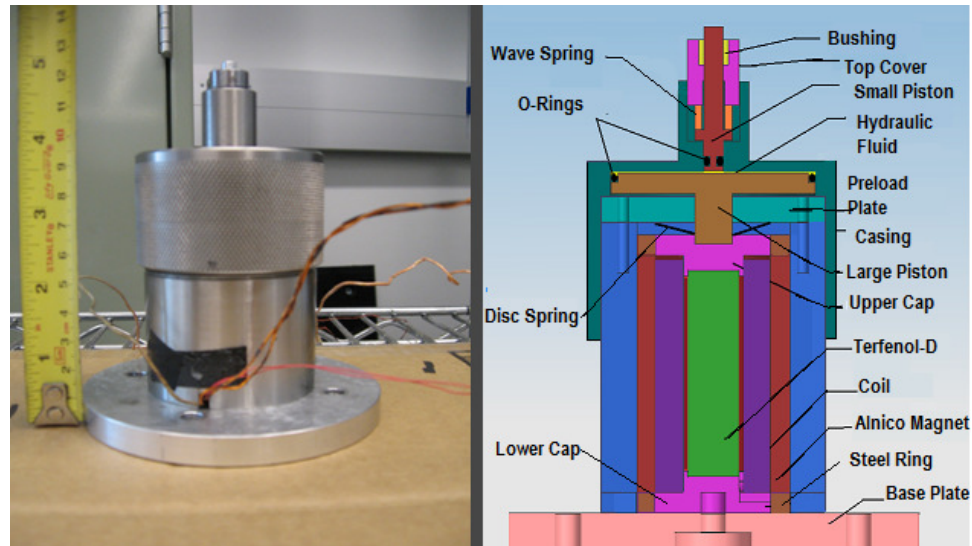


Figure 5.14: Physical actuator (left) and cutout (right).

to provide magnetic bias, a coil to generate the dynamic fields with Terfenol-D at its core, and iron pieces for flux return. Figure 5.15 shows the 2D axisymmetric version used for modeling. Some components like the stainless steel body and the preload plate have not been modeled as they only serve a geometrical purpose. The device is surrounded by air so that the magnetic potential boundary condition can be applied to the outer boundary of air. In general, flux density measurements are taken by winding a pick-up coil around the middle of the rod and strain measurements are taken by bonding a strain gage close to the midpoint of the rod. Breaking the magnetostrictive rod domain into 3 areas allows us to evaluate the variables in the central region separately and compare the behavior of the model against measurements. In this actuator, all components are considered to be ‘magnetically active’ meaning that the magnetic degree of freedom (A) is solved for in all the domains. Of these, the base plate, Terfenol-D rod, end caps, pistons, and casing are considered to be structurally active also which means that the mechanical degrees of freedom are solved for in only these components. This partitioning of the solution domain reduces the total degrees of freedom in the model thus reducing the solution time.

5.3.2 Model augmentation

This section describes the additional physics that was combined with the finite element model to describe the fluid-structure interaction and friction at the fluid seals.

Fluid domain

Due to the extremely small volume of fluid used in the actuator, inertial effects in the fluid have been neglected. Also, since the seal friction forces are much higher

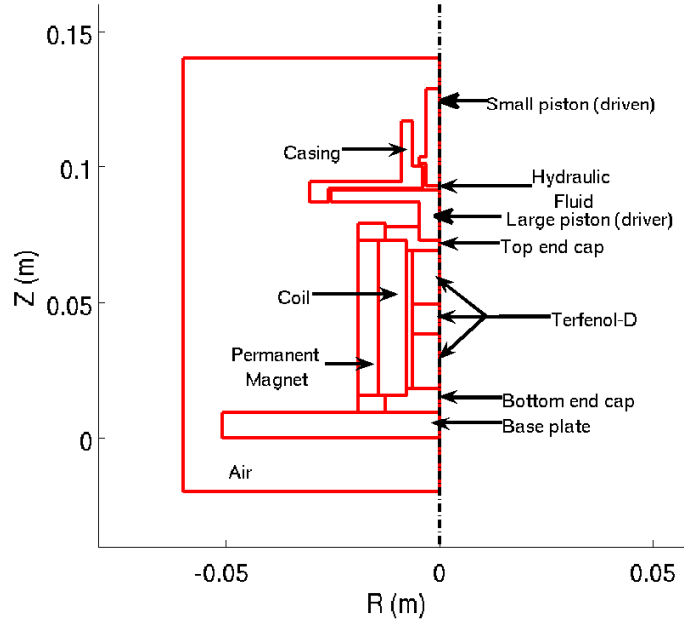


Figure 5.15: Geometry of the transducer used in this study.

compared to viscous forces in the fluid, damping in the fluid is assumed to be negligible. Thus, only fluid compliance is modeled. The change in volume of the fluid domain ΔV_f can be written as a sum of contributions from the driver piston ΔV_P , the driven piston ΔV_L , and the casing ΔV_C as

$$\Delta V_f = -\Delta V_P + \Delta V_L + \Delta V_C, \quad (5.44)$$

where each of these volume changes are calculated using the integral

$$\Delta V_i = \int_{l_i} 2\pi r w dr, \quad (5.45)$$

over the length of the edge l_i exposed to the fluid domain. The pressure change in the fluid is

$$\Delta p = -\frac{\beta}{V_{ref}} \Delta V_f, \quad (5.46)$$

which is coupled to the structural model through traction on the edges exposed to the fluid. The model describes the effect of compliance of the fluid chamber components. Here, β is the effective bulk modulus of the fluid, while in the lumped parameter model [14], β_{eff} represented an effective modulus describing the combined compliance of the fluid and fluid chamber components.

Friction model

Friction forces are present at the o-ring seals on the two pistons. At the smaller (driven) piston seal, actuation forces are low and velocities are high. Hence, even a small friction force at this seal has a significant impact on the dynamic performance of the actuator. On the other hand at the larger (drive) piston, actuation forces are high and velocities are low. Hence a small frictional force at this end does not affect the dynamic response of the actuator. Thus, friction has been modeled only at the smaller piston seal.

In the LuGre model [64], friction between two sliding surfaces in contact is described as an interaction force between microscopic bristles on both surfaces. The bristle deflection state Z_L is governed by a nonlinear first order differential equation;

$$\dot{Z}_L + \sigma_0 \frac{|v_L|}{g(v_L)} Z_L - v_L = 0, \quad (5.47)$$

where v_L is the relative sliding velocity between the two surfaces, which in this case is the average velocity of the driven piston calculated by integrating $2\pi r\dot{w}$ over the edge of the piston adjacent to the casing, divided by the area of that surface. Function $g(v_L)$ is given by

$$g(v_L) = F_c + (F_s - F_c)e^{-(v_L/v_s)^2}, \quad (5.48)$$

where F_s and F_c are the static and Coulomb friction forces and v_s is the Stribeck velocity. The friction force is given by

$$FR_L = \sigma_0 Z_L + \sigma_1 \dot{Z}_L + \sigma_2 v_L, \quad (5.49)$$

where σ_0 and σ_1 are the bristle stiffness and bristle damping coefficient, respectively. This force is applied as traction on the boundary of the smaller piston adjacent to the casing.

Boundary conditions

Boundary conditions for an axisymmetric problem must be implemented carefully such that none of the variables become infinite at the $r = 0$ boundary. In this case, the axial symmetry condition is enforced using $(\partial A / \partial r)_{(r=0)} = 0$ in the magnetically active domains, $u_{(r=0)} = 0$ in the radially active domains, and $(\partial w / \partial r)_{(r=0)} = 0$ in the axially active domains. These conditions remove shear stresses and constrain the radial displacement at the $r = 0$ boundary. The magnetostrictive system is encapsulated by a large volume of air. At the outer boundaries of this air volume, the magnetic potential is set to zero. The bottom face of the base plate and the casing are considered to be mechanically fixed.

5.3.3 Results and parametric study

Obtaining the bias point

Computation of the dynamic response of the actuator requires accurate determination of its bias point. The actuator is biased both mechanically and magnetically. The mechanical bias is due to the compression of the wave spring whose force is transmitted (and amplified) through the fluid to the Terfenol-D rod. The stress developed

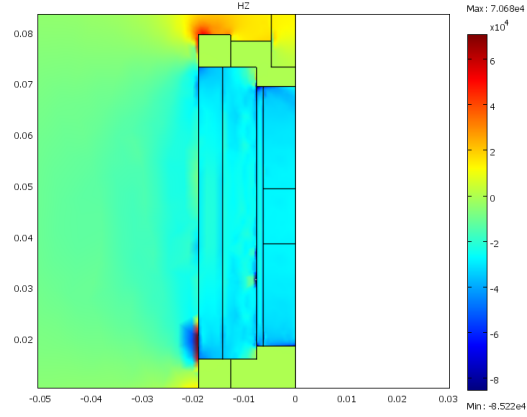


Figure 5.16: Axial magnetic field distribution in the magnetic circuit due to the permanent magnet.

in the Terfenol-D under an axial load can be assumed uniform. Therefore, this stress is superimposed directly on the applied stress in the constitutive model function. The magnetic bias is due to the residual flux density in the permanent magnet. This field depends on the geometry of the magnetic circuit and cannot be assumed to be homogeneously distributed in the rod. The magnetic bias point is obtained by increasing the residual flux density of the magnet from zero to its actual value using a hyperbolic tangent function and storing the solution from the final step. Figure 5.16 shows that the axial magnetic field at the bias point is uniformly distributed in the central region of the rod with a somewhat lower value at the ends. The average magnetic field in the Terfenol-D rod is ≈ 30 kA/m.

Response to harmonic inputs

Figure 5.17 shows the actuator response at 20, 50, 100, and 200 Hz. As expected the phase between voltage and displacement increases with increasing frequency resulting in counter-clockwise rotation of the loops. One shortcoming of the model

is the assumed anhysteretic Terfenol-D behavior which causes a discrepancy in the phase of the response. At lower frequencies this is not visible but at 200 Hz this difference in phase is prominent.

An interesting feature that is observed in both the experimental and modeled voltage-current loops is that the actuator draws a biased current even though it is driven with an unbiased sinusoidal voltage input. This happens because of the nonlinear behavior of Terfenol-D. Because the permeability of the material is field dependent, the back emf in the coil also varies with voltage giving rise to an asymmetric current signal. Such effects can only be described accurately with models where electromagnetic and mechanical responses are fully coupled.

Parametric study

The proposed finite element model can be a useful tool for optimizing device geometry and material selection. To illustrate, the effect of fluid Bulk modulus, thickness of the fluid chamber components, conductivity and permeability of the permanent magnet, and seal friction force on the unloaded displacement response of the actuator is studied at 20, 50, 100 and 200 Hz.

The effective fluid bulk modulus usually plays a key role in the dynamic performance of hydraulic devices. To investigate the effect of stiffening up the fluid (by degassing etc.), the model is executed with $\beta = 2\beta_0$ and $\beta = 4\beta_0$, where β_0 is the bulk modulus value tuned to describe the actuator behavior. Figure 5.18(a) shows that increasing the bulk modulus 4 times achieves a mere 2-3 % increase in the unloaded stroke of the actuator below 100 Hz while a more noticeable 8.5 % increase is observed at 200 Hz. This weak dependence of the actuator performance on the fluid bulk modulus suggests that the performance of the MHA is limited by structural

compliance and not the fluid's compliance which is very low because of the small volume of fluid used in this actuator (≈ 1.3 c.c).

Next, the effect of structural compliance of the fluid chamber components on transducer performance is investigated. The model is run with the thickness of the larger piston and the casing doubled. A remarkable 30 - 35 % stroke increase is recorded in the 20 - 100 Hz range while a staggering 143 % increase is obtained at 200 Hz. Thus, the primary source of compliance in the transducer comes from the components enclosing the fluid.

Another vital factor which influences the performance of hydraulic devices is seal friction. The friction force at the smaller piston seal is reduced to $fr = 0.5 fr_0$ and $fr = 0.25 fr_0$ where fr_0 is the friction force value tuned to describe the experimentally observed transducer behavior. With the friction force reduced to half, the stroke increases by 10-12 % in the 20 - 100 Hz range while a 60 % increase is recorded at 200 Hz. With the friction force reduced to one-fourth of the original value, a 15-20 % stroke increase is recorded below 100 Hz and a substantial 85 % increase is recorded at 200 Hz. Thus, as expected, reduction in seal friction can bring about considerable improvements in the unloaded stroke of the transducer.

Finally, to illustrate the advantages of a fully coupled model, the effect of some electromagnetic parameters on the mechanical performance of the actuator is computed. The permeability of the permanent magnet is increased to twice and four times the initial value while the conductivity of the permanent magnet is reduced to zero to study the effect of eliminating eddy currents in the permanent magnet. Both parameters do not have any appreciable effect on system performance. Increasing the permeability of the permanent magnet four times leads to a 4 % stroke increase at

20 Hz and reduces to a 0.25 % increase at 200 Hz. Setting the conductivity of the permanent magnet to zero results in negligible improvement at 20 Hz and gradually increases up to a 3.6 % stroke improvement at 200 Hz. These trends are expected because increase in permeability increases the total flux flowing in the circuit thus getting higher performance. However increased flux also results in higher eddy currents as the drive frequency increases. Thus the advantage of having higher permeability keeps reducing with increasing drive frequency. Conversely, reducing the conductivity of the permanent magnet has little effect at 20 Hz since eddy currents are negligible at such low frequencies. With increasing frequency the effect of reduced eddy currents becomes more apparent (Figure 5.18(b)).

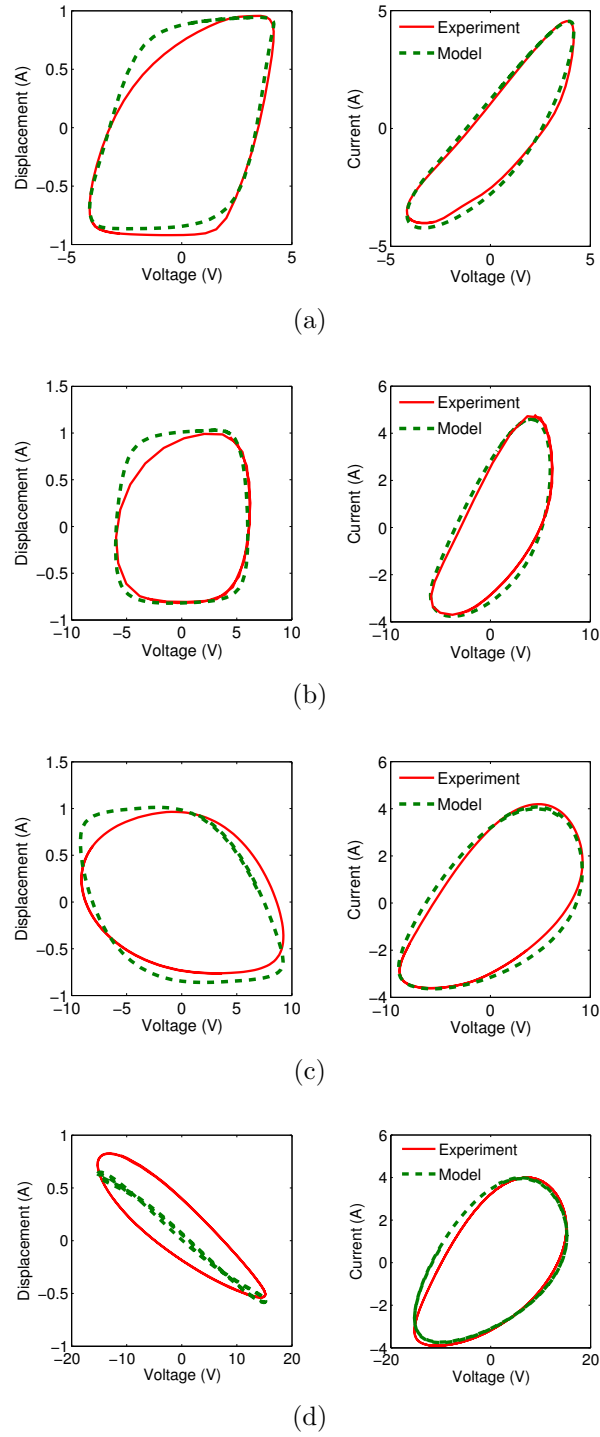
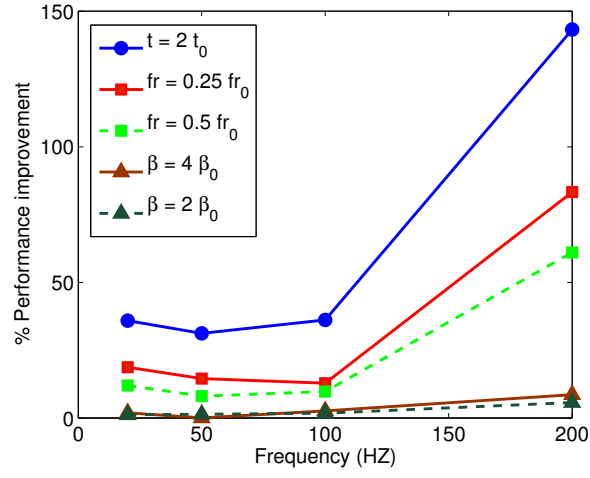
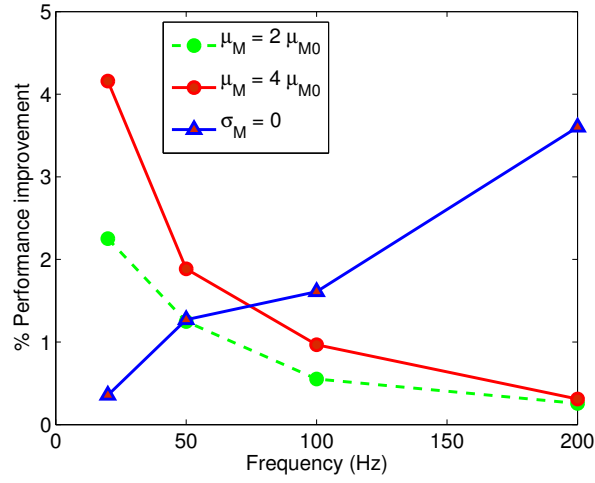


Figure 5.17: Comparison of modeled voltage-displacement and voltage-current loops with measurements. (a) 20 Hz, (b) 50 Hz, (c) 100 Hz, and (d) 200 Hz.



(a)



(b)

Figure 5.18: Percentage improvement in the unloaded stroke of the actuator with variation in (a) mechanical model parameters and (b) magnetic model parameters.

Chapter 6: SUMMARY AND FUTURE WORK

Magnetostrictive materials have the potential to be applied in many engineering applications as high bandwidth sensors and actuators. Efficient design of such transducers requires an adequate modeling framework which fully describes the nonlinear electro-magneto-mechanical coupling present in them. The primary aim of this dissertation was to construct a comprehensive modeling tool which describes this coupling and is sufficiently general in construction such that it can be applied to any magnetostrictive alloy when provided with a constitutive model for the alloy. The work presented in this dissertation falls under three main categories:

1. Incorporation of nonlinear constitutive laws into a 3D finite element framework and development of efficient solution schemes to solve the resulting system depending on the drive conditions.
2. Development of constitutive models for Galfenol and Terfenol-D suitable for integration with the finite element model.
3. Presentation of case studies which validate the model's ability to describe transducer level dynamic responses

This chapter summarizes the key achievements of this research and possible future work which can be carried out using this research as a starting point.

6.1 Research Summary

6.1.1 Unified model

This work was aimed at developing a finite element framework for modeling 3D magnetostrictive transducers driven over nonlinear regimes with dynamic inputs. Weak form equations derived from Maxwell's equations for electromagnetic systems and Navier's equation for mechanical systems are coded into COMSOL (a commercial finite element package used for meshing, global assembly of matrices and post-processing). A piecewise linear solution procedure was developed to describe the transducer response under quasistatic conditions. The solution was obtained in the form of piecewise increments and the magnetostrictive material was modeled using linear piezomagnetic equations within each incremental step. The piezomagnetic coefficients were updated at the end of each step by analytical differentiation of the constitutive law. Reduction in computational effort was achieved by declaring the material coefficients as interpolated data functions and computing them only at selected locations. The piecewise linear procedure was found to be useful for obtaining quasi-static major loops for the system and accurate determination of bias points. A linear dynamic simulation with the magnetostrictive material coefficients computed at the bias point was proposed for describing the system dynamics for moderate inputs about the bias point. An implicit time integration scheme based on the trapezoidal rule was devised to describe dynamic system responses for large-scale inputs.

6.1.2 Application to Galfenol transducers

In this chapter a nonlinear discrete energy averaged model for Galfenol was implemented in the unified modeling framework. First, an optimization algorithm was developed to find the parameters of the discrete energy-averaged model based on the 1D characterization curves of the Galfenol alloy. With the parameter search algorithm, the only inputs required by the finite element model were the constitutive parameters of the passive materials (permeability, conductivity, stiffness etc.) and the 1D magnetomechanical characterization curves for Galfenol. In the parameter optimization routine, good initial guesses for the parameters were selected based on analytical relationships. The algorithm was shown to work for a wide variety of Galfenol alloys including single crystal $\text{Fe}_{81.5}\text{Ga}_{18.5}$ and textured polycrystalline $\text{Fe}_{81.6}\text{Ga}_{18.4}$ with and without annealing. Although the optimization routine produced the best results with the full set of characterization curves (i.e. both actuation and sensing) with a mean error of approximately 2 %, the results obtained with only a single actuation measurement were also remarkably accurate (≈ 3 %).

For incorporation into the piecewise-linear model, the constitutive law was analytically differentiated and analytical expressions for the components of the material Jacobian matrix were obtained. For the nonlinear dynamic solution, the constitutive model was inverted using the Quasi-Newton SR1 formula which directly updated the Jacobian inverse, eliminating the need for matrix inversion within the iteration loop. The computed Jacobian inverse in the final iteration of the inversion process was used for the assembly of the global stiffness matrix. The inversion routine was coded up such that a single execution calculated the 6 components of stress, 3 components of

field and 81 components of the Jacobian inverse, thereby enhancing the overall computational efficiency of the model. The inability of COMSOL to take vector valued inputs from MATLAB functions was tackled by coding up the material model such that it was executed only once for a particular set of input values after which the corresponding ninety outputs were stored in a data structure. For the subsequent eighty-nine runs with the same inputs, the desired output was returned directly from the stored data structure. The model was compared to experiments conducted on a Galfenol unimorph actuator. Results showed that the model is capable of describing system level input-output relationships under both quasistatic and dynamic conditions.

6.1.3 Application to Terfenol-D transducers

This chapter dealt with the methods used to apply the unified finite element model to Terfenol-D transducers. The work was split into three major segments: (1) Development of a constitutive model for Terfenol-D which could be incorporated in the finite element framework. (2) Reduction of the 3D framework to a 2D axisymmetric form to take advantage of the axisymmetric nature of Terfenol-D transducers, and (3) A case study on a Terfenol-D engine mount actuator to validate the model's ability to quantify Terfenol-D transducer dynamics.

Terfenol-D constitutive modeling: A fully coupled energy averaged constitutive model was formulated to describe the magnetomechanical response of Terfenol-D. Two main discrepancies of previous energy averaged models in modeling Terfenol-D response were recognized as presence of an additional kink in the modeled response which is absent in measurements and absence of the slow approach to saturation

present in Terfenol-D magnetostriction. It was shown that use of a weighted global anisotropy energy combined with a variable smoothing factor based on the deviation of domain volume fractions from a homogeneous distribution tackles both the issues successfully. Because of the implicit relationship for the domain volume fractions, equilibrium iterations were required to achieve convergence. Nevertheless, the iteration procedure was found to be extremely efficient and took only 20 % longer than solving without iterations. A reduced version of the model was also proposed in which the four minima corresponding to the four easy axes which caused the kinks were eliminated. This approach was more efficient but suffered from lack of accuracy under high stress or field for actuation and low stress or field for sensing. A hysteretic extension to the model was also formulated based on an evolution equation for the domain volume fractions. It was shown that the model is capable of reproducing the magnetomechanical behavior of a variety of Terfenol-D alloys provided an optimum parameter set is computed for the alloy. Both regions and amount of hysteresis were accurately modeled with mean errors below 5 % in all cases.

Axisymmetric finite element formulation: The 3D unified model was reduced to the 2D axisymmetric form to take advantage of the axisymmetric nature of Terfenol-D transducers. Vector magnetic potential \mathbf{A} and current density \mathbf{J} were reduced to scalars defined in the out-of-plane direction. The weak form equations were obtained by converting the volume integrals to area integrals. A coordinate transformation was integrated with the Terfenol-D constitutive law as the global and material coordinate systems did not coincide. The material Jacobian was computed using a two-stage vectorized transformation process to avoid direct computation of third and

fourth order tensor transformations which would require for-loops. Implementation of the piecewise-linear and nonlinear dynamic solution was done in a manner identical to the 3D case.

Case study on a Terfenol-D engine mount actuator: The axisymmetric finite element framework was used to describe the dynamic performance of a hydraulically amplified Terfenol-D mount actuator. The FEA model was combined with lumped equations for the LuGre model to describe seal friction and fluid-structure interaction which modeled the compliance of the hydraulic fluid but neglected fluid inertia and damping due to the extremely small volume of fluid used in the actuator. Results showed that the magnitude of the mechanical and electrical performance of the actuator was accurately predicted up to 200 Hz. Because of the anhysteretic nature of the constitutive law for Terfenol-D, the response had small errors in phase which became particularly noticeable at frequencies above 100 Hz. A parametric study on the unloaded displacement response of the actuator showed that over 100 % performance improvements can be achieved by doubling the thickness of the fluid chamber components and reducing the seal friction to one-fourth of its original value can yield approximately 80 % performance improvement. The actuators performance was found not to be very sensitive to changes in bulk modulus of the fluid. A four-fold increase in the bulk modulus caused a mere 8.5% increase in stroke. This was possibly due to the extremely small fluid volume contained in the hydraulic chamber. Variation of the electrical and magnetic constitutive parameters (permeability and conductivity) of the permanent magnet also showed no appreciable improvements in

transducer performance. However, the example illustrated the utility of the fully-coupled finite element model in describing the effects of mechanical, magnetic and electrical constitutive parameters, and transducer geometry on the dynamic performance of the transducer.

6.2 Contributions

The main contributions of this dissertation are:

1. Formulation of a unified modeling framework which is capable of describing the full nonlinear coupling between electrical, magnetic, and mechanical domains in magnetostrictive transducers. It can simultaneously describe the effects of flux leakages, structural dynamics, eddy currents, and nonlinear constitutive behavior on transducer performance. The framework is unified in the sense that the solution algorithms that are developed and implemented can be used to describe the dynamic behavior of transducers employing any magnetostrictive material whose constitutive behavior can be quantified. The framework is shown to model transducers employing the two most common magnetostrictive alloys, Terfenol-D and Galfenol, based on nonlinear analytical constitutive models. The work was concentrated in two areas:

- Development of solution algorithms to efficiently solve the system equations:
 - A fast piecewise-linear solution method was devised based on an incremental formulation for quasistatic operating conditions.

- An implicit time integration method based on the trapezoidal rule was implemented to quantify nonlinear dynamic system responses for large scale dynamic inputs.
 - Development of strategies to incorporate nonlinear constitutive models in the finite element framework:
 - A parameter optimization algorithm for a discrete energy averaged constitutive law was incorporated in the framework to determine the constitutive model parameters from 1D measurements on the material.
 - Analytical differentiation of constitutive models was done to obtain piezomagnetic coefficients for the piecewise-linear solution.
 - Terfenol-D and Galfenol constitutive laws were numerically inverted using the Quasi-Newton SR1 formula for use in the nonlinear dynamic solution.
2. Development and refinement of nonlinear constitutive laws suitable for incorporation into transducer level models:
- A fully coupled discrete energy-averaged model for Terfenol-D was formulated based on an implicit domain volume fraction definition.
 - An energy-averaged model for Galfenol was refined to eliminate instabilities at high magnetic fields making it more suitable for use in finite element models.

6.3 Findings

- The developed finite element framework can accurately quantify the mechanical and electrical responses of a Galfenol unimorph actuator and a Terfenol-D engine mount actuator.
- Approximation of hysteretic material behavior with anhysteretic constitutive laws caused errors in the phase of the modeled response. These errors were negligible till 100 Hz and became more noticeable with increasing frequency.
- The framework can be successfully augmented with lumped parameter equations describing additional physics as was done for seal friction and fluid-structure interaction to model the response of a Terfenol-D engine mount actuator.
- A parametric study on the engine mount actuator showed that the model is useful for design optimization. Effects of electrical, magnetic, and mechanical constitutive parameters on transducer performance can be predicted.

6.4 Future Work

This research provided a tool for modeling 3D magnetostrictive systems as well as presented applications of this tool to specific Galfenol and Terfenol-D transducers. The following list discusses possible future work which could be done using this research as a platform

- One of the limitations of the current implementation is that it assumes use of anhysteretic constitutive laws. Development of methods to incorporate hysteretic material behavior will be a useful addition to the framework. The challenge

involved in this is that hysteretic constitutive models depend on the history of the material. In case of the energy-averaged models, it would mean keeping track of the volume fractions on all the nodes inside the magnetostrictive material. Further, methods for ensuring convergence of hysteretic systems must be applied.

- Significant computational effort is used up in numerical inversion of the constitutive laws. Thus, formulation of efficient inverse constitutive models can considerably improve the efficiency of the finite element model.
- The accuracy of 3D constitutive laws developed or refined in this work have not been tested against 3D measurements. 3D characterization of magnetostrictive alloys will provide valuable information about the validity of these constitutive models.
- In this work supplemental physics was added in the form of LuGre friction and fluid-structure interaction (based on only fluid compliance) while modeling the mount actuator. More complex components can be added to the finite element framework. For example, structural-acoustic interactions can be incorporated to model sonar transduction devices or magnetostrictive speakers. Complete fluid-structure interaction models including fluid inertia, damping, and compliance can be integrated with the framework to model magnetostrictive-hydraulic pumps.

Appendix A: VECTOR CALCULUS

A.1 Vector Calculus Operators

Gradient: Gradient of a scalar f is a vector and is written as

$$\text{grad}(f) = \nabla f, \quad (\text{A.1})$$

where the operator ∇ in cartesian coordinates is defined as

$$\nabla = \frac{\partial}{\partial x} \hat{\mathbf{i}} + \frac{\partial}{\partial y} \hat{\mathbf{j}} + \frac{\partial}{\partial z} \hat{\mathbf{k}}. \quad (\text{A.2})$$

Divergence: Divergence of a vector field \mathbf{F} is a scalar and is defined as

$$\text{div}(\mathbf{F}) = \nabla \cdot \mathbf{F}. \quad (\text{A.3})$$

Curl: Curl of a vector field is a vector and is defined as

$$\text{curl}(\mathbf{F}) = \nabla \times \mathbf{F}. \quad (\text{A.4})$$

Laplacian: The Laplacian operator is defined differently for scalars and vectors.

For scalars it is defined as

$$\Delta f == \nabla^2 f = (\nabla \cdot \nabla) f, \quad (\text{A.5})$$

and for vectors it is defined as

$$\nabla^2 \mathbf{F} = \nabla (\nabla \cdot \mathbf{F}) - \nabla \times (\nabla \times \mathbf{F}). \quad (\text{A.6})$$

In Cartesian coordinates the Laplacian of a vector is a vector whose components are the scalar Laplacian of the corresponding components of the original vector. Thus $\nabla^2 \mathbf{F} = \nabla^2 F_x \hat{\mathbf{i}} + \nabla^2 F_y \hat{\mathbf{j}} + \nabla^2 F_z \hat{\mathbf{k}}$.

A.2 Vector Calculus Identities

The following is a list of identities relating these operators which have been used in this dissertation.

$$\nabla \cdot (\nabla \times \mathbf{F}) = 0, \quad (\text{A.7})$$

$$\nabla \times \nabla f = 0, \quad (\text{A.8})$$

$$\mathbf{F} \times (\nabla \times \mathbf{F}) = \frac{1}{2} \nabla (\mathbf{F} \cdot \mathbf{F}) - (\mathbf{F} \cdot \nabla) \mathbf{F}, \quad (\text{A.9})$$

$$\nabla \cdot (\mathbf{F}_1 \times \mathbf{F}_2) = \mathbf{F}_2 \cdot (\nabla \times \mathbf{F}_1) - \mathbf{F}_1 \cdot (\nabla \times \mathbf{F}_2). \quad (\text{A.10})$$

A.3 Theorems

Stoke's theorem: The stoke's theorem relates the surface integral of the curl of a vector field over a surface S to the line integral of the vector field over its boundary ∂S :

$$\int_{\partial S} \mathbf{F} \cdot d\mathbf{X} = \int_S (\nabla \times \mathbf{F}) \cdot \mathbf{n} dS. \quad (\text{A.11})$$

Divergence theorem: The divergence theorem states that the volume integral of the divergence of the vector field over a volume V equals the flux of the vector field

through the boundary enclosing the volume ∂V :

$$\int_V \nabla \cdot \mathbf{F} = \int_{\partial V} \mathbf{F} \cdot \mathbf{n} dS. \quad (\text{A.12})$$

When the divergence theorem is applied to the product of a scalar f and a constant vector, the following theorem can be obtained for the scalar

$$\int_V \nabla f dV = \int_{\partial V} f dS. \quad (\text{A.13})$$

Appendix B: MAGNETO-HYDRAULIC ACTUATOR FOR ACTIVE ENGINE MOUNTS: DESIGN AND COMPARISON WITH A COMMERCIAL MOUNT ACTUATOR

B.1 Introduction to Active Engine Mounts

A typical engine mount has two main purposes. First, to isolate the high frequency engine vibrations from the chassis and second to prevent engine bounce from low frequency, high amplitude road excitations. The two functions are contradictory since the first requires the mount to be compliant and the second requires the mount to be stiff. This suggests that an ideal engine mount would have frequency and amplitude dependent stiffness characteristics.

Despite advances in passive mount design (see, e.g., Yu et al. [87] and Jazar et al. [44]), the trend of increased engine power combined with lighter vehicle frames poses vibration isolation problems which passive mounts alone cannot adequately address. Hence, significant emphasis is now placed on investigating designs and methods to develop effective active mounts.

This work presents the development of a compact bidirectional magnetostrictive actuator for active engine mounts and shows how it compares with a commercial mount actuator in terms of performance.

B.2 Actuator Design

B.2.1 Estimation of actuator requirements

Figure B.1 shows a schematic of the lumped parameter model used to determine the actuator requirements. In this model, the transfer function actuator displacement over engine displacement is given by

$$\frac{X_d}{X}(s) = \left[\left(1 + \frac{K_r}{K_b} \right) \frac{A_e}{A_d} + \frac{K_r A_t^2}{A_e A_d (ms^2 + cs + K_e)} \right], \quad (\text{B.1})$$

and the transfer function actuator force over engine displacement is

$$\frac{F}{X}(s) = \left(\frac{A_d}{A_e} \right) K_r, \quad (\text{B.2})$$

which is obtained by equating the net transmitted force on the base to zero.

The input to the transfer functions is the engine displacement which is selected as 0.5 mm at the idling frequency (20 Hz), decaying linearly to 0.1 mm at 100 Hz and then decreasing linearly to 0.05 mm at 1000 Hz based on which the requirement of the actuator is calculated from (B.1) as 1.6 mm at 20 Hz, 0.35 mm at 100 Hz, and 0.175 mm at 1000 Hz.

The stroke of the proposed actuator is decided by the dimensional constraints on the Terfenol-D rod. In this case a Terfenol-D rod of diameter 0.5 in (12.7 mm) and length 2 in (50.8 mm) is chosen. Thus, the expected blocked force of the rod is 4560 N (assuming $E = 30$ GPa) and the unloaded stroke is 60 μm (assuming $\lambda = 1200$ ppm).

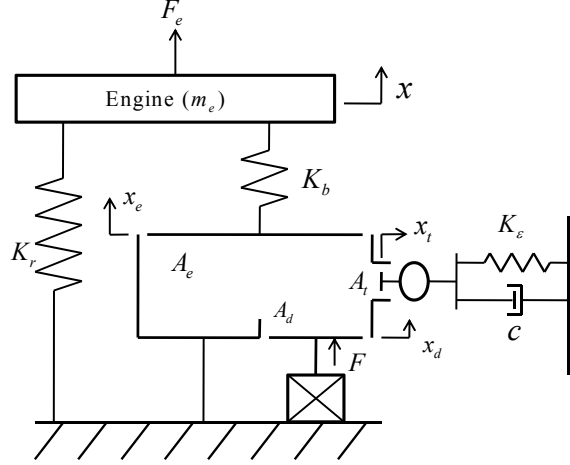


Figure B.1: Schematic of the active mount model (Lee et. al. [57]).

B.2.2 Actuator gain

The calculation of kinematic gain for an induced-strain actuator must incorporate loading effects since the maximum strain is obtained when the load is zero and the maximum load is supported when the displacement is zero. The stroke of a displacement amplified induced-strain actuator is derived by Giurgiutiu et al. [38] as

$$\frac{u_e}{u_{ref}} = \frac{G}{1 + rG^2}, \quad (\text{B.3})$$

where G is the kinematic gain, r is the ratio of load stiffness to the smart material rod stiffness, and u_{ref} is the unloaded displacement of the smart material driver. For a given r , the value of G which maximizes the stroke can be obtained by differentiating (B.3) with respect to G and equating to zero. This gives the optimal gain G_{opt} as

$$G_{opt} = 1/\sqrt{r}. \quad (\text{B.4})$$

The effective stiffness of the load on the driver is obtained by dividing (B.2) by (B.1). To calculate G_{opt} , the value of r at idling frequency is selected because the engine

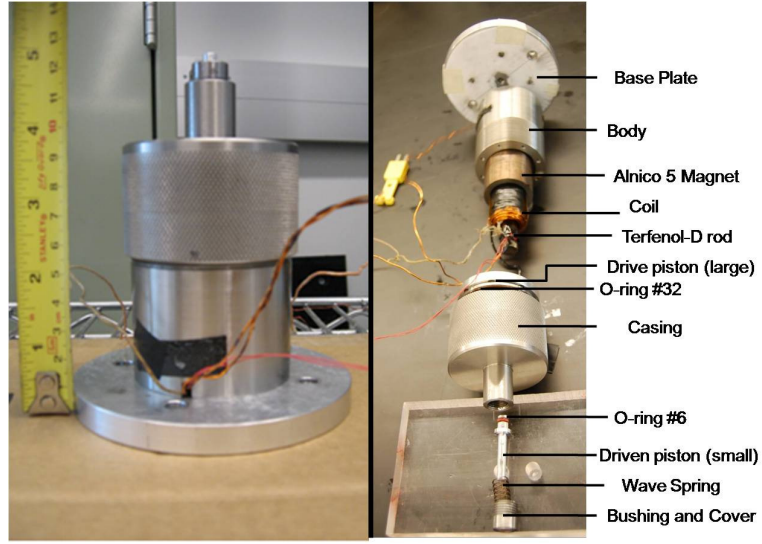


Figure B.2: Assembled and exploded view of the magneto-hydraulic actuator.

vibration amplitude is maximum at idling conditions and hence the gain must be such that the actuator performs at its optimum when the engine is idling. The optimal gain G_{opt} is calculated to be 69.

B.2.3 Magnetic circuit and preload

The magnetic circuit consists of three cylindrical Alnico permanent magnets of ID 1.125 in (28.575 mm) and OD 1.5 in (38.1 mm), an AWG 20 wire coil for generating the dynamic field, iron pieces for flux return and a Terfenol-D rod. The coil has an ID of 0.6 in (15.24 mm) and an OD of 1 in (25.4 mm). Alnico magnets are selected because they provide an optimum level of bias field (≈ 40 kA/m) on the Terfenol-D rod in order to achieve symmetric bidirectional motion. Figure B.2 shows the physical actuator and a cutout showing the various components. The mechanical preload on

Table B.1: List of Terfenol-D actuator components.

Component	Specification
Length of Terfenol-D rod	2 in (50.8 mm)
Diameter of Terfenol-D rod	0.5 in (12.7 mm)
Alnico magnet (ID \times OD \times L)	(1.125 in (28.58 mm) \times 1.5 in (38.1 mm) \times 2.25 in (57.15 mm))
Mass of larger Piston	74.67 g
Mass of smaller Piston	2.30 g
Volume of fluid(DTE 25)	1.30 c.c
Wave spring stiffness	3.5×10^3 N/m
Finger disc spring Stiffness	2.25×10^5 N/m

the Terfenol-D rod is created by a wave spring situated above the driven piston and by a disc spring located between the magnetic circuit and drive piston. The force produced by the wave spring on the rod is magnified by the fluid. One advantage of this configuration is that the fluid remains in compression during operation, thus reducing the chances of cavitation. The wave spring should be able to produce the desired force in order to generate the preload, yet it must be as compliant as possible to produce little force variation over a large range of deformation ($\approx \pm 1$ mm) so that little energy from the Terfenol-D is used in compressing the spring. The fluid is sealed by two o-rings (#6 on the smaller piston and #32 for the larger piston). Table B.1 lists the specifications for different actuator components.

B.3 Benchmarking Against a Commercial Electrodynamic Mount Actuator

The Terfenol-D magnetohydraulic actuator (MHA) is benchmarked against a commercial electrodynamic mount actuator (CMA) in the frequency domain. Figure B.3

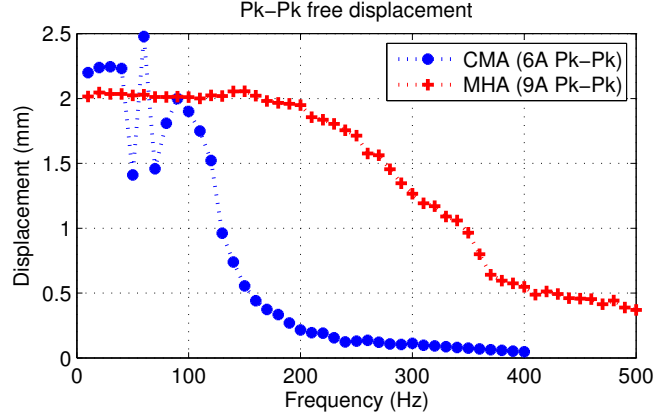


Figure B.3: Displacement in mechanically-free condition with both devices driven at full power.

shows the pk-pk unloaded displacement for both devices, obtained by running histogram tests at discrete frequencies from 10 Hz to 500 Hz and measuring the actuator output with a laser displacement sensor. The response at full power shows that the MHA has a 3-dB cutoff of 280 Hz compared with a 110 Hz cutoff for the CMA. The gain-bandwidth products are 575 mm Hz and 274 mm Hz, respectively.

Figures B.4(a) and B.4(b) show the first three harmonics for each of the two free displacement responses. The MHA exhibits a flat response over the frequency band, with a strong first-order harmonic and almost nonexistent second and third harmonics. This linear response is advantageous for control purposes. Conversely, the CMA exhibits significant distortion due to second and third harmonics. Similar measurements were also performed under mechanically blocked condition [13]

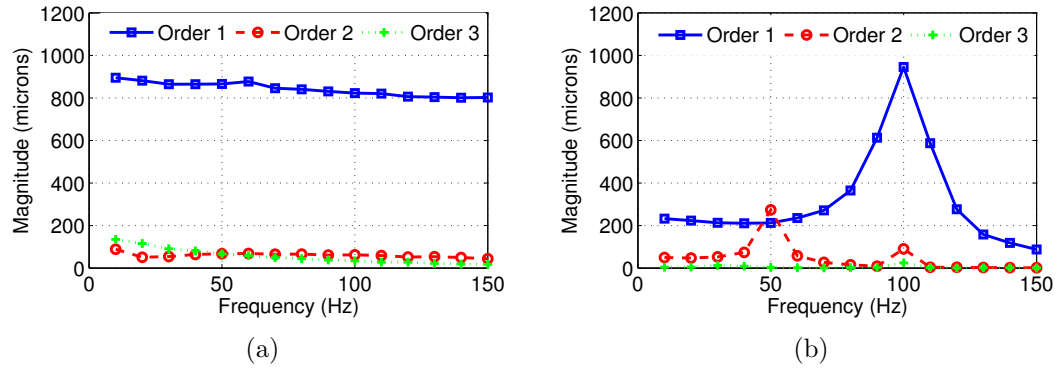


Figure B.4: Free displacement orders of (a) MHA and (b) CMA.

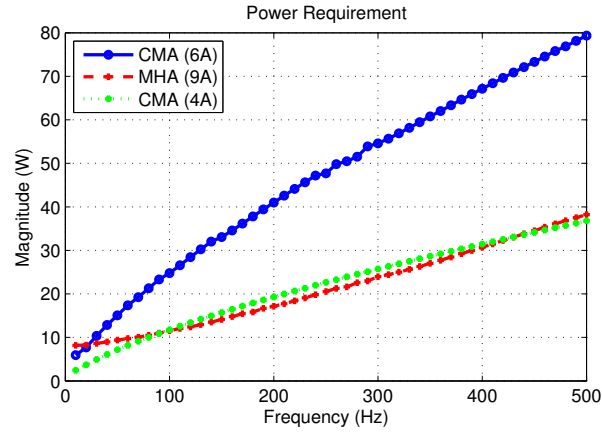
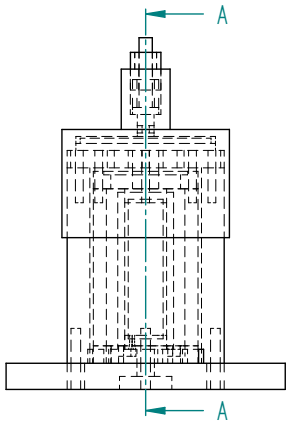
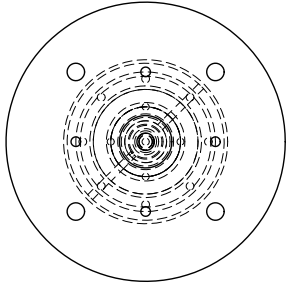


Figure B.5: Power consumption of the MHA and CMA.

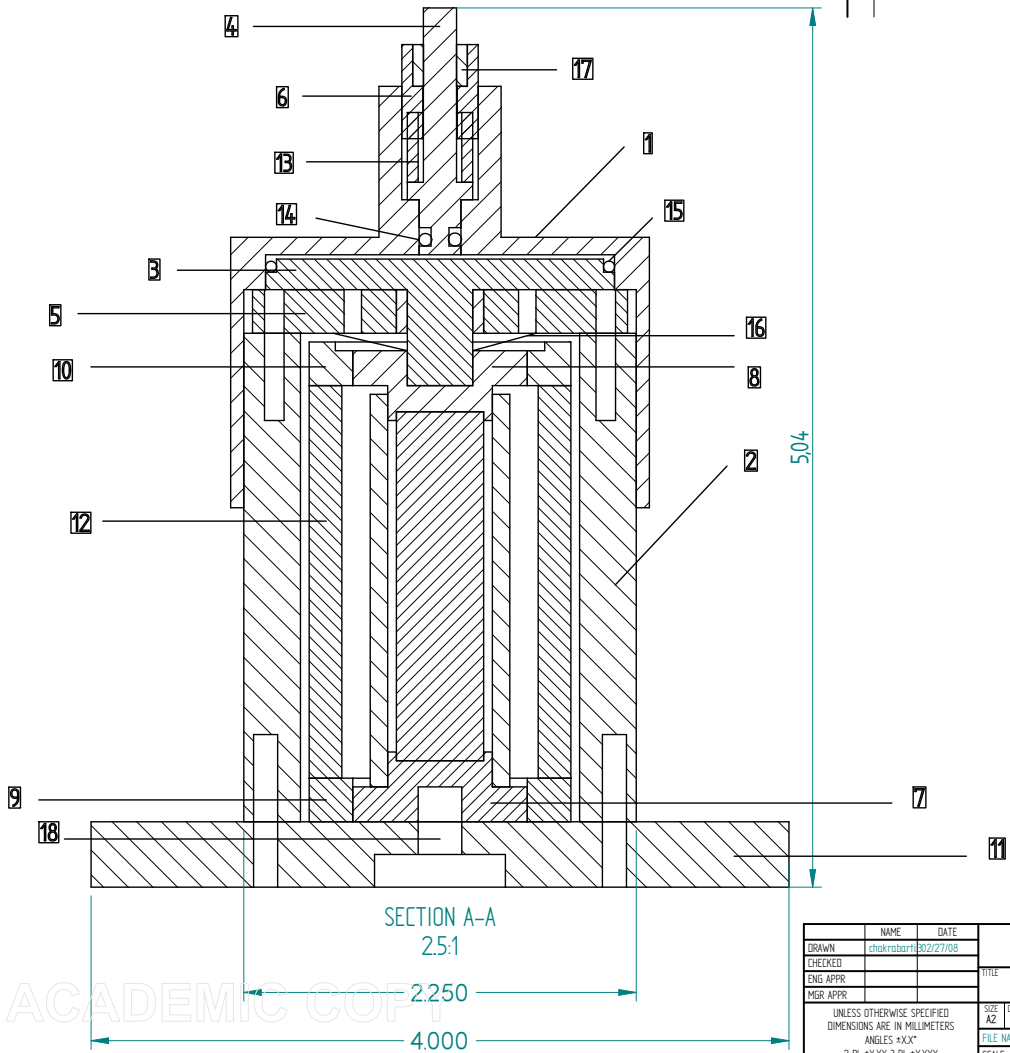
B.3.1 Electrical power requirement

Figure. B.5 compares the electrical power consumption of the two devices in the blocked condition. The MHA inductance is significantly lower leading to lower power consumption even when it is driven at higher current.

Appendix C: MAGNETO-HYDRAULIC ACTUATOR DRAWINGS



All Dimensions are in Inches



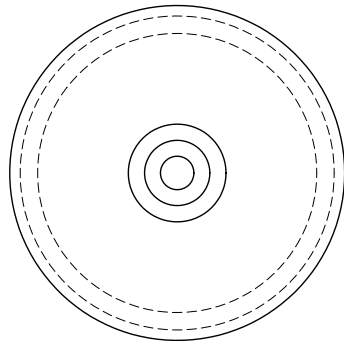
REVISION HISTORY			
REV	DESCRIPTION	DATE	APPROVED

NAME		DATE	SOLID EDGE UGS - The PLM Company	
DRAWN	chikraborti	8/22/2008		
CHECKED			TITLE	
ENG. APPR.			FILE NAME: ActuatorAssembly2.rvt	
MGR. APPR.			SCALE WEIGHT SHEET 1 OF 1	
UNLESS OTHERWISE SPECIFIED DIMENSIONS ARE IN MILLIMETERS ANGLES *XX*			SIZE A2	DWG NO.
2 PL *XXX 3 PL *XXXX				REV

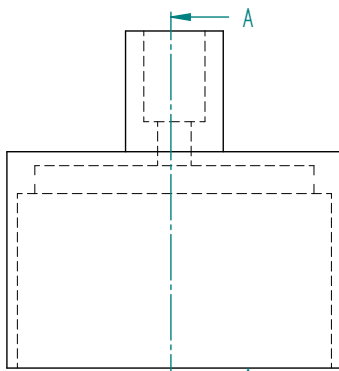
1

All Dimensions in Inches
Material: Stainless Steel

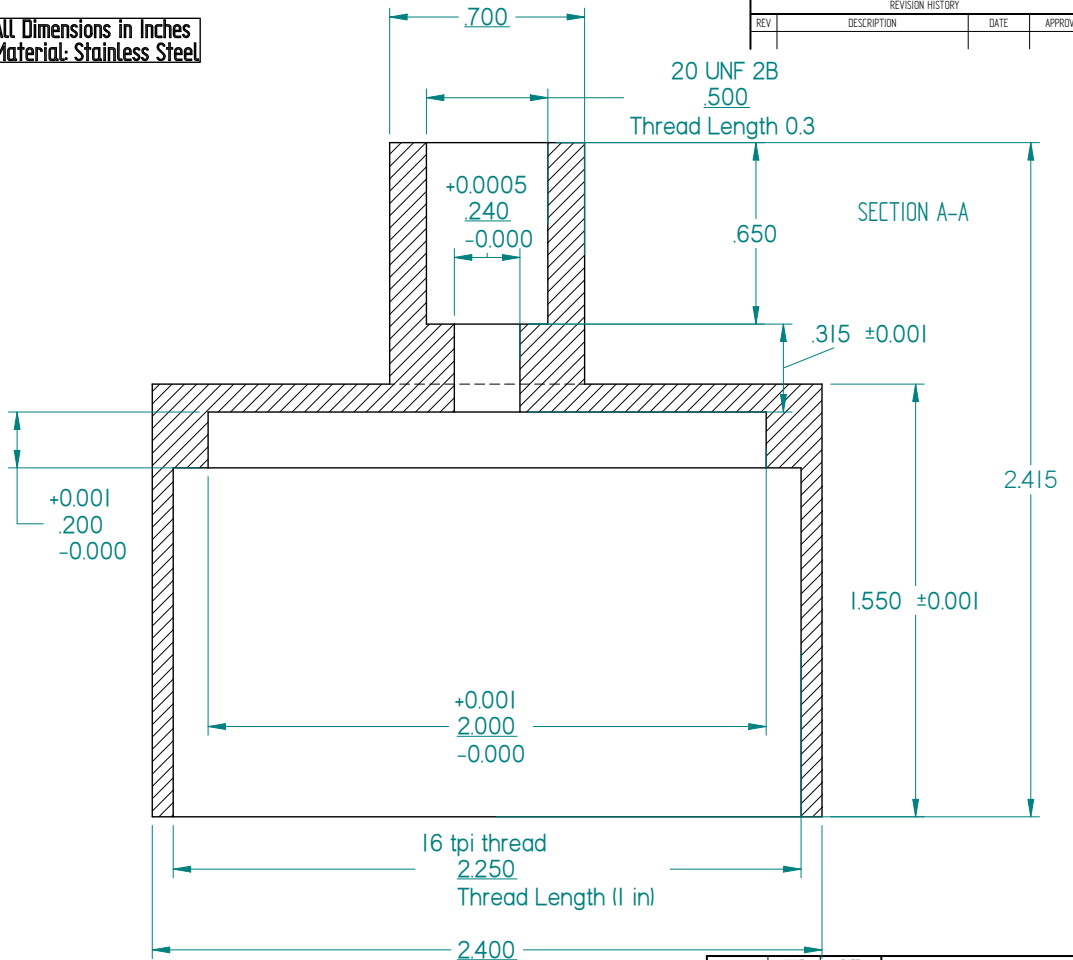
REVISION HISTORY			
REV	DESCRIPTION	DATE	APPROVED



2.1



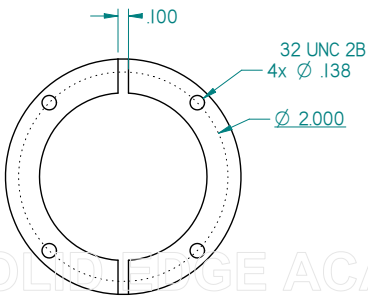
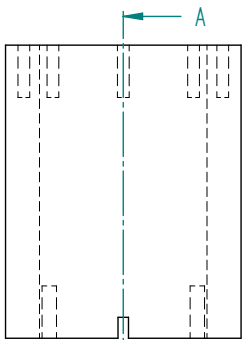
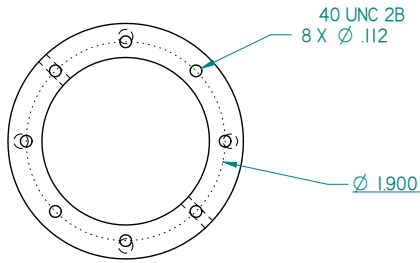
2.1



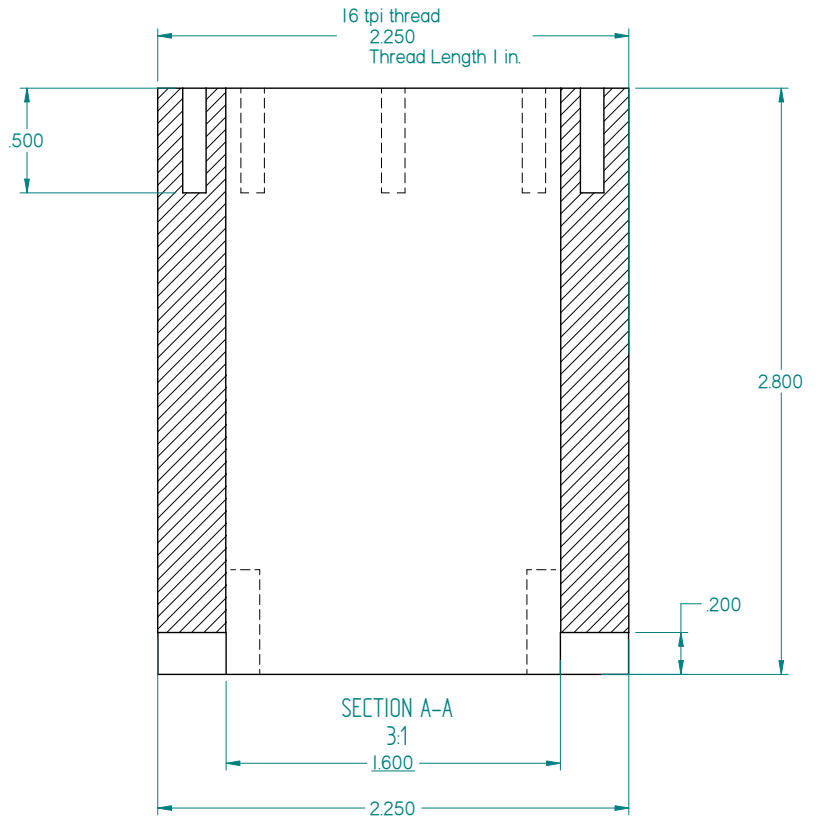
All tolerances 0.01 in. unless otherwise mentioned

NAME		DATE	SOLID EDGE UGS - The PLM Company	
DRAWN	chikraborti	02/14/08		
CHECKED			TITLE	
ENG. APPR.			SIZE	
MGR. APPR.			DWG NO.	
UNLESS OTHERWISE SPECIFIED DIMENSIONS ARE IN MILLIMETERS ANGLES "XX"			REV	
			FILE NAME: Casinoff	
2 PL ±XXXX 3 PL ±XXXX			SCALE	WEIGHT
			SHEET 1 OF 1	

2



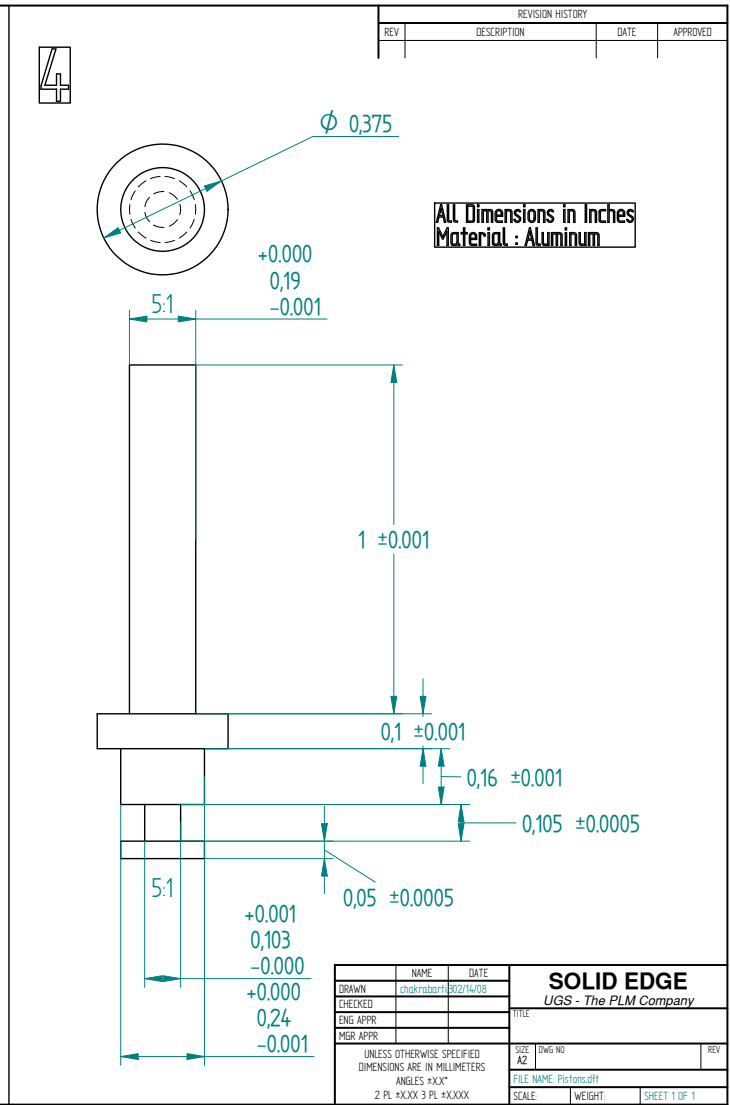
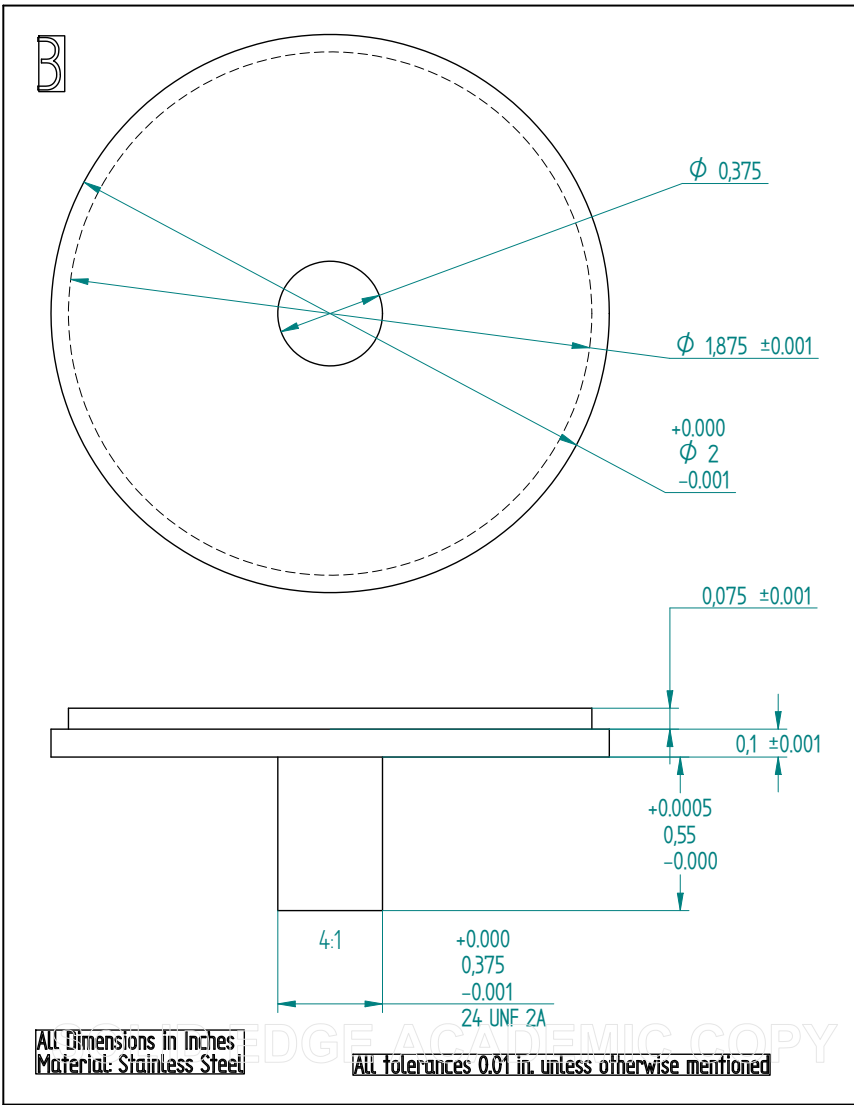
All Dimensions in Inches
Material: Stainless Steel

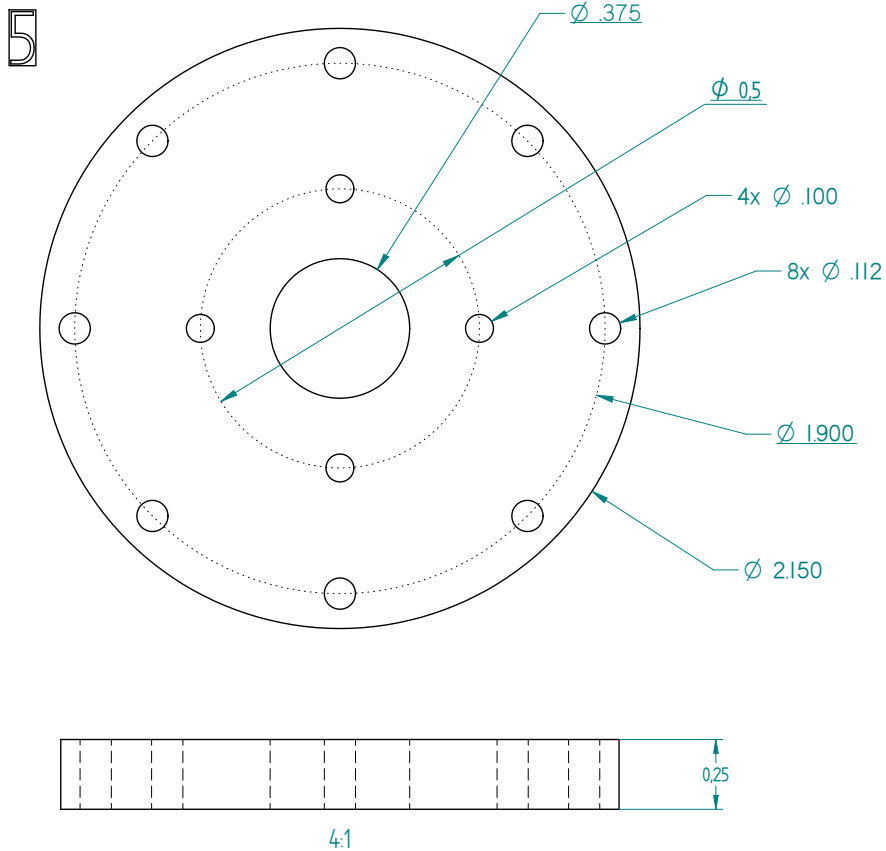


All tolerances 0.01 unless otherwise mentioned

REVISION HISTORY			
REV	DESCRIPTION	DATE	APPROVED

NAME		DATE	SOLID EDGE UGS - The PLM Company	
DRAWN	chikraborty	02/14/08		
CHECKED			TITLE	
ENG APPR			SIZE	
MGR APPR			DWG NO	
UNLESS OTHERWISE SPECIFIED DIMENSIONS ARE IN MILLIMETERS ANGLES *XX*			REV	
			FILE NAME: body.dft	
2 PL *XXXX 3 PL *XXXX			SCALE	WEIGHT
			SHEET 1 OF 1	



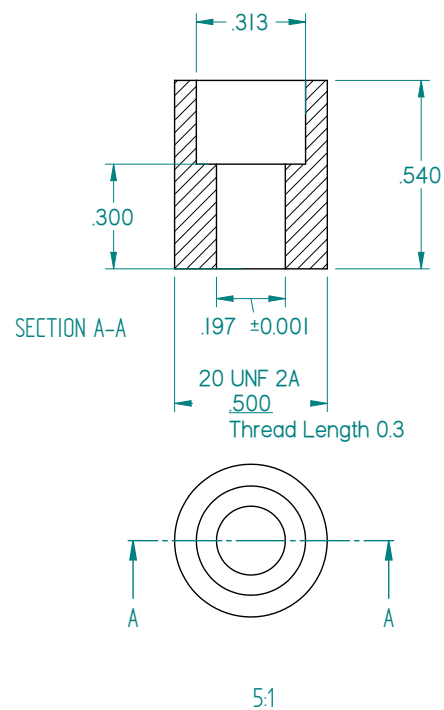


All Dimensions in Inches

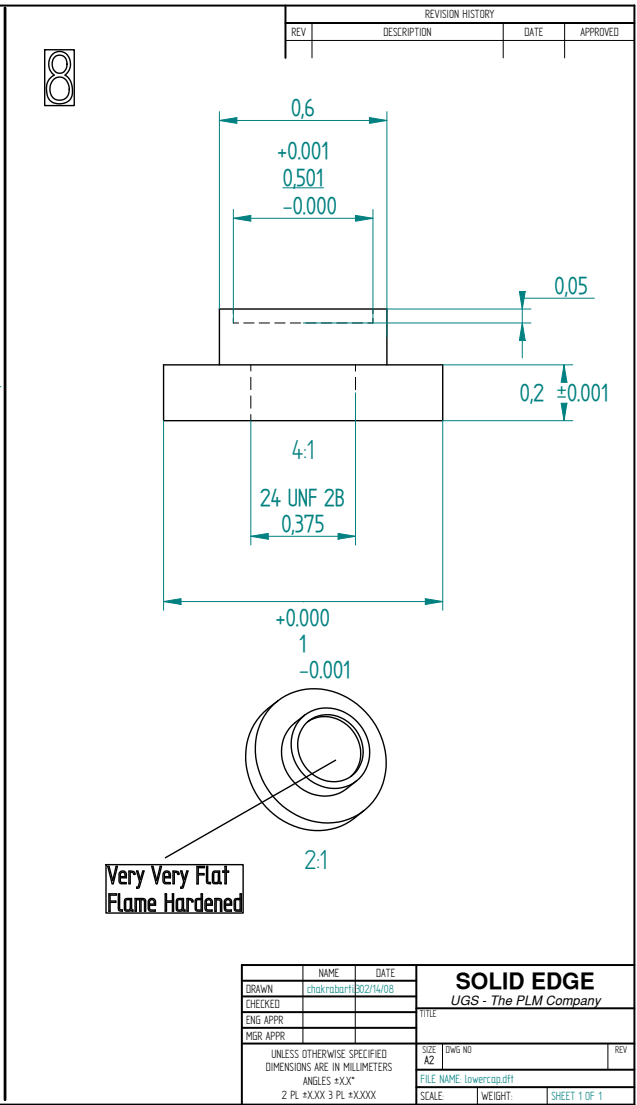
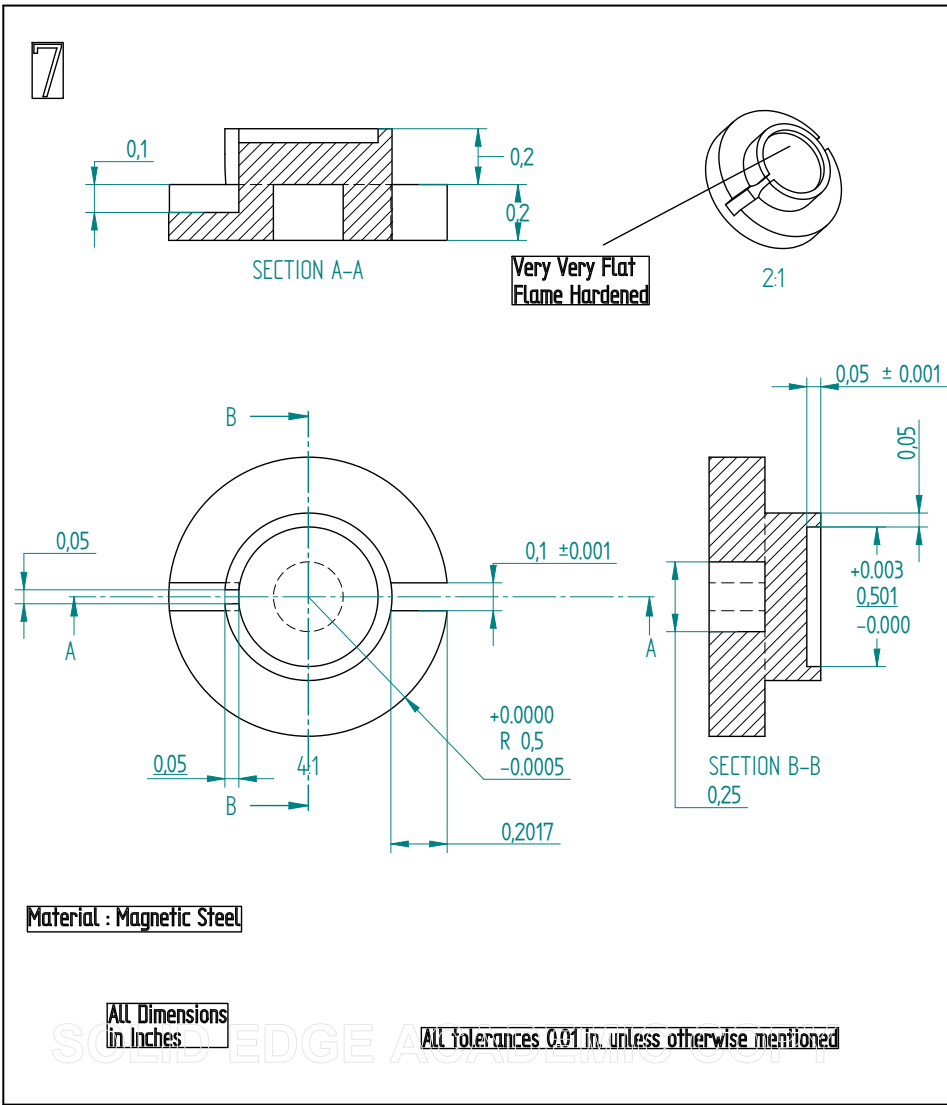
All tolerances 0.01 unless otherwise mentioned

SOLID EDGE ACADEMIC COPY

REVISION HISTORY			
REV	DESCRIPTION	DATE	APPROVED

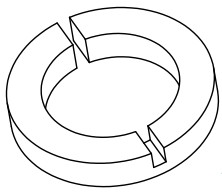


	NAME	DATE	SOLID EDGE <i>UGS - The PLM Company</i>		
DRAWN	chakrabarti	30/12/04/08			
CHECKED					
ENG APPR					
MGR APPR			TITLE		
UNLESS OTHERWISE SPECIFIED DIMENSIONS ARE IN MILLIMETERS ANGLES = °X'X" 2 PL = XXXX X PL = XXXXX			SIZE A2	DWG NO	REV
			FILE NAME: PreloadPlate-TopCover.dft SCALE W/FIGHT SHEET 1 OF 1		

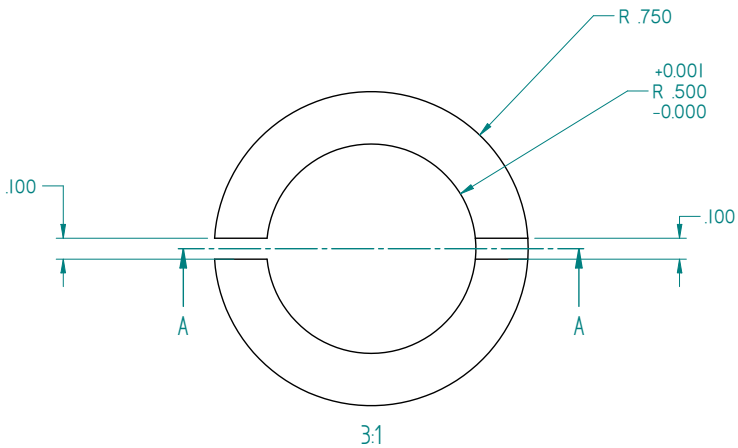


REVISION HISTORY			
REV	DESCRIPTION	DATE	APPROVED
1			

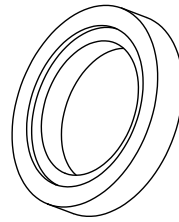
NAME	DATE	SOLID EDGE UGS - The PLM Company	
DRAWN: chikraborti	8/27/08		
CHECKED:		TITLE	
ENG. APPR:		SIZE: A2	DWG NO.
MGR. APPR:		FILE NAME: lowercad.dft	REV
UNLESS OTHERWISE SPECIFIED DIMENSIONS ARE IN MILLIMETERS ANGLES °XX' 2 PL ±XXX 3 PL ±XXXX		SCALE	WEIGHT
		SHEET 1 OF 1	



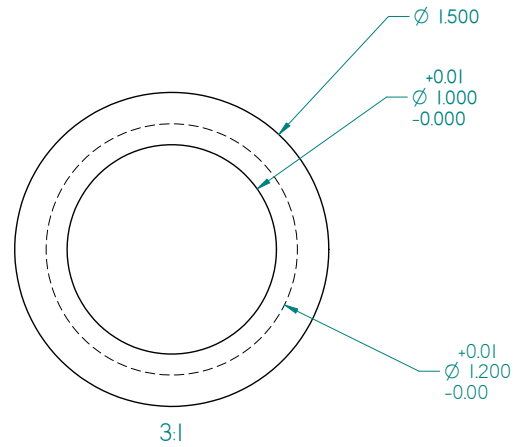
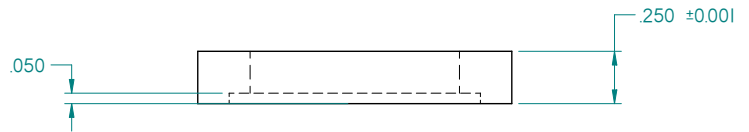
9



All Tolerances 0.01 in unless otherwise mentioned
Material : Magnetic Steel
All Dimensions in Inches



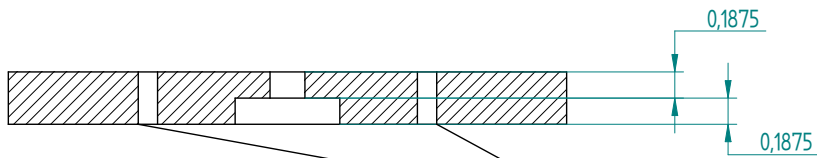
10



REVISION HISTORY			
REV	DESCRIPTION	DATE	APPROVED

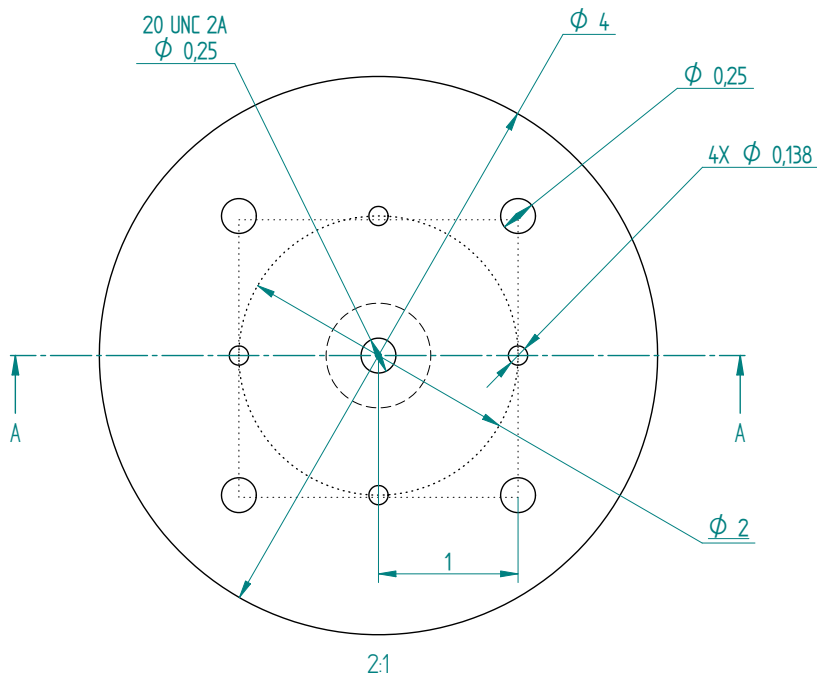
DRAWN	NAME	DATE	SOLID EDGE UGS - The PLM Company	
CHECKED	chakraharthi	8/3/03/08		
ENG APPR			TITLE	
MGR APPR				
UNLESS OTHERWISE SPECIFIED DIMENSIONS ARE IN MILLIMETERS ANGLES °XX'			SIZE	DWG NO
2 PL ±XXX 3 PL ±XXXX			A2	
			FILE NAME	upperandlowering.dft
			SCALE	WEIGHT
			SHEET 1 OF 1	

11



SECTION A-A

Enlarge Holes for socket head bolts to sit flush on the surface



ALL Dimensions in Inches
Material: Aluminum

ALL Tolerances 0.01 unless otherwise mentioned

REVISION HISTORY			
REV	DESCRIPTION	DATE	APPROVED

NAME		DATE	SOLID EDGE UGS - The PLM Company	
DRAWN	chikraborti	8/2/14/08		
CHECKED			TITLE	
ENG APPR				
MGR APPR				
UNLESS OTHERWISE SPECIFIED DIMENSIONS ARE IN MILLIMETERS ANGLES *XX* 2 PL *XXX 3 PL *XXXX			SIZE	DWG NO
			A2	
			FILE NAME: Baseplate.dft	
			SCALE	WEIGHT
			SHEET 1 OF 1	

Appendix D: DYNAMIC MODEL FOR A DISPLACEMENT AMPLIFIED MAGNETOSTRICTIVE DRIVER FOR ACTIVE MOUNTS

This work discusses the development of a lumped parameter 1D model for the Terfenol-D mount actuator. The primary use of the proposed model is device design and control. A 1D magnetic field diffusion equation is used to describe the spatial variation of magnetic field in the Terfenol-D sample due to eddy currents. The Jiles-Atherton model is used to describe the 1D magnetization response of Terfenol-D to magnetic fields. Magnetostriction, which is modeled as a single-valued function of magnetization, provides an input to the lumped parameter model describing the mechanical system vibrations. Friction at the elastomeric seals is described with the LuGre dynamic friction model. Structural dynamics of the support has also been considered to increase the model accuracy.

D.1 Model Structure

Figure D.1 shows the basic structure of the model. The radial dependence of magnetic field inside the magnetostrictive rod is established by solving the magnetic field diffusion equation. The magnetostrictive material response to this radially varying magnetic field is computed using the Jiles-Atherton constitutive model and coupled

to a mechanical system model. The mechanical system consists of a hydraulic amplification mechanism with compliances and frictional losses at the seals which makes the system nonlinear. Hence, the entire model is solved numerically in the time domain and the Fourier components of the final periodic waveform obtained is analyzed.

D.2 Magnetic Field Diffusion

The magnetic field diffusion equation for quasi-stationary operating conditions can be obtained by using the curl operator on Faraday's law:

$$\begin{aligned}
 \nabla \times \nabla \times \mathbf{H} &= \nabla \times \mathbf{J} \\
 &= \nabla \times (\sigma \mathbf{E}) \\
 &= -\sigma \left(\frac{\partial \mathbf{B}}{\partial t} \right) \\
 &= -\sigma \mu \left(\frac{\partial \mathbf{H}}{\partial t} \right).
 \end{aligned} \tag{D.1}$$

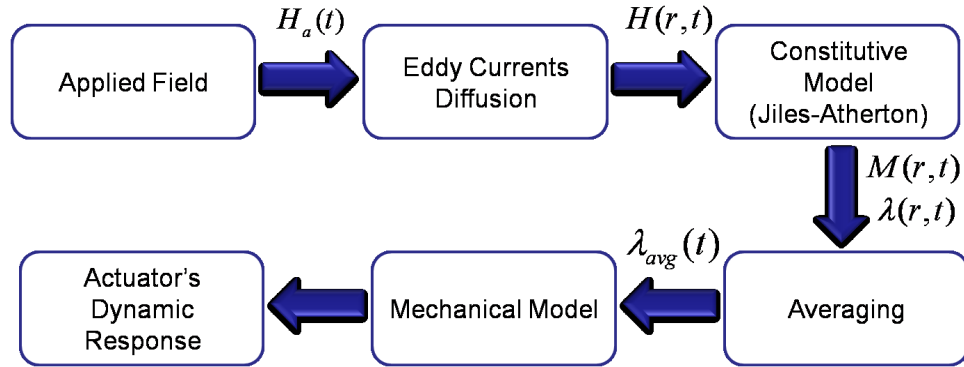


Figure D.1: Flowchart for the actuator model.

where μ is the constant magnetic permeability of the material. The left hand side of (D.1) can be simplified to give

$$\begin{aligned}\nabla \times \nabla \times \mathbf{H} &= \nabla (\nabla \cdot \mathbf{H}) - \nabla^2 \mathbf{H} \\ &= \nabla \left(\nabla \cdot \mathbf{B} \frac{1}{\mu} \right) - \nabla^2 \mathbf{H} \\ &= -\nabla^2 \mathbf{H} \quad (\because \nabla \cdot \mathbf{B} = 0).\end{aligned}\tag{D.2}$$

For cylindrical geometries the diffusion equation takes the form

$$\frac{\partial^2 H}{\partial r^2} + \frac{1}{r} \frac{\partial H}{\partial r} = \sigma \mu \frac{\partial H}{\partial t}.\tag{D.3}$$

The boundary condition at the surface of the rod for a harmonically applied field is $H(R, t) = H_0 e^{i\omega t}$. The solution to be of the form $H_0 \tilde{h}(r) e^{i\omega t}$ where $\tilde{h}(r)$ is a complex function of the radius r . Equation (D.3) then reduces to

$$\frac{\partial^2 \tilde{h}}{\partial r^2} + \frac{1}{r} \frac{\partial \tilde{h}}{\partial r} - i\sigma\mu\omega \tilde{h} = 0.\tag{D.4}$$

Assuming μ to be constant over the range of applied fields, the solution to (D.4) can be written as done in [56],

$$\tilde{h}(r) = \frac{I_0(q(r))}{I_0(q(R))},\tag{D.5}$$

where I_0 is the modified Bessel function of order zero, $q(r) = (\sqrt{i\sigma\mu\omega}) r$ and R is the radius of the magnetostrictive rod.

D.3 Jiles-Atherton Equations

The Jiles-Atherton model is used to describe the magnetization state of the material as a function of the applied field. The total magnetization is written as a combination of an anhysteretic and an irreversible component,

$$M = cM_{an} + (1 - c)M_{irr}.\tag{D.6}$$

c is a reversibility parameter which accounts for reversible bowing of domain walls. When $c = 1$ domain wall motion is completely reversible and when $c = 0$, domain wall motion is completely irreversible. The anhysteretic magnetization is given by the Langevin function as

$$M_{an} = M_s \left(\coth \left(\frac{H_e}{a} \right) - \left(\frac{a}{H_e} \right) \right), \quad (\text{D.7})$$

where a is a shape parameter for M_{an} which controls the slope of the anhysteretic magnetization curve, M_s is the saturation magnetization of the material and H_e is an effective field given by [28]

$$H_e = H + \underbrace{\left(\alpha + \frac{9}{2} \frac{\sigma_{bias} \lambda_s}{\mu_0 M_s^2} \right)}_{\tilde{\alpha}} M. \quad (\text{D.8})$$

σ_{bias} is the applied bias stress on the rod and α is a parameter which quantifies magnetic domain interactions.

The derivative of the irreversible magnetization with respect to the effective field is

$$\frac{dM_{irr}}{dH_e} = \frac{M_{an} - M_{irr}}{\delta k}, \quad (\text{D.9})$$

With some mathematical manipulation [14] the final differential equation for the total magnetization in terms of magnetic field can be obtained as

$$\frac{dM}{dH}(r) = \left(\frac{\Phi_{(M(r))}}{1 - \tilde{\alpha} \Phi_{(M(r))}} \right). \quad (\text{D.10})$$

where

$$\Phi_{(M(r))} = \left[c \frac{dM_{an}}{dH_e}(r) + \frac{M_{an}(r) - M(r)}{\delta(r)k} \right]. \quad (\text{D.11})$$

Magnetostriction (λ) is modeled as a single valued function of magnetization through the relation

$$\lambda(r) = \frac{3}{2} \frac{\lambda_s}{M_s^2} M(r)^2. \quad (\text{D.12})$$

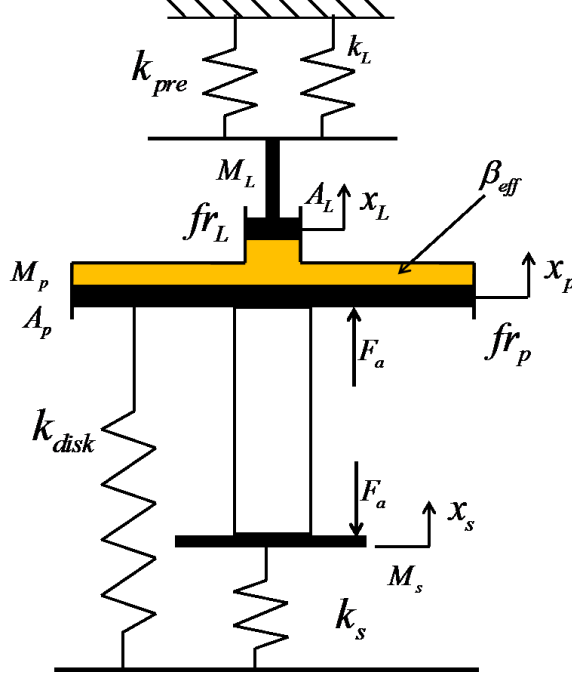


Figure D.2: Schematic representation of the actuator's mechanical model.

Since the mechanical model is lumped, magnetostriction is averaged over the cross-section of the rod to yield an average magnetostriction λ_{avg}

D.4 Mechanical Model

Figure D.2 shows the schematic of the mechanical system model. The pressure differential in the fluid can be written as

$$\Delta p = \beta_{eff} (A_p x_p - A_L x_L), \quad (\text{D.13})$$

where β_{eff} is an effective modulus which quantifies the compliance of the fluid and fluid chamber components [15]. The total strain in the rod is a superposition of the average magnetostriction and the strain induced by compressive stress (σ_c),

$$\epsilon = \lambda_{avg} - \frac{\sigma_c}{E} = \frac{x_p - x_s}{l_a}. \quad (\text{D.14})$$

The force produced by the rod is given by the stress on the rod multiplied by its cross-sectional area A_r ,

$$F_a = \sigma_c A_r = E A_r \lambda_{avg} - \frac{E A_r}{l_a} (x_p - x_s). \quad (\text{D.15})$$

The equations of motion for the two pistons and the support structure are

$$M_p \ddot{x}_p + (k_{disk}) x_p + f r_p = -\Delta p A_p - \sigma_c A_r, \quad (\text{D.16})$$

$$M_L \ddot{x}_L + (k_L + k_{pre}) x_L + f r_L = \Delta p A_L, \quad (\text{D.17})$$

$$M_s \ddot{x}_s + k_s x_s = -F_a, \quad (\text{D.18})$$

where k_L and k_{pre} are the stiffness of the load and preload springs attached to the driven piston, and k_{disk} is the stiffness of the disk spring attached to the Terfenol-D rod. Variables $f r_L$ and $f r_p$ respectively denote the friction forces at the small and large piston which are described by the LuGre friction model [64].

D.5 Model Results

The actuator was run at discrete frequencies from 10 Hz to 500 Hz with a mechanical pre-stress of ≈ 1 ksi on the rod generated by the preload spring in contact with the driven piston. The preload spring also acts as the load spring since no external loading spring is attached to the pushrod. The Terfenol-D rod is magnetically biased by an Alnico magnet with a field of ≈ 27 KA/m. The actuator is driven with a 4.5 A sinusoidal current with no d.c bias. The strain on the surface of the Terfenol-D rod is measured with a strain gage and the displacement of the pushrod is measured with a laser displacement sensor.

Figure D.3 shows the experimental and simulated time domain responses of the pushrod displacement at varied actuation frequencies. The model is able to describe

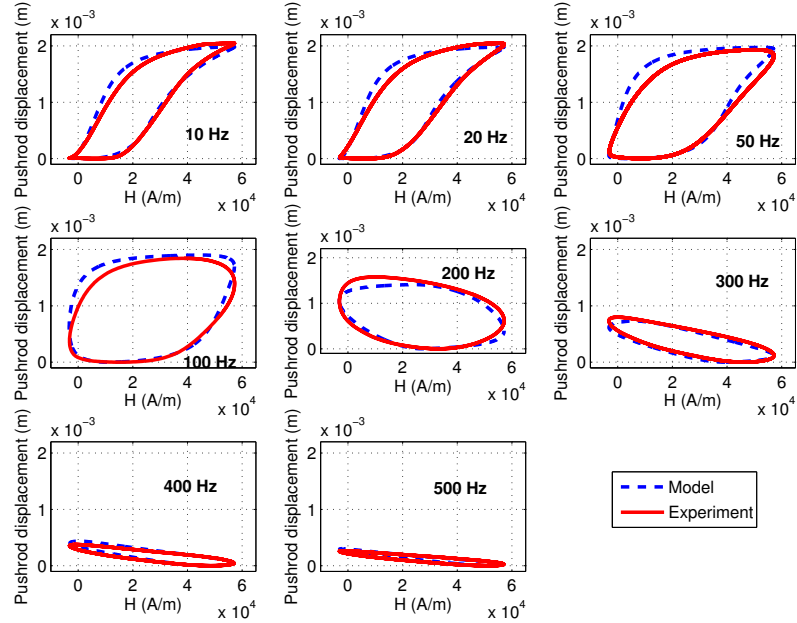


Figure D.3: Output pushrod displacement at different actuation frequencies.

the initial hysteresis and the nonlinear shape of the response both in terms of amplitude and phase.

A Fourier analysis on the experimental and modeled responses yielded the spectral content of the waveforms at different frequencies. Figure D.4 shows that the model accurately describes trends in the higher order components of the Terfenol-D strain and pushrod displacement.

Figure D.5 shows the magnitude and phase of the first order component of the pushrod displacement. Strong correlation is obtained in both magnitude and phase.

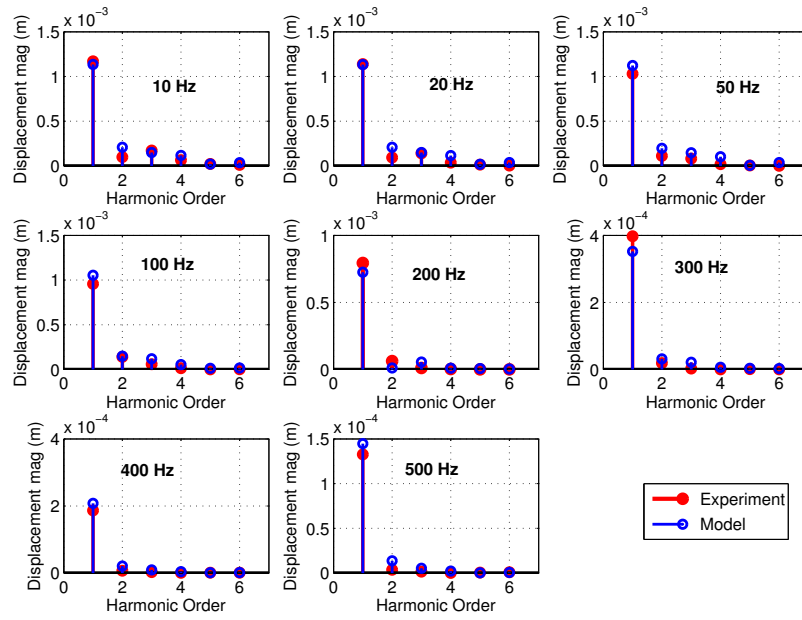


Figure D.4: Output pushrod displacement orders.

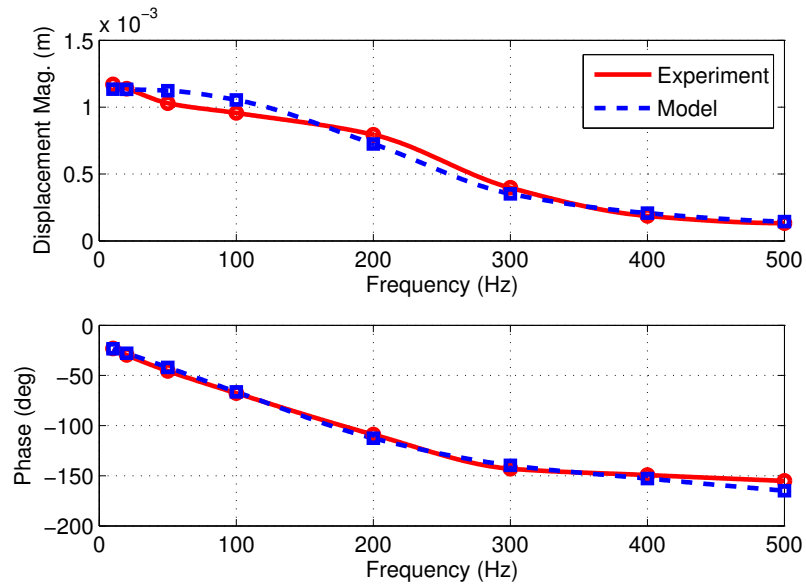


Figure D.5: Output pushrod displacement magnitude and phase (first order).

Bibliography

- [1] M. Al-Jiboory, D.G. Lord, Y.J. Bi, J.S. Abell, A.M.H. Hwang, and J.P. Teter. Magnetic domains and microstructural defects in Terfenol-D. *Journal of Applied Physics*, 73(10):6168–6170, 1993.
- [2] W. D. Armstrong. An incremental theory of magneto-elastic hysteresis in pseudo-cubic ferro-magnetostrictive alloys. *Journal of Magnetism and Magnetic Materials*, 263:208, 2003.
- [3] W.D. Armstrong. Magnetization and magnetostriction processes in $\text{tb}_{0.27} - 0.30\text{dy}_{0.73} - 0.70\text{fe}_{1.9} - 2.0$. *Journal of Applied Physics*, 81(5):2321–2326, 1997.
- [4] J. Atulasimha, G. Akhras, and A.B. Flatau. Comprehensive 3-d hysteretic magnetomechanical model and its validation with experimental $\langle 110 \rangle$ single-crystal iron-gallium behavior. *Journal of Applied Physics*, 103:07–336, 2008.
- [5] J. Atulasimha, A.B. Flatau, and R.A. Kellogg. Sensing behavior of varied stoichiometry single crystal fe-ga. *Journal of Intelligent Material Systems and Structures*, 17:97–105, 2006.
- [6] K.J. Bathe. *Finite Element Procedures*. Prentice Hall, Upper Saddle River, New Jersey 07458, 1996.
- [7] M.E.H. Benbouzid, R. Beguenane, G. Reyne, and G. Meunier. Finite element modeling of Terfenol-D magneto-mechanical coupling: application to a direct micro-stepping rotary motor. 1997.
- [8] M.E.H. Benbouzid, G. Reyne, G. Meunier, L. Kvarnsjo, and G. Engdahl. Dynamic modelling of giant magnetostriction in Terfenol-D rods by the finite element method. *Magnetics, IEEE Transactions on*, 31(3):1821–1824, 1995.
- [9] A.J. Bergqvist. A simple vector generalization of the jiles-atherton model of hysteresis. *IEEE Transactions on Magnetics*, 32(5):4213–4215, September 1996.
- [10] S.C. Busbridge, L.Q. Meng, G.H. Wu, B.W. Wang, Y.X. Li, S.X. Gao, C. Cai, and W.S. Zhan. Magnetomechanical properties of single crystal terfenol-d. *Magnetics, IEEE Transactions on*, 35(5):3823–3825, 1999.

- [11] F.T. Calkins, R.C. Smith, and A.B. Flatau. Energy-based hysteresis model for magnetostrictive transducers. *IEEE Transactions on Magnetics*, 36(2):429–439, 2000.
- [12] G.P. Carman and M. Mitrovic. Nonlinear constitutive relations for magnetostrictive materials with applications to 1-D problems. *Journal of Intelligent Material Systems and Structures*, 6(5):673, 1995.
- [13] S. Chakrabarti and M. J. Dapino. Hydraulically amplified terfenol-d actuator for adaptive powertrain mounts. *ASME Journal of Vibration and Accoustics*, accepted for publication.
- [14] S. Chakrabarti and M.J. Dapino. A dynamic model for a displacement amplified magnetostrictive driver for active mounts. *Smart Materials and Structures*, 19:055009, 2010.
- [15] S. Chakrabarti and M.J. Dapino. Design and modeling of a hydraulically amplified magnetostrictive actuator for automotive engine mounts. volume 7645, page 76450G. SPIE, 2010.
- [16] S. Chakrabarti and M.J. Dapino. Coupled axisymmetric finite element model of a magneto-hydraulic actuator for active engine mounts. volume 7979, page 79790C. SPIE, 2011.
- [17] Suryarghya Chakrabarti and Marcelo J Dapino. Nonlinear finite element model for 3D Galfenol systems. *Smart Materials and Structures*, 20(10):105034, 2011.
- [18] T.R. Chandrupatla and A.D. Belegundu. *Introduction to Finite Elements in Engineering*. Prentice-Hall, Upper Saddle River, New Jersey 07458, 3rd edition, 2002.
- [19] A. Clark, R. Abbundi, and W. Gillmor. Magnetization and magnetic anisotropy of tbfe₂, dyfe₂, tb_{0.27}dy_{0.73}fe₂ and tmfe₂. *Magnetics, IEEE Transactions on*, 14(5):542 – 544, sep 1978.
- [20] A. Clark and D. Crowder. High temperature magnetostriction of tbfe₂ and tb_{0.27}dy_{0.73}fe₂. *Magnetics, IEEE Transactions on*, 21(5):1945 – 1947, sep 1985.
- [21] A. Clark, J. Verhoven, O. McMasters, and E. Gibson. Magnetostriction in twinned [112] crystals of tb_{0.27}dy_{0.73}fe₂. *Magnetics, IEEE Transactions on*, 22(5):973–975, 1986.
- [22] A. E. Clark. Magnetic and magnetoelastic properties of highly magnetostrictive rare earth-iron laves phase compounds. *AIP Conference Proceedings*, 18(1):1015–1029, 1974.

- [23] A.E. Clark, K.B. Hathaway, M. Wun-Fogle, J. B. Restorff, T. A. Lograsso, J. M. Keppins, G. Petculescu, and R.A. Taylor. Extraordinary magnetoelasticity and lattice softening in bcc fe-ga alloys. *Journal of Applied Physics*, 93(10):8621–8624, 2003.
- [24] A.E. Clark, J.B. Restorff, M. Wun-Fogle, T.A. Lograsso, and D.L. Schlagel. Magnetostrictive properties of body-centered cubic fe-ga and fe-ga-al alloys. *IEEE Trans. Magn.*, 36(5):3238–3240, 2000.
- [25] A.E. Clark, J.P. Teter, and O.D. McMasters. Magnetostriction “jumps” in twinned Tb_{0.3}Dy_{0.7}Fe_{1.9}. *Journal of applied physics*, 63:3910–3912, 1988.
- [26] A.E. Clark, M. Wun-Fogle, J.B. Restorff, and T.A. Lograsso. Magnetostrictive properties of Galfenol alloys under compressive stress. *Material transactions*, 43(5):881–886, 2002.
- [27] M.J. Dapino, A.B. Flatau, and F.T. Calkins. Statistical analysis of Terfenol-D material properties. *Journal of intelligent material systems and structures*, 17(7):587, 2006.
- [28] M.J. Dapino, R.C. Smith, F.T. Calkins, and A.B. Flatau. A coupled magnetomechanical model for magnetostrictive transducers and its application to villari-effect sensors. *Journal of Intelligent Material Systems and Structures*, 13(11):737–748, 2002.
- [29] M.J. Dapino, R.C. Smith, L.A.E. Faidley, and A.B. Flatau. A coupled structural-magnetic strain and stress model for magnetostrictive transducers. *Journal of intelligent material systems and structures*, 11(2):135, 2000.
- [30] M.J. Dapino, R.C. Smith, and A.B. Flatau. Structural magnetic strain model for magnetostrictive transducers. *IEEE Transactions on Magnetism*, 36(3):545–556, May 2000.
- [31] G. Engdahl. *Handbook of Giant Magnetostrictive Materials*. Academic Press, New York, 1st edition, 2000.
- [32] P. G. Evans and M. J. Dapino. Efficient magnetic hysteresis model for field and stress application in magnetostrictive galfenol. *Journal of Applied Physics*, 107(6):063906, 2010.
- [33] P.G. Evans. *Nonlinear Magnetomechanical Modeling and Characterization of Galfenol and System-Level Modeling of Galfenol-Based Transducers*. PhD thesis, The Ohio State University, 2009.
- [34] P.G. Evans and M.J. Dapino. Stress-dependent susceptibility of Galfenol and application to force sensing. *Journal of Applied Physics*, 108(7):074517, 2010.

- [35] P.G. Evans and M.J. Dapino. Dynamic Model for 3-D Magnetostrictive Transducers. *Magnetics, IEEE Transactions on*, 47(1):221–230, 2011.
- [36] J. Garcia-Bonito, M.J. Brennan, S.J. Elliott, A. David, and R.J. Pinnington. A novel high-displacement piezoelectric actuator for active vibration control. *Smart Materials and Structures*, 7(1):31–42, 1998.
- [37] D.P. Ghosh and S. Gopalakrishnan. Coupled analysis of composite laminate with embedded magnetostrictive patches. *Smart Materials and Structures*, 14:1462, 2005.
- [38] V. Giurgiutiu, Z. Chaudhry, and C.A. Rogers. Stiffness issues in the design of isa displacement amplification devices. In *Proc. SPIE*, volume 2443, pages 105–119, 1995.
- [39] V. Giurgiutiu, C.A. Rogers, and R. Rusovici. Solid-State Actuation of Rotor Blade Servo-Flap for Active Vibration Control. *Journal of Intelligent Material Systems and Structures*, 7(2):192–202, 1996.
- [40] F.C. Graham, C. Mudivarathi, S. Datta, and A.B. Flatau. Modeling of a Galfenol transducer using the bidirectionally coupled magnetoelastic model. *Smart Materials and Structures*, 18:104013, 2009.
- [41] W. Huang, B. Wang, S. Cao, Y. Sun, L. Weng, and H. Chen. Dynamic strain model with eddy current effects for giant magnetostrictive transducer. *IEEE Transactions on Magnetics*, 43(4):1381–1384, April 2007.
- [42] Y.Y. Huang and Y.M. Jin. Phase field modeling of magnetization processes in growth twinned Terfenol-D crystals. *Applied Physics Letters*, 93:142504, 2008.
- [43] Etrema Products Inc. Terfenol-D data sheet.
- [44] G. Nakhaie Jazar and F. Golnaraghi. Engine mounts for automobile applications - a survey. *Shock and Vibration Digest*, 34:363–379, September 2002.
- [45] D.C. Jiles. The development of highly magnetostrictive rare earth-iron alloys. *Journal of Physics D: Applied Physics*, 27:1, 1994.
- [46] D.C. Jiles. Modeling the effects of eddy current losses on frequency dependent hysteresis loops in electrically conducting media. *IEEE Transactions on Magnetics*, 30(6):4326–4328, 1994.
- [47] D.C. Jiles. *Introduction to Magnetism and Magnetic Materials*. Chapman and Hall, London, UK, 1995.

- [48] D.C. Jiles. Theory of the magnetomechanical effect. *Journal of Applied Physics*, 28:1537–1546, 1995.
- [49] D.C. Jiles and D.L. Atherton. Theory of ferromagnetic hysteresis. *Journal of Magnetism and Magnetic Materials*, 61(1-2):48 – 60, 1986.
- [50] K.S. Kannan and A. Dasgupta. A nonlinear Galerkin finite-element theory for modeling magnetostrictive smart structures. *Smart Materials and Structures*, 6:341–350, 1997.
- [51] R. Kellogg and A. Flatau. Experimental Investigation of Terfenol-D’s Elastic Modulus. *Journal of Intelligent Material Systems and Structures*, 19(5):583, 2008.
- [52] R.A. Kellogg. *Development and modeling of iron-gallium alloys*. PhD thesis, Iowa State University, 2003.
- [53] R.A. Kellogg, A.B. Flatau, A.E. Clark, M. Wun-Fogle, and T.A. Lograsso. Quasi-static transduction characterization of Galfenol. *Journal of Intelligent Material Systems and Structures*, 16:471–479, 2005.
- [54] R.A. Kellogg, A.M. Russell, T.A. Lograsso, A.B. Flatau, A.E. Clark, and M. Wun-Fogle. Tensile properties of magnetostrictive iron-gallium alloys. *Acta Materialia*, 52:5043–5050, 2004.
- [55] J. Kim and E. Jung. Finite element analysis for acoustic characteristics of a magnetostrictive transducer. *Smart Materials and Structures*, 14:1273–1280, 2005.
- [56] H. E. Knoepfel. *Magnetic Fields: A Comprehensive Theoretical Treatise for Practical Use*. John Wiley and Sons, New York, NY, 2000.
- [57] Y.W. Lee and C.W. Lee. Dynamic analysis and control of an active engine mount system. In *Proc Instn Mech Engrs Part D: J Automobile Engineering*, volume 216, pages 921–931, 2002.
- [58] L. Li and DC Jiles. Modeling of the magnetomechanical effect: Application of the Rayleigh law to the stress domain. *Journal of Applied Physics*, 93:8480, 2003.
- [59] A. Mahadevan, PG Evans, and MJ Dapino. Dependence of magnetic susceptibility on stress in textured polycrystalline FeGa and FeGa Galfenol alloys. *Applied Physics Letters*, 96:012502, 2010.
- [60] A. Manbachi and R.S.C. Cobbold. Development and application of piezoelectric materials for ultrasound generation and detection. *Ultrasound*, 2011.

- [61] W. Mei, T. Okane, and T. Umeda. Magnetostriction of Tb–Dy–Fe crystals. *Journal of applied physics*, 84:6208, 1998.
- [62] M.B. Moffett, A.E. Clark, M. Wun-Fogle, J. Linberg, J.P. Teter, and E.A. McLaughlin. Characterization of Terfenol-D for magnetostrictive transducers. *The Journal of the Acoustical Society of America*, 89:1448, 1991.
- [63] C. Mudivartha, S. Datta, J. Atulasimha, and A.B. Flatau. A bidirectionally coupled magnetoelastic model and its validation using a galferol unimorph sensor. *Smart Materials and Structures*, 17, 2008.
- [64] H. Olsson, K. J. Astrom, C. C. de Wit, M. Gafvert, and P. Lischinsky. Friction models and friction compensation. *Eur. J. Control*, 4(3):176–195, 1998.
- [65] J.L. Pérez-Aparicio and H. Sosa. A continuum three-dimensional, fully coupled, dynamic, non-linear finite element formulation for magnetostrictive materials. *Smart Materials and Structures*, 13:493–502, 2004.
- [66] F. Preisach. Uber die magnetische nachwirkung. *Zeitschrift fur Physik*, 94:277–302, 1935.
- [67] S. Rafique, J.R. Cullen, M. Wuttig, and J. Cui. Magnetic anisotropy of fega alloys. *J. Appl. Phys.*, 95(11):6939–6941, 2004.
- [68] A. Raghunathan, Y. Melikhov, JE Snyder, and DC Jiles. Generalized form of anhysteretic magnetization function for Jiles–Atherton theory of hysteresis. *Applied Physics Letters*, 95:172510, 2009.
- [69] A. Ramesh, D.C. Jiles, and Y. Bi. Generalization of hysteresis modeling to anisotropic materials. *Journal of Applied Physics*, 81(8):5585–5587, 1997.
- [70] A. Reimers and E. Della Torre. Fast preisach based magnetosriction model for highly magnetostrictive materials. *IEEE Transactions on Magnetics*, 35(3):1239–1242, may 1999.
- [71] A. Reimers and E. Della Torre. Parameter identification of bimodal, magnetostrictive material model. *Journal of Applied Physics*, 85(8):4497, apr 1999.
- [72] James Restorff. Personal communication.
- [73] J.B. Restorff, M. Wun-Fogle, A.E. Clark, and K.B. Hathaway. Induced magnetic anisotropy in stress-annealed Galferol alloys. *IEEE Transactions on Magnetics*, 42(10):3087–3089, 2006.
- [74] N.N. Sarawate and M.J. Dapino. A dynamic actuation model for magnetostrictive materials. *Smart Materials and Structures*, 17:065013, 2008.

- [75] T. Shibayama, K. Ito, T. Gami, T. Oku, Z. Nakajima, and A. Ichikawa. Active engine mount for a large amplitude of engine vibration. *SAE*, (951298), 1995.
- [76] J.C. Slaughter. Coupled structural and magnetic models: Linear magnetostriction in comsol. *Proceedings of COMSOL Conference*, 2009.
- [77] E. Summers, T.A. Lograsso, J.D. Snodgrass, and J. Slaughter. Magnetic and mechanical properties of polycrystalline galfenol. *Proceedings of SPIE*, 5387:448–459, 2004.
- [78] T. Ueno, E. Summers, and T. Higuchi. Machining of iron-gallium for microactuator. *Proceedings of SPIE*, 6170:617000–7, 2006.
- [79] T. Ueno, E. Summers, M. Wun-Fogle, and T. Higuchi. Micro-magnetostrictive vibrator using iron-gallium alloy. *Sensors & Actuators A: Physical*, 148(1):–280, 2008.
- [80] T. Ushijima and S. Kumakawa. Active engine mount with piezo-actuator for vibration control. *SAE*, (930201), 1993.
- [81] JD Verhoeven, ED Gibson, OD McMasters, and HH Baker. The growth of single crystal terfenol-d crystals. *Metallurgical and Materials Transactions A*, 18(3):223–231, 1987.
- [82] Y. Wan, D. Fang, and K.C. Hwang. Non-linear constitutive relations for magnetostrictive materials. *International Journal of Non-Linear Mechanics*, 38(7):1053–1065, 2003.
- [83] J. Wang and B. Tong. Calculation of 3d eddy current problems using a modified T- Ω method. *Magnetics, IEEE Transactions on*, 24(1):114–117, 1988.
- [84] M. Wun-Fogle, J.B. Restorff, and A.E. Clark. Magnetomechanical coupling in stress-annealed Fe-Ga (Galfenol) alloys. *IEEE Transactions on Magnetics*, 42(10):3120–3122, October 2006.
- [85] M. Wun-Fogle, J.B. Restorff, and A.E. Clark. Magnetostriction of stress-annealed Fe-Ga and Fe-Ga-Al alloys under compressive and tensile stress. *Journal of Intelligent Material Systems and Structures*, 17:117–122, 2006.
- [86] Hwan-Sik Yoon, G. Washington, P. Eyabi, M. Radhamohan, S.W. Woodard, and R. Dayton. A millimeter-stroke piezoelectric hybrid actuator using hydraulic displacement amplification mechanism. *IEEE International Symposium on Industrial Electronics*, 4:2809–2813, July 2006.

- [87] Y. Yu, N.G. Naganathan, and R.V Dukkupati. A literature review of automobile engine mounting systems. In *Mechanisms and Machines Theory*, volume 36, pages 123–142, at <http://www.abc.edu>, May 1999. PDF file.
- [88] X.G. Zhao and D.G. Lord. Magnetostriction and susceptibilities of twinned single crystals of Terfenol-D. *Journal of Applied Physics*, 83:7276, 1998.
- [89] X.G. Zhao and D.G. Lord. Effect of demagnetization fields on the magnetization processes in Terfenol-D. *Journal of Magnetism and Magnetic Materials*, 195(3):699–707, 1999.
- [90] X.J. Zheng and X.E. Liu. A nonlinear constitutive model for Terfenol-D rods. *Journal of applied physics*, 97(5):053901, 2005.
- [91] X.J. Zheng and L. Sun. A nonlinear constitutive model of magneto-thermo-mechanical coupling for giant magnetostrictive materials. *Journal of Applied Physics*, 100(6):063906, 2006.
- [92] H. Zhou and Y. Zhou. Vibration suppression of laminated composite beams using actuators of giant magnetostrictive materials. *Smart materials and structures*, 16:198–206, 2007.